

YALINA Analytical Benchmark Analyses Using the Deterministic ERANOS Code System

Nuclear Engineering Division

About Argonne National Laboratory

Argonne is a U.S. Department of Energy laboratory managed by UChicago Argonne, LLC under contract DE-AC02-06CH11357. The Laboratory's main facility is outside Chicago, at 9700 South Cass Avenue, Argonne, Illinois 60439. For information about Argonne and its pioneering science and technology programs, see www.anl.gov.

Availability of This Report

This report is available, at no cost, at <http://www.osti.gov/bridge>. It is also available on paper to the U.S. Department of Energy and its contractors, for a processing fee, from:

U.S. Department of Energy

Office of Scientific and Technical Information

P.O. Box 62

Oak Ridge, TN 37831-0062

phone (865) 576-8401

fax (865) 576-5728

reports@adonis.osti.gov

Disclaimer

This report was prepared as an account of work sponsored by an agency of the United States Government. Neither the United States Government nor any agency thereof, nor UChicago Argonne, LLC, nor any of their employees or officers, makes any warranty, express or implied, or assumes any legal liability or responsibility for the accuracy, completeness, or usefulness of any information, apparatus, product, or process disclosed, or represents that its use would not infringe privately owned rights. Reference herein to any specific commercial product, process, or service by trade name, trademark, manufacturer, or otherwise, does not necessarily constitute or imply its endorsement, recommendation, or favoring by the United States Government or any agency thereof. The views and opinions of document authors expressed herein do not necessarily state or reflect those of the United States Government or any agency thereof, Argonne National Laboratory, or UChicago Argonne, LLC.

YALINA Analytical Benchmark Analyses Using the Deterministic ERANOS Code System

by
G. Aliberti and Y. Gohar
Nuclear Engineering Division, Argonne National Laboratory

work supported by the
Office of Global Nuclear Material Threat Reduction
U.S. Department of Energy
Under Contract DE-AC02-06CH11357

August 2009

YALINA Analytical Benchmark Analyses Using the Deterministic ERANOS Code System

Table of Contents

	Page
I. Introduction	2
II. YALINA Benchmark Specifications of the IAEA Coordinated Research Projects.....	2
II.1. YALINA-Booster Facility.....	2
II.1.a. The Lead Target.....	7
II.1.b. The Inner Part of the Fast Zone	7
II.1.c. The Outer Part of the fast Zone.....	7
II.1.d. The Absorber Zone	7
II.1.e. The Thermal Zone.....	7
II.1.f. The Deuteron Beam Tube.....	8
II.2. YALINA-Thermal Facility.....	8
II.2.a. Lead Target.....	13
II.2.b. Fuel Assembly.....	13
III. Performed Calculations.....	13
III.1. YALINA-Booster.....	13
III.2. YALINA Thermal	14
III.3. Additional Calculations.....	15
IV. Computational Tools.....	16
V. Cross-Section Processing	16
VI. Deterministic Results	17
VI.1. Multiplication Factor.....	17
VI.1.a. Perturbation Calculation	20
VI.2. Source Multiplication Factor, k_S	22
VI.3. Kinetic Parameters	30
VI.4. Neutron Spectra	34

VI.4.a. Neutron Spectra of the YALINA-Booster	35
VI.4.b. Neutron Spectra of the YALINA-Thermal	36
VI.4.c. Comparison of Neutron Spectra in the YALINA-Thermal Calculated with Different Approximations	37
VI.5. Reaction Rate Distributions	37
VI.5.a. Reaction Rate Distributions in the YALINA-Booster	39
VI.5.b. Reaction Rate Distributions in the YALINA-Thermal	41
VI.5.c. Comparison of Reaction Rate Distributions in the YALINA-Booster	42
VI.6. Pulse Calculations	43
VII. Conclusions	46
References	47
A.1. Fuel Pin Calculations	49
A.2. YALINA-Booster	51
A.3. YALINA-Thermal	62
Appendix F	79
Comparison of Neutron Spectra Calculated with Different Nuclear Data Libraries	79
Appendix G	84
Comparison of Reaction Rates Calculated with Different Nuclear Data Libraries	84
G.1. YALINA-Booster	84
H.1. ENDF/B-VI.8 Results	95

YALINA Analytical Benchmark Analyses Using the Deterministic ERANOS Code System

List of Figures

Page

Figure 1. XY Cross-Sectional View of the YALINA-Booster Assembly, Dimensions in mm	4
Figure 2. Fuel Loading of the YALINA-Booster Configuration with 902 EK-10 Fuel Rods.....	5
Figure 3. Fuel Loading of the YALINA-Booster Configuration with 1141 EK-10 Fuel Rods.....	5
Figure 4. YZ Cross-Sectional View of the YALINA-Booster Assembly (at X=4), Dimensions in mm.....	6
Figure 5. XZ Cross-Sectional View of the YALINA-Booster Assembly (at Y=4), Dimensions in mm.....	6
Figure 6. XZ and XY Cross-Sectional Views of a Fuel Rod Inside the Steel Casing, Dimensions in cm	9
Figure 7. XZ and XY Cross-Sectional View of the Boron Carbide Rod, Dimensions in cm	9
Figure 8. XZ and XY Cross-Sectional Views of the EK-10 Fuel Rod, Dimensions in cm.	9
Figure 9. Deuteron Beam Tube Design, Dimensions in mm.....	10
Figure 10. XY Cross-Sectional View of the YALINA-Thermal Assembly, Dimensions in mm.....	10
Figure 11. XY Cross-Section of the YALINA-Thermal Assembly with 216 EK-10 Fuel Rods	11
Figure 12. XY Cross-Section of the YALINA-Thermal Assembly with 245 EK-10 Fuel Rods	11
Figure 13. XY Cross-Section of the YALINA-Thermal Assembly with 280 EK-10 Fuel Rods (Target Side)	11
Figure 14. XY Cross-Section of the YALINA-Thermal Assembly with 280 EK-10 Fuel Rods (Beam Tube Side)	11
Figure 15. XZ Cross-Section of the YALINA-Thermal Assembly (Y=0), Dimensions in mm	12
Figure 16. YZ Cross-Section of the YALINA-Thermal Assembly (X=0), Dimensions in mm	12
Figure 17. EC2B Neutron Spectra in the YALINA-Booster	35
Figure 18. EC6T Neutron Spectra in the YALINA-Booster	35
Figure 19. EC8R Neutron Spectra in the YALINA-Booster	35
Figure 20. EC1 Neutron Spectra in the YALINA-Thermal.....	36
Figure 21. EC2 Neutron Spectra in the YALINA-Thermal.....	36
Figure 22. EC3 Neutron Spectra in the YALINA-Thermal.....	36
Figure 23. EC5 Neutron Spectra in the YALINA-Thermal.....	36
Figure 24. EC6 Neutron Spectra in the YALINA-Thermal.....	37

Figure 25. EC2 Neutron Spectra in the YALINA-Thermal with Different Approximations	37
Figure 26. EC6T He-3 (n,p) Reaction Rates	39
Figure 27. EC2B U-235 Fission Reaction Rates	39
Figure 28. EC6T U-235 fission Reaction Rates	39
Figure 29. EC2B In-115 Capture Reaction Rates	39
Figure 30. EC5T In-115 Capture Reaction Rates	39
Figure 31. EC6T In-115 Capture Reaction Rates in the YALINA-Booster. Polyethylene Holder is Modeled.....	39
Figure 32. EC7T In-115 Capture Reaction Rates	40
Figure 33. EC10R In-115 Capture Reaction Rates in the YALINA-Booster. Polyethylene Holder is Modeled.....	40
Figure 34. EC2B Au-197 Capture Reaction Rates	40
Figure 35. EC6T Au-197 Capture Reaction Rates in the YALINA-Booster. Polyethylene Holder is Modeled.....	40
Figure 36. EC2B Mn-55 Capture Reaction Rates	40
Figure 37. EC6T Mn-55 Capture Reaction Rates in the YALINA-Booster. Polyethylene Holder is Modeled.....	40
Figure 38. EC1 He-3 (n,p) Reaction Rates	41
Figure 39. EC2 He-3 (n,p) Reaction Rates	41
Figure 40. EC3 He-3 (n,p) Reaction Rates	41
Figure 41. EC1 U-235 Fission Reaction Rates	41
Figure 42. EC2 U-235 Fission Reaction Rates	41
Figure 43. EC3 U-235 Fission Reaction Rates	41
Figure 44. EC2 In-115 Capture Reaction Rates	42
Figure 45. EC7 In-115 Capture Reaction Rates in the YALINA-Thermal. Polyethylene Holder is Modeled.....	42
Figure 46. EC2 Au-197 Capture Reaction Rates.....	42
Figure 47. EC2 Mn-55 Capture Reaction Rates in the YALINA-Thermal. Polyethylene Holder is Modeled.....	42
Figure 48. EC6T He-3 (n,p) Reaction Rates	42
Figure 49. EC2B U-235 Fission Reaction Rates.....	42
Figure 50. JEF3.1 EC6T Detector Response with (d,t) Neutron Source for the YALINA-Booster	43
Figure 51. JEF3.1 EC8R Detector Response with (d,t) Neutron Source for the YALINA-Booster.....	43
Figure 52. JEF3.1 EC1B Detector Response with (d,t) Neutron Source for the YALINA-Booster.....	44

Figure 53. JEF3.1 EC2B Detector Response with (d,t) Neutron Source for the YALINA-Booster.....	44
Figure 54. JEF3.1 EC3B Detector Response with (d,t) Neutron Source for the YALINA-Booster.....	44
Figure 55. JEF3.1 EC6T Detector Response with (d,d) Neutron Source for the YALINA-Booster.....	44
Figure 56. JEF3.1 EC8R Detector Response with (d,d) Neutron Source for the YALINA-Booster.....	44
Figure 57. JEF3.1 EC1B Detector Response with (d,d) Neutron Source for the YALINA-Booster.....	44
Figure 58. JEF3.1 EC2B Detector Response with (d,d) Neutron Source for the YALINA-Booster.....	45
Figure 59. JEF3.1 EC3B Detector Response with (d,d) Neutron Source for the YALINA-Booster.....	45
Figure 60. JEF3.1 EC2 Detector Response with (d,t) Neutron Source for the YALINA-Thermal.....	45
Figure 61. JEF3.1 EC5 Detector Response with (d,t) Neutron Source for the YALINA-Thermal.....	45
Figure 62. JEF3.1 EC1 Detector Response with (d,t) Neutron Source for the YALINA-Thermal.....	45
Figure 63. JEF3.1 EC2 Detector Response with (d,d) Neutron Source for the YALINA-Thermal.....	45
Figure 64. JEF3.1 EC5 Detector Response with (d,d) Neutron Source for the YALINA-Thermal.....	46
Figure 65. JEF3.1 EC1 Detector Response with (d,d) Neutron Source for the YALINA-Thermal.....	46
Figure 66. YALINA-Thermal Fuel Cell.....	49
Figure 67. Comparison of MCNPX and ERANOS Averaged Fuel Cell Neutron Spectra.....	50
Figure 68. Comparison of MCNPX and ERANOS Averaged Fuel Pin Neutron Spectra.....	50
Figure 69. Comparison of MCNPX and ERANOS Averaged Aluminum Clad Neutron Spectra.....	50
Figure 70. Comparison of MCNPX and ERANOS Averaged Air Gap Neutron Spectra.....	50
Figure 71. Comparison of MCNPX and ERANOS Averaged Polyethylene Neutron Spectra.....	50
Figure 72. Comparison of MCNPX Fuel Pin Neutron Spectra and ERANOS Neutron Spectra from Different Fuel Pin regions.....	50
Figure 73. Comparison of MCNPX Polyethylene Neutron Spectra and ERANOS Neutron Spectra from Different Polyethylene regions.....	51
Figure 74. XZ Layout of the YALINA-Booster Deterministic Model (Experimental Channels are not Represented).....	52
Figure 75. YZ Layout of the YALINA-Booster Deterministic Model (Experimental Channels are not Represented).....	52
Figure 76. XY Layout of the YALINA-Booster Deterministic Model.....	53
Figure 77. Homogenization of the Air Gap with the Graphite Reflector (Zones 24 and 26) and of the Air with Borated Polyethylene (Zone 23).....	54
Figure 78. Cell Scheme for Zone 9.....	54
Figure 79. Cell Scheme for Zone 13.....	54
Figure 80. Cell Scheme for Zone 17A.....	54

Figure 81. Cell Scheme for Zone 17B.....	55
Figure 82. Cell Scheme for Zone 21A.....	55
Figure 83. Cell Scheme for Zone 21B.....	55
Figure 84. Cell Scheme and Representation of the Assembly Steel Structure.....	55
Figure 85. Bottom Part of the 90% U-235 Enriched Metallic, the 36% U-235 Enriched Uranium Oxide, and the Natural Uranium Fuel Rods	56
Figure 86. Top Part of the 90% U-235 Enriched Metallic, the 36% U-235 Enriched Uranium Oxide, and the Natural Uranium Fuel Rods	56
Figure 87. Bottom Part of B ₄ C Rods	56
Figure 88. Top Part of B ₄ C Rods	56
Figure 89. Bottom Part of EK-10 Fuel Rods	57
Figure 90. Top Part of EK-10 Fuel Rods.....	57
Figure 91. Cell Scheme for Zone 8 (8.4<Z<13.4 and 63.4<Z<67.9).....	57
Figure 92. Cell Scheme for Zone 7 (6.4<Z<8.4) and 10 (67.9<Z<70.9)	57
Figure 93. Cell Scheme for Zone 12 (8.4<Z<13.4 and 63.4<Z<67.9).....	57
Figure 94. Cell Scheme for Zone 11 (6.4<Z<8.4) and 14 (67.9<Z<70.9)	58
Figure 95. Cell Scheme for Zone 16 (8.4<Z<13.4 and 63.4<Z<67.9).....	58
Figure 96. Cell Scheme for Zone 15 (6.4<Z<8.4) and 18 (67.9<Z<70.9)	58
Figure 97. Cell Scheme for Zone 16 (8.4<Z<13.4 and 63.4<Z<67.9) at the Corner.....	58
Figure 98. Cell Scheme for Zone 15 (6.4<Z<8.4) and 18 (67.9<Z<70.9) at the Corner	58
Figure 99. Cell Scheme for Zone 20 (10.7<Z<13.4 and 63.4<Z<66.1).....	58
Figure 100. Cell Scheme for Zone 19 (8.4<Z<10.7) and 22 (66.1<Z<67.9)	59
Figure 101. YALINA-Booster Calculational Models of the Central Assembly	60
Figure 102. EC4B Experimental Channel	61
Figure 103. EC1B Experimental Channel	61
Figure 104. EC1B Calculational Model	61
Figure 105. EC5T Experimental Channel	62
Figure 106. EC5T Calculational Model	62
Figure 107. Three Void Channels for the Boron Carbide Rods	62
Figure 108. The calculational model of the three Void Channels for the Boron Carbide Rods.....	62
Figure 109. XZ Model for the YALINA-Thermal Deterministic Model (Experimental Channels are not Represented).....	64

Figure 110. YZ Model for the YALINA-Thermal Deterministic Model (Experimental Channels are not Represented).....	64
Figure 111. XY Layout of the YALINA-Thermal Deterministic Model	65
Figure 112. Homogenization of Air with Graphite Reflector of Zone 12.....	65
Figure 113. Cell Scheme for Zone 9A.....	66
Figure 114. Cell Scheme for Zone 9B.....	66
Figure 115. Cell Scheme for MC1 – MC4 Measurement Channels.....	66
Figure 116. Bottom Part of EK-10 Fuel Rods	66
Figure 117. Top Part of EK-10 Fuel Rods.....	66
Figure 118. Cell Scheme for Zone 20 ($2.2 < Z < 4.9$ and $54.9 < Z < 57.6$).....	67
Figure 119. Cell Scheme for Zone 19 ($0 < Z < 2.2$) and 22 ($57.6 < Z < 59.5$)	67
Figure 120. YALINA-Thermal Calculational Models of the Central Assembly	68
Figure 121. EC2 Experimental Channel	69
Figure 122. EC2 Experimental Channel Model.....	69
Figure 123. Three Channel for the B ₄ C Rods	69
Figure 124. Calculational Model of the Three Channels for the B ₄ C Rods	69
Figure 125. RZ Geometrical Model of the YALINA-Booster.....	70
Figure 126. RZ Geometrical Model of the YALINA-Thermal.....	71
Figure 127. EC2B Neutron Spectra of the YALINA-Booster with (d,t) Neutron Source.....	79
Figure 128. EC6T Neutron Spectra of the YALINA-Booster with (d,t) Neutron Source	79
Figure 129. EC8R Neutron Spectra of the YALINA-Booster with (d,t) Neutron Source.....	79
Figure 130. EC2B Neutron Spectra of the YALINA-Booster with (d,d) Neutron Source	79
Figure 131. EC6T Neutron Spectra of the YALINA-Booster with (d,d) Neutron Source	80
Figure 132. EC8R Neutron Spectra of the YALINA-Booster with (d,d) Neutron Source.....	80
Figure 133. EC2B Neutron Spectra of the YALINA-Booster with Cf Neutron Source.....	80
Figure 134. EC6T Neutron Spectra of the YALINA-Booster with Cf Neutron Source	80
Figure 135. EC8R Neutron Spectra of the YALINA-Booster with Cf Neutron Source.....	80
Figure 136. EC1 Neutron Spectra of the YALINA-Thermal with (d,t) Neutron Source.....	81
Figure 137. EC2 Neutron Spectra of the YALINA-Thermal with (d,t) Neutron Source.....	81
Figure 138. EC3 Neutron Spectra of the YALINA-Thermal with (d,t) Neutron Source.....	81
Figure 139. EC5 Neutron Spectra of the YALINA-Thermal with (d,t) Neutron Source.....	81
Figure 140. EC6 Neutron Spectra of the YALINA-Thermal with (d,t) Neutron Source.....	81

Figure 141. EC1 Neutron Spectra of the YALINA-Thermal with (d,d) Neutron Source.....	81
Figure 142. EC2 Neutron Spectra of the YALINA-Thermal with (d,d) Neutron Source.....	82
Figure 143. EC3 Neutron Spectra of the YALINA-Thermal with (d,d) Neutron Source.....	82
Figure 144. EC5 Neutron Spectra of the YALINA-Thermal with (d,d) Neutron Source.....	82
Figure 145. EC6 Neutron Spectra of the YALINA-Thermal with (d,d) Neutron Source.....	82
Figure 146. EC1 Neutron Spectra of the YALINA-Thermal with Cf Neutron Source	82
Figure 147. EC2 Neutron Spectra of the YALINA-Thermal with Cf Neutron Source	82
Figure 148. EC3 Neutron Spectra of the YALINA-Thermal with Cf Neutron Source	83
Figure 149. EC5 Neutron Spectra of the YALINA-Thermal with Cf Neutron Source	83
Figure 150. EC6 Neutron Spectra of the YALINA-Thermal with Cf Neutron Source	83
Figure 151. He-3(n,p) Reaction Rate in EC6T Experimental Channel of the YALINA-Booster with (d,t) Source	84
Figure 152. U-235 Fission Reaction Rate in EC2B Experimental Channel of the YALINA-Booster with (d,t) Source.....	84
Figure 153. U-235 Fission Reaction Rate in EC6T Experimental Channel of the YALINA-Booster with (d,t) Source.....	84
Figure 154. In-115 Capture Reaction Rate in EC2B Experimental Channel of the YALINA-Booster with (d,t) Source. Lead Holder is Modeled.....	84
Figure 155. In-115 Capture Reaction Rate in EC5T Experimental Channel of the YALINA-Booster with (d,t) Source. Polyethylene Holder is Modeled	84
Figure 156. In-115 Capture Reaction Rate in EC6T Experimental Channel of the YALINA-Booster with (d,t) Source. Polyethylene Holder is Modeled	84
Figure 157. In-115 Capture Reaction Rate in EC7T Experimental Channel of the YALINA-Booster with (d,t) Source. Polyethylene Holder is Modeled	85
Figure 158. In-115 Capture Reaction Rate in EC10R Experimental Channel of the YALINA-Booster with (d,t) Source. Polyethylene Holder is Modeled.....	85
Figure 159. Au-197 Capture Reaction Rate in EC2B Experimental Channel of the YALINA-Booster with (d,t) Source. Lead Holder is Modeled	85
Figure 160. Au-197 Capture Reaction Rate in EC6T Experimental Channel of the YALINA-Booster with (d,t) Source. Polyethylene Holder is Modeled.....	85
Figure 161. Mn-55 Capture Reaction Rate in EC2B Experimental Channel of the YALINA-Booster with (d,t) Source. Lead Holder is Modeled.....	85
Figure 162. Mn-55 Capture Reaction Rate in EC6T Experimental Channel of the YALINA-Booster with (d,t) Source. Polyethylene Holder is Modeled	85
Figure 163. He-3(n,p) Capture Reaction Rate in EC6T Experimental Channel of the YALINA-Booster with (d,d) Source	86

Figure 164. U-235 Fission Capture Reaction Rate in EC2B Experimental Channel of the YALINA-Booster with (d,d) Source	86
Figure 165. U-235 Fission Capture Reaction Rate in EC6T Experimental Channel of the YALINA-Booster with (d,d) Source	86
Figure 166. In-115 Capture Reaction Rate in EC2B Experimental Channel of the YALINA-Booster with (d,d) Source. Lead Holder is Modeled.....	86
Figure 167. In-115 Capture Reaction Rate in EC5T Experimental Channel of the YALINA-Booster with (d,d) Source. Polyethylene Holder is Modeled	86
Figure 168. In-115 Capture Reaction Rate in EC6T Experimental Channel of the YALINA-Booster with (d,d) Source. Polyethylene Holder is Modeled	86
Figure 169. In-115 Capture Reaction Rate in EC7T Experimental Channel of the YALINA-Booster with (d,d) Source. Polyethylene Holder is Modeled	87
Figure 170. In-115 Capture Reaction Rate in EC10R Experimental Channel of the YALINA-Booster with (d,d) Source. Polyethylene Holder is Modeled.....	87
Figure 171. Au-197 Capture Reaction Rate in EC2B Experimental Channel of the YALINA-Booster with (d,d) Source. Lead Holder is Modeled	87
Figure 172. Au-197 Capture Reaction Rate in EC6T Experimental Channel of the YALINA-Booster with (d,d) Source. Polyethylene Holder is Modeled.....	87
Figure 173. Mn-55 Capture Reaction Rate in EC2B Experimental Channel of the YALINA-Booster with (d,d) Source. Lead Holder is Modeled.....	87
Figure 174. Mn-55 Capture Reaction Rate in EC6T Experimental Channel of the YALINA-Booster with (d,d) Source. Polyethylene Holder is Modeled	87
Figure 175. He-3(n,p) Reaction Rate in EC6T Experimental Channel of the YALINA-Booster with Cf Neutron Source	88
Figure 176. U-235 Fission Reaction Rate in EC2B Experimental Channel of the YALINA-Booster with Cf Neutron Source.....	88
Figure 177. U-235 Fission Reaction Rate in EC6T Experimental Channel of the YALINA-Booster with Cf Neutron Source.....	88
Figure 178. In-115 Capture Reaction Rate in EC2B Experimental Channel of the YALINA-Booster with Cf Neutron Source. Lead Holder is Modeled.....	88
Figure 179. In-115 Capture Reaction Rate in EC5T Experimental Channel of the YALINA-Booster with Cf Neutron Source. Polyethylene Holder is Modeled	88
Figure 180. In-115 Capture Reaction Rate in EC6T Experimental Channel of the YALINA-Booster with Cf Neutron Source. Polyethylene Holder is Modeled	88
Figure 181. In-115 Capture Reaction Rate in EC7T Experimental Channel of the YALINA-Booster with Cf Neutron Source. Polyethylene Holder is Modeled	89
Figure 182. In-115 Capture Reaction Rate in EC10R Experimental Channel of the YALINA-Booster with Cf Neutron Source. Polyethylene Holder is Modeled.....	89
Figure 183. Au-197 Capture Reaction Rate in EC2B Experimental Channel of the YALINA-Booster with Cf Neutron Source. Lead Holder is Modeled	89

Figure 184. Au-197 Capture Reaction Rate in EC6T Experimental Channel of the YALINA-Booster with Cf Neutron Source. Polyethylene Holder is Modeled	89
Figure 185. Mn-55 Capture Reaction Rate in EC2B Experimental Channel of the YALINA-Booster with Cf Neutron Source. Lead Holder is Modeled.....	89
Figure 186. Mn-55 Capture Reaction Rate in EC6T Experimental Channel of the YALINA-Booster with Cf Neutron Source. Polyethylene Holder is Modeled	89
Figure 187. He-3(n,p) Reaction Rate in EC1 Experimental Channel of the YALINA-Thermal with (d,t) Neutron Source	90
Figure 188. He-3(n,p) Reaction Rate in EC2 Experimental Channel of the YALINA-Thermal with (d,t) Neutron Source	90
Figure 189. He-3(n,p) Reaction Rate in EC3 Experimental Channel of the YALINA-Thermal with (d,t) Neutron Source	90
Figure 190. U-235 Fission Reaction Rate in EC1 Experimental Channel of the YALINA-Thermal with (d,t) Neutron Source	90
Figure 191. U-235 Fission Reaction Rate in EC2 Experimental Channel of the YALINA-Thermal with (d,t) Neutron Source	90
Figure 192. U-235 Fission Reaction Rate in EC3 Experimental Channel of the YALINA-Thermal with (d,t) Neutron Source	90
Figure 193. In-115 Capture Reaction Rate in EC2 Experimental Channel of the YALINA-Thermal with (d,t) Neutron Source. Polyethylene Holder is Modeled	91
Figure 194. In-115 Capture Reaction Rate in EC7 Experimental Channel of the YALINA-Thermal with (d,t) Neutron Source. Polyethylene Holder is Modeled	91
Figure 195. Au-197 Capture Reaction Rate in EC2 Experimental Channel of the YALINA-Thermal with (d,t) Neutron Source. Polyethylene Holder is Modeled	91
Figure 196. Mn-55 Capture Reaction Rate in EC2 Experimental Channel of the YALINA-Thermal with (d,t) Neutron Source. Polyethylene Holder is Modeled	91
Figure 197. He-3(n,p) Reaction Rate in EC1 Experimental Channel of the YALINA-Thermal with (d,d) Neutron Source	91
Figure 198. He-3(n,p) Reaction Rate in EC2 Experimental Channel of the YALINA-Thermal with (d,d) Neutron Source	91
Figure 199. He-3(n,p) Reaction Rate in EC3 Experimental Channel of the YALINA-Thermal with (d,d) Neutron Source	92
Figure 200. U-235 Fission Reaction Rate in EC1 Experimental Channel of the YALINA-Thermal with (d,d) Neutron Source	92
Figure 201. U-235 Fission Reaction Rate in EC2 Experimental Channel of the YALINA-Thermal with (d,d) Neutron Source	92
Figure 202. U-235 Fission Reaction Rate in EC3 Experimental Channel of the YALINA-Thermal with (d,d) Neutron Source	92
Figure 203. In-115 Capture Reaction Rate in EC2 Experimental Channel of the YALINA-Thermal with (d,d) Neutron Source. Polyethylene Holder is modeled	92

Figure 204. In-115 Capture Reaction Rate in EC7 Experimental Channel of the YALINA-Thermal with (d,d) Neutron Source. Polyethylene Holder is modeled	92
Figure 205. Au-197 Capture Reaction Rate in EC2 Experimental Channel of the YALINA-Thermal with (d,d) Neutron Source. Polyethylene Holder is modeled	93
Figure 206. Mn-55 Capture Reaction Rate in EC2 Experimental Channel of the YALINA-Thermal with (d,d) Neutron Source. Polyethylene Holder is modeled	93
Figure 207. He-3(n,p) Reaction Rate in EC1 Experimental Channel of the YALINA-Thermal with Cf Neutron Source	93
Figure 208. He-3(n,p) Reaction Rate in EC2 Experimental Channel of the YALINA-Thermal with Cf Neutron Source	93
Figure 209. He-3(n,p) Reaction Rate in EC3 Experimental Channel of the YALINA-Thermal with Cf Neutron Source	93
Figure 210. U-235 Fission Reaction Rate in EC1 Experimental Channel of the YALINA-Thermal with Cf Neutron Source.....	93
Figure 211. U-235 Fission Reaction Rate in EC2 Experimental Channel of the YALINA-Thermal with Cf Neutron Source.....	94
Figure 212. U-235 Fission Reaction Rate in EC3 Experimental Channel of the YALINA-Thermal with Cf Neutron Source.....	94
Figure 213. In-115 Capture Reaction Rate in EC2 Experimental Channel of the YALINA-Thermal with Cf Neutron Source. Polyethylene Holder is modeled	94
Figure 214. In-115 Capture Reaction Rate in EC7 Experimental Channel of the YALINA-Thermal with Cf Neutron Source. Polyethylene Holder is modeled	94
Figure 215. Au-197 Capture Reaction Rate in EC2 Experimental Channel of the YALINA-Thermal with Cf Neutron Source. Polyethylene Holder is modeled	94
Figure 216. Mn-55 Capture Reaction Rate in EC2 Experimental Channel of the YALINA-Thermal with Cf Neutron Source. Polyethylene Holder is modeled	94
Figure 217. He-3 Detector Response in EC6T Experimental Channel of the YALINA-Booster with (d,t) Neutron Source	95
Figure 218. He-3 Detector Response in EC8R Experimental Channel of the YALINA-Booster with (d,t) Neutron Source	95
Figure 219. He-3 Detector Response in EC1B Experimental Channel of the YALINA-Booster with (d,t) Neutron Source	95
Figure 220. He-3 Detector Response in EC2B Experimental Channel of the YALINA-Booster with (d,t) Neutron Source	95
Figure 221. He-3 Detector Response in EC3B Experimental Channel of the YALINA-Booster with (d,t) Neutron Source	96
Figure 222. He-3 Detector Response in EC6T Experimental Channel of the YALINA-Booster with (d,d) Neutron Source	96
Figure 223. He-3 Detector Response in EC8R Experimental Channel of the YALINA-Booster with (d,d) Neutron Source	96

Figure 224. He-3 Detector Response in EC1B Experimental Channel of the YALINA-Booster with (d,d) Neutron Source	96
Figure 225. He-3 Detector Response in EC2B Experimental Channel of the YALINA-Booster with (d,d) Neutron Source	96
Figure 226. He-3 Detector Response in EC3B Experimental Channel of the YALINA-Booster with (d,d) Neutron Source	96
Figure 227. He-3 Detector Response in EC2 Experimental Channel of the YALINA-Thermal with (d,t) Neutron Source	97
Figure 228. He-3 Detector Response in EC5 Experimental Channel of the YALINA-Thermal with (d,t) Neutron Source	97
Figure 229. He-3 Detector Response in EC1 Experimental Channel of the YALINA-Thermal with (d,t) Neutron Source	97
Figure 230. He-3 Detector Response in EC2 Experimental Channel of the YALINA-Thermal with (d,t) Neutron Source	97
Figure 231. He-3 Detector Response in EC5 Experimental Channel of the YALINA-Thermal with (d,d) Neutron Source	97
Figure 232. He-3 Detector Response in EC1 Experimental Channel of the YALINA-Thermal with (d,d) Neutron Source	97
Figure 233. He-3 Detector Response in EC1B Experimental Channel of the YALINA-Booster with (d,t) Neutron Source	98
Figure 234. He-3 Detector Response in EC2B Experimental Channel of the YALINA-Booster with (d,t) Neutron Source	98
Figure 235. He-3 Detector Response in EC3B Experimental Channel of the YALINA-Booster with (d,t) Neutron Source	98
Figure 236. He-3 Detector Response in EC1B Experimental Channel of the YALINA-Booster with (d,d) Neutron Source	98
Figure 237. He-3 Detector Response in EC2B Experimental Channel of the YALINA-Booster with (d,d) Neutron Source	98
Figure 238. He-3 Detector Response in EC3B Experimental Channel of the YALINA-Booster with (d,d) Neutron Source	98

YALINA Analytical Benchmark Analyses Using the Deterministic ERANOS Code System

List of Tables

	Page
Table 1. Calculated keff (Reactivity) with VARIANT for the YALINA-Booster.....	18
Table 2. Calculated keff (Reactivity) with VARIANT for the YALINA-Thermal.....	18
Table 3. Calculated keff (Reactivity) with VARIANT for the YALINA-Booster.....	19
Table 4. Calculated keff (Reactivity) with VARIANT for the YALINA-Thermal.....	19
Table 5. Final keff (Reactivity) with VARIANT for the YALINA-Booster.....	19
Table 6. Final keff (Reactivity) with VARIANT for the YALINA-Thermal.....	20
Table 7. Calculated keff (Reactivity [pcm]) with RZ BISTRO Model for the YALINA-Booster.....	20
Table 8. Calculated keff (Reactivity [pcm]) with RZ BISTRO Model for the YALINA-Thermal.....	20
Table 9. Perturbation Components [pcm] for the YALINA-Booster.....	21
Table 10. Perturbation Components [pcm] for the YALINA-Thermal.....	22
Table 11. Neutron Balance per Neutron Source and kS for the YALINA-Booster.....	24
Table 12. Neutron Balance per Neutron Source and kS for the YALINA-Booster.....	25
Table 13. Neutron Balance per Neutron Source and kS for the YALINA-Booster.....	26
Table 14. Neutron Balance per Neutron Source and kS for the YALINA-Thermal.....	27
Table 15. Neutron Balance per Neutron Source and kS for the YALINA-Thermal.....	28
Table 16. ρ S Results for the YALINA-Booster.....	29
Table 17. ρ S Results for the YALINA-Thermal.....	29
Table 18. kS (ρ S) for the YALINA-Booster calculated with 172 Energy Group Set and P5P1 Approximations.....	29
Table 19. kS (ρ S) for the YALINA-Thermal calculated with 172 Energy Group Set and P5P1 Approximations.....	30
Table 20. Calculated β_{eff} Values for the YALINA-Booster.....	30
Table 21. Calculated β_{eff} Values for the YALINA-Thermal.....	31
Table 22. Calculated Λ_{eff} Values for the YALINA-Booster.....	31
Table 23. Calculated Λ_{eff} Values for the YALINA-Thermal.....	31
Table 24. Calculated β_{eff} [pcm] of the YALINA Configurations with RZ Geometry.....	32

Table 25. Calculated Λ_{eff} [μs] for the YALINA Configuration in RZ Geometry	32
Table 26. $\Delta\beta_{\text{eff}}$ [pcm] Due to the Use of Different External Neutron Source Relative to the case without External Neutron Source with RZ Geometry.....	33
Table 27. $\Delta\Lambda_{\text{eff}}$ [μs] Due to the Use of Different External Neutron Source Relative to the case without External Neutron Source with RZ Geometry	33
Table 28. β_{eff} [pcm] Adjoint Flux Weighted Values for the YALINA Configurations	33
Table 29. Λ_{eff} [μs] Adjoint Flux Weighted Values for the YALINA Configurations.....	34
Table 30. k_{eff} Values Comparison between MCNPx and ERANOS.....	49
Table 31. The 172-Energy Group Structure.....	72
Table 32. The 53-Energy Group Structure.....	73
Table 33. 172 Energy Group Distribution of the Cf-252 Source	74
Table 34. 53 Energy Group Distribution of the Cf-252 Source	75
Table 35. ENDF/B Delayed Time Constants [sec.-1].....	76
Table 36. ENDF/B β_v	76
Table 37. Calculated ENDF/B Delayed Neutron Spectra for the YALINA-Booster	77
Table 38. Calculated ENDF/B Delayed Neutron Spectra for the YALINA-Thermal	78

YALINA Analytical Benchmark Analyses Using the Deterministic ERANOS Code System

Abstract

This report presents the analytical analyses obtained with the deterministic ERANOS code system for the YALINA facility within: a) the collaboration between Argonne National Laboratory (ANL) of USA and the Joint Institute for Power and Nuclear Research (JIPNR) Sosny of Belarus; and b) the IAEA coordinated research projects for accelerator driven systems (ADS). This activity is conducted as a part of the Russian Research Reactor Fuel Return (RRRFR) Program and the Global Threat Reduction Initiative (GTRI) of DOE/NNSA.

YALINA Analytical Benchmark Analyses Using the Deterministic ERANOS Code System

I. Introduction

The growing stockpile of nuclear waste constitutes a severe challenge for the mankind for more than hundred thousand years. To reduce the radiotoxicity of the nuclear waste, the Accelerator Driven System (ADS) has been proposed [1,2]. One of the most important issues of ADSs technology is the choice of the appropriate neutron spectrum for the transmutation of Minor Actinides (MA) and Long Lived Fission Products (LLFP).

An experimental program has been launched by the Joint Institute for Power and Nuclear Research – SOSNY (JIPNR-SOSNY), National Academy of Sciences of Belarus [3,4] with the purpose to study the ADS physics and to investigate the transmutation of MA and LLFP using the YALINA facility.

In order to construct an ADS, calculations methods have to be developed in order to predict the performance of such systems. The IAEA has taken the initiative to start a set of ADS benchmarks [5,6]. These benchmarks, are part of the IAEA Coordinated Research Projects (CRP): “*Analytical and Experimental Analysis of Accelerator Driven Systems*” and “*Low Enriched Uranium Fuel Utilization in Accelerator Driven Sub-Critical Assembly Systems*” [7,8]. The main purpose is to compare the results from different calculational methods, performed by different research institutes, with each other and with the experimental data. The benchmarks are based on the current YALINA facility configurations, which provide the opportunity to verify the prediction capability of the different calculational methods. The YALINA facility has two subcritical assemblies: the YALINA-Booster and -Thermal. The two configurations and their operating conditions define the benchmark specifications and the required calculations with Cf-252, (d,d), and (d,t) neutron sources.

II. YALINA Benchmark Specifications of the IAEA Coordinated Research Projects

The subcritical assemblies object of the benchmark are the YALINA-Booster and -Thermal. In this section, a short description of the two assemblies followed by the required benchmark calculations are presented.

II.1. YALINA-Booster Facility

The YALINA-Booster has been designed to have both fast and thermal neutron spectra in one configuration and to achieve neutron flux densities as high as possible in a subcritical configuration. In addition, the subcritical assembly together with the highly intensive neutron generator makes the YALINA-Booster assembly interesting for performing ADS kinetics research [9].

The YALINA-Booster operates with $k_{eff} < 0.98$ under all conditions for safety purposes. The subcritical assembly is driven by an external neutron source: a Cf-252 neutron source or a deuteron accelerator with deuterium or tritium targets for neutron production. The YALINA-Booster shown in Figure 1 couples a fast zone (“booster”) of two U-235 enrichments (90%, and

36%) in a lead lattice and a thermal zone with 10% enrichment of U-235 (EK-10 fuel rods) in a polyethylene moderator. The booster zone multiplies the external neutrons through the fission reactions of Uranium and (n,xn) reactions of lead. The produced neutrons leak to the surrounding thermal zone. Between the two zones, there is an interface, called the “valve” zone, consisting of two layers. The inner layer has metallic natural uranium rods and the outer layer has boron carbide rods for absorbing the thermal neutrons. Such “valve” zone enables fast neutrons to scatter between the fast and the thermal zone and prevents thermal neutrons from entering the fast zone from the thermal zone.

The fast booster zone consists of 36 lead subassemblies. The thermal zone consists of 108 polyethylene subassemblies. For structural reasons, the subassemblies are encased into a stainless steel frame and nine subassemblies are arranged in each frame. The frame thickness is 4 mm and the total length along the z-axis is 771 mm in the thermal zone and 804 mm in the fast zone. The central part of the fast zone has highly enriched (90%) metallic uranium fuel rods inserted in a lead block as shown in Figures 2 and 3.

The YALINA-Booster is radially surrounded by a graphite reflector and axially by borated polyethylene. The radial reflector and the backside of the thermal zone are covered by organic glass sheets. There are four axial experimental channels (EC1B, EC2B, EC3B, and EC4B) in the fast zone, three axial experimental channels in the thermal zone (EC5T, EC6T, and EC7T), two axial experimental channels (EC8R, located 32 mm below the assembly mid-plane and 520 mm left of the assembly center line, and EC9R, located 356 mm below the assembly mid-plane and 600 mm right of the assembly center line) and one radial experimental channel in the reflector zone (EC10R). All experimental channels are shown in Figure 1.

Two YALINA-Booster configurations are considered in the benchmark. The number of EK-10 fuel rods in the two configurations are 1141 and 902. Figures 2 and 3 show the core loading of these two configurations. The geometrical details used for generating the calculation models are presented in the XZ and YZ cross-sectional views shown in Figures 4 and 5. Additional information can be found in Ref. 5.

The subcritical assembly of the YALINA-Booster facility is made of rectangular parallelepiped sections. The central axis of the assembly is aligned horizontally. The deuteron target can be situated along the central axis at different distances from the assembly center.

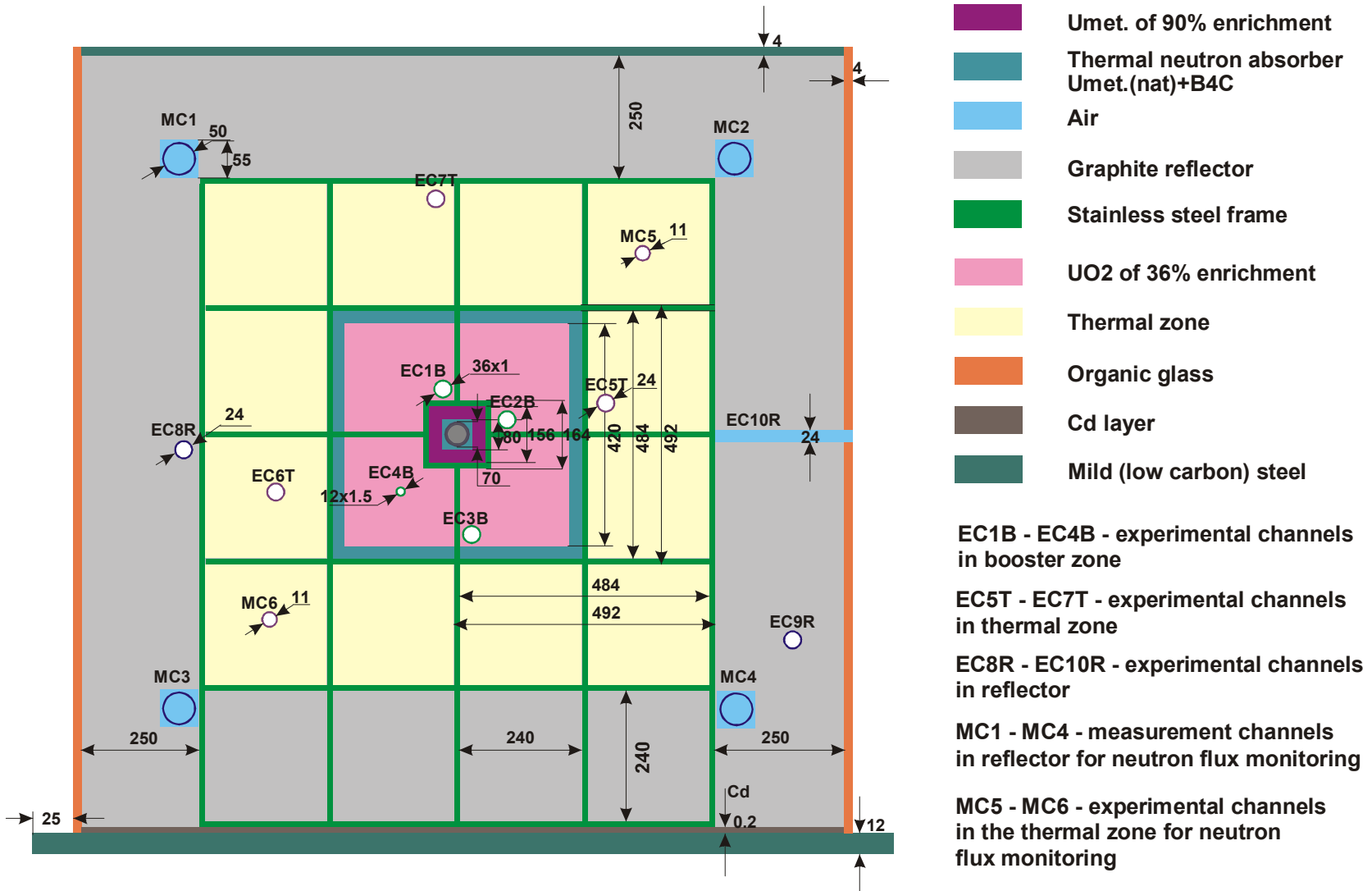
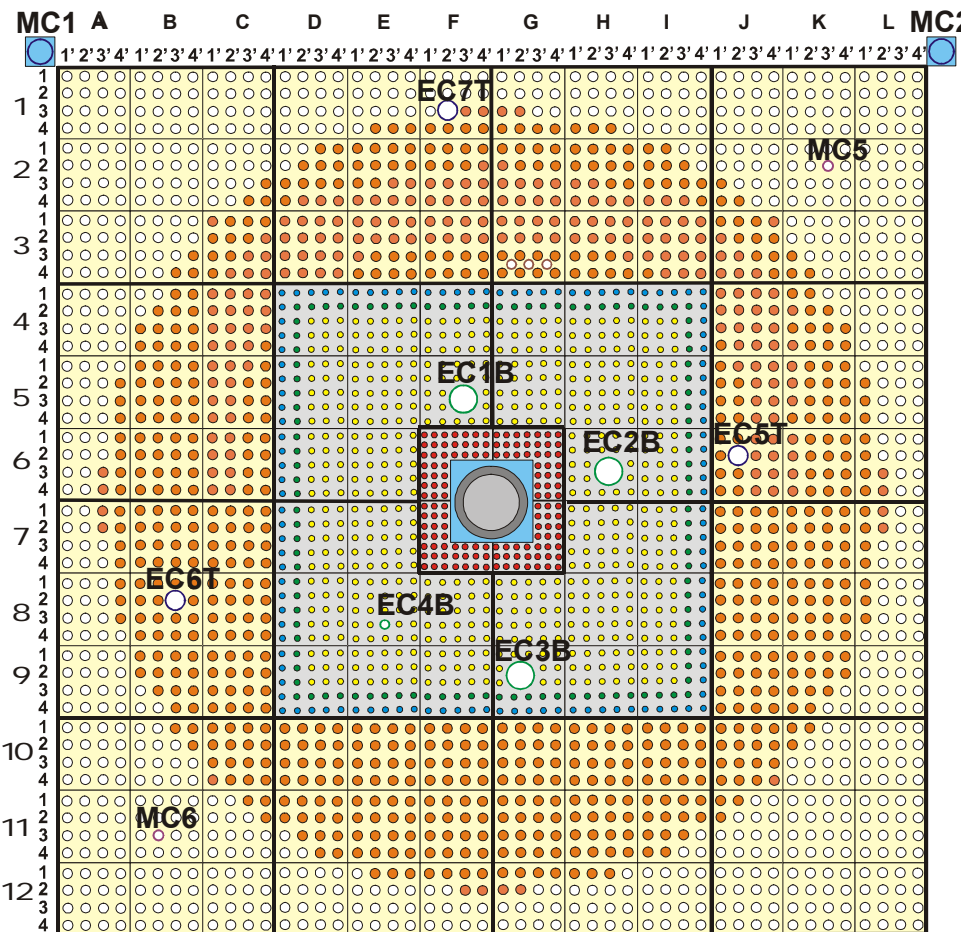
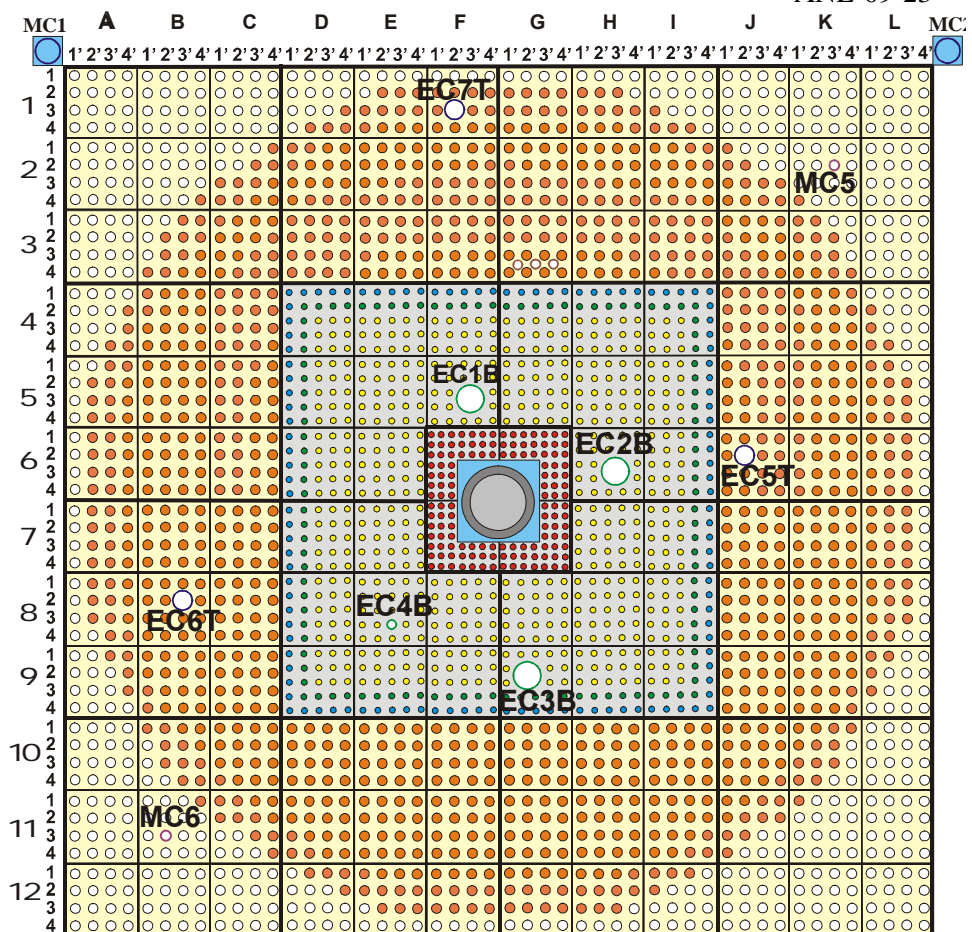


Figure 1. XY Cross-Sectional View of the YALINA-Booster Assembly, Dimensions in mm



- Pb
- Target
- Polyethylene moderator
- Experimental channels in booster zone EC1B, EC2B, EC3B
- Experimental channel in booster zone EC4B
- Experimental channels in thermal zone EC5T, EC6T, EC7T
- Measurement channels MC5, MC6 in thermal zone
- Measurement channels in reflector MC1-MC4
- Holes in block G3 for control rods (B4C) location
- Rods with B4C
- Rods with Umet.(nat.)
- Fuel rods with Umet.(90% U-235)
- Fuel rods with UO2(36% U-235)
- Fuel rods EK-10, load (902)

Figure 2. Fuel Loading of the YALINA-Booster Configuration with 902 EK-10 Fuel Rods



- Pb
- Target
- Polyethylene moderator
- Experimental channels in booster zone EC1B, EC2B, EC3B
- Experimental channel in booster zone EC4B
- Experimental channels in thermal zone EC5T, EC6T, EC7T
- Measurement channels MC5, MC6 in thermal zone
- Measurement channels in reflector MC1-MC4
- Holes for control rods (B4C) location
- Rods with B4C
- Rods with Umet.(nat.)
- Fuel pins with Umet.(90% U-235)
- Fuel pins with UO2(36% U-235)
- Fuel pins EK-10, load (1141)

Figure 3. Fuel Loading of the YALINA-Booster Configuration with 1141 EK-10 Fuel Rods

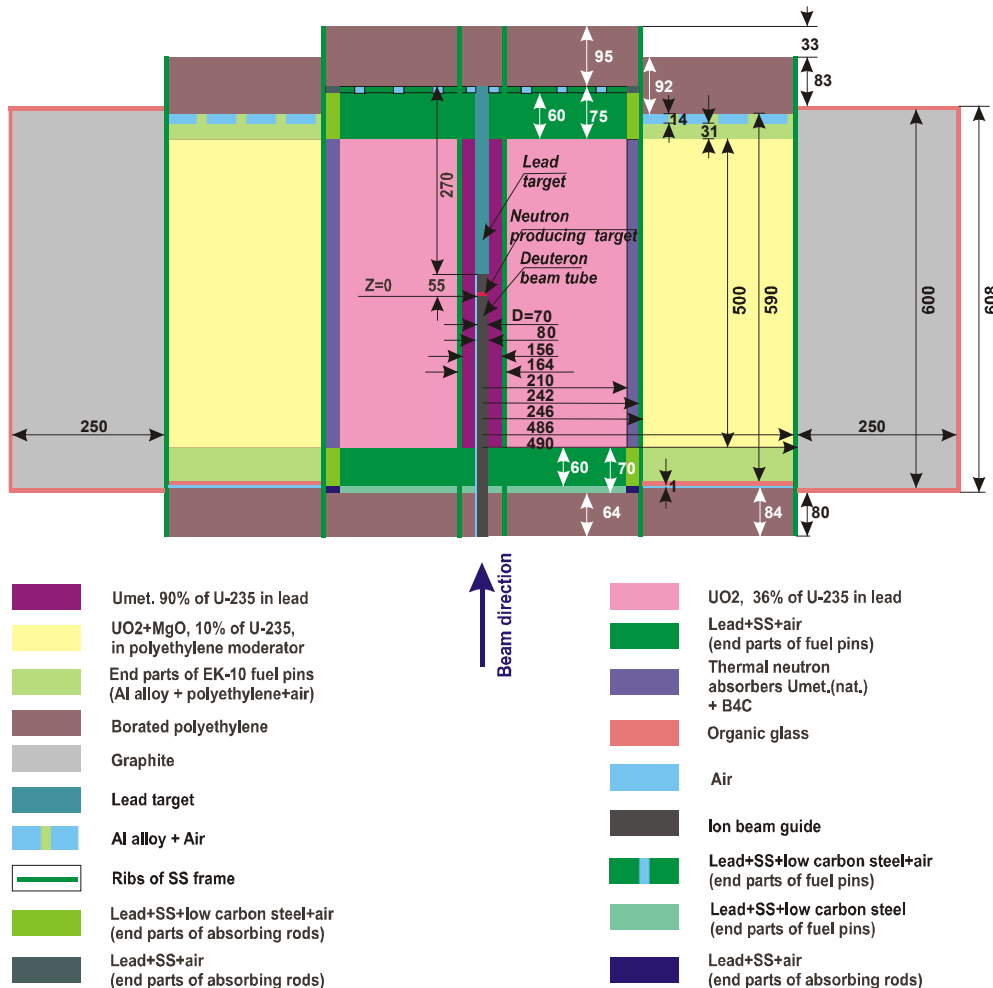


Figure 4. YZ Cross-Sectional View of the YALINA-Booster Assembly (at X=4), Dimensions in mm.

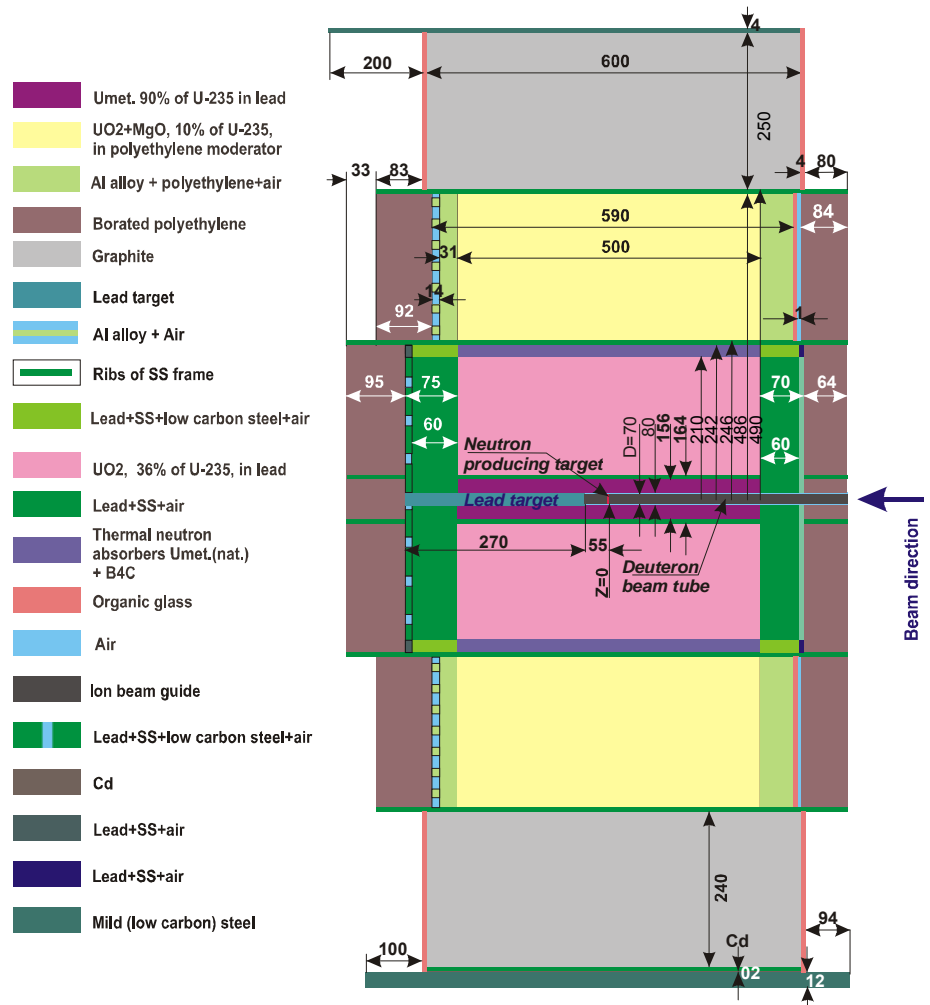


Figure 5. XZ Cross-Sectional View of the YALINA-Booster Assembly (at Y=4), Dimensions in mm.

II.1.a. The Lead Target

There is a hole with side dimensions of 80×80 mm in the center of the fast zone formed by cutting out the inner corners of the four central lead blocks. In the axial direction, a lead zone consisting of 12 blocks with a total length of 645 mm is used and each block has X-Y dimensions of 78×78 mm. When the deuteron accelerator is used for neutron production, part of the hole is occupied by the beam tube as shown in Figures 4 and 5.

II.1.b. The Inner Part of the Fast Zone

The innermost part of the fast zone surrounding the lead target contains 132 fuel rods in a lead block, which are marked by red color in Figures 2 and 3. The fuel material is metallic uranium with 90% U-235 enrichment arranged in a square lattice. The fuel rod pitch is 11.143 mm and the lead block dimension is 78×78 mm. The total length of the lead subassembly is 645 mm. A detailed description of the fuel rod design is shown in Figure 6.

II.1.c. The Outer Part of the fast Zone

The fast fuel zone surrounding the 90%-enriched zone consists of 32 lead subassemblies with 563 fuel rods arranged in a square lattice having a 16 mm pitch. The fuel material is ceramic UO_2 with 36% U-235 enrichment. The UO_2 density is 9.694 g/cm^3 . Each lead subassembly has 25 fuel rods and the fuel rod details are shown in Figure 6. The clad material is stainless steel alloy 12X18H10T. All fuel rods in the booster zone are inserted into stainless steel tubes with 9 mm outer diameter and 0.7 mm wall thickness. In this zone, four experimental channels, EC1B, EC2B, EC3B, and EC4B are located as shown in Figures 2 and 3. The first three experimental channels have stainless steel alloy 12X18H10T liner with 36 mm outer diameter and 1 mm wall thickness. The experimental channel EC4B has the same liner material but the outer diameter and the wall thickness are 12 and 1.5 mm, respectively.

II.1.d. The Absorber Zone

The absorber zone surrounds the fast zone and consists of an inner layer of natural metallic uranium rods with stainless steel clad. The clad outer diameter is 9 mm with 0.7 mm thickness as shown in Figure 6. The outer layer of the absorber zone consists of boron carbide (B_4C) rods having 1.38 g/cm^3 density as shown in Figure 7. The number of metallic natural uranium rods is 108 and the number of B_4C rods is 116. The B_4C rods use the same lattice of the uranium fuel rods in the fast zone, which is 16 mm pitch. This absorber zone permits fast neutrons to scatter between the fast and thermal zones, and prevents thermal neutrons from entering the fast zone from the thermal zone. The result is a fast neutron coupling of the fast and the thermal zones. The B_4C rods are constrained inside the assembly and cannot be removed out accidentally, which prevents undesired reactivity insertion.

II.1.e. The Thermal Zone

The thermal zone surrounds the absorber zone and consists of 108 polyethylene subassemblies with 16 holes each for loading the EK-10 fuel rods. The holes are arranged in a square lattice with 20 mm pitch. The active fuel length is 500 mm and the average amount of U-235 is 7.73 g

per rod. The total length of EK-10 fuel rods is 590 mm and the outer clad diameter is 10 mm. Each polyethylene subassembly has a total length of 576 mm obtained by arranging twelve blocks in the axial direction. The block dimensions are 80×80×48 mm and the polyethylene density is 0.859 g/cm³. The 20 mm lattice dimension is the optimum value for the neutron multiplication using the EK-10 fuel with polyethylene moderator in a square lattice. The detailed description of the EK-10 fuel rod is shown in Figure 8. Three experimental channels, EC5T, EC6T, and EC7T are inserted into the thermal zone as shown in Figures 2 and 3. Finally, the thermal zone is surrounded in the radial direction by a 250-mm graphite reflector containing three experimental channels EC8R, EC9R, and EC10R as shown in Figure 1. In the axial directions, borated polyethylene shields are used as shown in Figures 4 and 5. In the thermal zone and close to the fast zone, it is possible to insert three small B₄C rods as shown in Figures 2 and 3. During operation these rods are not inserted and, consequently, the holes are filled with air. The diameter of each hole is 11 mm with an aluminum alloy liner of 0.5 mm thickness.

II.1.f. The Deuteron Beam Tube

The detailed design of the deuteron beam tube is shown in Figure 9.

II.2. YALINA-Thermal Facility

The YALINA-Thermal has been designed to have a thermal neutron spectrum and to achieve neutron flux densities as high as possible in a subcritical configuration. In addition, the subcritical assembly together with the highly intensive neutron generator makes the YALINA-Thermal assembly interesting for performing ADS kinetics research [9].

The YALINA-Thermal operates with $k_{eff} < 0.98$ under all conditions for safety reasons. The assembly is driven by an external neutron source: a Cf-252 neutron source or a deuteron accelerator with deuterium or tritium targets for neutron production. The deuteron energy is 240 keV impinging on the target located at the center of the subcritical assembly.

The YALINA-Thermal consists of uranium dioxide nuclear fuel rods and polyethylene moderator. The assembly is surrounded by a graphite reflector in the radial direction. The fuel rods are arranged horizontally. The front side of the assembly opposite to the beam entrance is covered by borated polyethylene. The backside is covered by organic glass sheets where the entrance of the deuteron beam tube is located. Three axial experimental channels (EC1, EC2, and EC3) are located in the fuel zone and they are parallel to the fuel rods. One axial experimental channel (EC4) is positioned in the target zone and two axial experimental channels (EC5, EC6) are included in the reflector zone. One radial experimental channel EC7 is inserted in the reflector zone at the fuel midplane. The experimental channels are shown in Figure 10.

Three YALINA-Thermal configurations are considered for the benchmark. The number of EK-10 fuel rods are 216, 245 and 280. Figures 11 to 14 show the core loading of the three configurations. The geometrical details for generating the calculation models are presented in the XZ and YZ cross-sectional views shown in Figures 15 and 16. Additional information can be found in Ref. 6.

The subcritical assembly of the YALINA-Thermal facility is made of rectangular parallelepiped sections. The central axis of the assembly is aligned horizontally. The target can be situated along the central axis at different distances from the assembly center.

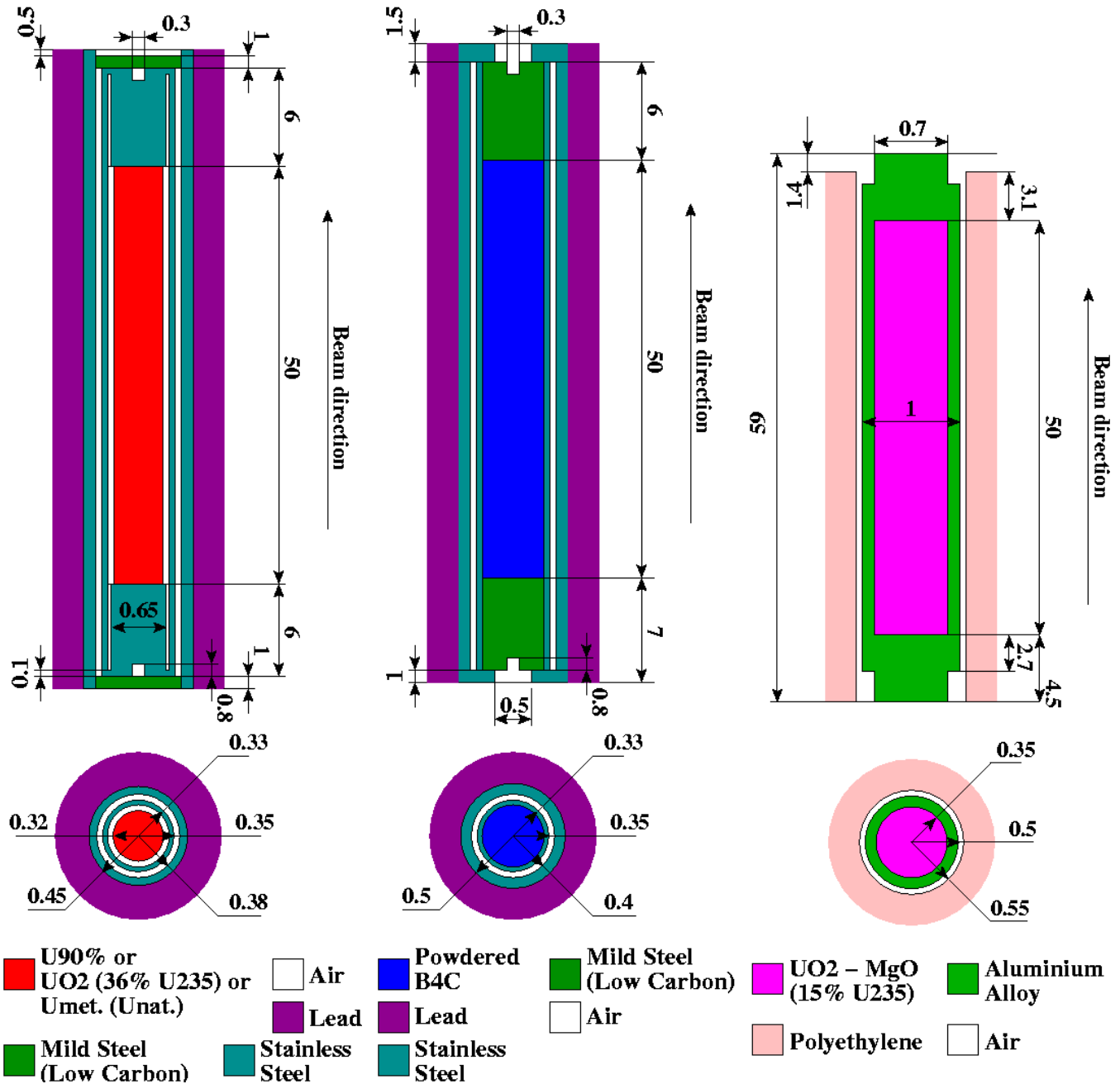


Figure 6. XZ and XY Cross-Sectional Views of a Fuel Rod Inside the Steel Casing, Dimensions in cm

Figure 7. XZ and XY Cross-Sectional View of the Boron Carbide Rod, Dimensions in cm

Figure 8. XZ and XY Cross-Sectional Views of the EK-10 Fuel Rod, Dimensions in cm.

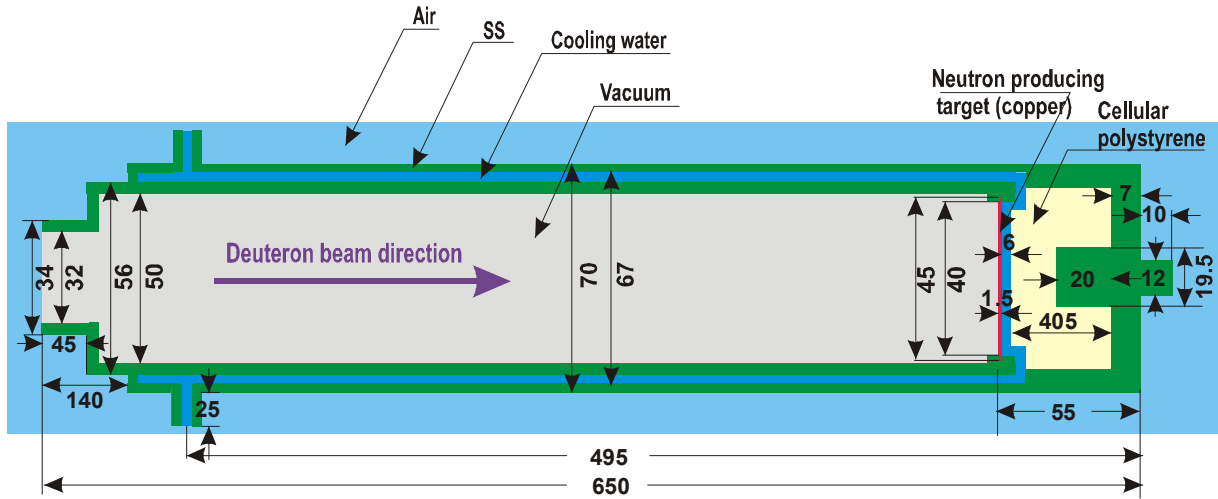


Figure 9. Deuteron Beam Tube Design, Dimensions in mm

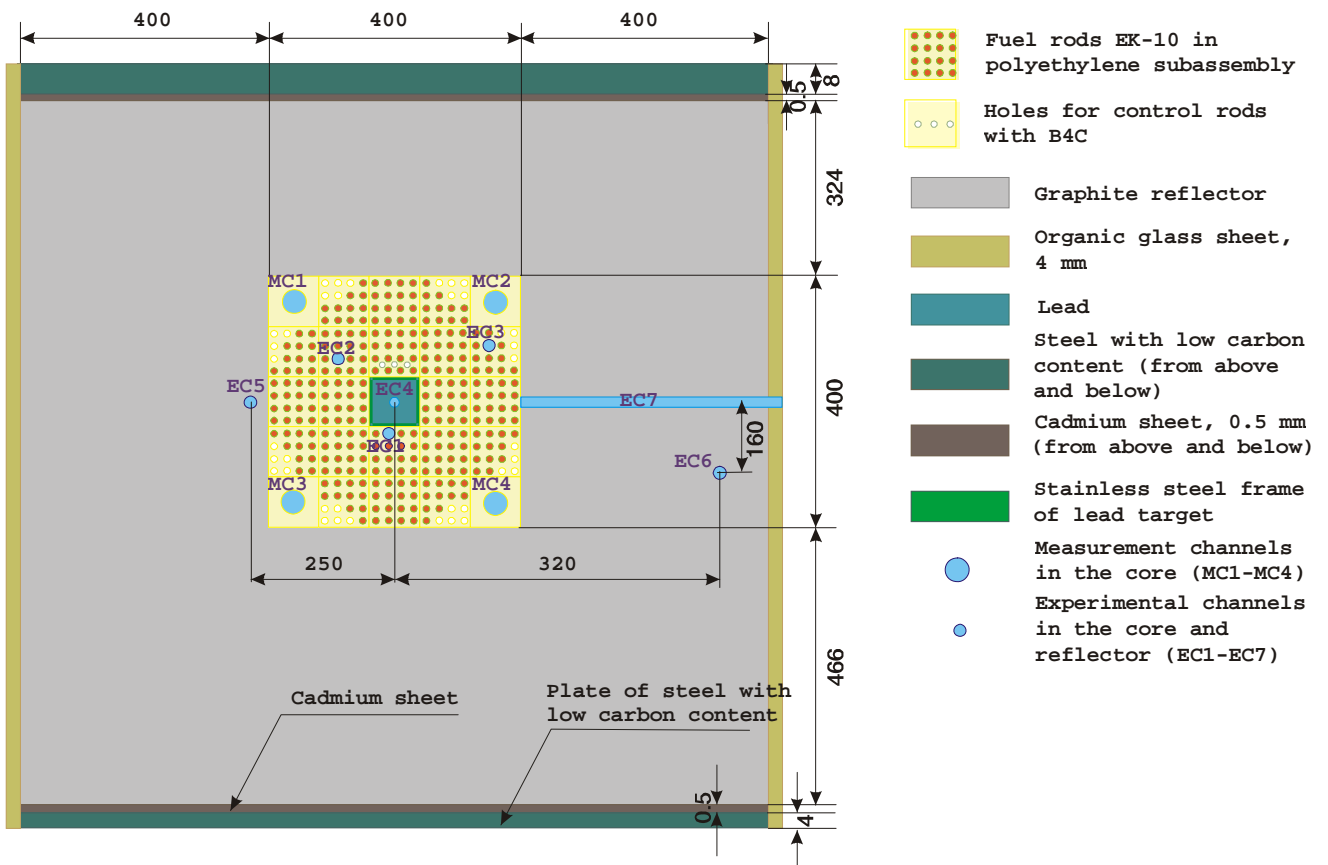


Figure 10. XY Cross-Sectional View of the YALINA-Thermal Assembly, Dimensions in mm

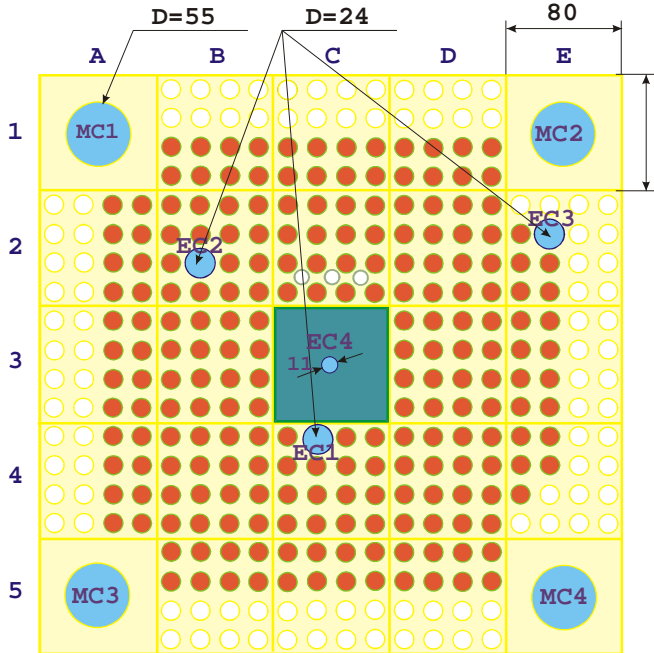
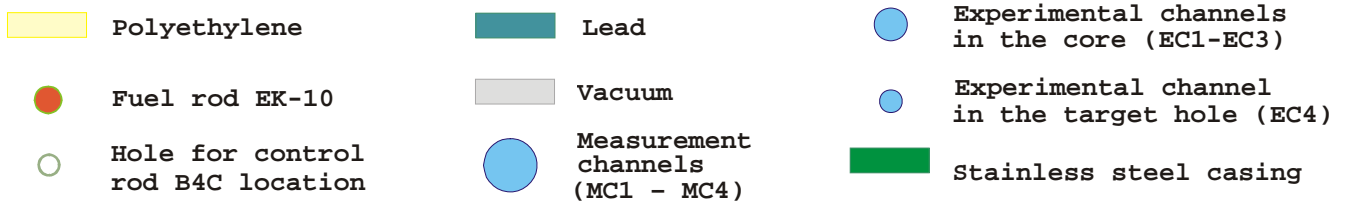


Figure 11. XY Cross-Section of the YALINA-Thermal Assembly with 216 EK-10 Fuel Rods

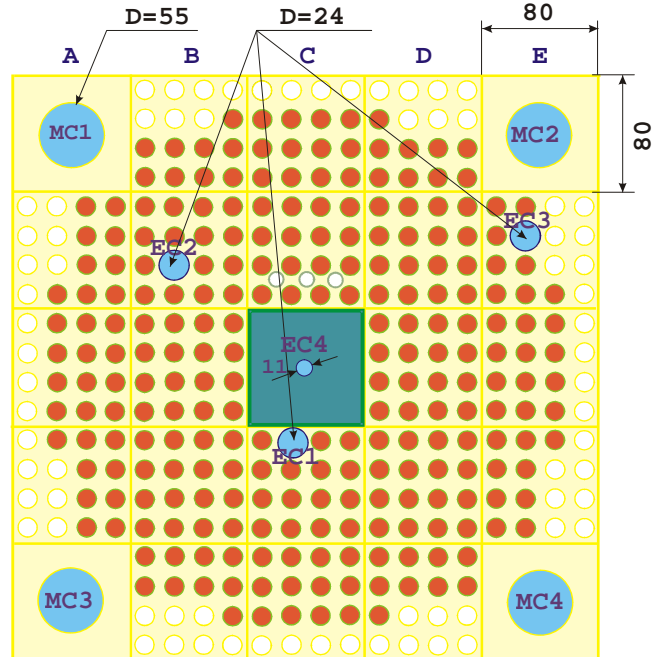


Figure 12. XY Cross-Section of the YALINA-Thermal Assembly with 245 EK-10 Fuel Rods

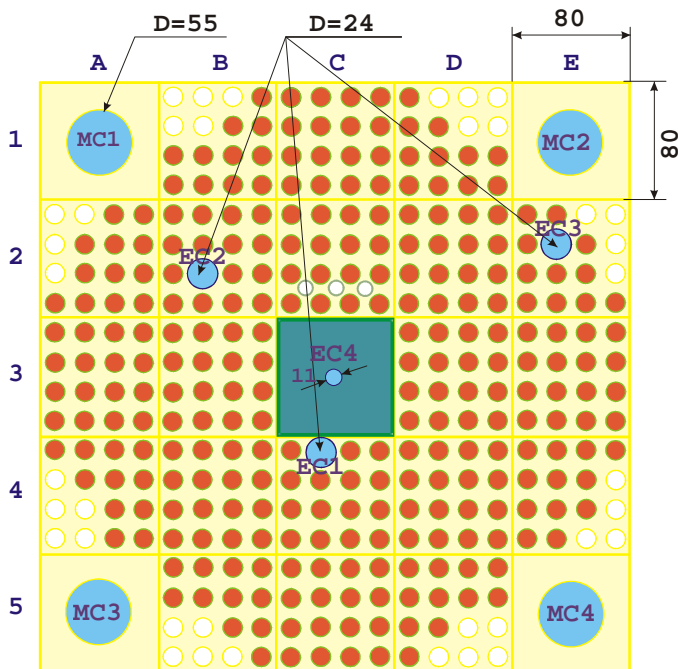


Figure 13. XY Cross-Section of the YALINA-Thermal Assembly with 280 EK-10 Fuel Rods (Target Side)

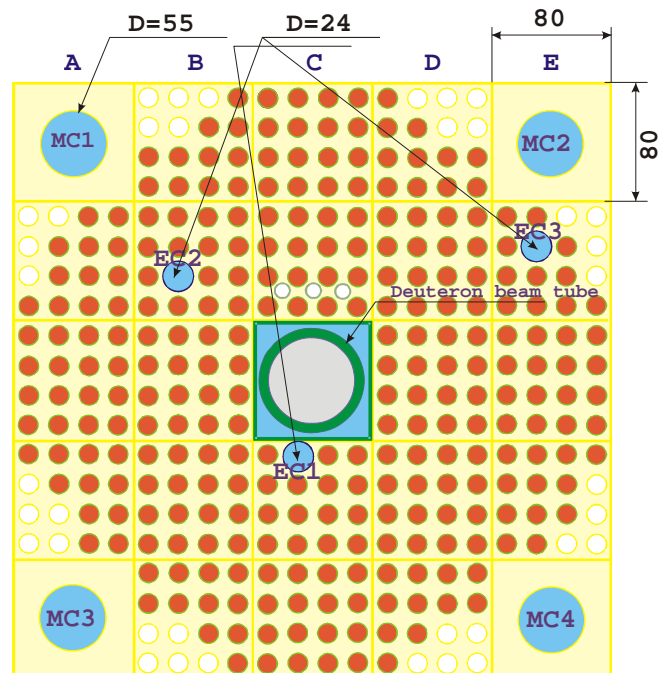
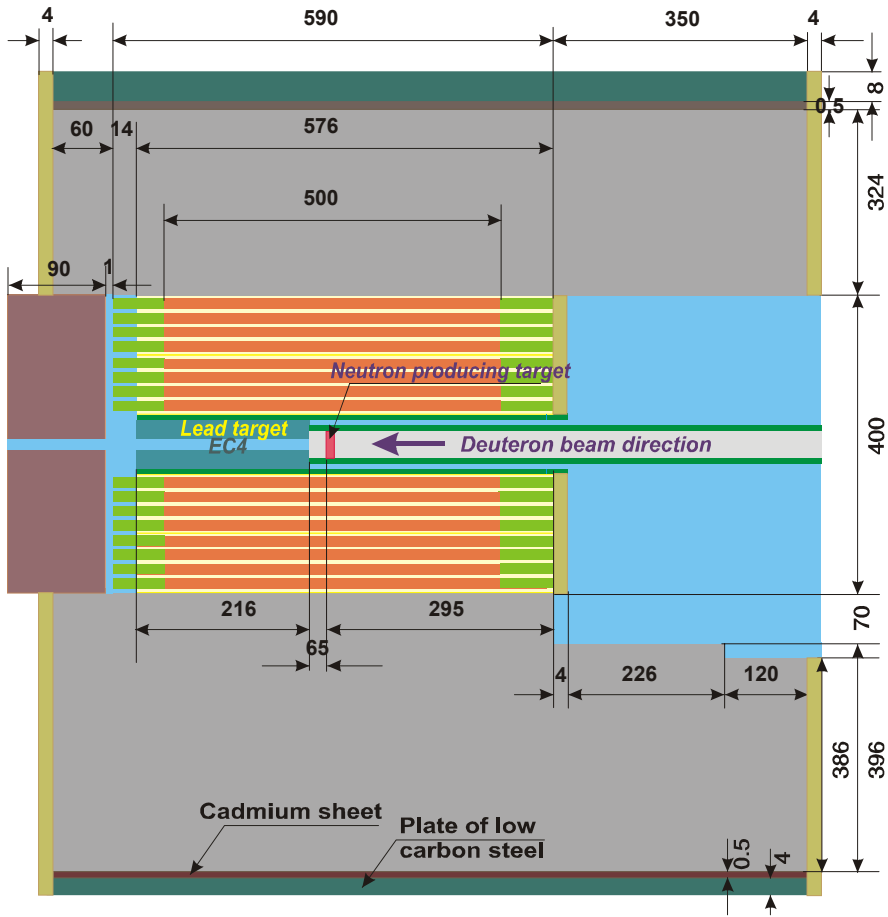


Figure 14. XY Cross-Section of the YALINA-Thermal Assembly with 280 EK-10 Fuel Rods (Beam Tube Side)

















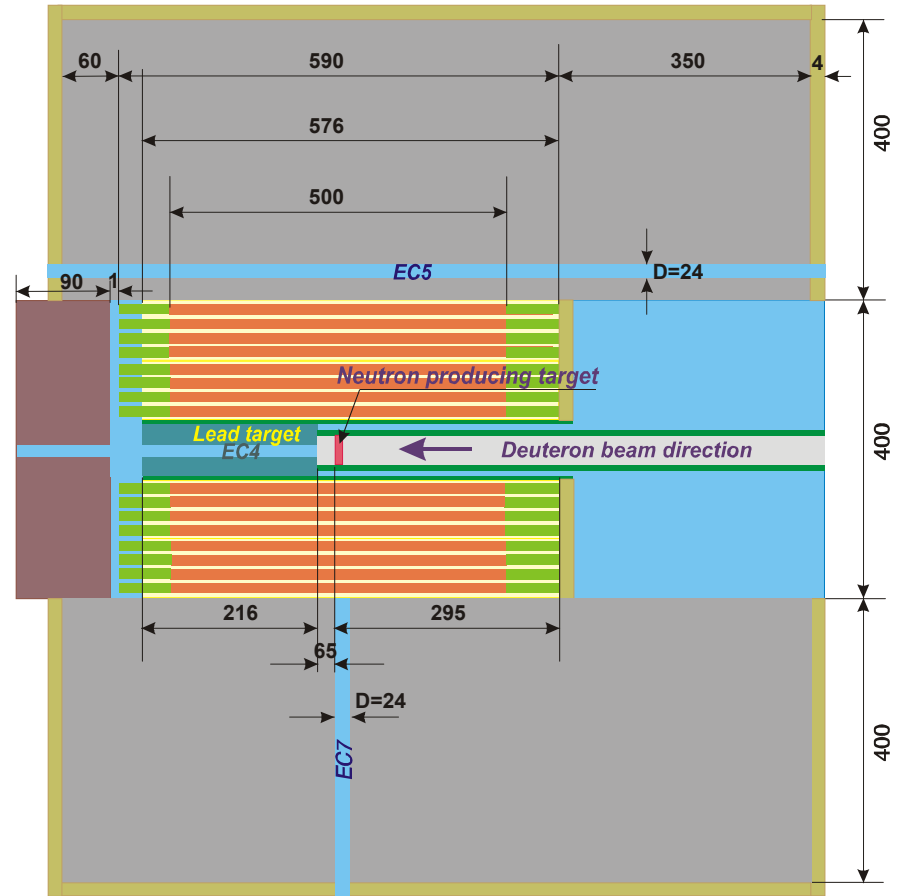
- | | |
|--|---|
|  Polyethylene |  Deuterium beam tube |
|  Fuel rod |  Lead target |
|  End part of fuel rod |  Air |
|  Aluminium alloy |  Graphite reflector |
|  Stainless steel |  Organic glass |
|  Steel with low content of carbon |  Borated polyethylene |
|  Cadmium sheet, 0.5 mm |  Neutron producing target (copper) |

Figure 15. XZ Cross-Section of the YALINA-Thermal Assembly (Y=0), Dimensions in mm



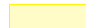
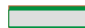












- | | |
|--|---|
|  Polyethylene |  Deuterium beam tube |
|  Fuel rod |  Lead target |
|  End part of fuel rod |  Air |
|  Aluminium alloy |  Graphite reflector |
|  Stainless steel |  Organic glass |
|  Steel with low content of carbon |  Borated polyethylene |
|  Cadmium sheet, 0.5 mm |  Neutron producing target (copper) |

Figure 16. YZ Cross-Section of the YALINA-Thermal Assembly (X=0), Dimensions in mm

II.2.a. Lead Target

There is a hole with side dimensions of 80×80 mm in the assembly center with a stainless steel frame. A lead zone consisting of 12 blocks with a total length of 576 mm in the axial direction is used, and each block has X-Y dimensions of 78×78 mm. When the deuteron accelerator is used for neutron production, part of the hole is occupied by the beam tube as shown in Figures 15 and 16.

II.2.b. Fuel Assembly

The assembly consists of 20 polyethylene subassemblies with 16 holes each for the loading of 16 EK-10 fuel rods. The holes are arranged in a square lattice with 20 mm pitch as shown in Figures 11 to 14. The active fuel length is 500 mm and the average amount of U-235 is 7.73 g per rod. The total length of EK-10 fuel rod is 590 mm and the outer and inner clad diameters are 10 and 7 mm respectively. Each subassembly has a total length of 576 mm obtained by arranging twelve blocks in the axial direction. The block dimensions are 80×80×48 mm and the polyethylene density is 0.923 g/cm³. The 20 mm lattice dimension is the optimum configuration for neutron multiplication using the EK-10 fuel with polyethylene moderator in a square lattice. The detailed description of the EK-10 fuel rods is shown in Figure 8.

Three experimental channels, EC1, EC2, and EC3 are embedded in the fuel zone, while the experimental channel EC4 is located inside the lead target zone. The fuel zone is surrounded in the radial direction by a graphite reflector, whose dimensions are shown in Figures 10, 15, and 16. There are two axial experimental channels, EC5 and EC6, and one radial experimental channel, EC7, in the graphite reflector. Borated polyethylene blocks are used in the front section of the fuel zone and organic glass sheets are used at the backside of the assembly and in the front section of the graphite reflector as shown in Figures 15 and 16.

In the fuel zone and close to the target zone, it is possible to insert three small B₄C rods as shown in Figures 11 to 14. During the operation these rods are not inserted and, consequently, the holes are filled with air. The diameter of each hole is 11 mm with aluminum alloy liner of 0.5 mm thickness.

III. Performed Calculations

Several calculations were performed for the YALINA-Booster and –Thermal using different nuclear data files. The following three sections describe the performed calculations.

III.1. YALINA-Booster

Two subcritical configurations are considered in the YALINA-Booster benchmark. These configurations have different fuel loadings in the thermal zone: 902 and 1141 EK-10 fuel rods as shown in Figures 2 and 3 respectively. In both configurations, the booster zone is fully loaded. The deuterons are accelerated to 240 keV and the target is located at the center of the subcritical assembly. The neutron source is (d,t), (d,d), or Cf-252 neutrons. The Cf-252 neutron source is located at (x,y,z) = (0,0,62) mm with the deuteron beam tube still in place. The assembly center corresponds to the point (x,y,z) = (0,0,0). For each configuration, the following results are obtained (see Ref. 5 for additional details):

1. Axial distribution of the following nuclear reaction rates:
 - a. He-3(n,p) reaction rate in the EC6T experimental channel, normalized to one external neutron source and one He-3 atom. The reaction rate values are calculated using the average neutron

flux, $\phi(E)$, in cylindrical cells from $Z = -250$ mm to $Z = 250$ mm in steps of 50 mm. The cells description is given in Ref. 5. The detector is not modeled in the calculation.

- b. U-235(n,f) reaction rate in the EC2B and EC6T experimental channels, normalized to one external neutron source and one U-235 atom. In both channels, the reaction rate values are calculated using the average neutron flux, $\phi(E)$, in cylindrical cells from $Z = -250$ mm to $Z = 250$ mm in steps of 50 mm. The cells description is given in Ref. 5. The U-235 material is not modeled in the calculation.
 - c. In-115(n, γ) reaction rate in the EC2B, EC5T, EC6T, and EC7T experimental channels, normalized to one external neutron source and one In-115 atom. Values are to be calculated in the In-115 samples located from $Z = -242$ mm to $Z = 208$ mm in steps of 50 mm. The In-115 samples are explicitly simulated together with their polyethylene holder, without loading any other isotopes in the holder. The description of the polyethylene holder is given in Ref. 5.
2. Radial distribution of the In-115(n, γ) reaction rate in the EC10R radial experimental channel at the radial distances of 480, 530, 580, 630, 680 and 730 mm. All reaction rate values are normalized to one neutron source and one In-115 atom. The samples are simulated together with their polyethylene holder. The description of the polyethylene holder is given in Ref. 5.
 3. Au-197(n, γ) and Mn-55(n, γ) reaction rates in the EC2B, EC6T experimental channels, normalized to one external neutron source and one isotope atom. The samples are simulated together with their holder, as done in the previous calculations. The calculation is performed with the holder containing only Au-197 or Mn-55.
 4. Neutron energy spectra in the EC2B, EC6T and EC8R experimental channels, calculated at $Z = 0$ with the 172 energy groups structure given in Appendix C. The integral of the neutron spectrum over the total energy range is normalized to 1.0 ($\int \Phi(E)dE = 1.0$).
 5. The neutron flux is calculated as a function of time after a neutron pulse insertion. The pulse consists of (d,t) or (d,d) neutrons at $Z = 0$ with 5 μ s duration. The neutron flux calculations are performed for a period of 20 ms with two different detectors:
 - a. He-3(n,p) detector in the EC6T and EC8R experimental channels without explicit modeling of the detector. The results are normalized to the maximum value in the EC6T experimental channel.
 - b. U-235(n,f) detector in the EC1B, EC2B, and EC3B experimental channels without explicit modeling of the detector. The results are normalized to the maximum value in the EC1B experimental channel.

The calculations are done using a 10 μ s time step from 0 to 1 ms and a 100 μ s time step from 1 ms to 20 ms.
 6. The static and the kinetic neutronic parameters for both configurations:
 - a. Effective multiplication factor, k_{eff} .
 - b. Source multiplication factor, k_s .
 - c. Mean neutron generation time, Λ .
 - d. Effective delayed neutron fraction, β_{eff} .

III.2. YALINA Thermal

Three different fuel loadings are considered for the YALINA-Thermal benchmark. These loadings have 216, 245 and 280 EK-10 fuel rods and the corresponding U-235 masses are 1.67, 1.89, 2.16 kg, respectively. The fuel loadings are shown in Figures 11 to 14. The neutron source is (d,t), (d,d), or Cf-252 neutrons. For each configuration the following results are obtained, as explained in Ref. 6:

1. Axial distribution of the following reaction rates:
 - a. He-3(n,p) reaction rate in the EC1, EC2, and EC3 experimental channels, normalized to one external neutron source and one He-3 atom. The reaction values are calculated using the

- average neutron flux, $\phi(E)$, in cylindrical cells from $Z = -250$ mm to $Z = 250$ mm in steps of 50 mm. The cells description is given in Ref. 6. The detector is not modeled in the calculation.
- b. U-235(n,f) reaction rate in the EC1, EC2, and EC3 experimental channels, normalized to one external neutron source and one U-235 atom. In all the channels, the reaction rate values are calculated using the average neutron flux, $\phi(E)$, in cylindrical cells from $Z = -250$ mm to $Z = 250$ mm in steps of 50 mm. The cells description is given in Ref. 6. The U-235 material is not modeled in the calculation.
 - c. In-115(n, γ) reaction rate in the EC2 experimental channel, normalized to one external neutron source and one In-115 atom. Reaction rate values are calculated in the In-115 samples located from $Z = -242$ mm to $Z = 208$ mm in steps of 50 mm. The In-115 samples are simulated together with their polyethylene holder, without loading any other isotopes in the holder. The description of the polyethylene holder is explained in Ref. 6.
2. Radial distribution of the In-115(n, γ) reaction rate in the EC7 radial experimental channel at the radial distances of 200, 250, 300, 350, 400, 450, 500, 550 and 600 mm. All reaction rate values are normalized to one neutron source and one In-115 atom. The samples are simulated together with their polyethylene holder. The description of the polyethylene holder is explained in Ref. 6.
 3. Au-197(n, γ) and Mn-55(n, γ) reaction rates in the EC2 experimental channel, normalized to one external neutron source and one isotope atom. The samples are simulated together with their holder, as done in the above calculation. The calculation has performed with the holder containing only Au-197 or Mn-55.
 4. Neutron energy spectra in the EC1, EC2, EC3, EC5, and EC6 experimental channels, calculated at $Z = 0$ with the 172 energy groups structure given in Appendix C. The integral of the neutron spectrum over the total energy range is normalized to 1.0 ($\int \Phi(E)dE = 1.0$).
 5. Neutron flux calculated as a function of time after a neutron pulse insertion. The pulse consists of (d,t) or (d,d) neutrons at $Z = 0$ with 5 μ s duration. The neutron flux calculations are performed for a period of 20 ms with two different detectors:
 - a. He-3(n,p) detector in the EC2 and EC5 experimental channels without explicit modeling of the detector. The results are normalized to the maximum value in the EC2 experimental channel.
 - b. U-235(n,f) detector in the EC1 experimental channels without explicit modeling of the detector. The results are normalized to the maximum value in the EC1 experimental channel.
 The calculations are done using a 10 μ s time step from 0 to 1 ms and a 100 μ s time step from 1 ms to 20 ms.
 6. The static and the kinetic neutronic parameters for the three configurations:
 - a. Effective multiplication factor, k_{eff} .
 - b. Source multiplication factor, k_s .
 - c. Mean neutron generation time, Λ .
 - d. Effective delayed neutron fraction, β_{eff} .

Some of the YALINA-Thermal results have been also presented in Ref. 10.

III.3. Additional Calculations

An additional study was performed to calculate the kinetic parameters of the YALINA-Booster and -Thermal according to the following formulations:

$$\beta_{eff} = \sum_{i=1}^{NF} \frac{1}{\langle \Phi_S^*, F\Phi_S \rangle} \cdot \iint \chi_{d,i}(E') \Phi_S^*(\vec{r}, E') dE' \int \beta_i \nu \Sigma_f(E) \Phi_S(\vec{r}, E) dE d\vec{r} \quad \text{Eq. 1}$$

$$\Lambda_{eff} = \frac{1}{\langle \Phi_S^*, F\Phi_S \rangle} \cdot \iint \Phi_S^*(\vec{r}, E') dE' \int \frac{1}{v(E)} \Phi_S(\vec{r}, E) dE d\vec{r} \quad \text{Eq. 2}$$

where:

- $\chi_{d,i}$ are the delayed neutron spectra for the group family $i = 1, \dots, NF$;

- β_i are the delayed neutron fraction for the i^{th} group family;
- $v(E)$ is the neutron velocity;
- F is the fission production operator of the Boltzmann equation.

Generally, the kinetic parameters are obtained with homogeneous (source-free) fluxes, Φ^* and Φ , solutions of the equations: $A\Phi^*=(1/k_{\text{eff}})F\Phi^*$ and $A\Phi=(1/k_{\text{eff}})F\Phi$.

In Eqs. 1 and 2, Φ_S^* and Φ_S are inhomogeneous (source-driven) fluxes, adjoint and direct respectively, solution of the transport equations: $A\Phi_S^* = F\Phi_S^* + v\Sigma_f$ and $A\Phi_S = F\Phi_S + S$, where $v\Sigma_f$ is the macroscopic cross-section associated to the assembly fission source and S is the external source driving the subcritical system, (d,t), (d,d) or Cf-252 neutron source.

IV. Computational Tools

Considerable efforts have been made in order to create a deterministic model using the ERANOS (European Reactor Analysis Optimized code System) code package [11] for the analysis of the YALINA configurations. ERANOS, essentially developed for the analysis of fast neutron systems, with extended capabilities for the slowing down treatment with up to 1968 energy groups, is also used for the analysis of thermal reactors. Cross-sections have been processed with the ECCO code [12] of ERANOS using JEF2.2 [13], JEF3.1 [14] and ENDF/B-VI.8 [15] nuclear data. The VARIANT module [16] of ERANOS has been used to perform reactivity and flux calculations. The kinetic study is carried out with the KIN3D module [17]. For complementary studies, the 2D S_n code BISTRO [18] of ERANOS has been also used. All calculations have been performed with the ERANOS version 2.0, except the VARIANT and KIN3D calculations that have been carried out with the version 2.1 recently available at ANL.

In the present report, the YALINA-Booster and -Thermal with 1141 and 280 EK-10 fuel rods have been considered.

V. Cross-Section Processing

The cross-sections have been processed with the ECCO code using the nuclear data from the JEF2.2, JEF3.1 and ENDF/B-VI.8 libraries. The cell calculations are performed for each zone assumed to be infinite. The ECCO code utilizes the sub-group method for the treatment of the resonances and performs cell calculations in homogeneous (0D) and heterogeneous geometry (1D: cylindrical or slab; 2D: XY or hexagonal) using the collision probability method. In the YALINA configurations, heterogeneous effects are quite important, as consequence, the cross-sections have been processed for most zones in XY geometry. The cross-sections are calculated over a fine energy group structure (up to 1968 energy groups) and collapsed to a broader energy group structure specified by the user using the cell flux as a weighting function. For the present work, the condensation has been performed over the 172 group structure according to the benchmark specifications. However, deterministic calculations for reactivity or neutron flux determination of the YALINA configurations with 172 energy groups require significant computational resources. As consequence, the cross-sections have been also processed with a lower number of energy groups. A 53 energy group structure was derived from the standard 33 group structure used for fast reactor analysis. Two energy groups have been added at the highest energy to represent the 14 MeV (d,t) neutron source and the lowest two energy groups of the original 33 group structure have been replaced by 20 energy groups for a more appropriate treatment of the thermal part of the neutron spectrum. The 53 and 172 energy group structures are given in Appendix C. After the individual material cross-sections are condensed using the heterogeneous geometry, a homogeneous cross-

section is generated over the cell volume. For structural zone, the cell flux is calculated by introducing a source term given by the neutron leakage from the neighbour zone. The term DB^2 , where D is the diffusion coefficient and B is the buckling value, of the ECCO calculation is given by a semi-empirical

formula ($B^2 = \frac{5}{8} \left(\frac{\pi}{h} \right)^2$, where h is the zone thickness). This formula has been historically developed for

the treatment of fertile blankets and, as consequence, it could be inappropriate in other cases. In the absence of appropriate information, in the present study it has been assigned $B^2=0$. However, the dependence of the results on the value provided for the buckling has been investigated. The results indicate that the effect of this term is negligible: for instance, the change in reactivity for the YALINA-

Booster between the cases $B^2 = \frac{5}{8} \left(\frac{\pi}{h} \right)^2$ and $B^2 = 0$ is about 10 to 20 pcm. The differences decreases

as the number of energy groups increases. Appendix A contains all the geometrical details for the cross-sections processing used for the deterministic model of the YALINA configurations. A particular attention has been devoted to the calculation of the thermal cells, as explained in Appendix A.1.

VI. Deterministic Results

Reactivity and flux calculations have been performed in XYZ geometry with the VARIANT code implemented in the new ERANOS version 2.1, using JEF2.2, JEF3.1, and ENDF/B-VI.8 nuclear data. In the VARIANT code, the transport equation is derived in terms of an “even” and an “odd” fluxes, expanded in Legendre’s polynomials and in spherical harmonics for the spatial and angular variables respectively, as shown in the following equations:

$$\Phi_S^+(\vec{r}, \vec{\Omega}) = \frac{1}{2} \left[\Phi_S(\vec{r}, \vec{\Omega}) + \Phi_S(\vec{r}, -\vec{\Omega}) \right] = \sum_{i,m} f_i(\vec{r}) g_m(\vec{\Omega}) \zeta_{i,m} \quad \text{Eq. 3}$$

$$\Phi_{S,\gamma}^-(\vec{r}, \vec{\Omega}) = \frac{1}{2} \left[\Phi_S(\vec{r}, \vec{\Omega}) - \Phi_S(\vec{r}, -\vec{\Omega}) \right] = \sum_{j,n} h_j(\vec{r}) k_n(\vec{\Omega}) \chi_{j,n,\gamma} \quad \text{Eq. 4}$$

VARIANT uses the nodal variational method. This implies that the solutions of the equation are integrated over the mesh volumes and they are obtained by the minimization of a function, that contains the total cross-section, Σ_t , at the denominator. Due to these features, the VARIANT code does not work properly with fine meshes. Moreover, difficulties are encountered in presence of void regions, characterized by low values of Σ_t . Therefore, the void zones of the original YALINA configurations were homogenized with other neighbor zones as shown in Appendix A.

The VARIANT method is also the basis of the time-dependent ERANOS calculation modules, implemented in the KIN3D code, used for the kinetic studies presented in this report.

VI.1. Multiplication Factor

The impact of the number of energy groups, the angular flux expansion order, and the anisotropic scattering expansion order on the calculated k_{eff} values has been investigated for the YALINA-Booster and –Thermal. Concerning the number of energy groups used, the obtained results in Tables 1 and 2 show that increasing the energy group number from 53 to 172 results in a negligible impact on the calculated reactivity values. The obtained effect is less than 50 pcm for the YALINA-Booster and -Thermal, depending on the used nuclear data files. Therefore, it is concluded that the 53 energy group structure is adequate for the analyses of the current configurations.

Table 1. Calculated k_{eff} (Reactivity) with VARIANT for the YALINA-Booster

Number of Energy Groups	JEF2.2	JEF3.1	ENDF/B-VI.8
53 ^(a)	0.96235 (-3912 pcm)	0.95983 (-4185 pcm)	0.95895 (-4281 pcm)
172 ^(a)	0.96246 (-3900 pcm)	0.95998 (-4169 pcm)	0.95915 (-4259 pcm)

^(a) Results obtained in SP_3P_0 approximation: full P_3 angular flux expansion with simplified spherical harmonics; anisotropic scattering order 0

Table 2. Calculated k_{eff} (Reactivity) with VARIANT for the YALINA-Thermal

Number of Energy Groups	JEF2.2	JEF3.1	ENDF/B-VI.8
53 ^(a)	0.91002 (-9888 pcm)	0.94170 (-6191 pcm)	0.93994 (-6390 pcm)
172 ^(a)	0.91042 (-9840 pcm)	0.94180 (-6180 pcm)	0.94004 (-6379 pcm)
53 ^(b)	0.91276 (-9558 pcm)	0.94476 (-5847 pcm)	0.94294 (-6051 pcm)
172 ^(b)	0.91341 (-9480 pcm)	0.94514 (-5804 pcm)	0.94333 (-6008 pcm)

^(a) Results obtained in SP_3P_0 approximation: full P_3 angular flux expansion with simplified spherical harmonics; anisotropic scattering order 0

^(b) Results obtained in SP_3P_1 approximation: full P_3 angular flux expansion with simplified spherical harmonics; anisotropic scattering order 1

Tables 3 and 4 show the calculated reactivity values with different angular flux expansion or anisotropic scattering order approximations. The use of the 53 energy group structure is used for obtaining these results.

In Table 3, the first four sets of calculations (A, B, C, and D) used heterogeneous cell calculations for obtaining the zone average cross-section for each zone of the YALINA-Booster geometrical model. The fifth calculational set (F) was obtained by applying a correction factor to the fourth calculation set since the current computational resources do not permit the use of the heterogeneous cell calculations for SP_3P_3 zone average cross-sections. The correction factor was obtained by performing SP_3P_1 and SP_3P_3 simulations using homogenous cell calculations based on the number densities of each isotope averaged over the volume of the cell. In Table 4, similar approach was performed for the YALINA-Thermal. The first five calculational sets utilized heterogeneous cell calculations for getting average cross-sections sets for the different zones and the sixth calculation set obtained by using a correction factor.

The obtained results for the two assemblies suggest that the angular expansion of the flux and the anisotropic scattering should be increased to the orders 5 and 3 respectively or more. The P_5P_3 calculation is not possible with the current computer resources. Therefore, the results for the desired approximation orders have been obtained by separate investigations for angular flux and the anisotropic scattering orders. This kind of analysis is commonly performed when deterministic codes are used.

Table 3. Calculated k_{eff} (Reactivity) with VARIANT for the YALINA-Booster

Calculation	JEF2.2	JEF3.1	ENDF/B-VI.8
A: $SP_3^{(a)} P_0^{(b)}$	0.96235 (-3912 pcm)	0.95983 (-4185 pcm)	0.95895 (-4281 pcm)
B: P_3P_0	0.96388 (-3747 pcm)	0.96089 (-4070 pcm)	0.96002 (-4165 pcm)
C: P_5P_0	0.96516 (-3610 pcm)	0.96211 (-3938 pcm)	0.96123 (-4033 pcm)
D: SP_3P_1	0.96877 (-3224 pcm)	0.96620 (-3498 pcm)	0.96537 (-3587 pcm)
F ^(c) : SP_3P_3	0.97329 (-2744 pcm)	0.97069 (-3019 pcm)	0.96989 (-3104 pcm)

(a) Angular flux expansion (SP_3 : full P_3 angular flux expansion with simplified spherical harmonics, P_3 : angular flux expansion order 3);

(b) Anisotropic scattering order;

(c) Simplified geometrical model is used

Table 4. Calculated k_{eff} (Reactivity) with VARIANT for the YALINA-Thermal

Calculation	JEF2.2	JEF3.1	ENDF/B-VI.8
A: $SP_3^{(a)} P_0^{(b)}$	0.91002 (-9888 pcm)	0.94170 (-6191 pcm)	0.93994 (-6390 pcm)
B: P_3P_0	0.91634 (-9130 pcm)	0.94421 (-5909 pcm)	0.94242 (-6110 pcm)
C: P_5P_0	0.91897 (-8818 pcm)	0.94611 (-5696 pcm)	0.94431 (-5897 pcm)
D: SP_3P_1	0.91276 (-9558 pcm)	0.94476 (-5847 pcm)	0.94294 (-6051 pcm)
E: P_3P_1	0.92107 (-8569 pcm)	0.94923 (-5349 pcm)	0.94739 (-5553 pcm)
F ^(c) : SP_3P_3	0.91533 (-9250 pcm)	0.94758 (-5532 pcm)	0.94570 (-5742 pcm)

(a) Angular flux expansion (SP_3 : full P_3 angular flux expansion with simplified spherical harmonics, P_n : angular flux expansion order n);

(b) Anisotropic scattering order;

(c) Simplified geometrical model is used

The reactivity change due to increasing the angular flux expansion is obtained with P_0 anisotropic scattering; similarly, the correction due higher anisotropic scattering order is obtained with SP_3 expansion for the neutron flux. From the results of Tables 3 and 4, for instance, the reactivity results assuming P_5P_3 approximation are given in Tables 5 and 6. In the case of the YALINA-Booster, a quite good agreement in the reactivity values is observed for the three different nuclear data libraries, the obtained results vary within a range of ~400 pcm. Regarding the YALINA-Thermal, JEF3.1 and ENDF/B-VI.8 provide comparable results, but JEF2.2 gives a lower reactivity value of ~3000 pcm. The calculated reactivity differences from different data libraries will be discussed further in the next Section.

Table 5. Final k_{eff} (Reactivity) with VARIANT for the YALINA-Booster

Calculation	JEF2.2	JEF3.1	ENDF/B-VI.8
SP_3P_1	0.96877 (-3224 pcm)	0.96620 (-3498 pcm)	0.96537 (-3587 pcm)
Correction ^(a) : $P_5P_0 - SP_3P_0$	302 pcm	247 pcm	248 pcm
Correction ^(a) : $SP_3P_3 - SP_3P_1$	480 pcm	479 pcm	483 pcm
P_5P_3	0.97616 (-2442 pcm)	0.97303 (-2772 pcm)	0.97223 (-2856 pcm)

^(a) See values given in Table 3

Table 6. Final k_{eff} (Reactivity) with VARIANT for the YALINA-Thermal

Calculation	JEF2.2	JEF3.1	ENDF/B-VI.8
P_3P_1	0.92107 (-8569 pcm)	0.94923 (-5349 pcm)	0.94739 (-5553 pcm)
Correction ^(a) : $P_5P_0 - P_3P_0$	312 pcm	213 pcm	213 pcm
Correction ^(a) : $SP_3P_3 - SP_3P_1$	308 pcm	315 pcm	309 pcm
P_5P_3	0.92636 (-7949 pcm)	0.95401 (-4821 pcm)	0.95210 (-5031 pcm)

^(a) See values given in Table 4

VI.1.a. Perturbation Calculation

Perturbation calculations were performed to examine the reactivity differences obtained from the use of different nuclear data libraries. Since the ERANOS perturbation modules are only available in two dimensional geometry, an RZ model has been developed for the YALINA-Booster and -Thermal as shown in Appendix B.

The reactivity values obtained for the RZ model with the BISTRO code using S_4P_1 approximation are presented in Tables 7 and 8 for the YALINA-Booster and -Thermal, respectively. Using the same library, the difference between the BISTRO and VARIANT reactivity results shown in Tables 5 and 6 compared to Tables 7 and 8 are essentially due to the omission of the YALINA experimental channels from the RZ model. These channels are included in the three dimensional model of the VARIANT calculations.

Table 7. Calculated k_{eff} (Reactivity [pcm]) with RZ BISTRO Model for the YALINA-Booster

Model-Calculation	JEF2.2	JEF3.1	ENDF/B-VI.8
RZ- S_4P_1	0.980579 (-1980.6 pcm)	0.974383 (-2629.0 pcm)	0.973531 (-2718.9 pcm)

Table 8. Calculated k_{eff} (Reactivity [pcm]) with RZ BISTRO Model for the YALINA-Thermal

Model-Calculation	JEF2.2	JEF3.1	ENDF/B-VI.8
RZ- S_4P_1	0.941637 (-6198.0 pcm)	0.958009 (-4383.2 pcm)	0.955992 (-4603.4 pcm)

Table 9 gives the perturbation components of the observed BISTRO reactivity change due to the use of different nuclear data libraries for the YALINA-Booster. Isotopes that produce $\Delta\rho$ of less than 0.05 pcm are not listed in the table. It can be seen that the total reactivity change is +670 pcm for the (JEF2.2 - JEF3.1) results and -90 pcm for (ENDF/B-VI.8 - JEF3.1). The difference is consistent with the Table 7 results. U-235, Pb, C, Al, U-238 isotopes are the main contributors to the $\Delta\rho$ for the (JEF2.2 - JEF3.1) case. U-238, H and Pb isotopes are the main contributors to the $\Delta\rho$ for (ENDF/B-VI.8 - JEF3.1) case. However, it is important to notice that the perturbation components have different signs, which reduce the net reactivity difference.

Table 9. Perturbation Components [pcm] for the YALINA-Booster

$\Delta\rho$ (JEF2.2 – JEF3.1)								$\Delta\rho$ (ENDF/B-VI.8 – JEF3.1)							
Isotope	Capture	Fission	Leakage	Elastic	Inelastic	N,xN	Total	Isotope	Capture	Fission	Leakage	Elastic	Inelastic	N,xN	Total
U235	113.4	262.7	2.1	-0.1	-0.9	-	377.3	U235	-6.3	34.7	-0.2	-0.2	-	-	28.1
U238	-45.6	-14.3	-16.5	-0.9	-6.3	-4.1	-87.7	U238	-40.0	-12.4	-6.4	-0.6	-45.8	-0.3	-105.4
Fe54	-49.3	-	1.1	-	-0.5	-	-48.7	Fe54	-1.8	-	-3.5	-0.3	-0.5	-	-6.1
Fe56	-3.3	-	54.9	1.0	16.1	-	68.7	Fe56	-15.7	-	19.6	-0.4	5.0	-	8.4
Fe57	-5.7	-	-0.4	-0.5	-1.5	-	-8.1	Fe57	0.6	-	-6.5	-0.7	-2.1	-	-8.7
Fe58	0.1	-	-1.2	-0.1	-0.1	-	-1.2	Fe58	0.7	-	-1.6	-0.1	-0.1	-	-1.1
Cr50	1.0	-	-0.4	-0.1	-	-	0.5	Cr50	-0.2	-	-	-	-	-	-0.2
Cr52	-2.6	-	38.2	3.6	2.6	-	41.9	Cr52	7.7	-	14.4	1.3	4.7	-	28.1
Cr53	-11.4	-	3.7	0.9	-0.4	-	-7.0	Cr53	-0.2	-	-	-	-	-	-0.2
Cr54	0.1	-	-0.6	-0.1	-0.1	-	-0.6	Ni58	-0.3	-	-	-0.4	0.8	-	0.1
Ni58	0.5	-	0.6	-0.4	0.8	-	1.5	Ni60	0.6	-	0.7	0.1	0.1	-	1.5
Ni60	0.9	-	0.8	-	0.1	-	1.8	B10	-0.6	-	-	-	-	-	-0.6
Ni61	-0.2	-	0.1	-	-	-	-0.1	Pb207	-19.8	-	46.8	1.0	4.4	-2.1	30.3
Ni62	-0.1	-	-	-	-	-	-0.1	Pb208	-0.3	-	-22.9	-0.8	5.7	-2.0	-20.3
B10	-1.1	-	0.2	-	-	-	-0.9	Al27	1.5	-	-1.0	-0.1	-	-	0.4
B11	-	-	0.1	-0.1	-	-	-	P31	-0.3	-	0.2	-	-	-	-0.2
P31	-0.1	-	0.7	-	-	-	0.7	Sb121	2.4	-	0.1	-	-	-	2.5
Sb121	1.4	-	1.0	-	-0.1	-	2.3	Sb123	-1.3	-	-	-	-	-	-1.3
Sb123	-1.1	-	0.8	-	-0.2	-	-0.5	As75	-0.1	-	-	-	-	-	-0.1
H ^(a)	-7.8	-	18.6	5.4	-	-	16.2	Mn55	-0.1	-	0.1	-	-	-	-
C ^(b)	-2.1	-	-111.1	-1.5	-0.6	-	-115.5	Na23	-	-	-0.1	-	-	-	-0.1
Pb	-5.7	-	317.5	15.4	-14.1	-3.1	310.1	O16	-0.1	-	0.1	-0.1	-	-	-0.1
Ca	0.8	-	-	-	-	-	0.8	H ^(c)	-9.6	-	-62.0	-29.3	-	-	-100.9
Cu	-0.5	-	0.1	-	-	-	-0.4	C	-	-	-	-0.2	-	-	-0.3
Mg	1.3	-	-11.3	0.9	-0.8	-	-10.0	graphite	-	-	-0.1	-0.1	-	-	-0.1
Ti	-0.1	-	-	0.1	-0.1	-	-0.2	Mo	-2.2	-	0.1	-	-0.1	-	-2.2
Si	-	-	0.1	-	-	-	0.1	Ca	0.8	-	-	-	-	-	0.8
O	-1.7	-	5.7	1.0	-	-	5.0	Mg	1.4	-	-9.2	-1.6	-2.1	-	-11.5
Al	96.2	-	34.6	4.6	-20.3	-	115.1	Ti	-	-	-0.4	-	-0.1	-	-0.6
Mn	-8.9	-	0.4	0.1	0.5	-	8.0	S	0.2	-	-0.1	-	0.1	-	0.3
Zn	1.1	-	0.1	-	0.1	-	1.3	Pb204 ^(d)	19.4	-	48.3	0.8	0.3	-0.8	67.9
Total	69.6	248.5	340.1	29.2	-25.8	-7.2	670.4	Pb206 ^(d)	-	-	-	-	-	-	-
								Zn	4.6	-	-1.6	-0.1	-0.1	-	2.7
								Total	-59.0	22.3	14.8	-31.8	-30.0	-5.3	-89.0

(a) For JEF2.2 the isotope “bdH” is used for each hydrogenated material;

For JEF3.1 the isotope “HCH2” is used for polyethylene; “HH2O” for water; “H1” for other hydrogenated materials.

(b) For JEF2.2 the isotope “C” is used for the graphite reflector;

For JEF3.1 the isotope “Cgra” is used for the graphite reflector.

(c) For ENDF/B-VI.8 the isotope “POLY” is used for polyethylene; “H2OL” for water; “H1” for other hydrogenated materials;

For JEF3.1 the isotope “HCH2” is used for polyethylene; “HH2O” for water; “H1” for other hydrogenated materials.

(d) In ENDF/B-VI.8 the isotope Pb-204 is absent: the Pb-206 density is Pb-204 + Pb-206.

Table 10 shows the perturbation components for the observed BISTRO reactivity change when different data libraries are used for the case of the YALINA-Thermal. Isotopes not presented in the table contribute to the $\Delta\rho$ for less than 0.05 pcm!

The total reactivity variation is of the order of -1800 pcm for the (JEF2.2 – JEF3.1) results and of -210 pcm for (ENDF/B-VI.8 – JEF3.1). The results provided in Table 10 show that U-238 and H are the main contributors to the $\Delta\rho$ (ENDF/B-VI.8 – JEF3.1), while the $\Delta\rho$ (JEF2.2 – JEF3.1) is essentially caused by the carbon. This study demonstrates that the carbon is inadequate to represent the graphite reflector and consequently it is decided to avoid the use of the JEF2.2 library for the calculations of the YALINA-Thermal.

Table 10. Perturbation Components [pcm] for the YALINA-Thermal

$\Delta\rho$ (JEF2.2 – JEF3.1)								$\Delta\rho$ (ENDF/B-VI.8 – JEF3.1)							
Isotope	Capture	Fission	Leakage	Elastic	Inelastic	N,xN	Total	Isotope	Capture	Fission	Leakage	Elastic	Inelastic	N,xN	Total
U235	25.0	334.2	-1.1	-	-0.1	-	358.0	U235	-1.0	25.6	-0.3	-	-	-	24.3
U238	-57.5	-11.8	-10.5	-0.2	-19.2	-3.8	-103.0	U238	-43.1	-9.8	-5.0	-	-46.7	-0.3	-104.8
Fe54	-7.5	-	-	-	-0.3	-	-7.8	Fe54	-0.2	-	-0.2	-	-0.2	-	-0.6
Fe56	-1.5	-	1.8	0.4	2.3	-	3.0	Fe56	-1.5	-	0.9	-	1.1	-	0.5
Fe57	-0.7	-	0.2	-	-0.2	-	-0.8	Fe57	0.2	-	-	-	-0.2	-	-0.1
Fe58	-	-	-0.2	-	-	-	-0.2	Fe58	0.1	-	-0.1	-	-	-	-0.1
Cr50	-0.1	-	-0.1	-	-	-	-0.1	Cr52	1.2	-	0.8	-	1.1	-	3.1
Cr52	-0.4	-	1.7	0.2	0.3	-	1.9	Ni58	-0.1	-	-	-	0.2	-	0.1
Cr53	-2.0	-	-	-	-0.2	-	-2.2	Ni60	-	-	-	-	0.1	-	0.1
Cr54	-	-	-	-	-	-	-0.1	Pb207	-0.6	-	2.4	0.1	-0.1	-0.3	1.5
Ni58	-0.1	-	-0.2	-	0.2	-	-0.2	Pb208	-	-	-1.3	-0.1	3.1	-0.2	1.5
Ni60	-	-	-	-	0.1	-	0.1	Al27	3.7	-	-1.4	-0.1	-	-	2.3
B10	-0.9	-	-	-	-	-	-0.9	P31	-0.1	-	-	-	-	-	-
P31	-	-	0.1	-	-	-	0.1	Sb121	0.6	-	-	-	-	-	0.6
Sb121	0.5	-	0.1	-	-	-	0.5	Sb123	-0.3	-	-	-	-	-	-0.3
Sb123	-0.3	-	-	-	-	-	-0.3	As75	-	-	-	-	-	-	-
H ^(a)	3.1	-	9.6	48.5	-	-	61.2	O16	-	-	0.2	-0.1	-	-	0.1
C ^(b)	-2.9	-	-2137.0	-3.9	-1.1	-	-2145.0	H ^(c)	-16.5	-	-84.4	-25.9	-	-	-126.7
Total	79.3	322.4	-2186.1	47.1	-55.7	-4.6	-1797.5	C ^(d)	-0.1	-	0.3	-0.1	-	-	0.2
								Total	-50.1	15.8	-97.9	-30.1	-46.9	-1.0	-210.2

(a) For JEF2.2 the isotope “bdH” is used for each hydrogenated material;

For JEF3.1 the isotope “HCH2” is used for polyethylene; “HH2O” for water; “H1” for other hydrogenated materials.

(b) For JEF2.2 the isotope “C” is used for the graphite reflector;

For JEF3.1 the isotope “cgra” is used for the graphite reflector.

(c) For ENDF/B-VI.8 the isotope “POLY” is used for polyethylene; “H2OL” for water; “H1” for other hydrogenated materials: H1 gives 0 contribution;

For JEF3.1 the isotope “HCH2” is used for polyethylene; “HH2O” for water; “H1” for other hydrogenated materials: H1 gives 0 contribution.

(d) “C” is not used in graphite reflector. For the graphite reflector “cgra” and “graphl” are used for JEF3.1 and ENDF/B-VI.8 respectively: the graphite gives 0 contribution.

VI.2. Source Multiplication Factor, k_S

Calculations have been performed to determine the source multiplication factor, k_S , of the YALINA-Booster and -Thermal configurations. Two formulations for the k_S have been considered:

$$k_S = \frac{\langle F\Phi_S \rangle}{\langle A\Phi_S \rangle - \langle P_{n,xn}\Phi_S \rangle} \quad \text{Eq. 5}$$

and

$$k_S = \frac{\langle F\Phi_S \rangle + \langle P_{n,xn}\Phi_S \rangle}{\langle A\Phi_S \rangle} \quad \text{Eq. 6}$$

where:

Φ_S is the inhomogeneous (source-driven) flux, solution of the transport equation

$$A\Phi_S = F\Phi_S + P_{N,xN}\Phi_S + S;$$

A is the loss term (absorption + leakage) of the Boltzmann operator;

F is the fission production term;

$P_{n,xn}$ is the (n,xn) production term;

S is the external source driving the subcritical system.

For similarity with the multiplication factor, an inhomogeneous reactivity can be defined: $\rho_S = 1 - \frac{1}{k_S}$.

The k_S has been calculated for the three external sources considered by the YALINA benchmark: the (d,t), (d,d) and Cf-252 sources. For this purpose, the external sources had to be represented in the deterministic model. The (d,t) and (d,d) sources have been modeled as mono-energetic (14.1 MeV and 2.45MeV respectively) and uniformly distributed in an opportune volume at the assembly center of both YALINA configurations. Point neutron source cannot be represented explicitly in deterministic calculational models. The JEF3.1 energy spectrum of the Cf-252 source is used in the calculations, which is shown in Appendix D. The use of the Cf-252 fission spectrum from the JEF2.2 or the ENDF/B-VI.8 nuclear data files results in negligible differences relative to the spectrum from JEF3.1. The Cf-252 source has been distributed in an opportune volume located at the assembly center similar to the (d,t) and (d,d) neutron sources in the YALINA-Thermal and at $Z = 6.2$ cm in the YALINA-Booster, assuming that $Z = 0$ corresponds to the assembly midplane. The k_S calculations have been performed using the JEF2.2, JEF3.1 and ENDF/B-VI.8 data libraries for the YALINA-Booster and JEF3.1 and ENDF/B-VI.8 for the YALINA-Thermal.

As in the case of the multiplication factor, the impact on the calculated k_S values due to the number of energy groups, the angular flux expansion and the anisotropic scattering orders has been investigated. The results of the neutron balance and the corresponding k_S calculated with both Eqs. 5 and 6 have been presented in Tables 11 to 13 for the YALINA-Booster and in Tables 14 and 15 for the YALINA-Thermal.

Tables 11 to 15 give the calculated neutron balance per neutron source for the YALINA-Booster and -Thermal using different nuclear data files with different group structure sets and approximations. The approximations were imposed by the available computer resources for performing the calculations. For the same flux and cross-sections approximations, increasing the energy group number from 53 to 172 results in negligible change in the calculated ρ_S values. This change is about 10 pcm except for the YALINA-Thermal with (d,t) neutron source, where the effect is of the range of 100 pcm. In fact, the slowing down of the 14 MeV neutrons requires fine group structure for accurately presenting the neutron spectrum. For the same energy group structure, increasing the anisotropic scattering order results in less effect on the k_S values compared to the obtained effect for the multiplication factor.

The results presented in Tables 11 to 15 were used to obtain k_S with P_5P_1 approximation using 172 energy groups. For this purpose, as already done for the multiplication factor, the results with 53-energy group structure have been corrected as indicated in Tables 16 and 17 for the YALINA-Booster and -Thermal respectively. The obtained results are compiled in Tables 18 and 19.

For (d,t) neutron source, the highest k_S values are obtained in the YALINA-Booster and the lowest values are instead obtained in the YALINA-Thermal. The k_S value is lower than the k_{eff} value for the YALINA-Thermal as shown in Tables 5 and 6. Because the neutron leakage per fission neutron is increased and the number of fission reaction per source neutron is decreased as shown in Tables 14 and 15, which explains the lower k_S values. Equations. 5 and 6 do practically yield the same values for k_S as the k_{eff} of the assembly approach criticality.

Table 11.: Neutron Balance per Neutron Source and k_S for the YALINA-Booster
Using JEF2.2 Nuclear Data Files

(d,t) Source						
53gr	Leakage	Absorption	(n,xn)	Fission Source	k_S (ρ_S [pcm])⁽¹⁾	k_S (ρ_S [pcm])⁽²⁾
SP ₃ P ₀	4.515	69.294	0.520	72.288	0.98635 (-1384 pcm)	0.98644 (-1374 pcm)
P ₃ P ₀	4.253	67.227	0.525	70.171	0.98894 (-1118 pcm)	0.98902 (-1110 pcm)
P ₅ P ₀	4.676	73.513	0.515	76.706	0.98755 (-1261 pcm)	0.98763 (-1252 pcm)
SP ₃ P ₁	4.890	84.470	0.535	87.826	0.98875 (-1137 pcm)	0.98882 (-1131 pcm)
172gr	Leakage	Absorption	(n,xn)	Fission Source	k_S (ρ_S [pcm])⁽¹⁾	k_S (ρ_S [pcm])⁽²⁾
SP ₃ P ₀	4.714	72.403	0.580	75.538	0.98694 (-1324 pcm)	0.98703 (-1314 pcm)
(d,d) Source						
53gr	Leakage	Absorption	(n,xn)	Fission Source	k_S (ρ_S [pcm])⁽¹⁾	k_S (ρ_S [pcm])⁽²⁾
SP ₃ P ₀	2.843	43.823	0.025	45.644	0.97861 (-2186 pcm)	0.97862 (-2185 pcm)
P ₃ P ₀	2.890	45.590	0.025	47.456	0.97939 (-2105 pcm)	0.97940 (-2104 pcm)
P ₅ P ₀	2.999	47.277	0.020	49.252	0.98001 (-2040 pcm)	0.98002 (-2039 pcm)
SP ₃ P ₁	3.076	53.275	0.025	55.324	0.98220 (-1812 pcm)	0.98221 (-1811 pcm)
172gr	Leakage	Absorption	(n,xn)	Fission Source	k_S (ρ_S [pcm])⁽¹⁾	k_S (ρ_S [pcm])⁽²⁾
SP ₃ P ₀	2.854	44.022	0.025	45.854	0.97870 (-2176 pcm)	0.97871 (-2175 pcm)
Cf-252 Source						
53gr	Leakage	Absorption	(n,xn)	Fission Source	k_S (ρ_S [pcm])⁽¹⁾	k_S (ρ_S [pcm])⁽²⁾
SP ₃ P ₀	2.753	42.743	0.020	44.471	0.97789 (-2261 pcm)	0.97790 (-2260 pcm)
P ₃ P ₀	2.808	44.626	0.030	46.408	0.97898 (-2147 pcm)	0.97899 (-2146 pcm)
P ₅ P ₀	2.910	46.207	0.020	48.090	0.97949 (-2094 pcm)	0.97950 (-2093 pcm)
SP ₃ P ₁	2.984	52.032	0.030	53.986	0.98181 (-1853 pcm)	0.98182 (-1852 pcm)
172gr	Leakage	Absorption	(n,xn)	Fission Source	k_S (ρ_S [pcm])⁽¹⁾	k_S (ρ_S [pcm])⁽²⁾
SP ₃ P ₀	2.759	42.871	0.030	44.604	0.97816 (-2233 pcm)	0.97818 (-2231 pcm)

⁽¹⁾ Formulation according to Eq. 5; ⁽²⁾ Formulation according to Eq. 6.

Table 12. Neutron Balance per Neutron Source and k_S for the YALINA-Booster
Using JEF3.1 Nuclear Data Files

(d,t) Source						
53gr	Leakage	Absorption	(n,xn)	Fission Source	k_S (ρ_S [pcm])⁽¹⁾	k_S (ρ_S [pcm])⁽²⁾
SP ₃ P ₀	3.579	64.661	0.570	66.668	0.98519 (-1503 pcm)	0.98532 (-1490 pcm)
P ₃ P ₀	3.342	62.102	0.570	64.073	0.98765 (-1251 pcm)	0.98776 (-1240 pcm)
P ₅ P ₀	3.644	67.336	0.565	69.447	0.98626 (-1393 pcm)	0.98637 (-1382 pcm)
SP ₃ P ₁	3.731	77.444	0.585	79.590	0.98760 (-1255 pcm)	0.98769 (-1246 pcm)
172gr	Leakage	Absorption	(n,xn)	Fission Source	k_S (ρ_S [pcm])⁽¹⁾	k_S (ρ_S [pcm])⁽²⁾
SP ₃ P ₀	3.675	66.374	0.600	68.447	0.98557 (-1465 pcm)	0.98569 (-1452 pcm)
(d,d) Source						
53gr	Leakage	Absorption	(n,xn)	Fission Source	k_S (ρ_S [pcm])⁽¹⁾	k_S (ρ_S [pcm])⁽²⁾
SP ₃ P ₀	2.184	39.689	0.020	40.850	0.97605 (-2454 pcm)	0.97606 (-2453 pcm)
P ₃ P ₀	2.191	40.702	0.020	41.870	0.97660 (-2396 pcm)	0.97661 (-2395 pcm)
P ₅ P ₀	2.264	42.022	0.025	43.262	0.97744 (-2309 pcm)	0.97745 (-2307 pcm)
SP ₃ P ₁	2.280	47.530	0.030	48.783	0.97997 (-2044 pcm)	0.97999 (-2042 pcm)
172gr	Leakage	Absorption	(n,xn)	Fission Source	k_S (ρ_S [pcm])⁽¹⁾	k_S (ρ_S [pcm])⁽²⁾
SP ₃ P ₀	2.198	39.963	0.020	41.139	0.97621 (-2437 pcm)	0.97622 (-2436 pcm)
Cf-252 Source						
53gr	Leakage	Absorption	(n,xn)	Fission Source	k_S (ρ_S [pcm])⁽¹⁾	k_S (ρ_S [pcm])⁽²⁾
SP ₃ P ₀	2.106	38.609	0.020	39.689	0.97529 (-2533 pcm)	0.97531 (-2532 pcm)
P ₃ P ₀	2.118	39.706	0.030	40.798	0.97617 (-2441 pcm)	0.97618 (-2440 pcm)
P ₅ P ₀	2.186	40.939	0.020	42.098	0.97665 (-2391 pcm)	0.97666 (-2390 pcm)
SP ₃ P ₁	2.201	46.277	0.030	47.448	0.97936 (-2107 pcm)	0.97937 (-2106 pcm)
172gr	Leakage	Absorption	(n,xn)	Fission Source	k_S (ρ_S [pcm])⁽¹⁾	k_S (ρ_S [pcm])⁽²⁾
SP ₃ P ₀	2.114	38.782	0.020	39.871	0.97540 (-2522 pcm)	0.97541 (-2521 pcm)

⁽¹⁾ Formulation according to Eq. 5; ⁽²⁾ Formulation according to Eq. 6.

Table 13. Neutron Balance per Neutron Source and k_S for the YALINA-Booster
Using ENDF/B-VI.8 Nuclear Data Files

(d,t) Source						
53gr	Leakage	Absorption	(n,xn)	Fission Source	k_S (ρ_S [pcm])⁽¹⁾	k_S (ρ_S [pcm])⁽²⁾
SP ₃ P ₀	3.495	63.209	0.545	65.157	0.98485 (-1538 pcm)	0.98497 (-1526 pcm)
P ₃ P ₀	3.276	60.935	0.550	62.852	0.98728 (-1288 pcm)	0.98739 (-1277 pcm)
P ₅ P ₀	3.554	65.755	0.545	67.800	0.98598 (-1422 pcm)	0.98609 (-1411 pcm)
SP ₃ P ₁	3.633	75.507	0.555	77.581	0.98722 (-1294 pcm)	0.98731 (-1285 pcm)
172gr	Leakage	Absorption	(n,xn)	Fission Source	k_S (ρ_S [pcm])⁽¹⁾	k_S (ρ_S [pcm])⁽²⁾
SP ₃ P ₀	3.601	65.110	0.580	67.129	0.98530 (-1492 pcm)	0.98542 (-1479 pcm)
(d,d) Source						
53gr	Leakage	Absorption	(n,xn)	Fission Source	k_S (ρ_S [pcm])⁽¹⁾	k_S (ρ_S [pcm])⁽²⁾
SP ₃ P ₀	2.157	39.264	0.020	40.401	0.97584 (-2476 pcm)	0.97585 (-2475 pcm)
P ₃ P ₀	2.164	40.248	0.020	41.391	0.97639 (-2419 pcm)	0.97640 (-2417 pcm)
P ₅ P ₀	2.234	41.529	0.020	42.742	0.97710 (-2344 pcm)	0.97711 (-2342 pcm)
SP ₃ P ₁	2.248	46.943	0.025	48.167	0.97967 (-2075 pcm)	0.97968 (-2074 pcm)
172gr	Leakage	Absorption	(n,xn)	Fission Source	k_S (ρ_S [pcm])⁽¹⁾	k_S (ρ_S [pcm])⁽²⁾
SP ₃ P ₀	2.174	39.570	0.020	40.723	0.97602 (-2457 pcm)	0.97603 (-2456 pcm)
Cf-252 Source						
53gr	Leakage	Absorption	(n,xn)	Fission Source	k_S (ρ_S [pcm])⁽¹⁾	k_S (ρ_S [pcm])⁽²⁾
SP ₃ P ₀	2.079	38.175	0.020	39.231	0.97507 (-2557 pcm)	0.97508 (-2556 pcm)
P ₃ P ₀	2.091	39.256	0.020	40.324	0.97571 (-2489 pcm)	0.97572 (-2488 pcm)
P ₅ P ₀	2.156	40.439	0.020	41.570	0.97641 (-2416 pcm)	0.97642 (-2415 pcm)
SP ₃ P ₁	2.170	45.683	0.020	46.825	0.97895 (-2151 pcm)	0.97895 (-2150 pcm)
172gr	Leakage	Absorption	(n,xn)	Fission Source	k_S (ρ_S [pcm])⁽¹⁾	k_S (ρ_S [pcm])⁽²⁾
SP ₃ P ₀	2.091	38.400	0.020	39.467	0.97520 (-2543 pcm)	0.97522 (-2541 pcm)

⁽¹⁾ Formulation according to Eq. 5; ⁽²⁾ Formulation according to Eq. 6.

Table 14. Neutron Balance per Neutron Source and k_S for the YALINA-Thermal
Using JEF3.1 Nuclear Data Files

(d,t) Source						
53gr	Leakage	Absorption	(n,xn)	Fission Source	k_S (ρ_S [pcm])⁽¹⁾	k_S (ρ_S [pcm])⁽²⁾
SP ₃ P ₀	2.698	13.531	0.070	15.158	0.93806 (-6603 pcm)	0.93832 (-6573 pcm)
P ₃ P ₀	2.787	14.196	0.070	15.911	0.94077 (-6296 pcm)	0.94101 (-6269 pcm)
P ₅ P ₀	2.890	14.837	0.075	16.654	0.94345 (-5994 pcm)	0.94369 (-5967 pcm)
SP ₃ P ₁	2.774	14.331	0.080	16.023	0.94118 (-6249 pcm)	0.94146 (-6218 pcm)
P ₃ P ₁	2.930	15.532	0.085	17.380	0.94579 (-5732 pcm)	0.94604 (-5704 pcm)
172gr	Leakage	Absorption	(n,xn)	Fission Source	k_S (ρ_S [pcm])⁽¹⁾	k_S (ρ_S [pcm])⁽²⁾
SP ₃ P ₀	2.674	13.355	0.075	14.952	0.93719 (-6702 pcm)	0.93748 (-6668 pcm)
SP ₃ P ₁	2.759	14.224	0.085	15.896	0.94072 (-6302 pcm)	0.94101 (-6268 pcm)
(d,d) Source						
53gr	Leakage	Absorption	(n,xn)	Fission Source	k_S (ρ_S [pcm])⁽¹⁾	k_S (ρ_S [pcm])⁽²⁾
SP ₃ P ₀	3.477	18.994	0.000	21.468	0.95534 (-4675 pcm)	0.95534 (-4675 pcm)
P ₃ P ₀	3.571	19.727	0.000	22.294	0.95692 (-4502 pcm)	0.95692 (-4502 pcm)
P ₅ P ₀	3.651	20.226	0.000	22.872	0.95796 (-4389 pcm)	0.95796 (-4389 pcm)
SP ₃ P ₁	3.617	20.389	0.005	23.001	0.95838 (-4343 pcm)	0.95839 (-4342 pcm)
P ₃ P ₁	3.830	22.036	0.005	24.861	0.96136 (-4020 pcm)	0.96136 (-4019 pcm)
172gr	Leakage	Absorption	(n,xn)	Fission Source	k_S (ρ_S [pcm])⁽¹⁾	k_S (ρ_S [pcm])⁽²⁾
SP ₃ P ₀	3.493	19.098	0.000	21.587	0.95558 (-4649 pcm)	0.95558 (-4649 pcm)
SP ₃ P ₁	3.650	20.629	0.005	23.275	0.95885 (-4292 pcm)	0.95886 (-4291 pcm)
Cf-252 Source						
53gr	Leakage	Absorption	(n,xn)	Fission Source	k_S (ρ_S [pcm])⁽¹⁾	k_S (ρ_S [pcm])⁽²⁾
SP ₃ P ₀	3.636	20.100	0.004	22.732	0.95786 (-4400 pcm)	0.95786 (-4399 pcm)
P ₃ P ₀	3.741	20.910	0.005	23.647	0.95945 (-4226 pcm)	0.95946 (-4225 pcm)
P ₅ P ₀	3.837	21.512	0.005	24.344	0.96056 (-4106 pcm)	0.96057 (-4105 pcm)
SP ₃ P ₁	3.798	21.653	0.004	24.446	0.96067 (-4094 pcm)	0.96068 (-4093 pcm)
P ₃ P ₁	4.034	23.460	0.005	26.489	0.96362 (-3776 pcm)	0.96362 (-3775 pcm)
172gr	Leakage	Absorption	(n,xn)	Fission Source	k_S (ρ_S [pcm])⁽¹⁾	k_S (ρ_S [pcm])⁽²⁾
SP ₃ P ₀	3.640	20.124	0.000	22.759	0.95775 (-4412 pcm)	0.95775 (-4412 pcm)
SP ₃ P ₁	3.818	21.801	0.000	24.614	0.96079 (-4081 pcm)	0.96079 (-4081 pcm)

⁽¹⁾ Formulation according to Eq. 5; ⁽²⁾ Formulation according to Eq. 6.

Table 15. Neutron Balance per Neutron Source and k_S for the YALINA-Thermal
Using ENDF/B-VI.8 Nuclear Data Files

(d,t) Source						
53gr	Leakage	Absorption	(n,xn)	Fission Source	k_S (ρ_S [pcm])⁽¹⁾	k_S (ρ_S [pcm])⁽²⁾
SP ₃ P ₀	2.606	13.000	0.065	14.538	0.93551 (-6894 pcm)	0.93578 (-6863 pcm)
P ₃ P ₀	2.689	13.625	0.065	15.245	0.93826 (-6581 pcm)	0.93850 (-6553 pcm)
P ₅ P ₀	2.783	14.210	0.070	15.924	0.94094 (-6277 pcm)	0.94118 (-6249 pcm)
SP ₃ P ₁	2.672	13.725	0.080	15.319	0.93887 (-6511 pcm)	0.93917 (-6477 pcm)
P ₃ P ₁	2.808	14.806	0.075	16.538	0.94287 (-6059 pcm)	0.94312 (-6032 pcm)
172gr	Leakage	Absorption	(n,xn)	Fission Source	k_S (ρ_S [pcm])⁽¹⁾	k_S (ρ_S [pcm])⁽²⁾
SP ₃ P ₀	2.579	12.811	0.075	14.317	0.93482 (-6973 pcm)	0.93514 (-6936 pcm)
SP ₃ P ₁	2.652	13.594	0.080	15.164	0.93798 (-6612 pcm)	0.93829 (-6577 pcm)
(d,d) Source						
53gr	Leakage	Absorption	(n,xn)	Fission Source	k_S (ρ_S [pcm])⁽¹⁾	k_S (ρ_S [pcm])⁽²⁾
SP ₃ P ₀	3.375	18.410	0.000	20.781	0.95394 (-4828 pcm)	0.95394 (-4828 pcm)
P ₃ P ₀	3.460	19.086	0.000	21.542	0.95549 (-4658 pcm)	0.95549 (-4658 pcm)
P ₅ P ₀	3.533	19.546	0.005	22.076	0.95672 (-4523 pcm)	0.95673 (-4522 pcm)
SP ₃ P ₁	3.502	19.718	0.005	22.216	0.95699 (-4495 pcm)	0.95699 (-4494 pcm)
P ₃ P ₁	3.696	21.237	0.005	23.929	0.95992 (-4175 pcm)	0.95993 (-4174 pcm)
172gr	Leakage	Absorption	(n,xn)	Fission Source	k_S (ρ_S [pcm])⁽¹⁾	k_S (ρ_S [pcm])⁽²⁾
SP ₃ P ₀	3.388	18.500	0.000	20.885	0.95417 (-4803 pcm)	0.95417 (-4803 pcm)
SP ₃ P ₁	3.532	19.934	0.000	22.462	0.95723 (-4468 pcm)	0.95723 (-4468 pcm)
Cf-252 Source						
53gr	Leakage	Absorption	(n,xn)	Fission Source	k_S (ρ_S [pcm])⁽¹⁾	k_S (ρ_S [pcm])⁽²⁾
SP ₃ P ₀	3.530	19.493	0.004	22.019	0.95656 (-4541 pcm)	0.95657 (-4541 pcm)
P ₃ P ₀	3.625	20.244	0.004	22.865	0.95809 (-4374 pcm)	0.95810 (-4373 pcm)
P ₅ P ₀	3.714	20.797	0.004	23.507	0.95919 (-4255 pcm)	0.95919 (-4254 pcm)
SP ₃ P ₁	3.677	20.948	0.004	23.621	0.95937 (-4235 pcm)	0.95937 (-4235 pcm)
P ₃ P ₁	3.894	22.623	0.004	25.513	0.96226 (-3923 pcm)	0.96226 (-3922 pcm)
172gr	Leakage	Absorption	(n,xn)	Fission Source	k_S (ρ_S [pcm])⁽¹⁾	k_S (ρ_S [pcm])⁽²⁾
SP ₃ P ₀	3.533	19.515	0.010	22.044	0.95686 (-4509 pcm)	0.95688 (-4507 pcm)
SP ₃ P ₁	3.696	21.085	0.000	23.777	0.95947 (-4224 pcm)	0.95947 (-4224 pcm)

⁽¹⁾ Formulation according to Eq. 5; ⁽²⁾ Formulation according to Eq. 6.

Table 16. ρ_s Results for the YALINA-Booster

Source	Calculation Parameters	JEF2.2		JEF3.1		ENDF/B-VI.8	
		ρ_s [pcm] ⁽¹⁾	ρ_s [pcm] ⁽²⁾	ρ_s [pcm] ⁽¹⁾	ρ_s [pcm] ⁽²⁾	ρ_s [pcm] ⁽¹⁾	ρ_s [pcm] ⁽²⁾
(d,t)	53gr - SP ₃ P ₁	-1137	-1131	-1255	-1246	-1294	-1285
	172gr SP ₃ P ₀ – 53gr SP ₃ P ₀	60	61	38	38	46	46
	53gr P ₅ P ₀ – 53gr SP ₃ P ₀	123	122	110	108	116	115
	172gr P₅P₁	-954	-948	-1107	-1100	-1132	-1124
(d,d)	Calculated: 53gr - SP ₃ P ₁	-1812	-1811	-2044	-2042	-2075	-2074
	172gr SP ₃ P ₀ – 53gr SP ₃ P ₀	10	10	17	17	19	19
	53gr P ₅ P ₀ – 53gr SP ₃ P ₀	146	146	145	146	133	133
	172gr P₅P₁	-1656	-1655	-1881	-1880	-1923	-1922
Cf-252	Calculated: 53gr - SP ₃ P ₁	-1853	-1852	-2107	-2106	-2151	-2150
	172gr SP ₃ P ₀ – 53gr SP ₃ P ₀	28	29	11	11	14	14
	53gr P ₅ P ₀ – 53gr SP ₃ P ₀	167	167	142	142	141	141
	172gr P₅P₁	-1658	-1656	-1954	-1953	-1995	-1994

⁽¹⁾ Formulation according to Eq. 5; ⁽²⁾ Formulation according to Eq. 6.

Table 17. ρ_s Results for the YALINA-Thermal

Source	Calculation Parameters	JEF3.1		ENDF/B-VI.8	
		ρ_s [pcm] ⁽¹⁾	ρ_s [pcm] ⁽²⁾	ρ_s [pcm] ⁽¹⁾	ρ_s [pcm] ⁽²⁾
(d,t)	53gr - P ₃ P ₁	-5732	-5704	-6059	-6032
	172gr SP ₃ P ₁ – 53gr SP ₃ P ₁	-53	-50	-101	-100
	53gr P ₅ P ₀ – 53gr P ₃ P ₀	302	302	304	303
	172gr P₅P₁	-5482	-5453	-5856	-5828
(d,d)	Calculated: 53gr - P ₃ P ₁	-4020	-4019	-4175	-4174
	172gr SP ₃ P ₁ – 53gr SP ₃ P ₁	51	51	27	26
	53gr P ₅ P ₀ – 53gr P ₃ P ₀	113	113	135	136
	172gr P₅P₁	-3855	-3854	-4014	-4013
Cf-252	53gr - P ₃ P ₁	-3776	-3775	-3923	-3922
	172gr SP ₃ P ₁ – 53gr SP ₃ P ₁	12	12	11	10
	53gr P ₅ P ₀ – 53gr P ₃ P ₀	120	120	119	119
	172gr P₅P₁	-3643	-3643	-3793	-3793

⁽¹⁾ Formulation according to Eq. 5; ⁽²⁾ Formulation according to Eq. 6.

Table 18.: k_s (ρ_s) for the YALINA-Booster calculated with 172 Energy Group Set and P₅P₁ Approximations
Using Different Nuclear Data Files

Source	JEF2.2		JEF3.1		ENDF/B-VI.8	
	k_s (ρ_s) ⁽¹⁾	k_s (ρ_s) ⁽²⁾	k_s (ρ_s) ⁽¹⁾	k_s (ρ_s) ⁽²⁾	k_s (ρ_s) ⁽¹⁾	k_s (ρ_s) ⁽²⁾
(d,t)	0.99055	0.99061	0.98905	0.98912	0.98881	0.98889
	(-954 pcm)	(-948 pcm)	(-1107 pcm)	(-1100 pcm)	(-1132 pcm)	(-1124 pcm)
(d,d)	0.98371	0.98372	0.98153	0.98155	0.98113	0.98114
	(-1656 pcm)	(-1655 pcm)	(-1881 pcm)	(-1880 pcm)	(-1923 pcm)	(-1922 pcm)
Cf-252	0.98369	0.98371	0.98083	0.98084	0.98044	0.98045
	(-1658 pcm)	(-1656 pcm)	(-1954 pcm)	(-1953 pcm)	(-1995 pcm)	(-1994 pcm)

⁽¹⁾ Formulation according to Eq. 5; ⁽²⁾ Formulation according to Eq. 6.

Table 19. k_s (ρ_s) for the YALINA-Thermal calculated with 172 Energy Group Set and P_5P_1 Approximations Using Different Nuclear Data Files

Source	JEF3.1		ENDF/B-VI.8	
	k_s (ρ_s) ⁽¹⁾	k_s (ρ_s) ⁽²⁾	k_s (ρ_s) ⁽¹⁾	k_s (ρ_s) ⁽²⁾
(d,t)	0.94803 (-5482 pcm)	0.94829 (-5453 pcm)	0.94468 (-5856 pcm)	0.94493 (-5828 pcm)
(d,d)	0.96288 (-3855 pcm)	0.96289 (-3854 pcm)	0.96141 (-4014 pcm)	0.96142 (-4013 pcm)
Cf-252	0.96485 (-3643 pcm)	0.96485 (-3643 pcm)	0.96346 (-3793 pcm)	0.96346 (-3793 pcm)

⁽¹⁾ Formulation according to Eq. 5; ⁽²⁾ Formulation according to Eq. 6.

VI.3. Kinetic Parameters

The KIN3D module implemented in the ERANOS version 2.1 has been used to determine the kinetic parameters β_{eff} and Λ_{eff} using the three dimensional geometrical model according to Eqs. 1 and 2. In the present study, the unweighted kinetic parameters have been also calculated by setting $\Phi^* = 1$ in Eqs. 1 and 2. First, the kinetic parameters have been determined using only neutron fluxes calculated in absence of the source term and obtained with the JEF2.2, JEF3.1 and ENDF/B-VI.8 data libraries for the YALINA-Booster and JEF3.1 and ENDF/B-VI.8 for the YALINA-Thermal.

The delayed neutron data were taken from ENDF/B nuclear data files. These data are given in Appendix E, which include the decay constants, the delayed neutron number per fission reaction (β^v), and the delayed neutron spectrum. ERANOS inputs require to provide the total spectra of the delayed neutrons, while ENDF/B data provide delayed neutron spectrum by family group per each isotope. As consequence, the spectra presented in Tables 37 and 38 of Appendix E are obtained by combining the U-235 and U-238 delayed neutron spectra with the respective fission reaction fraction in the YALINA configurations under consideration.

The obtained results for the kinetic parameters are presented in Tables 20 to 23 for the YALINA-Booster and -Thermal. For comparison, the values obtained in RZ geometry with the S_n code BISTRO of ERANOS, are also presented. Decimals are reported only for distinguishing the results.

Table 20. Calculated β_{eff} Values for the YALINA-Booster

Nuclear Data Library	JEF2.2	JEF3.1	ENDF/B-VI.8
$\beta^{(a)}$ [pcm] - RZ	695.4	695.6	695.6
$\beta_{\text{eff}}^{(b)}$ [pcm] - KIN3D	752.8	753.3	753.4
$\beta_{\text{eff}}^{(b)}$ [pcm] - RZ	751.1	752.1	752.2

^(a) Unweighted;

^(b) Weighted by the homogeneous adjoint flux.

Table 21. Calculated β_{eff} Values for the YALINA-Thermal

Nuclear Data Library	JEF3.1	ENDF/B-VI.8
$\beta^{(a)}$ [pcm] - RZ	692.1	692.0
$\beta_{\text{eff}}^{(b)}$ [pcm] - KIN3D	779.1	779.2
$\beta_{\text{eff}}^{(b)}$ [pcm] - RZ	775.2	775.3

(a) Unweighted;

(b) Weighted by the homogeneous adjoint flux.

Table 22. Calculated Λ_{eff} Values for the YALINA-Booster

Nuclear Data Library	JEF2.2	JEF3.1	ENDF/B-VI.8
$\Lambda^{(a)}$ [μ s] - RZ	62.6	70.2	70.3
$\Lambda_{\text{eff}}^{(b)}$ [μ s] - KIN3D	47.4	50.4	50.3
$\Lambda_{\text{eff}}^{(b)}$ [μ s] - RZ	45.9	47.9	47.7

(a) Unweighted;

(b) Weighted by the homogeneous adjoint flux.

Table 23. Calculated Λ_{eff} Values for the YALINA-Thermal

Nuclear Data Library	JEF3.1	ENDF/B-VI.8
$\Lambda^{(a)}$ [μ s] - RZ	206.3	207.7
$\Lambda_{\text{eff}}^{(b)}$ [μ s] - KIN3D	87.0	87.5
$\Lambda_{\text{eff}}^{(b)}$ [μ s] - RZ	79.0	79.4

(a) Unweighted;

(b) Weighted by the homogeneous adjoint flux.

The obtained results of Tables 20 to 23 show the following conclusions:

- The use of the three libraries JEF2.2, JEF3.1 and ENDFB-VI.8 produce similar results for the calculated kinetic parameter values;
- As expected, the RZ model is able to provide an accurate estimation of β_{eff} and Λ_{eff} .

As previously discussed, the above results have been obtained using direct and adjoint neutron fluxes calculated in absence of the source term in the equations for β_{eff} and Λ_{eff} . The kinetic parameters have also obtained using a direct flux from the solution of the source driven equation $A\Phi_S = F\Phi_S + S$ and an adjoint flux solution of the transport equation $A\Phi_S^* = F\Phi_S^* + \nu\Sigma_f$ as a weighting function. VARIANT computer code has the capability to solve a direct equation with external neutron source but it does not have the capability to solve an adjoint equation with external neutron source. It is possible with the BISTRO computer code to obtain the adjoint flux with an external neutron source. As a consequence, the RZ model is used to obtain the kinetic parameters with different external neutron sources. The previous results showed that the kinetic parameters from the use of the three dimensional model (XYZ geometry) and the two dimensional model (RZ geometry) are similar.

Table 24. Calculated β_{eff} [pcm] of the YALINA Configurations with RZ Geometry

YALINA Configuration	Booster			Thermal	
	Nuclear Data Library	JEF2.2	JEF3.1	ENDF/B-VI.8	JEF3.1
A - No external neutron source – Unweighted	695.4	695.6	695.6	692.1	692.0
B - No external neutron source – Weighted with Homogeneous Adjoint Flux	751.1	752.1	752.2	775.2	775.3
C - (d,t) neutron source – Unweighted	694.7	694.7	694.7	692.9	692.8
D - (d,t) neutron source – Weighted with Homogeneous Adjoint Flux	749.0	749.3	749.3	776.5	776.7
E - (d,t) neutron source – Weighted with Inhomogeneous Adjoint Flux	749.0	749.3	749.3	776.0	776.1
F - (d,d) neutron source – Unweighted	695.5	695.7	695.7	692.2	692.1
G - (d,d) neutron source – Weighted with Homogeneous Adjoint Flux	750.4	751.1	751.2	775.9	776.1
H - (d,d) neutron source – Weighted with Inhomogeneous Adjoint Flux	750.4	751.0	751.1	775.3	775.4
I - Cf neutron source – Unweighted	695.3	695.5	695.6	692.1	692.0
J - Cf neutron source – Weighted with Homogeneous Adjoint Flux	750.1	750.8	750.9	775.8	775.9
K - Cf neutron source – Weighted with Inhomogeneous Adjoint Flux	750.1	750.7	750.8	775.1	775.3

Table 25. Calculated Λ_{eff} [μs] for the YALINA Configuration in RZ Geometry

YALINA Configuration	YALINA-Booster			YALINA-Thermal	
	Nuclear Data Library	JEF2.2	JEF3.1	ENDF/B-VI.8	JEF3.1
A - No external neutron source – Unweighted	62.6	70.2	70.3	206.3	207.7
B - No external neutron source – Weighted with Homogeneous Adjoint Flux	45.9	47.9	47.7	79.0	79.4
C - (d,t) neutron source – Unweighted	60.4	66.9	66.9	204.7	206.1
D - (d,t) neutron source – Weighted with Homogeneous Adjoint Flux	44.2	45.6	45.4	78.4	78.8
E - (d,t) neutron source – Weighted with Inhomogeneous Adjoint Flux	44.4	45.9	45.7	78.8	79.3
F - (d,d) neutron source – Unweighted	60.4	67.0	66.9	200.7	201.8
G - (d,d) neutron source – Weighted with Homogeneous Adjoint Flux	44.3	45.7	45.5	78.2	78.5
H - (d,d) neutron source – Weighted with Inhomogeneous Adjoint Flux	44.5	46.0	45.8	78.5	78.9
I - Cf neutron source – Unweighted	60.4	66.9	66.9	199.3	200.3
J - Cf neutron source – Weighted with Homogeneous Adjoint Flux	44.3	45.7	45.5	78.0	78.3
K - Cf neutron source – Weighted with Inhomogeneous Adjoint Flux	44.5	46.0	45.8	78.3	78.7

The results of Tables 24 and 25 show that the use of source dependent fluxes to calculate the kinetic parameters has a small impact on their values. This implies that the external neutron sources in the YALINA configurations do not excite the high order harmonics especially in the case of the adjoint solution because the source term is distributed like the fission neutron source, $v\Sigma_f$. The change in the kinetic parameter values due to the use of external neutron source are given in Tables 26 and 27. By applying the corrections listed in Tables 26 and 27 to the values calculated in 3D geometry with KIN3D from Tables 20 to 23, the final results are listed in Tables 28 and 29.

Table 26. $\Delta\beta_{\text{eff}}$ [pcm] Due to the Use of Different External Neutron Source Relative to the case without External Neutron Source with RZ Geometry

YALINA Configuration	YALINA-Booster			YALINA-Thermal	
	Nuclear Data Library	JEF2.2	JEF3.1	ENDF/B-VI.8	JEF3.1
$\Delta\beta_{\text{eff}}$ [pcm] (case E – caseB)	-2.1	-2.8	-3.0	0.8	0.8
$\Delta\beta_{\text{eff}}$ [pcm] (case H – caseB)	-0.7	-1.1	-1.1	0.1	0.1
$\Delta\beta_{\text{eff}}$ [pcm] (case K – caseB)	-1.0	-1.4	-1.5	-0.1	-0.1

Table 27. $\Delta\Lambda_{\text{eff}}$ [μs] Due to the Use of Different External Neutron Source Relative to the case without External Neutron Source with RZ Geometry

YALINA Configuration	YALINA-Booster			YALINA-Thermal	
	Nuclear Data Library	JEF2.2	JEF3.1	ENDF/B-VI.8	JEF3.1
$\Delta\Lambda_{\text{eff}}$ [μs] (case E – caseB)	-1.5	-1.9	-2.0	-0.2	-0.2
$\Delta\Lambda_{\text{eff}}$ [μs] (case H – caseB)	-1.4	-1.9	-2.0	-0.5	-0.5
$\Delta\Lambda_{\text{eff}}$ [μs] (case K – caseB)	-1.4	-1.9	-2.0	-0.6	-0.7

Table 28. β_{eff} [pcm] Adjoint Flux Weighted Values for the YALINA Configurations

YALINA Configuration	Booster			Thermal	
	Nuclear Data Library	JEF2.2	JEF3.1	ENDF/B-VI.8	JEF3.1
(d,t) neutron source	750.7	750.4	750.4	779.8	780.0
(d,d) neutron source	752.0	752.2	752.2	779.2	779.3
Cf neutron source	751.8	751.8	751.9	779.0	779.2

Table 29. Λ_{eff} [μs] Adjoint Flux Weighted Values for the YALINA Configurations

YALINA Configuration	Booster			Thermal	
	Nuclear Data Library	JEF2.2	JEF3.1	ENDF/B-VI.8	JEF3.1
(d,t) neutron source	45.9	48.5	48.3	86.9	87.3 0
(d,d) neutron source	46.0	48.5	48.3	86.6	87.0
Cf neutron source	46.0	48.5	48.3	86.4	86.8

VI.4. Neutron Spectra

Neutron spectra have been calculated at the center of the experimental channels EC2B (fast zone), EC6T (thermal zone), EC8R (reflector) for the YALINA-Booster configuration, and EC1 (fuel zone), EC2 (fuel zone), EC3 (fuel zone), EC5 (reflector), EC6 (reflector) for the YALINA-Thermal configuration. The channel locations in the YALINA-Booster and -Thermal are shown in Figures 1 and 10, respectively. The calculations have been performed for three external neutron sources (d,t), (d,d) and Cf-252 using the JEF2.2, JEF3.1 and ENDF/B-VI.8 data libraries for the YALINA-Booster and JEF3.1 and ENDF/B-VI.8 for the YALINA-Thermal. In the present Section, the JEF3.1 results will be presented, while the comparison of the neutron spectra obtained with different libraries is shown in Appendix F.

The neutron spectra have been calculated in the 172 energy group structure with SP_3P_0 (P_3 angular flux expansion with simplified spherical harmonics and anisotropic scattering order 0) and SP_3P_1 (P_3 angular flux expansion with simplified spherical harmonics and anisotropic scattering order 1) for the YALINA-Booster and -Thermal respectively, as shown in Figures 17 through 24. The angular flux expansion and the anisotropic scattering order cannot be increased further because of the limitations of the computer resources when using 172 energy groups. However, the neutron spectra for the YALINA-Thermal with (d,d) neutron source calculated in 172 energy group structure with SP_3P_0 and SP_3P_1 approximations have been compared in Figure 25. The two spectra show a good agreement and minor differences are observed at high neutron energy. This indicates that the flux spectra obtained in SP_3P_0 approximation is adequate.

VI.4.a. Neutron Spectra of the YALINA-Booster

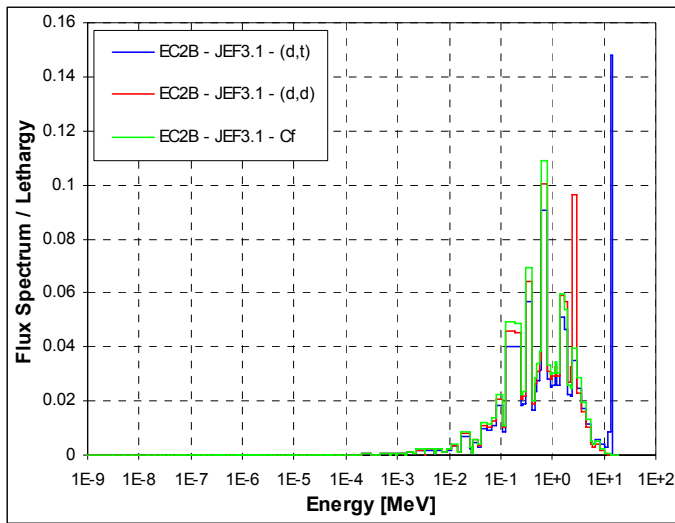


Figure 17. EC2B Neutron Spectra in the YALINA-Booster

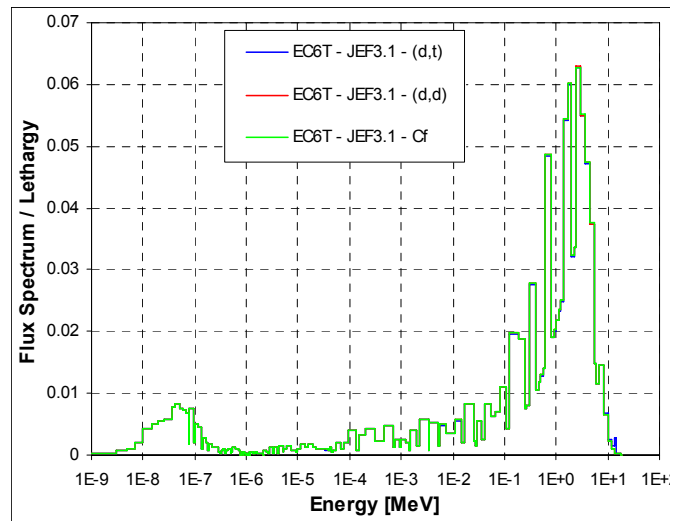


Figure 18. EC6T Neutron Spectra in the YALINA-Booster

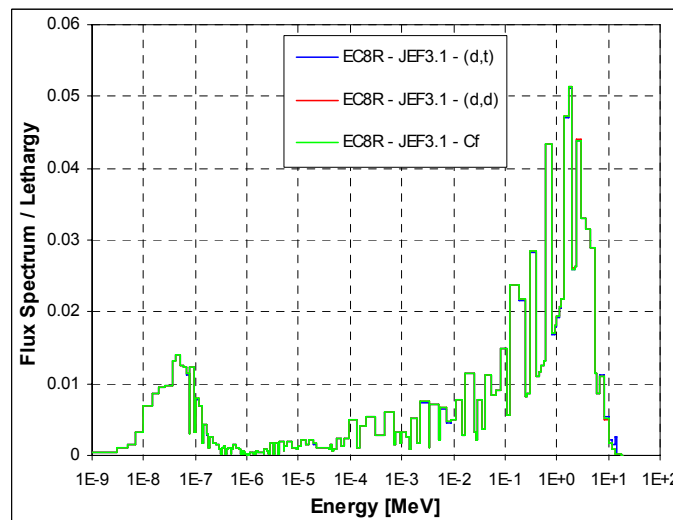


Figure 19. EC8R Neutron Spectra in the YALINA-Booster

VI.4.b. Neutron Spectra of the YALINA-Thermal

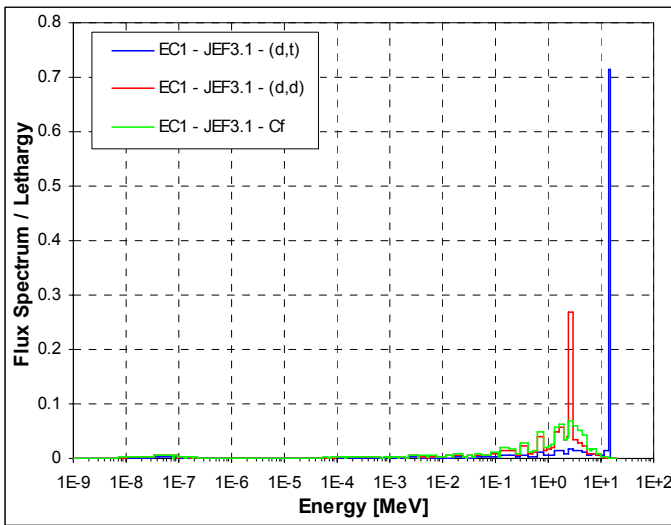


Figure 20. EC1 Neutron Spectra in the YALINA-Thermal

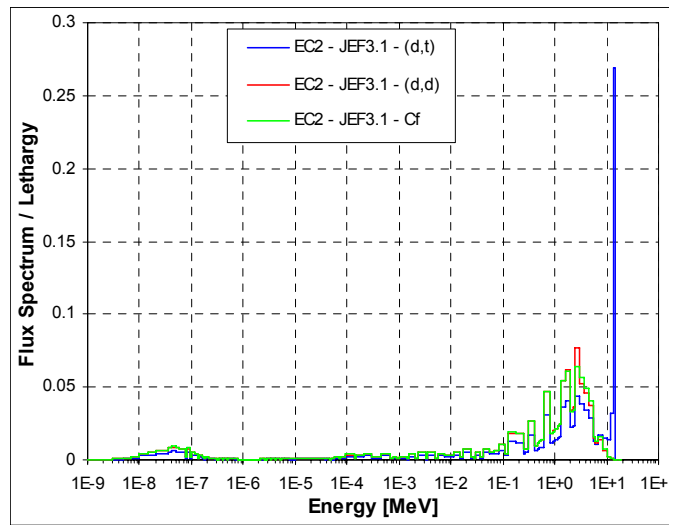


Figure 21. EC2 Neutron Spectra in the YALINA-Thermal

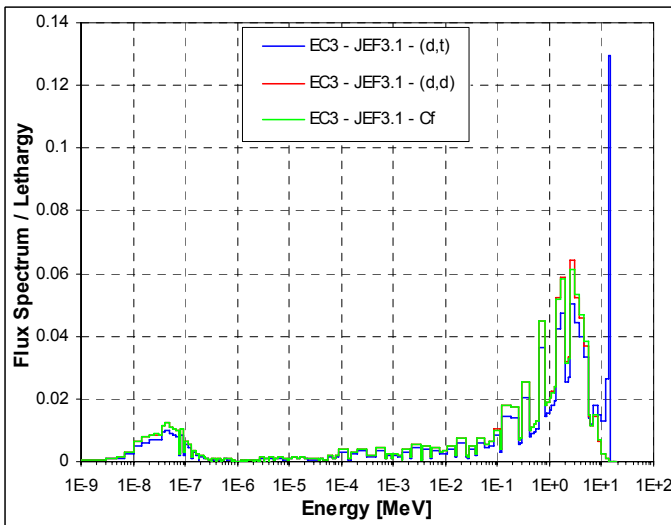


Figure 22. EC3 Neutron Spectra in the YALINA-Thermal

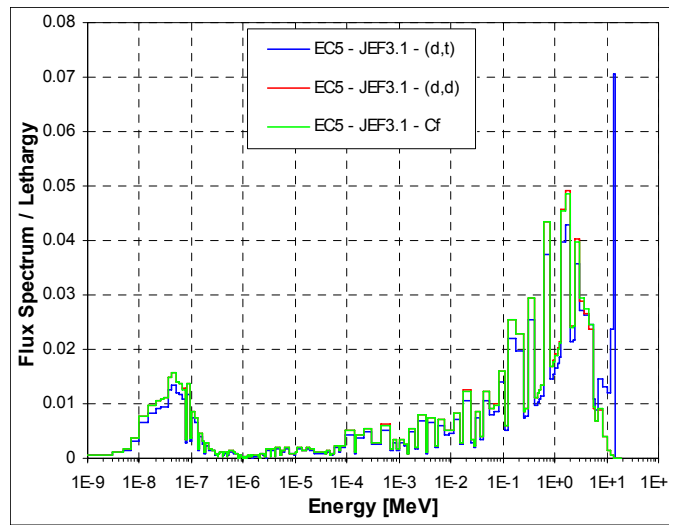


Figure 23. EC5 Neutron Spectra in the YALINA-Thermal

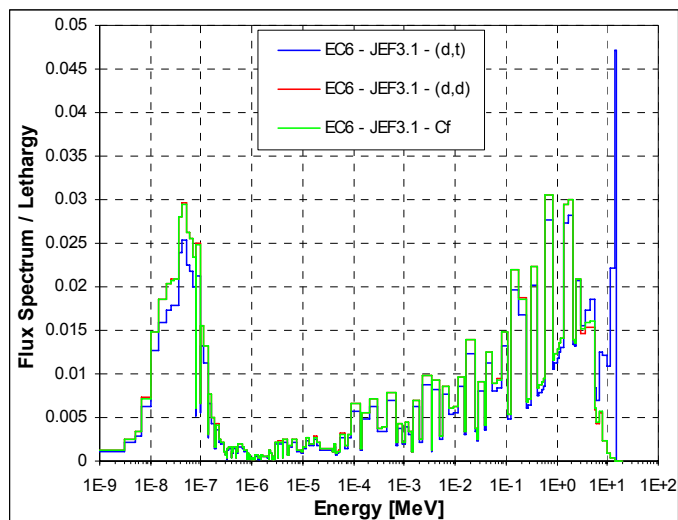


Figure 24. EC6 Neutron Spectra in the YALINA-Thermal

VI.4.c. Comparison of Neutron Spectra in the YALINA-Thermal Calculated with Different Approximations

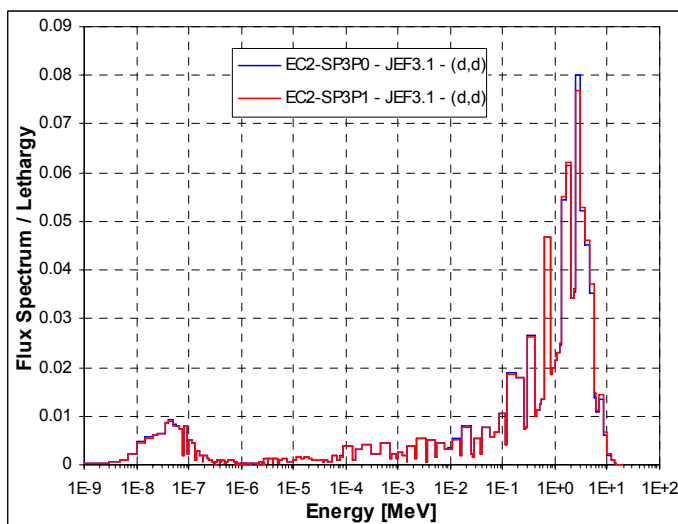


Figure 25. EC2 Neutron Spectra in the YALINA-Thermal with Different Approximations

VI.5. Reaction Rate Distributions

Reaction rates have been calculated along the experimental channels in presence of the three external neutron sources (d,t), (d,d) and Cf-252, using JEF2.2, JEF3.1 and ENDF/B-VI.8 for the YALINA-Booster, and JEF3.1 and ENDF/B-VI.8 for the YALINA-Thermal. The reaction rates have been obtained using the 53 energy groups fluxes with the most accurate approximation orders possible by the present computational resources: SP_3P_1 for the YALINA-Booster and P_3P_1 for the YALINA-Thermal. As discussed in Section VI.1, the final calculated reactivity values have been derived at higher approximation orders by applying appropriate correction factors. The absolute reaction rate values are function of the assembly reactivity since the neutron multiplication and consequently the neutron flux are function of the reactivity. It is assumed that the reaction rate value is inversely proportional to the associated reactivity. For this reason, the fluxes have been calculated

with the highest possible expansion orders allowed by the computer resources and an appropriate correction factor has been applied to v . This factor is the ratio between the final k_{eff} value and the k_{eff} normally calculated without any correction on v . So that, the neutron flux is corresponding to the most accurate reactivity value calculated for the subcritical assembly. As an alternative solution, the v could have been normalized to the measured reactivity rather than the calculated value. In addition, separate fluxes calculations have been performed for the cases where the reaction rates are required to be determined with the explicit modeling of the experimental channel holders. The other calculations assume air in the experimental channels.

In addition, the neutron detector cross-sections have been calculated in a separate cell calculation. For some reaction rates, the detectors are explicitly described along the experimental channel with their materials and geometrical details. In the deterministic calculation, often it is quite difficult to model the detector with accurate details, particularly due to the restrictions imposed by the cell code for the geometrical description. In this calculation, the detector cross-sections have been obtained with a single homogeneous cell calculation, where the detector compositions are “infinitely diluted”. This solution could affect the calculated results since the detector cross-sections do not account for the self-shielding effects associated with the detector material. After comparing the calculated reaction rates with the results obtained from Monte-Carlo calculations where the detectors can be explicitly described and the experimental measurements, further investigation could be performed in the attempt to quantify possible effects neglected in the present calculations.

In the present Section, the JEF3.1 results are presented, while the comparison of the reaction rates obtained with different nuclear data files is shown in Appendix G. For demonstration purpose, the He-3 (n,p) and U-235 fission reaction rates in the EC6T and EC2B experimental channels with (d,t) neutron source, respectively, have been calculated with and without correction on v as shown in Figures 48 and 49. The obtained values are approximately consistent with the previously mentioned formula:

$$\frac{T_{\text{without}_v\text{correction}}}{T_{\text{with}_v\text{correction}}} \cong \frac{\rho_{\text{with}_v\text{correction}}}{\rho_{\text{without}_v\text{correction}}}. \text{ From Tables 3 and 5, } \rho_{\text{without}_v\text{correction}} = -3498 \text{ pcm and}$$

$$\rho_{\text{with}_v\text{correction}} = -2772 \text{ pcm, } \frac{\rho_{\text{with}_v\text{correction}}}{\rho_{\text{without}_v\text{correction}}} = \frac{2772}{3498} = 0.79, \text{ which corresponds approximately to the}$$

ratio of the reaction rates shown in Figures 48 and 49.

In Appendix G, the He-3 (n,p) reaction rates for the YALINA-Booster have not been calculated with JEF2.2 nuclear data because He-3 is missing in this library. The JEF2.2 reaction rate values are higher values than the corresponding values from the other nuclear data libraries. This is due to the higher multiplication factor obtained with JEF2.2 relative to the other libraries, as discussed before.

VI.5.a. Reaction Rate Distributions in the YALINA-Booster

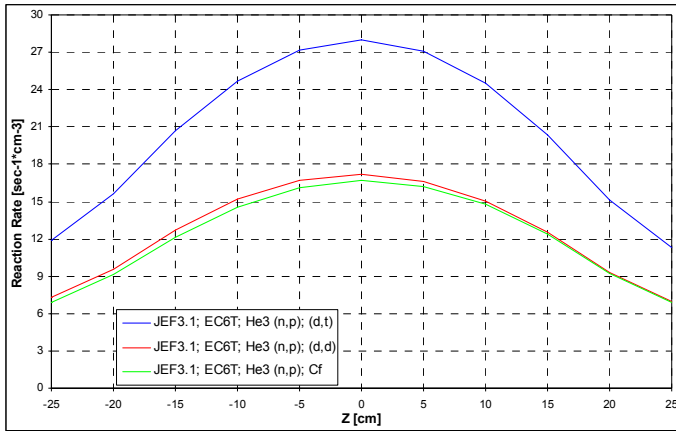


Figure 26. EC6T He-3 (n,p) Reaction Rates in the YALINA-Booster

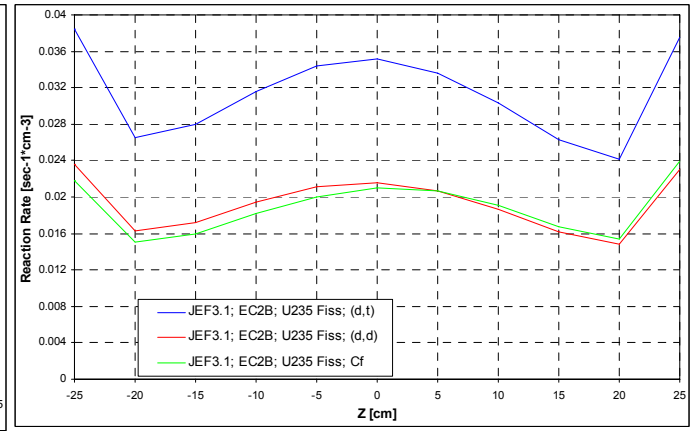


Figure 27. EC2B U-235 Fission Reaction Rates in the YALINA-Booster

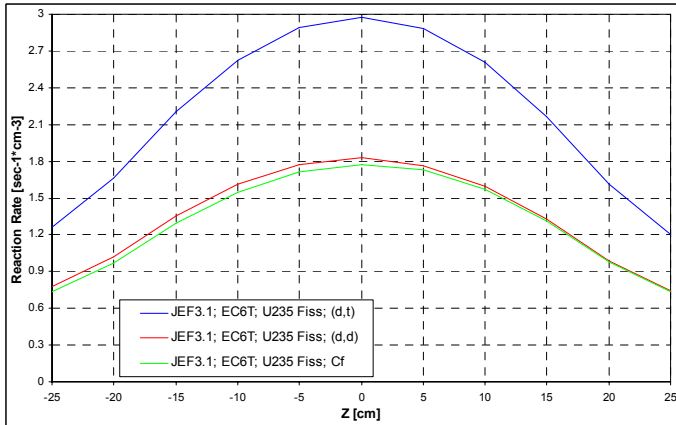


Figure 28. EC6T U-235 fission Reaction Rates in the YALINA-Booster

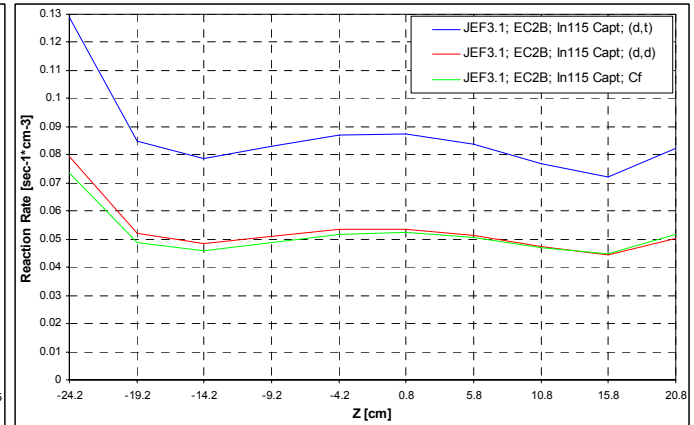


Figure 29. EC2B In-115 Capture Reaction Rates in the YALINA-Booster. Lead Holder is Modeled

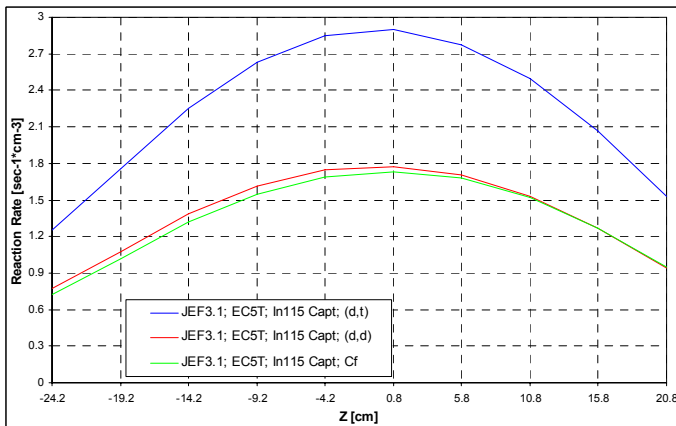


Figure 30. EC5T In-115 Capture Reaction Rates in the YALINA-Booster. Polyethylene Holder is Modeled

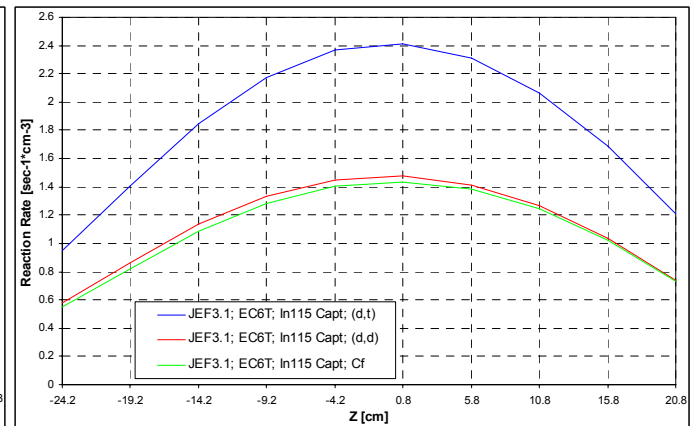


Figure 31. EC6T In-115 Capture Reaction Rates in the YALINA-Booster. Polyethylene Holder is Modeled

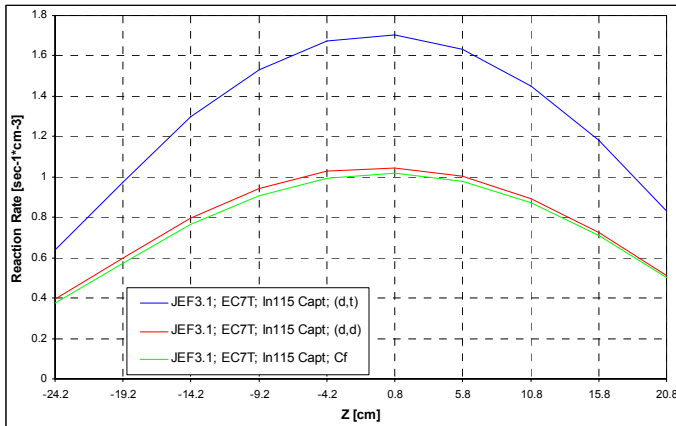


Figure 32. EC7T In-115 Capture Reaction Rates in the YALINA-Booster. Polyethylene Holder is Modeled

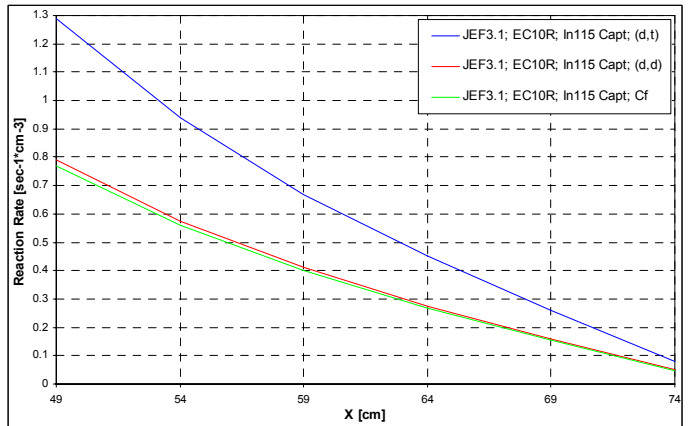


Figure 33. EC10R In-115 Capture Reaction Rates in the YALINA-Booster. Polyethylene Holder is Modeled

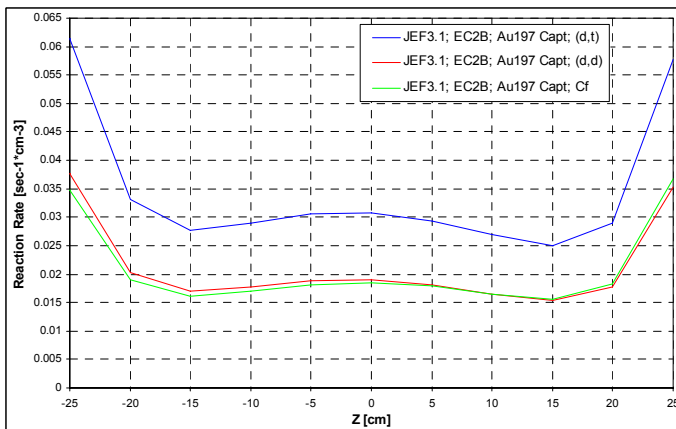


Figure 34. EC2B Au-197 Capture Reaction Rates in the YALINA-Booster. Lead Holder is Modeled

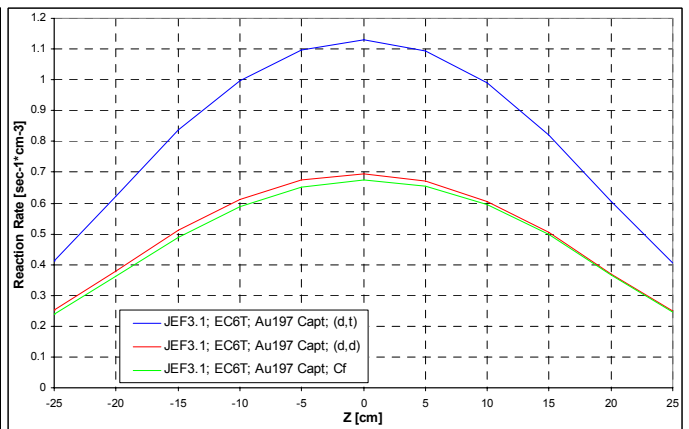


Figure 35. EC6T Au-197 Capture Reaction Rates in the YALINA-Booster. Polyethylene Holder is Modeled

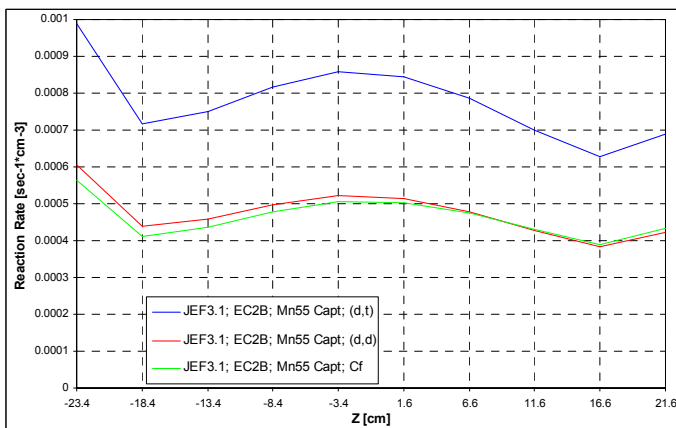


Figure 36. EC2B Mn-55 Capture Reaction Rates in the YALINA-Booster. Lead Holder is in Modeled

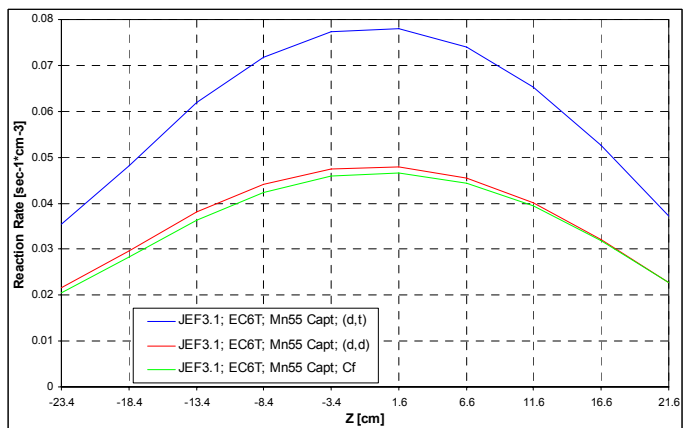


Figure 37. EC6T Mn-55 Capture Reaction Rates in the YALINA-Booster. Polyethylene Holder is Modeled

VI.5.b. Reaction Rate Distributions in the YALINA-Thermal

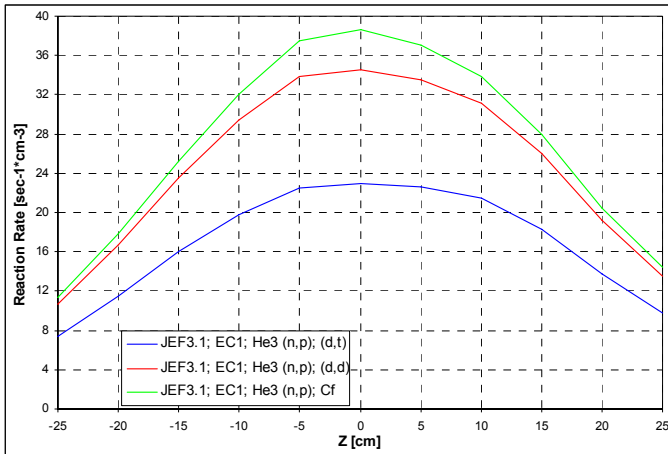


Figure 38. EC1 He-3 (n,p) Reaction Rates in the YALINA-Thermal

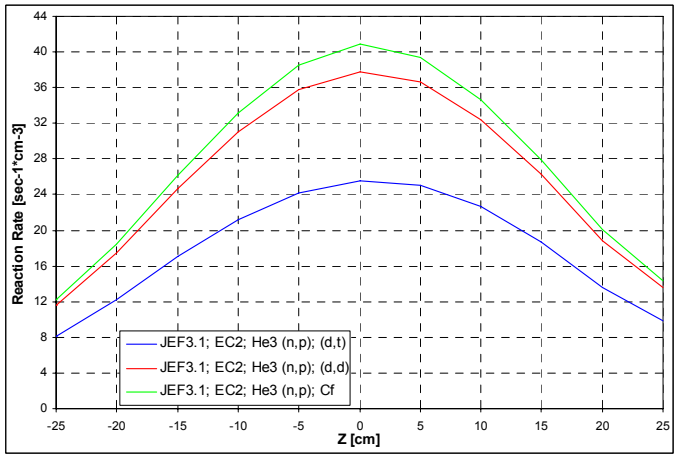


Figure 39. EC2 He-3 (n,p) Reaction Rates in the YALINA-Thermal

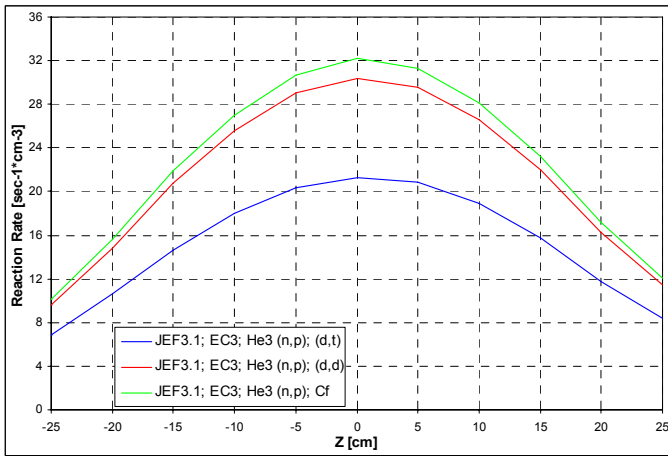


Figure 40. EC3 He-3 (n,p) Reaction Rates in the YALINA-Thermal

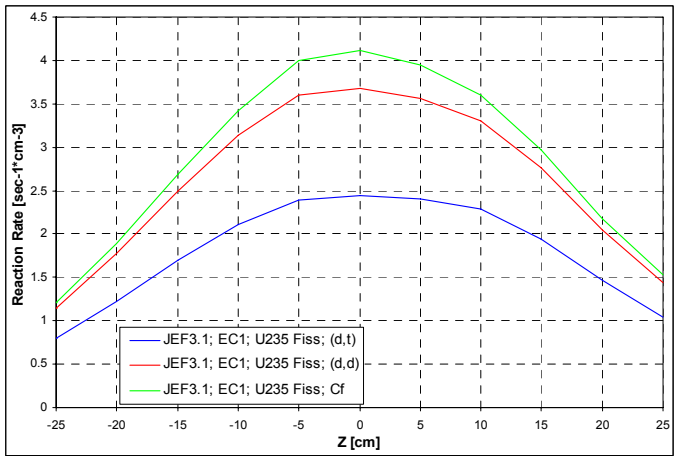


Figure 41. EC1 U-235 Fission Reaction Rates in the YALINA-Thermal

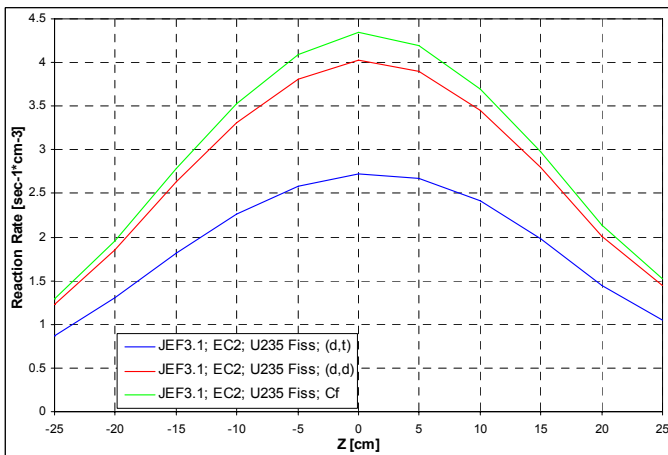


Figure 42. EC2 U-235 Fission Reaction Rates in the YALINA-Thermal

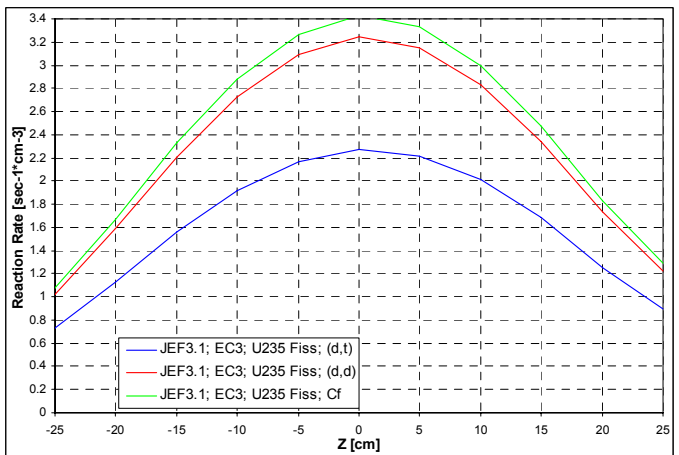


Figure 43. EC3 U-235 Fission Reaction Rates in the YALINA-Thermal

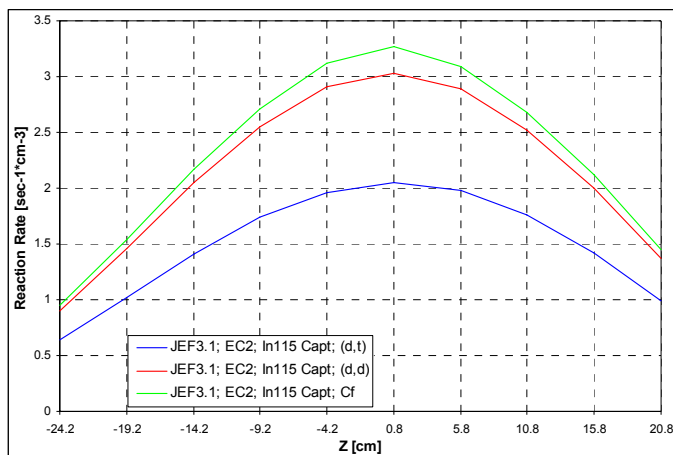


Figure 44. EC2 In-115 Capture Reaction Rates in the YALINA-Thermal. Polyethylene Holder is Modeled

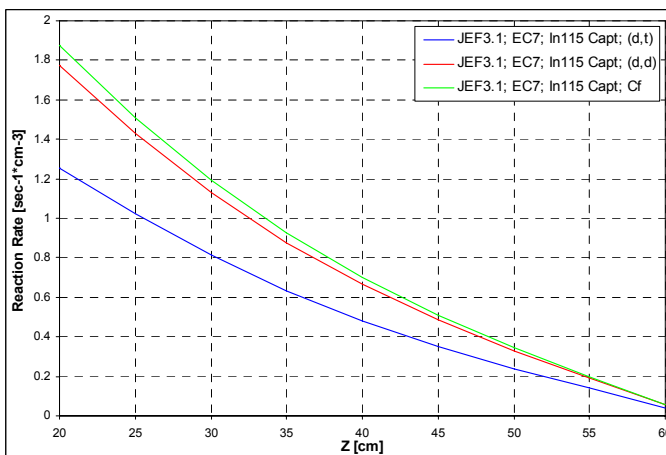


Figure 45. EC7 In-115 Capture Reaction Rates in the YALINA-Thermal. Polyethylene Holder is Modeled

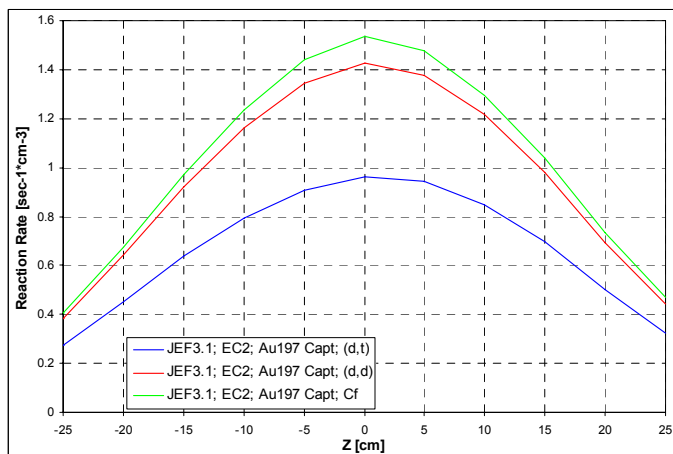


Figure 46. EC2 Au-197 Capture Reaction Rates in the YALINA-Thermal. Polyethylene Holder is Modeled

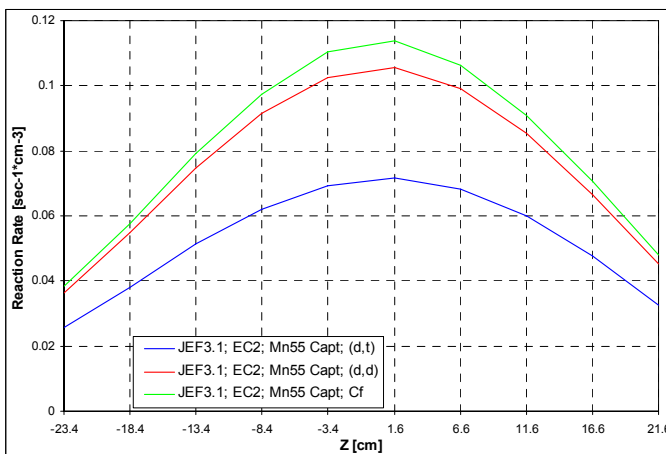


Figure 47. EC2 Mn-55 Capture Reaction Rates in the YALINA-Thermal. Polyethylene Holder is Modeled

VI.5.c. Comparison of Reaction Rate Distributions in the YALINA-Booster

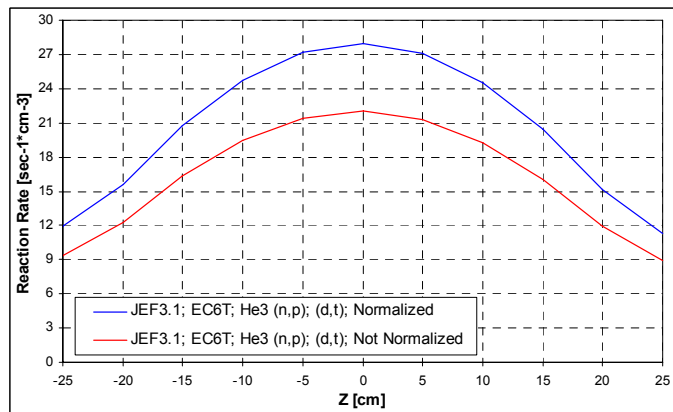


Figure 48. EC6T He-3 (n,p) Reaction Rates in the YALINA-Booster

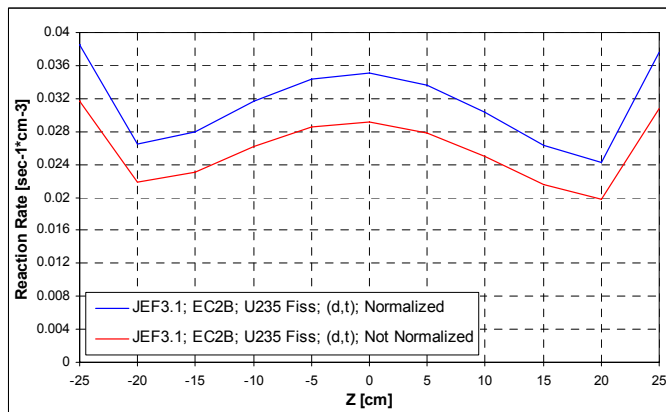


Figure 49. EC2B U-235 Fission Reaction Rates in the YALINA-Booster

VI.6. Pulse Calculations

The KIN3D code of ERANOS has been used to perform pulse calculations. The goal is to calculate the neutron detector response in the subcritical YALINA configurations to repeated neutron pulses with a very short pulse duration of $5\mu\text{s}$. In the calculations, the neutron pulse is simulated as having a triangular shape, with the intensity linearly increasing from 0 to a maximum value (MV) in the time interval $0 < t < 2.5\mu\text{s}$, then linearly decreasing from MV to 0 in $2.5 < t < 5\mu\text{s}$. The maximum amplitude, MV, reached by the neutron pulse in the calculations has been arbitrary fixed to 1000. Then, the calculated response is then normalized according to the benchmark specifications (see Section III).

KIN3D has capabilities to perform the calculations in transport and diffusion approximations. In this analyses, the simulation has been carried out with the diffusion approximation. Since the decay slope of the detector response is strictly dependent on the reactivity value of the calculated model, the multiplication factor has been normalized to the most accurate value obtained from the transport calculation. The normalization is made by multiplying v by an appropriate constant, which is the ratio between the desired multiplication factor and the k_{eff} value normally obtained by the calculation without introducing any change on v .

Kinetic calculations have been performed for the YALINA-Booster using the JEF2.2, JEF3.1 and ENDF/B-VI.8 and for the YALINA-Thermal using JEF3.1 and ENDF/B-VI.8. Results obtained with JEF3.1 are presented in this Section and Appendix H gives the results from the use of the other nuclear data files. The results show that the use of the two external sources (d,t) or (d,d) has only an effect on the amplitude of the detector response but not on the decay slope that remains practically the same.

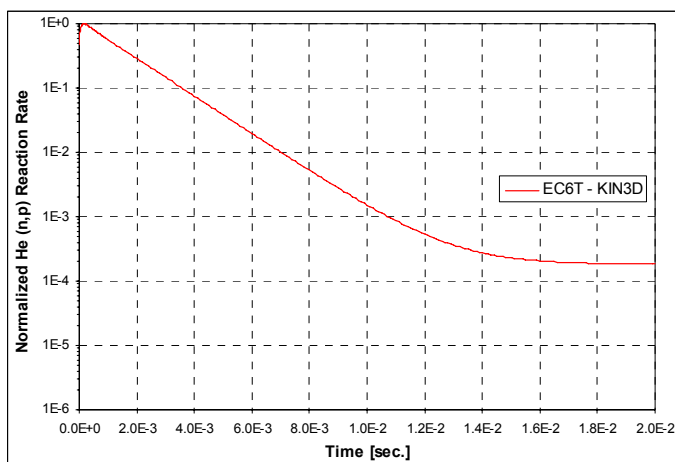


Figure 50. JEF3.1 EC6T Detector Response with (d,t) Neutron Source for the YALINA-Booster

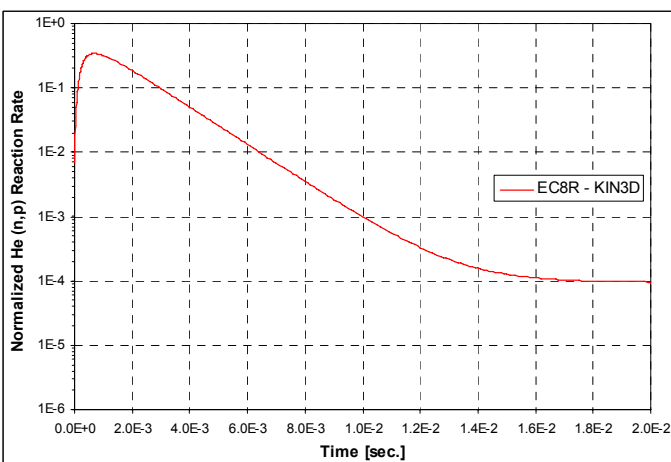


Figure 51. JEF3.1 EC8R Detector Response with (d,t) Neutron Source for the YALINA-Booster

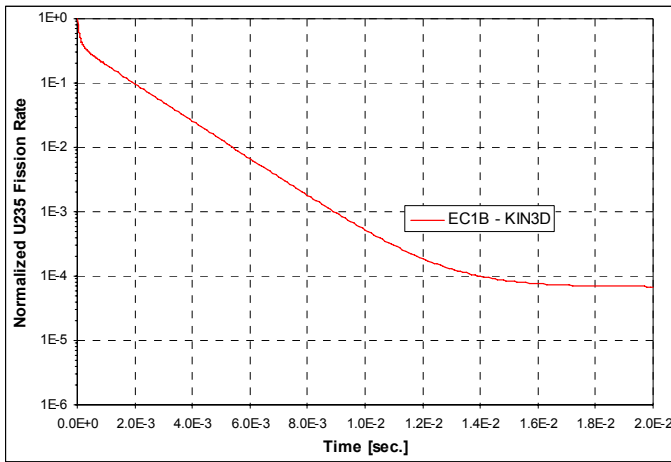


Figure 52. JEF3.1 EC1B Detector Response with (d,t) Neutron Source for the YALINA-Booster

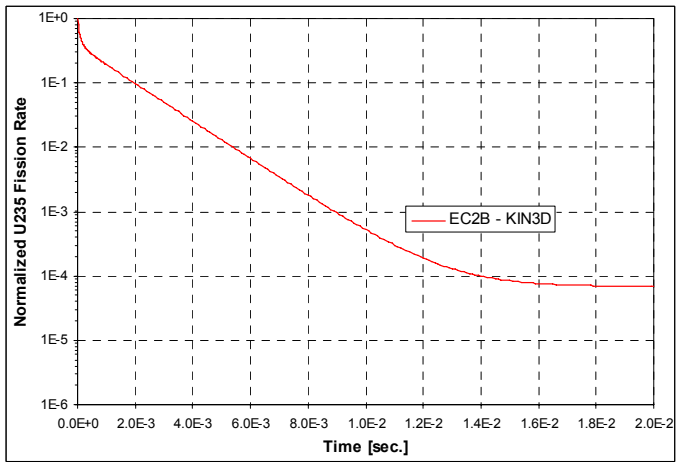


Figure 53. JEF3.1 EC2B Detector Response with (d,t) Neutron Source for the YALINA-Booster

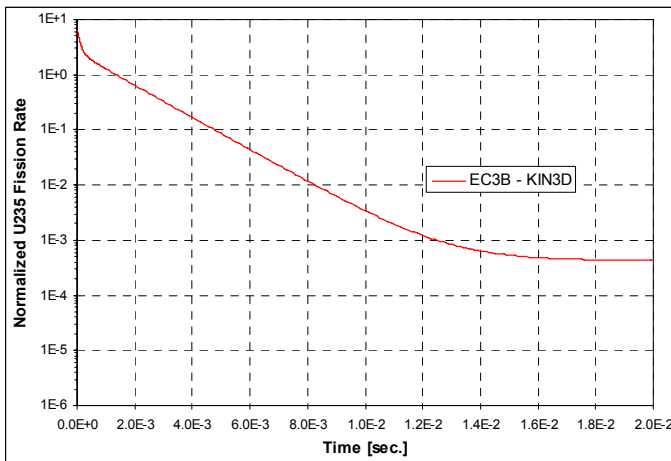


Figure 54. JEF3.1 EC3B Detector Response with (d,t) Neutron Source for the YALINA-Booster

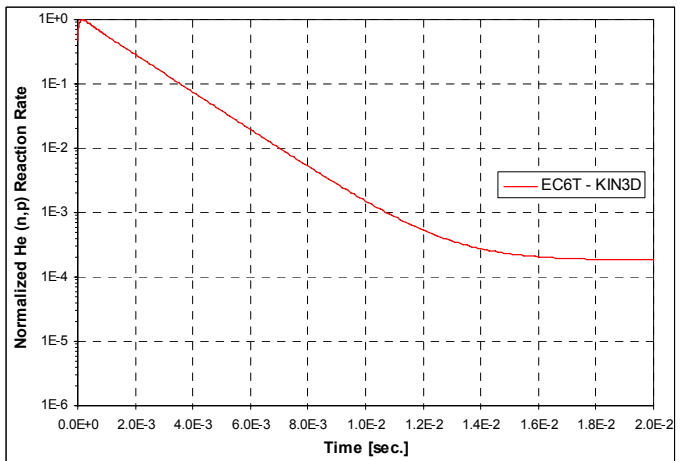


Figure 55. JEF3.1 EC6T Detector Response with (d,d) Neutron Source for the YALINA-Booster

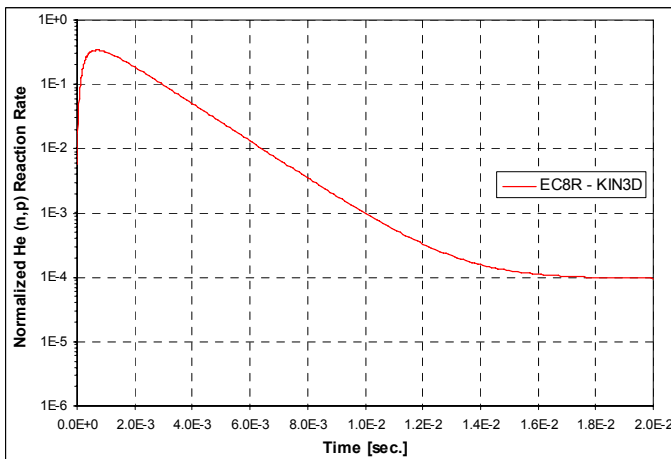


Figure 56. JEF3.1 EC8R Detector Response with (d,d) Neutron Source for the YALINA-Booster

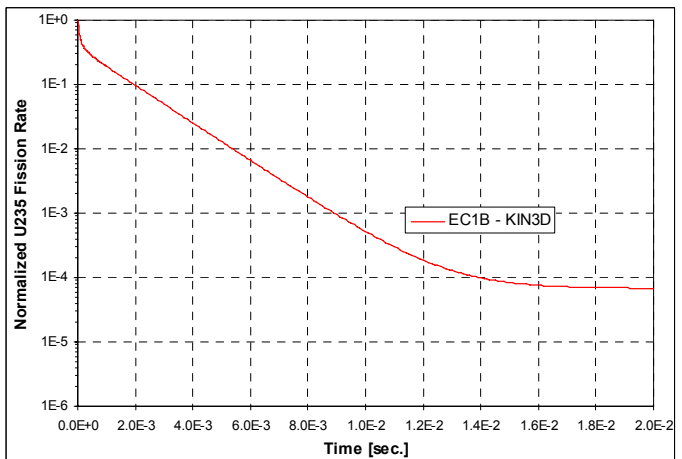


Figure 57. JEF3.1 EC1B Detector Response with (d,d) Neutron Source for the YALINA-Booster

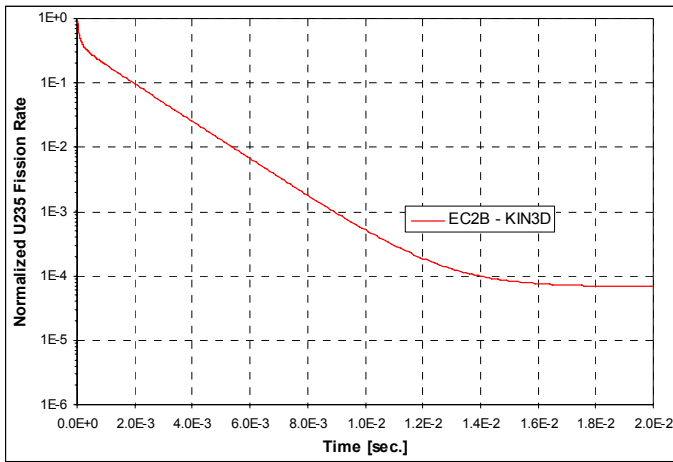


Figure 58. JEF3.1 EC2B Detector Response with (d,d) Neutron Source for the YALINA-Booster

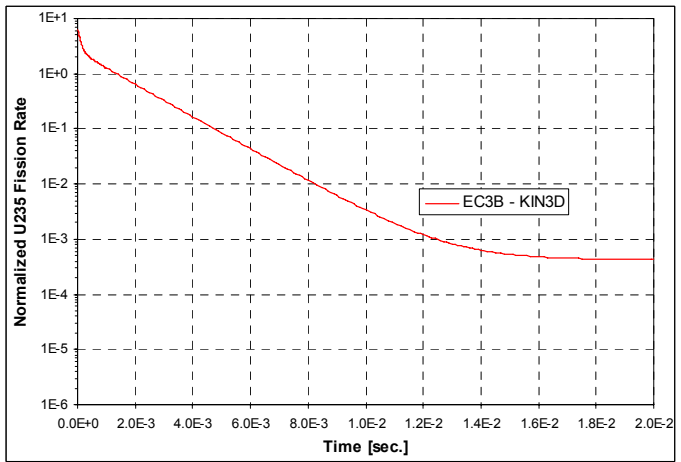


Figure 59. JEF3.1 EC3B Detector Response with (d,d) Neutron Source for the YALINA-Booster

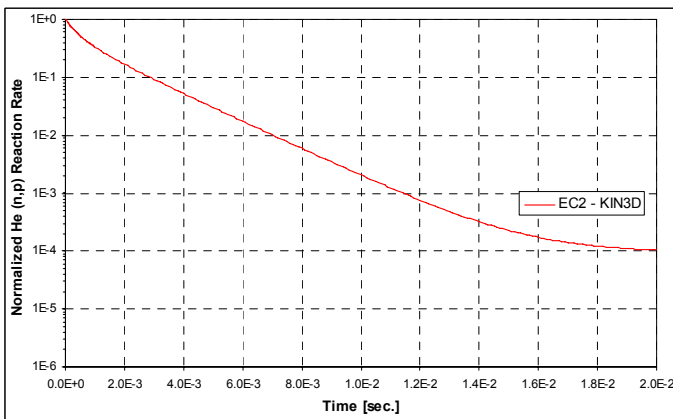


Figure 60. JEF3.1 EC2 Detector Response with (d,t) Neutron Source for the YALINA-Thermal

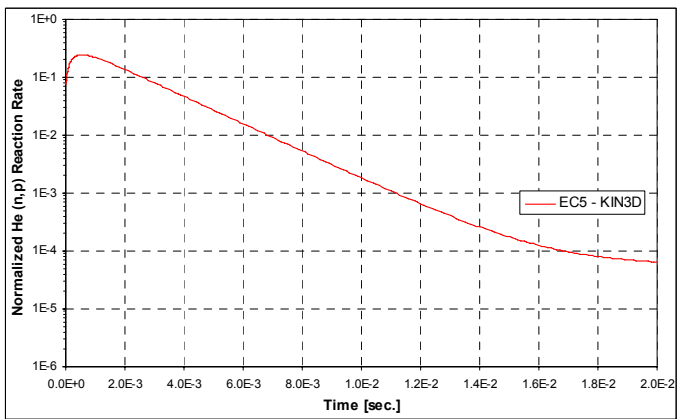


Figure 61. JEF3.1 EC5 Detector Response with (d,t) Neutron Source for the YALINA-Thermal

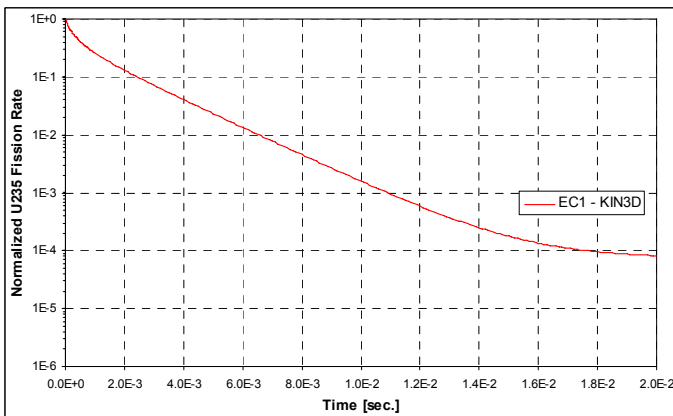


Figure 62. JEF3.1 EC1 Detector Response with (d,t) Neutron Source for the YALINA-Thermal

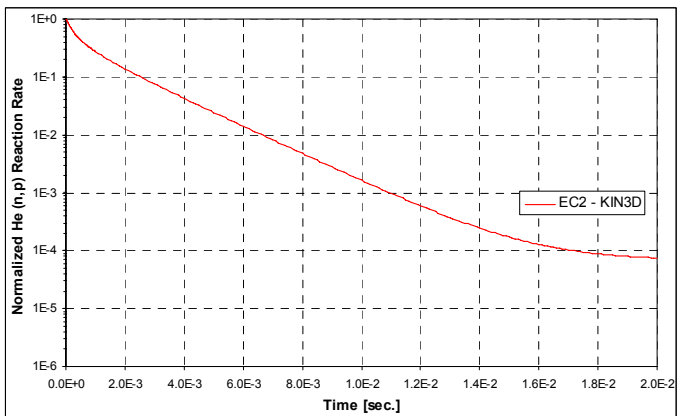


Figure 63. JEF3.1 EC2 Detector Response with (d,d) Neutron Source for the YALINA-Thermal

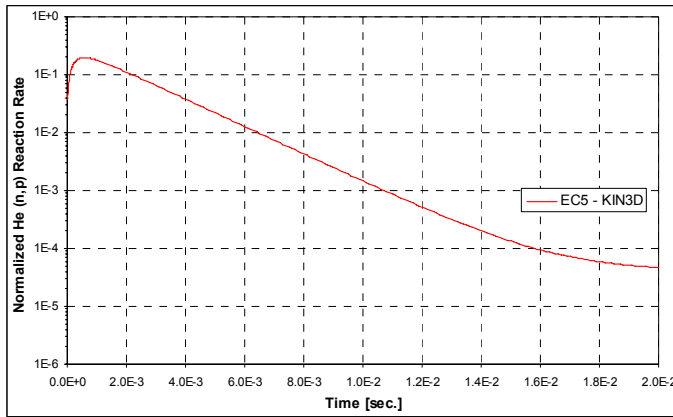


Figure 64. JEF3.1 EC5 Detector Response with (d,d) Neutron Source for the YALINA-Thermal

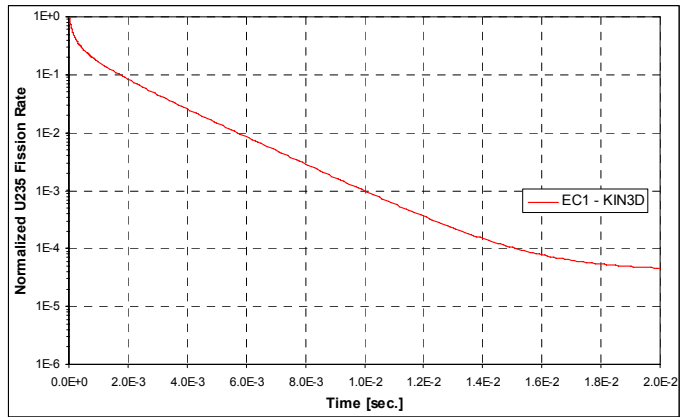


Figure 65. JEF3.1 EC1 Detector Response with (d,d) Neutron Source for the YALINA-Thermal

VII. Conclusions

This report presents the obtained results for the YALINA-Booster loaded with 1141 EK-10 rods and the YALINA-Thermal loaded with 280 EK-10 rods using the deterministic ERANOS code system. Considerable efforts have been made for creating deterministic models for the two assemblies using JEF2.2, JEF3.1, and ENDF/B-VI.8 nuclear data files.

The obtained reactivity values for the YALINA-Booster show a quite good agreement with the use of the three different nuclear data libraries. The calculated reactivity is -2700 pcm with variations of less than 250 pcm depending on the selected nuclear data files. Regarding the YALINA-Thermal, JEF3.1 and ENDF/B-VI.8 provide comparable results of ~ -4900 pcm. JEF2.2 gives a lower reactivity value of ~ -3000 pcm for YALINA-Thermal. Perturbation calculations demonstrated that the use of the JEF2.2 library is inappropriate for the YALINA-Thermal calculations because of the use of carbon instead of the missing graphite for the reflector.

The source multiplication factor is also calculated for the two assemblies. The use of (d,t) neutron source produces the highest k_S value for YALINA-Booster, the lowest value for YALINA-Thermal. The source multiplication factor is even lower than the corresponding k_{eff} value for the YALINA-Thermal. In YALINA-Thermal, the (d,t) neutron source significantly increases the neutron leakage relative to the induced fission reaction rate.

The kinetic parameters, effective fraction of delayed neutrons β_{eff} and mean generation time Λ_{eff} , have been calculated with the KIN3D module of ERANOS in 3D geometry. The use of the different nuclear data libraries (JEF2.2, JEF3.1 and ENDFB-VI.8) does not change the obtained results. The β_{eff} values are 753 pcm for the YALINA-Booster and 779 pcm for the YALINA-Thermal. The values for Λ_{eff} are 50 μ s for the YALINA-Booster and 87 μ s for the YALINA-Thermal.

Neutron spectra have been obtained in specific locations for the two assemblies as specified by the IAEA benchmark. In presence of (d,t) and (d,d) neutron sources, peaks in the neutron spectra are observed at the neutron source energy especially in the experimental channels close to the target for the two YALINA configurations. These peaks decrease with the distance from the source location and the peak values are significantly reduced in the reflector zone. The obtained neutron spectrum in the fast zone of the YALINA-Booster is typical of fast reactor systems, the highest fraction of neutrons being located at ~ 1 MeV. Similarly, in the fuel zone of YALINA-Thermal the neutron spectrum is typical of thermal reactors, with a large fraction of neutrons located below 1 eV.

The KIN3D code of ERANOS has been used to determine the response of the YALINA configurations to a very short neutron pulse, $5\mu\text{s}$ width. The neutron pulse is simulated with a triangular shape, with intensity linearly increasing from 0 to a Maximum Value (MV) in the time interval $0 < t < 2.5\mu\text{s}$, then linearly decreasing from MV to 0 in $2.5 < t < 5\mu\text{s}$. The simulation is carried out with the diffusion approximation. The decay slope of the detector response is strictly dependent on the reactivity value associated with the calculated model for (d,d) and (d,t) pulses.

The YALINA-Booster and -Thermal configurations have been successfully analyzed using the ERANOS modules, both steady-state and time dependent with different neutron sources.

References

1. D.G. Foster (ed.), Review of PNL study on transmutation processing of high level waste, LA-UR 74-74, Los Alamos National Laboratory (1974).
2. M. Salvatores et al., "Long-lived, radioactive waste transmutation and the role of accelerator driven (hybrid) systems", Nuclear Instruments and Methods in Physics Research, A 414 5-20, 1998.
3. S.E. Chigrinov et al., "Booster Subcritical Assembly, Driven by a Neutron Generator" (in Russian), JIPNR 14, Preprint of National Academy of Sciences of Belarus, Joint Institute for Power and Nuclear Research – Sosny, Minsk (2004).
4. S.E. Chigrinov et al., "Experimental Investigations on Neutronics of the Accelerator Driven Transmutation Technologies at the Subcritical Facility "YALINA" Proceedings of the ANA/ADTTA, Reno, Nevada, 11-15 November 2001. CD-ROM.
5. V. Bournos, A. Fokov, Y. Fokov, H. Kiyavitskaya, B. Martsynkevich, C. Routkovskaia, Y. Gohar, C-M Persson, W. Gudowski, "YALINA-Booster Benchmark Specifications for the IAEA Coordinated Research Projects on Analytical and Experimental Benchmark Analysis on Accelerator Driven Systems, and Low Enriched Uranium Fuel Utilization in Accelerator Driven Sub-Critical Assembly Systems", February 2007.
6. V. Bournos, I. Serafimovich, A. Fokov, Y. Fokov, H. Kiyavitskaya, A. Khilmanovich, B. Martsynkevich, C. Routkovskaia, Y. Gohar, C-M Persson, W. Gudowski, "YALINA-Thermal Benchmark Specifications for the IAEA Coordinated Research Projects on Analytical and Experimental Benchmark Analysis on Accelerator Driven Systems, and Low Enriched Uranium Fuel Utilization in Accelerator Driven Sub-Critical Assembly Systems", March 2007.
7. IAEA, Working Material, Research Coordinated Meeting of the Coordinated Research Project on "Analytical and Experimental Benchmark Analyses of Accelerator Driven Systems", 5-9 Dec 2005 Minsk, Belarus, IAEA-RC-1003.1, TWG-FR/127, Vienna (2006).
8. IAEA, Working Material, Workshop Meeting of the Coordinated Research Project on "Low Enriched Uranium Fuel Utilization in Accelerator Driven Sub-Critical Assembly Systems," 6-9 November 2006 Vienna, Austria.
9. C.-M. Persson et al., "Comparison of Neutron Kinetic Parameters of the Subcritical ADS Experiments Yalina and Yalina Booster", *12th International Conference on Emerging Nuclear Energy Systems (ICENES'2005)*, Brussels, Belgium, August 21-26, 2005, on CD-ROM, SCK•CEN, Mol, Belgium (2005).
10. G. Aliberti, Y. Gohar, F. Kondev, A. Talamo, H. Kiyavitskaya, V. Bournos, Y. Fokov, C. Routkovskaya, and I. Serafimovich, "YALINA-Thermal Experiment Analysis with the Deterministic Code System ERANOS", ANS Winter Meeting, Reno, NV, USA, November 2008.
11. G. Rimpault, et al., "The ERANOS Code and Data System for Fast Reactor Neutronic Analyses", in Proceedings of PHYSOR 2002 Conference (Seoul, South Korea, October 2002).
12. G. Rimpault, "Algorithmic Features of the ECCO Cell Code for treating Heterogeneous Fast Reactor Assemblies", International Topical Meeting on Reactor Physics and Computation, Portland - Oregon, May 1-5, 1995.
13. OECD/NEA Report 17, "The JEF-2.2 Nuclear Data Library", April 2000.
14. Bernard, D., et al., "Present Status of JEFF-3.1 Qualification for LWR. Reactivity and Fuel

- Inventory Prediction”, JEFF Meeting, Paris, France, 28-30 November 2005, JEFDOC-1122.
15. ENDF-102 Data Formats and Procedures for the Evaluated Nuclear Data File ENDF-6. BNL-NCS-44945, Rev. 10/91 (ENDF/B-VI), Brookhaven National Laboratory, October 1991.
 16. G. Palmiotti, C.B. Carrico and E.E. Lewis, "Variational Nodal Transport Methods with Anisotropic Scattering", Nucl. Sc. Eng., **115**, p.233 (1993).
 17. A. Rineiski, W. Mashek, G. Rimpault, "Performance of Neutron Kinetics Models for ADS Transient Analyses", AccAPP/ADTTA'01, ANS 2001 Winter Meeting November 11-15, 2001, Reno, Nevada, U.S.A.
 18. G. Palmiotti, J.M. Rieunier, C. Gho, M. Salvatores, "BISTRO Optimized Two Dimensional Sn Transport Code", Nucl. Sc. Eng. **104**, 26 (1990).
 19. G. Aliberti, Y. Gohar, F. Kondev, A. Talamo, H. Kiyavitskaya, V. Bournos, Y. Fokov, C. Routkovskaya, I. Serafimovich, "Deterministic Model for the Analysis of YALINA-Booster Experiments with the ERANOS Code System", International Conference AccApp09, Vienna, Austria, May 2009.

Appendix A

Deterministic Model Details

A.1. Fuel Pin Calculations

The ERANOS code system initially developed for the analysis of fast systems with extended capabilities for the slowing down treatment with up to 1968 energy groups and it can be used for the analysis of thermal reactors. In order to investigate the ERANOS performance when calculating thermal systems, calculations have been performed for the single fuel cell used in the YALINA-Thermal of Figure 66 and the obtained results have been compared with MCNPX results. The cell is assumed infinite in the axial direction (Z direction) with reflected boundary conditions in X and Y. The k_{eff} results of Table 30 and the neutron flux spectra of Figures 67 to 73 show excellent agreements between ERANOS and MCNPX if the polyethylene region is subdivided in an appropriate number of sub-regions in ERANOS calculations. Table 30 shows that subdividing the fuel region in ERANOS calculation does not play an important role: the use of three sub-regions for the fuel pin produces practically the same results of a single fuel region.

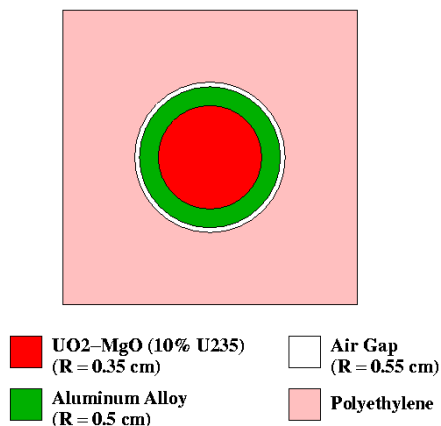


Figure 66. YALINA-Thermal Fuel Cell

Table 30. k_{eff} Values Comparison between MCNPx and ERANOS

Computer code and Nuclear Data Library	k_{eff}
MCNPX – ENDF/B-VI.6	1.36510 ± 0.00012
ERANOS - ENDF/B-VI.8 (1 Region Fuel; 1 Region Polyethylene)	1.37993
ERANOS - ENDF/B-VI.8 (3 Subregions Fuel; 4 Subregions Polyethylene)	1.37021
ERANOS - ENDF/B-VI.8 (3 Subregions Fuel; 5 Subregions Polyethylene)	1.36640
ERANOS - ENDF/B-VI.8 (3 Subregions Fuel; 6 Subregions Polyethylene)	1.36451
ERANOS - ENDF/B-VI.8 (3 Subregions Fuel; 7 Subregions Polyethylene)	1.36347
ERANOS - ENDF/B-VI.8 (1 Region Fuel; 7 Subregions Polyethylene)	1.36347

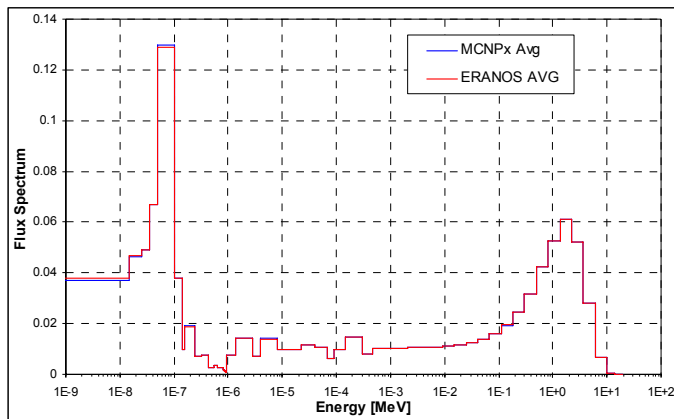


Figure 67. Comparison of MCNPX and ERANOS Averaged Fuel Cell Neutron Spectra

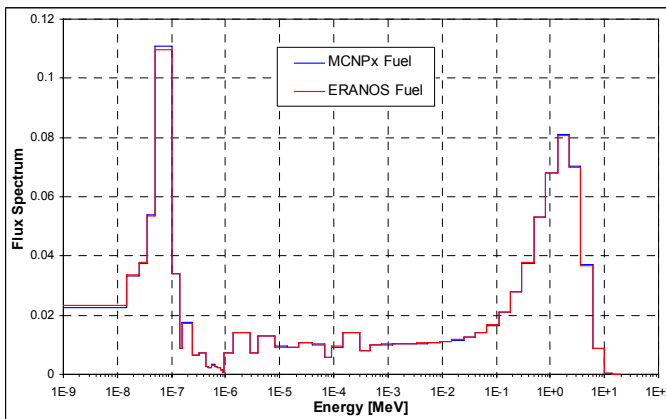


Figure 68. Comparison of MCNPX and ERANOS Averaged Fuel Pin Neutron Spectra

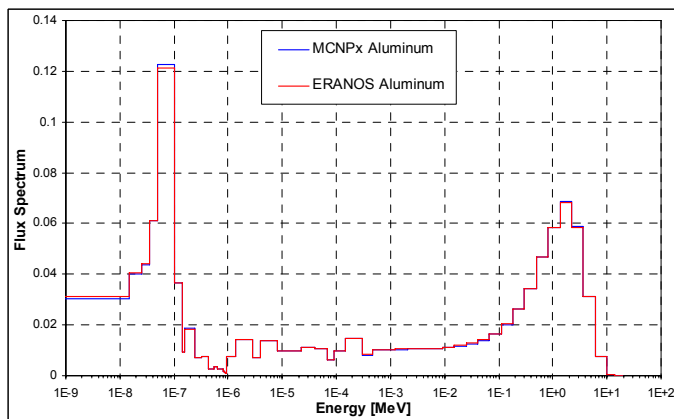


Figure 69. Comparison of MCNPX and ERANOS Averaged Aluminum Clad Neutron Spectra

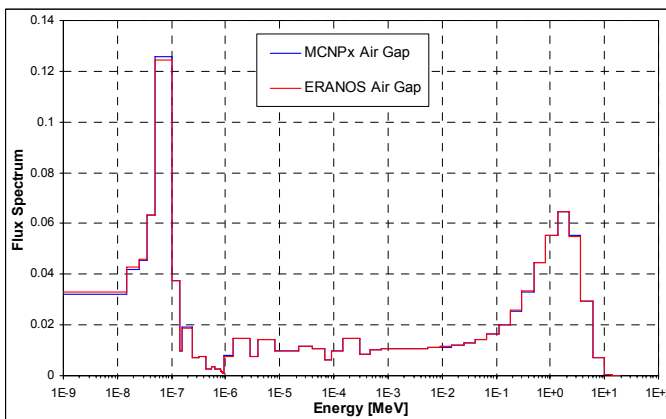


Figure 70. Comparison of MCNPX and ERANOS Averaged Air Gap Neutron Spectra

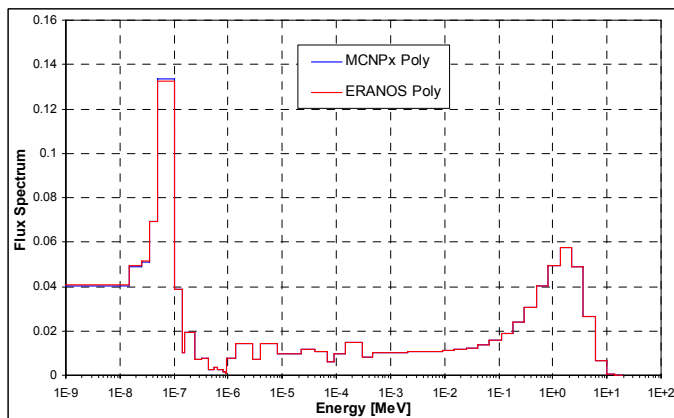


Figure 71. Comparison of MCNPX and ERANOS Averaged Polyethylene Neutron Spectra

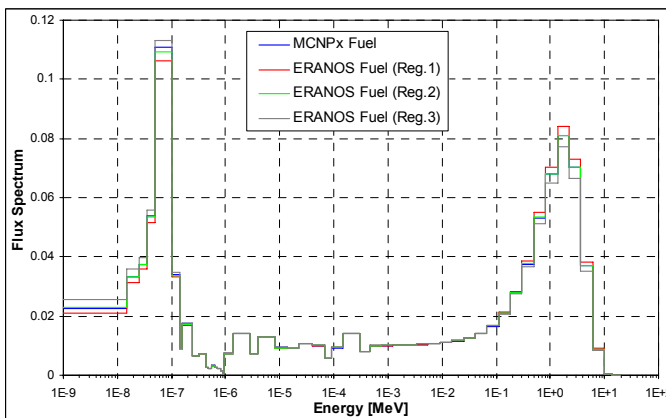


Figure 72. Comparison of MCNPX Fuel Pin Neutron Spectra and ERANOS Neutron Spectra from Different Fuel Pin regions

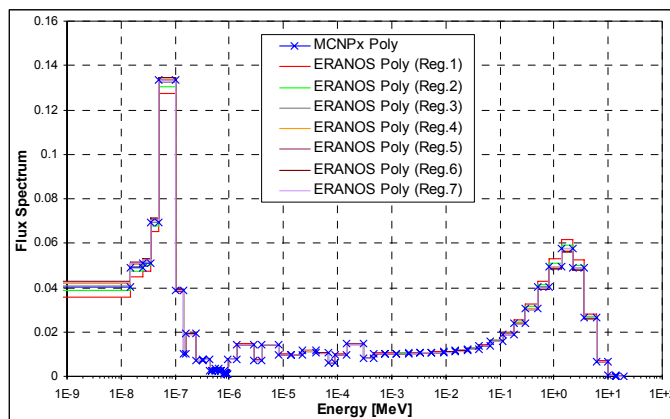


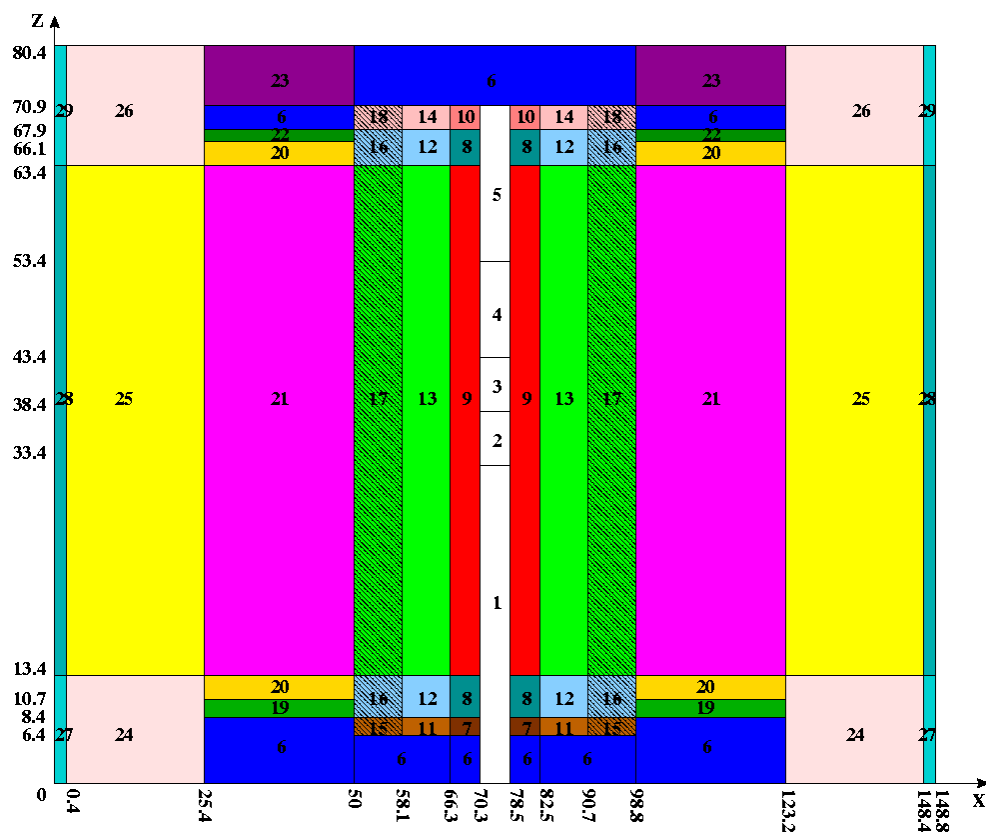
Figure 73. Comparison of MCNPX Polyethylene Neutron Spectra and ERANOS Neutron Spectra from Different Polyethylene regions

A.2. YALINA-Booster

The deterministic calculational model [19] developed for the YALINA-Booster is shown in Figures 74 and 75 (the axial views) and in Figure 76 (the XY view). Figures 74 to 76 show the zones where the cross-sections have been separately processed: e.g., a homogeneous set of cross-sections is associated to each zone number. The zones containing experimental channels have not been represented in Figures 74 and 75. Taking into consideration the zones with experimental channels, a total of 113 cell calculations were performed to describe the deterministic model of the YALINA-Booster.

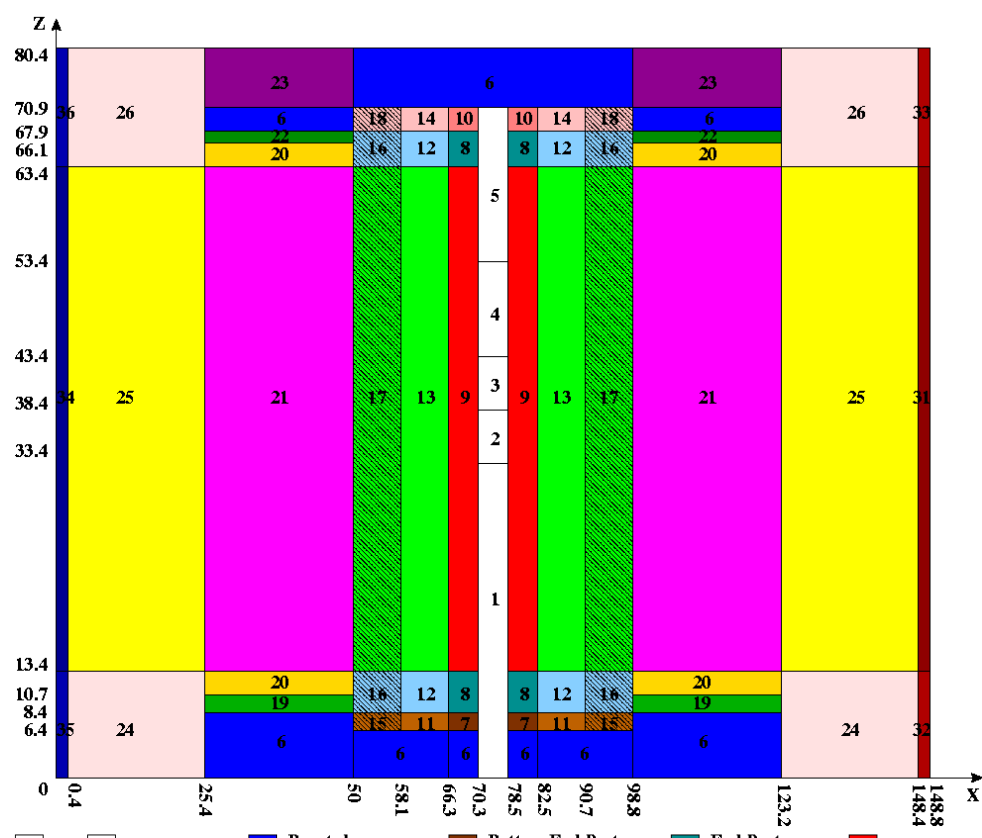
As explained before, void regions should be avoided in the geometrical model. Therefore, the void regions are homogenized with the neighbor regions. For instance, zones 24 and 26 have been obtained from the homogenization of the graphite reflector and the air gap as shown in Figure 77. Similarly, zone 23 is the result of homogenizing the borated polyethylene blocks and the air gap. Additional homogenizations have been performed for the end part of the fuel rods and for the experimental channels, details will be discussed later.

Heterogeneity effects are very important for the YALINA configurations, as consequence, the cross-sections of most of the regions have been processed with heterogeneous cell calculations. Figures 78 to 83 and 91 to 100, show the cell configurations used to process the cross-sections of the separate assembly regions.



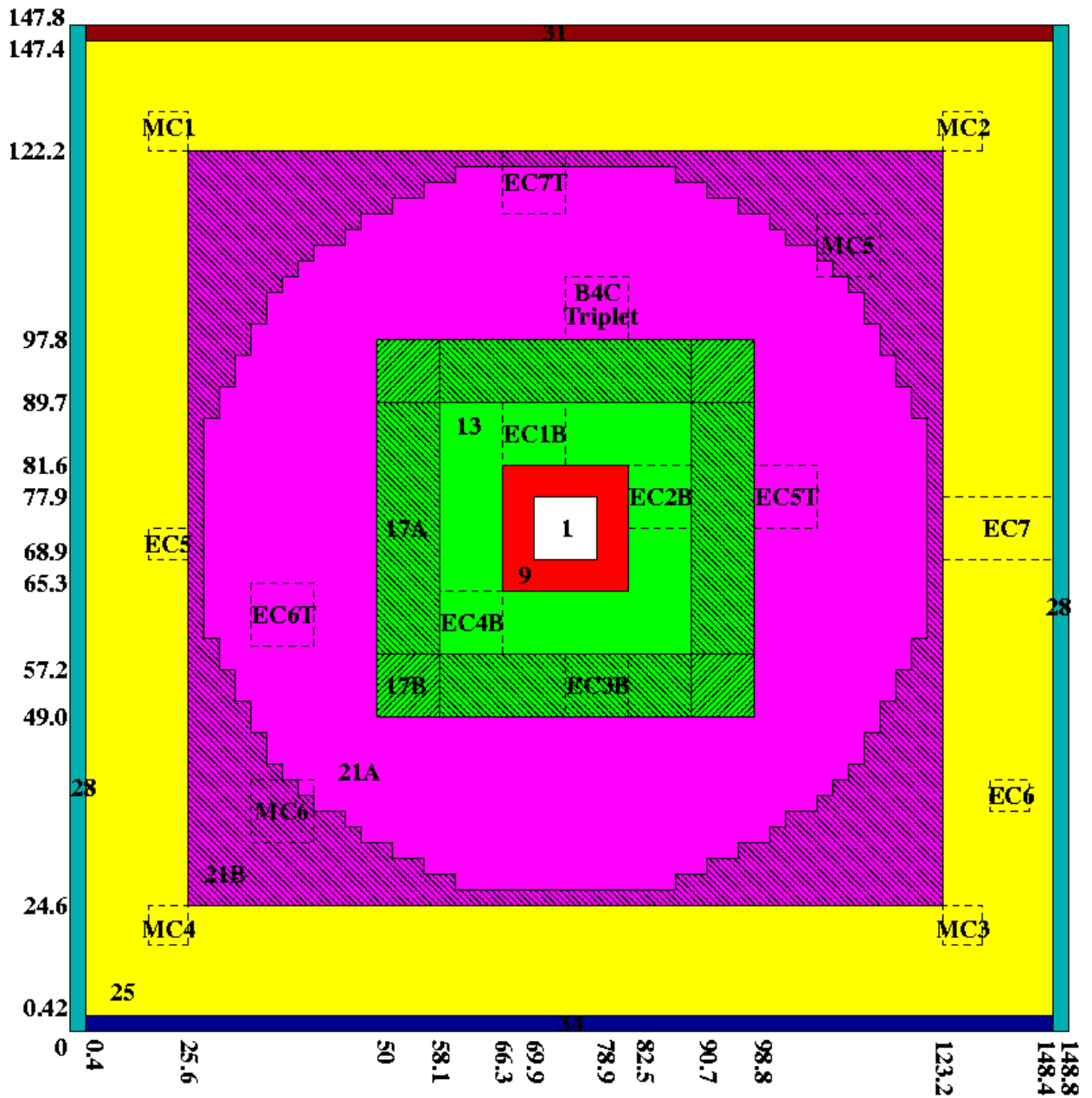
- | | | | | | | | | | |
|--------|---|----|--------------------------------------|----|-------------------------------|----|----------------------|----|-------------------------------|
| 1 TO 5 | Beam Tube | 6 | Borated Polyethylene | 7 | Bottom End Part U90% Rods | 8 | End Part U90% Rods | 9 | U90% |
| 10 | Upper End Part U90% Rods | 11 | Bottom End Part UO2 (36% U235) Rods | 12 | End Part UO2 (36% U235) Rods | 13 | UO2 (36% U235) | | |
| 14 | Upper End Part UO2 (U36%) Rods | 15 | Bottom End Part Absorber Subassembly | 16 | End Part Absorber Subassembly | 17 | Absorber Subassembly | | |
| 18 | Upper End Part Absorber Subassembly | 19 | Bottom End Part UO2 (10% U235) | 20 | End Part UO2 (10% U235) | 21 | UO2 (10% U235) | 22 | Upper End Part UO2 (10% U235) |
| 23 | Mixture of Borated Polyethylene and Air | 24 | Mixture of Reflector and Air | 25 | Reflector | 28 | Glass | 27 | 29 |
| | | | | | | | | | Mixture of Glass and Air |

Figure 74. XZ Layout of the YALINA-Booster Deterministic Model (Experimental Channels are not Represented)



- | | | | | | | | | | |
|--------|---|----|--------------------------------------|----|-------------------------------|----|----------------------|----|-------------------------------|
| 1 TO 5 | Beam Tube | 6 | Borated Polyethylene | 7 | Bottom End Part U90% Rods | 8 | End Part U90% Rods | 9 | U90% |
| 10 | Upper End Part U90% Rods | 11 | Bottom End Part UO2 (36% U235) Rods | 12 | End Part UO2 (36% U235) Rods | 13 | UO2 (36% U235) | | |
| 14 | Upper End Part UO2 (U36%) Rods | 15 | Bottom End Part Absorber Subassembly | 16 | End Part Absorber Subassembly | 17 | Absorber Subassembly | | |
| 18 | Upper End Part Absorber Subassembly | 19 | Bottom End Part UO2 (10% U235) | 20 | End Part UO2 (10% U235) | 21 | UO2 (10% U235) | 22 | Upper End Part UO2 (10% U235) |
| 23 | Mixture of Borated Polyethylene and Air | 24 | Mixture of Reflector and Air | 25 | Reflector | 31 | Fe360 | 32 | 33 |
| | | | | | | | | | Mixture of Fe360 and Air |
| | | | | | | | | | |

Figure 75. YZ Layout of the YALINA-Booster Deterministic Model (Experimental Channels are not Represented)



- | | | | |
|--|---|---|--|
| 1 Beam Tube | 9 U90% | 13 UO ₂ (36% U ₂₃₅) | 21A UO ₂ (10% U ₂₃₅) |
| 17A 17B Absorber Subassembly | 21B Polyethylene Blocks with Empty Holes | 25 Reflector | |
| 28 Glass | 31 Fe360 | 34 Fe360 + Cadmium | |

Denotes the Location of the Cells for the Experimental Channel Modelization

Figure 76. XY Layout of the YALINA-Booster Deterministic Model

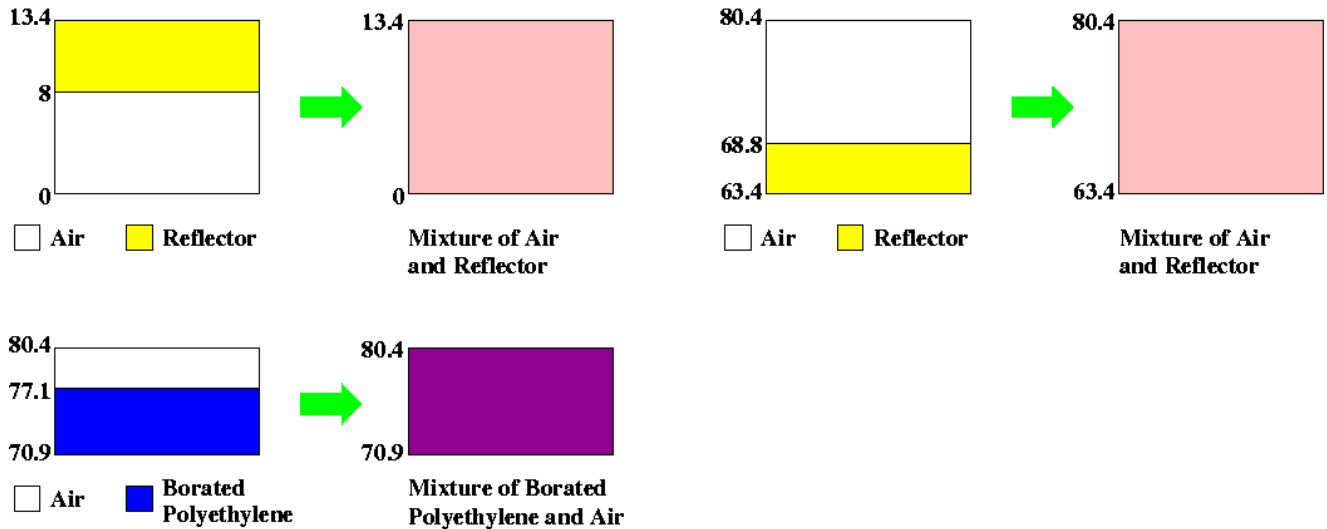


Figure 77. Homogenization of the Air Gap with the Graphite Reflector (Zones 24 and 26) and of the Air with Borated Polyethylene (Zone 23)

Fuel Regions

Generally, the cells are chosen to represent the XY cut of the lead or polyethylene blocks shown in Figures 78 to 83. A particular attention has been devoted to the absorber subassemblies with the B₄C pins. For these subassemblies, the cross-sections have been processed according to the schemes indicated in Figures 80 and 81, depending on the cell position in the subcritical assembly, whether it is located at the corner or not; the cell calculations have been performed with neutron leakage from the thermal zone. The stainless steel frame surrounds nine blocks of polyethylene or lead in the YALINA-Booster assembly as shown in Figure 84. The heterogeneous cell calculation conserve the stainless steel volume and each block has its share of stainless steel as shown on the right of Figure 84. The heterogeneous cell model includes explicit representation for each fuel pin. YALINA-Thermal does not have a stainless steel frame.

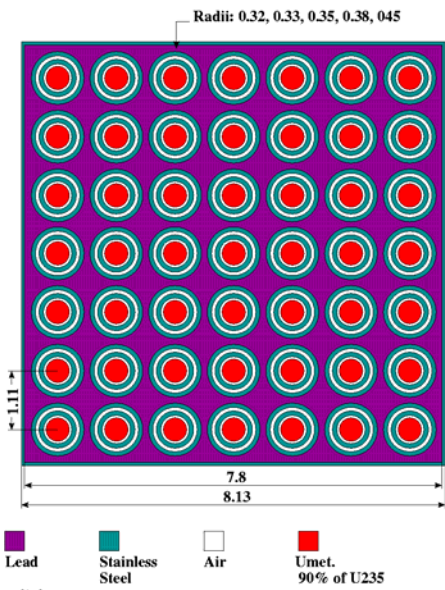


Figure 78. Cell Scheme for Zone 9

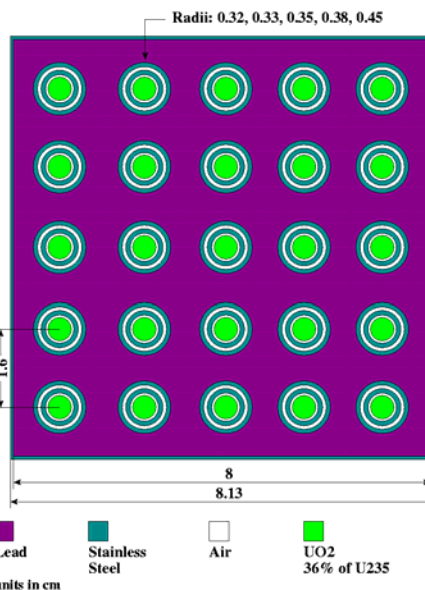


Figure 79. Cell Scheme for Zone 13

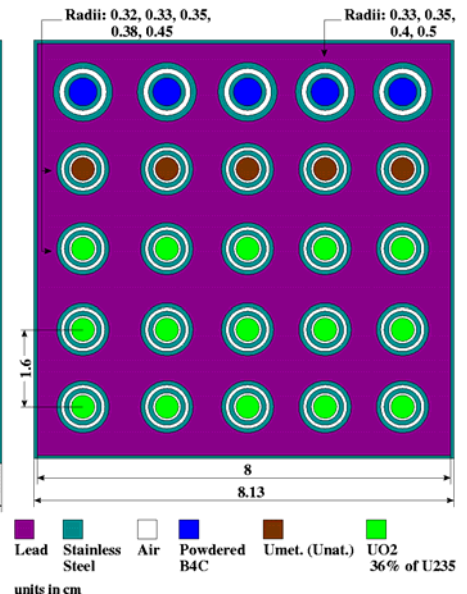


Figure 80. Cell Scheme for Zone 17A

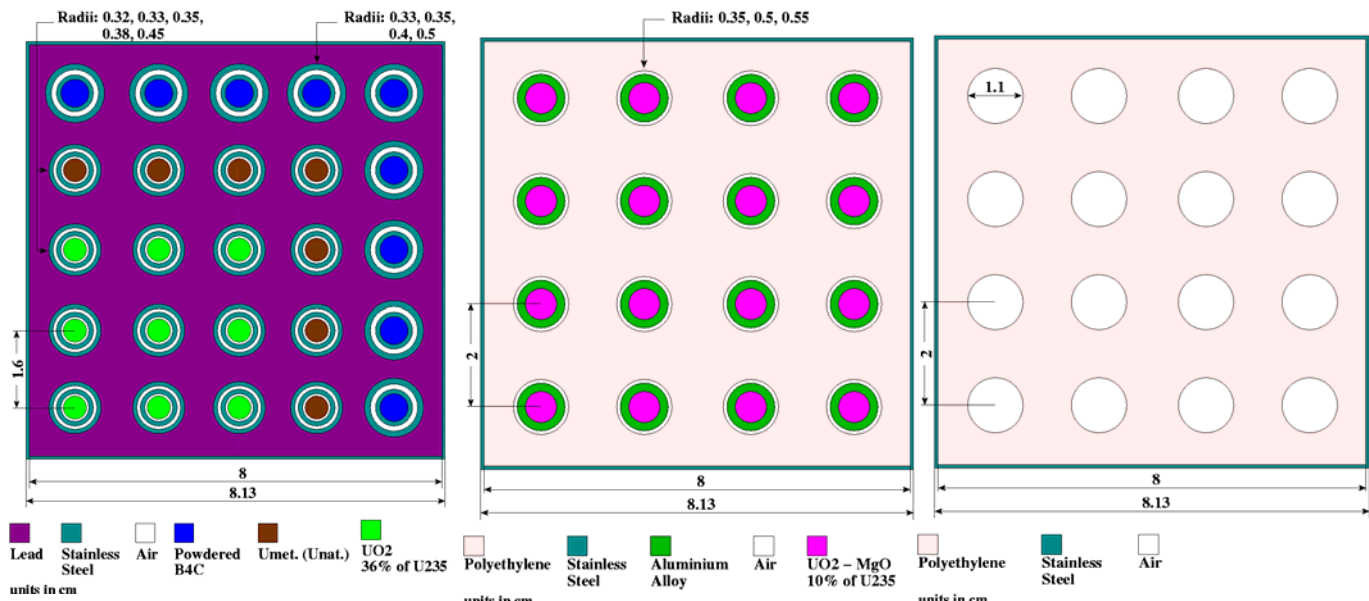


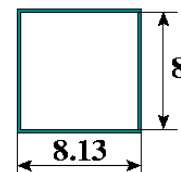
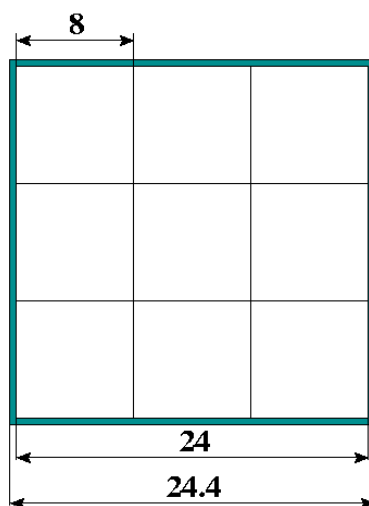
Figure 81. Cell Scheme for Zone 17B

Figure 82. Cell Scheme for Zone 21A

Figure 83. Cell Scheme for Zone 21B

Booster Assembly

Cell



- Lead or Polyethylene
- Stainless Steel

Figure 84. Cell Scheme and Representation of the Assembly Steel Structure

End Part of the Fuel and Absorber Rods

The selected axial meshes match the geometries of the fuel rods shown in Figures 6 to 8. The following are the axial boundaries used for each fuel rod design:

- Bottom part of the 90% U-235 enriched metallic fuel rods, the 36% U-235 enriched uranium oxide fuel rods, and the natural uranium fuel rods: Z = 6.4, 8.4, and 13.4 cm as shown in Figure 85.;
- Top part of the 90% U-235 enriched metallic fuel rods, the 36% U-235 enriched uranium oxide fuel rods, and the natural uranium fuel rods: Z = 63.4, 67.9, and 70.9 cm as shown in Figure 86;
- Bottom part of the boron carbide rods: Z = 6.4, 8.4, and 13.4 cm as shown in Figure 87;
- Top part of the boron carbide rods: Z = 63.4, 67.9, and 70.9 cm as shown in Figure 88;
- Bottom part of EK-10 fuel rods: Z = 8.4, 10.7, and 13.4 cm as shown in Figure 89;
- Top part of EK-10 fuel rods: Z = 63.4, 66.1, and 67.9 cm as shown in Figure 90.

For these regions, the cross-sections have been obtained with heterogeneous geometry, as shown in Figures 91 to 100. However, for some zones material homogenization were used as shown in Figures 85 to 90.

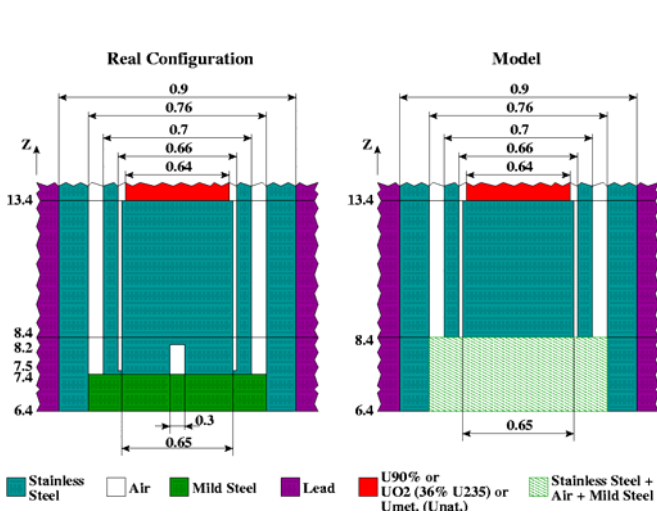


Figure 85. Bottom Part of the 90% U-235 Enriched Metallic, the 36% U-235 Enriched Uranium Oxide, and the Natural Uranium Fuel Rods

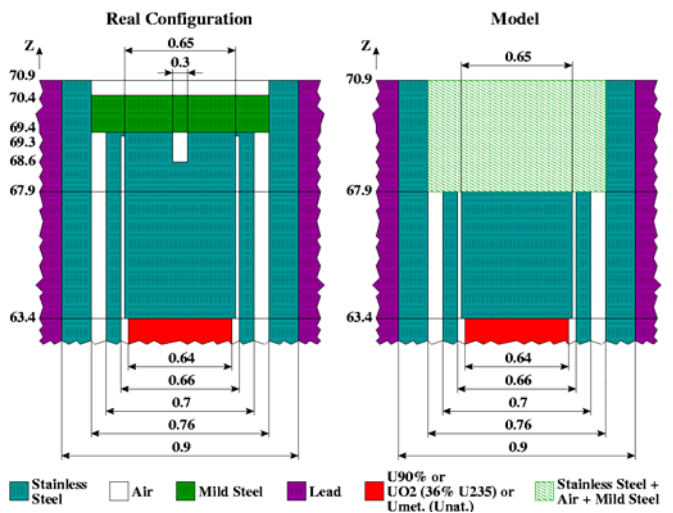


Figure 86. Top Part of the 90% U-235 Enriched Metallic, the 36% U-235 Enriched Uranium Oxide, and the Natural Uranium Fuel Rods

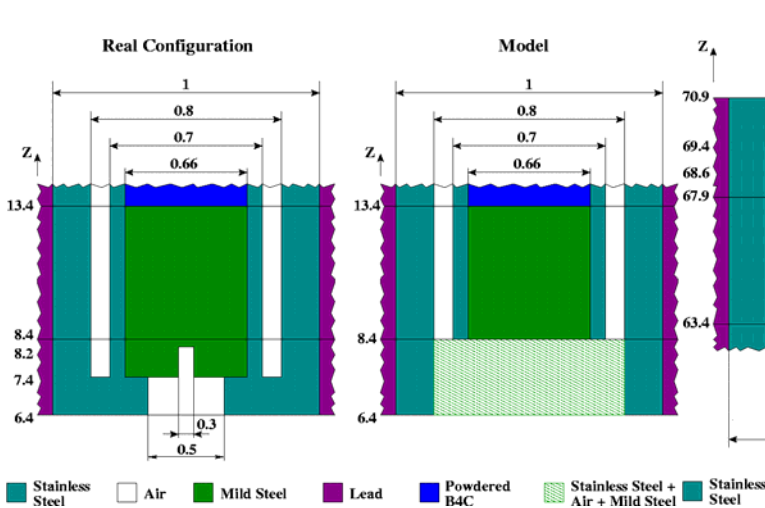


Figure 87. Bottom Part of B₄C Rods

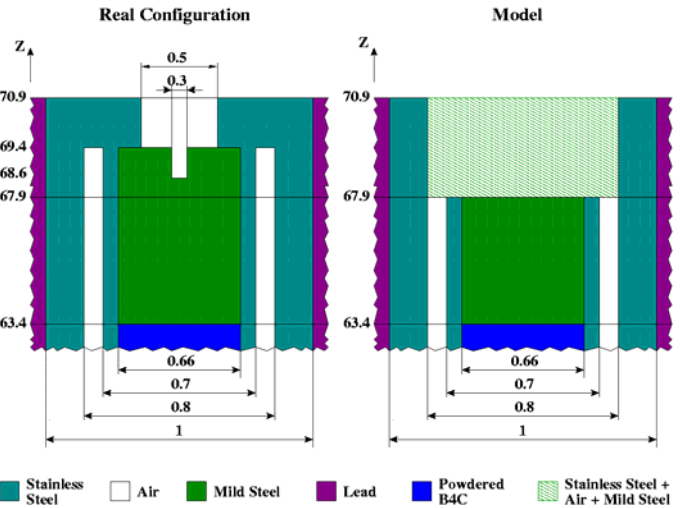


Figure 88. Top Part of B₄C Rods

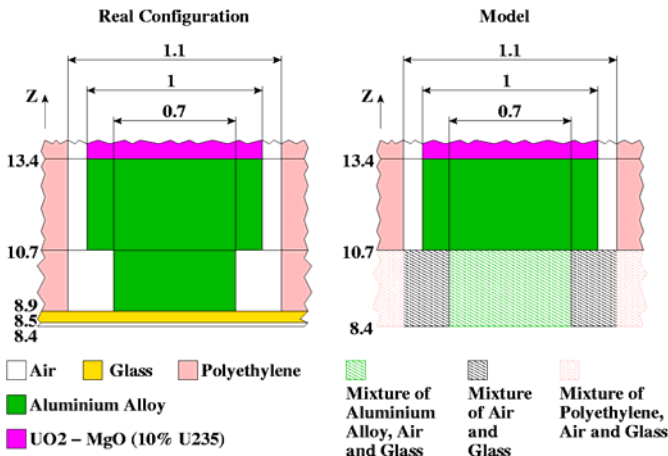


Figure 89. Bottom Part of EK-10 Fuel Rods

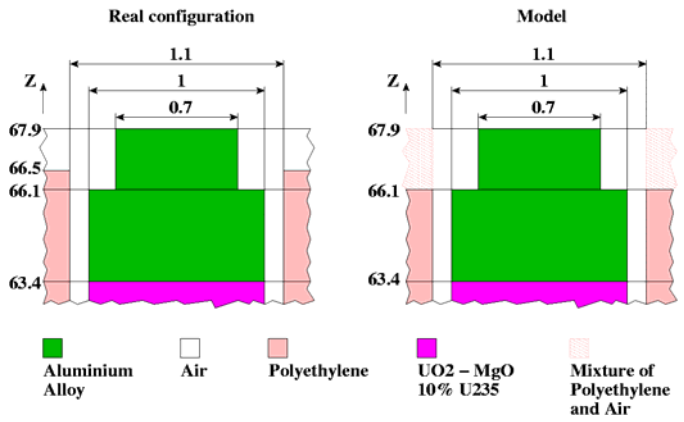


Figure 90. Top Part of EK-10 Fuel Rods

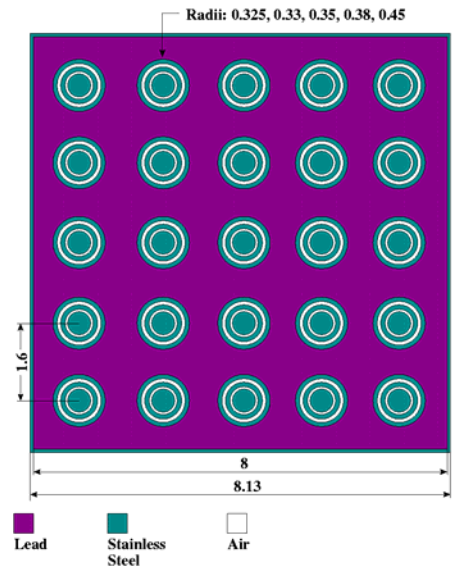
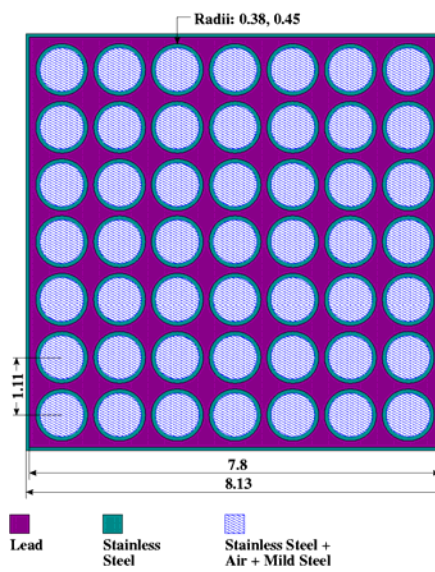
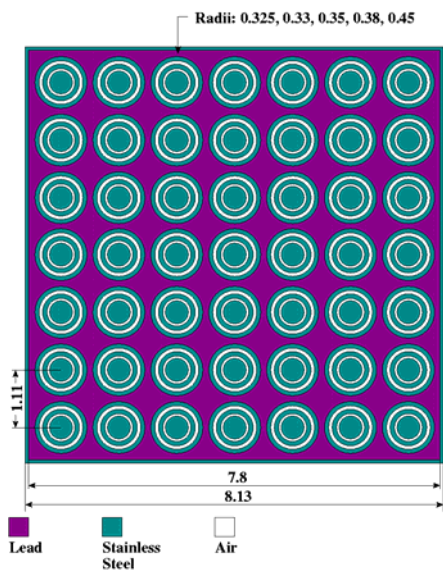


Figure 91. Cell Scheme for Zone 8 (8.4<Z<13.4 and 63.4<Z<67.9) Figure 92. Cell Scheme for Zone 7 (6.4<Z<8.4) and 10 (67.9<Z<70.9) Figure 93. Cell Scheme for Zone 12 (8.4<Z<13.4 and 63.4<Z<67.9)

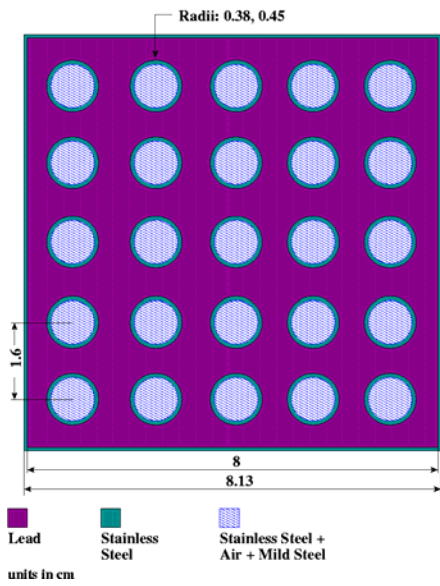


Figure 94. Cell Scheme for Zone 11 ($6.4 < Z < 8.4$) and 14 ($67.9 < Z < 70.9$)

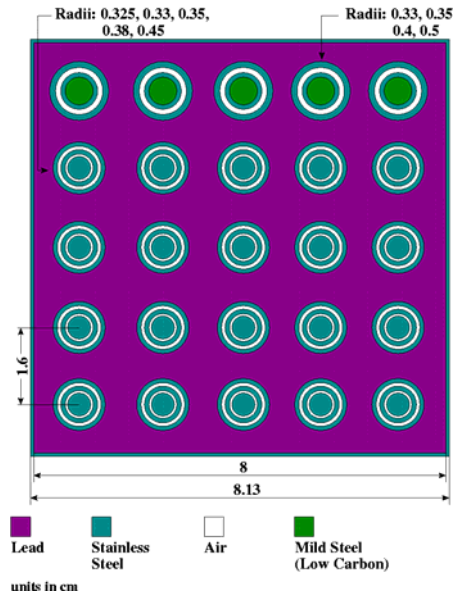


Figure 95. Cell Scheme for Zone 16 ($8.4 < Z < 13.4$ and $63.4 < Z < 67.9$)

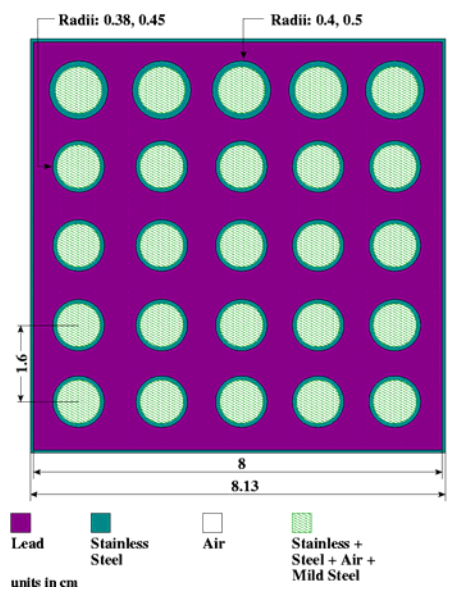


Figure 96. Cell Scheme for Zone 15 ($6.4 < Z < 8.4$) and 18 ($67.9 < Z < 70.9$)

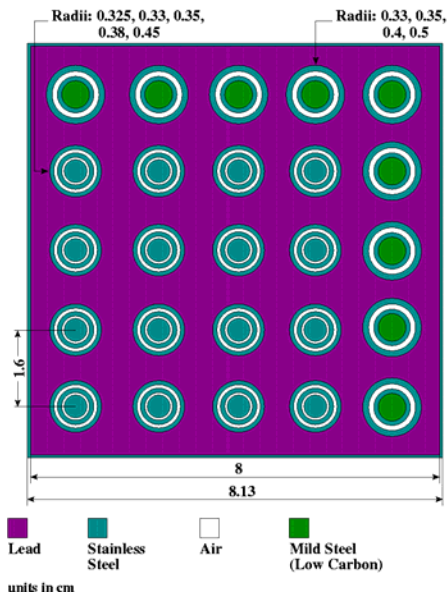


Figure 97. Cell Scheme for Zone 16 ($8.4 < Z < 13.4$ and $63.4 < Z < 67.9$) at the Corner

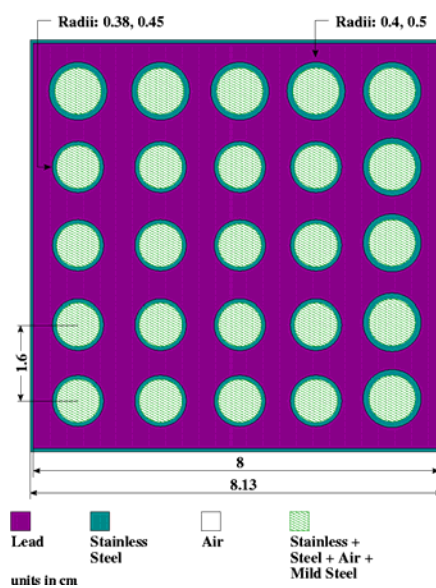


Figure 98. Cell Scheme for Zone 15 ($6.4 < Z < 8.4$) and 18 ($67.9 < Z < 70.9$) at the Corner

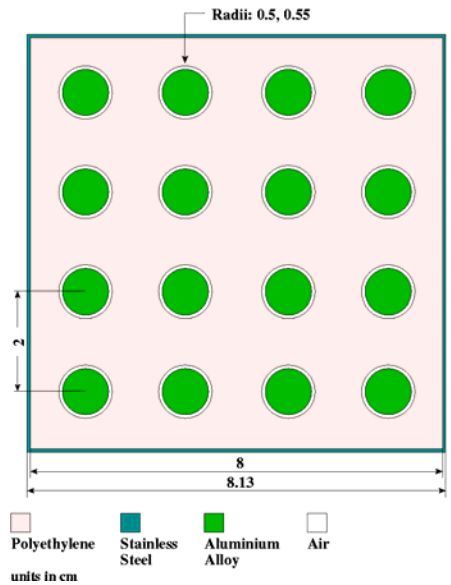


Figure 99. Cell Scheme for Zone 20 ($10.7 < Z < 13.4$ and $63.4 < Z < 66.1$)

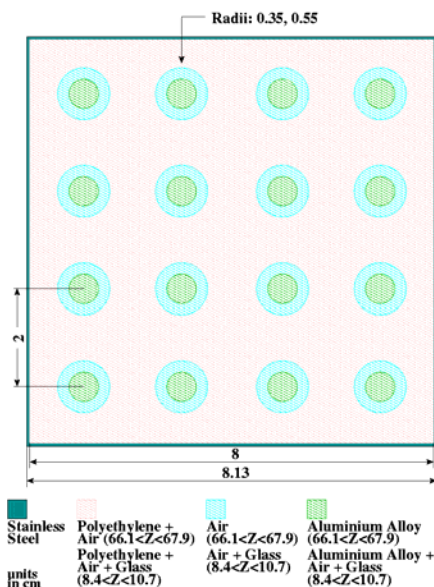


Figure 100. Cell Scheme for Zone 19 ($8.4 < Z < 10.7$) and 22 ($66.1 < Z < 67.9$)

Borated Polyethylene Region

Cross-sections have been processed with a homogeneous cell calculation with homogenized borated polyethylene and stainless steel.

Reflector Region

Cross-section have been processed with a homogeneous cell calculation with homogenized graphite, stainless steel and glass.

Deuteron Beam Duct and Target

The central subassembly of the YALINA-Booster, including the deuteron beam duct and the target, has been modeled with six axial zones as shown in Figure 101. The XY views of the cells used for the cross-section processing are shown on the right side of Figure 101. The geometrical layout of these cells includes part of the lead material outside the beam duct and target area. The XY view of the YALINA-Booster shows the 8×8 cm square central subassembly inside the fast zone with the highly enriched uranium. The fast zone extends for 15.6×15.6 cm. The space between the two squares $[(15.6 - 8) / 2 = 3.8$ cm] has three 90% U-235 enriched metallic uranium fuel rods. The fuel pitch is 1.114 cm, which leaves 0.458 cm on each side of the 8-cm deuteron beam duct and target. This space has lead material as shown in the YALINA-Booster configuration. To avoid the introduction of fine meshes in the deterministic model, this lead material is included with the deuteron beam duct and target in its heterogeneous geometrical model as shown in Figure 101.

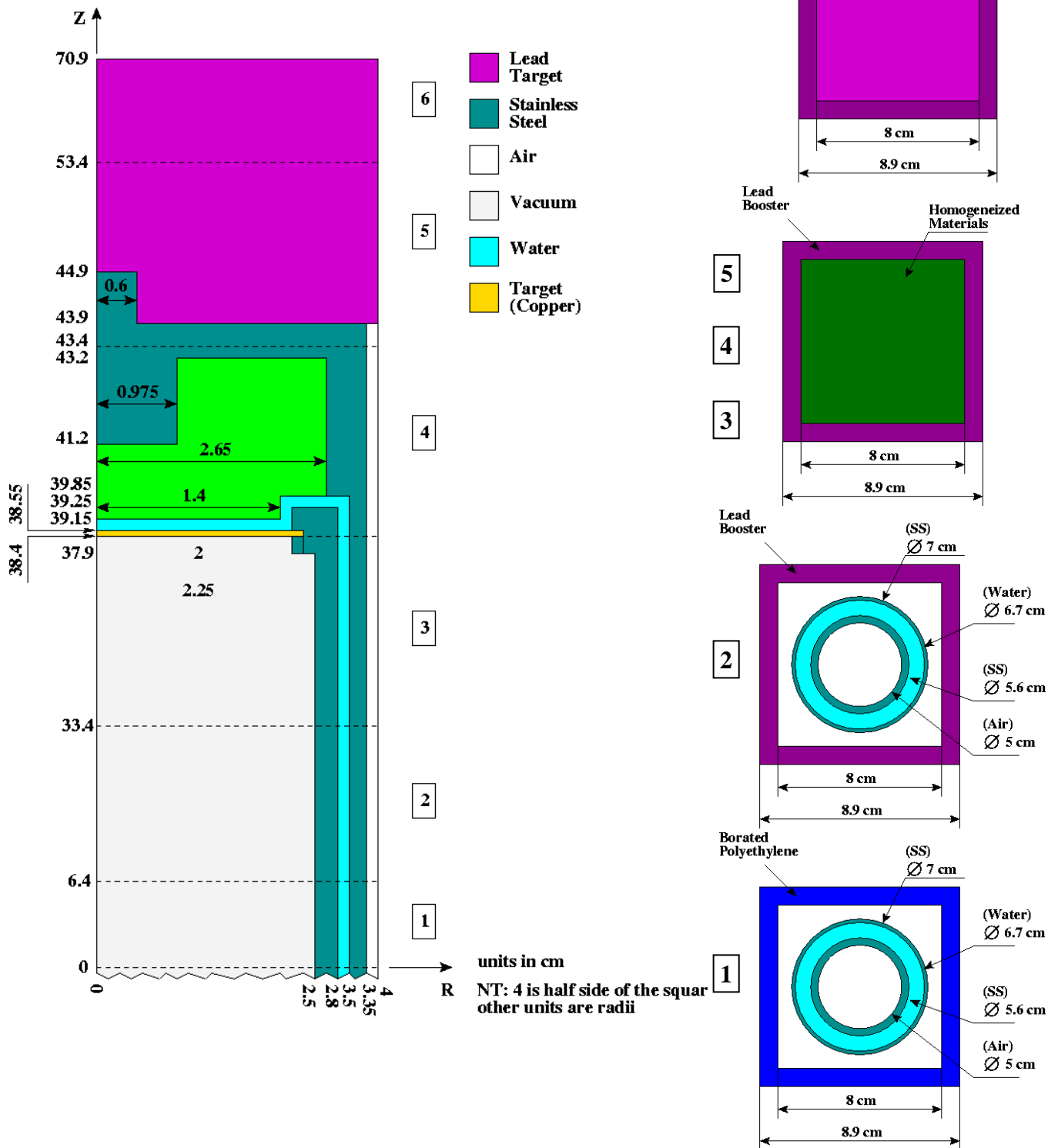


Figure 101. YALINA-Booster Calculational Models of the Central Assembly

Experimental Channels

In order to avoid the presence of void regions and fine meshes in the deterministic model, the experimental channels have been homogenized with the regions where they are located. As consequence, the experimental channels located in the reflector are homogenized with an opportune volume of the reflector itself. The experimental channels located in the fuel zones are homogenized over the volume of the cell used to create the cross-section for the fuel region where they are located. Figure 102 shows the cell scheme adopted for the EC4B experimental channel. Additionally, due to the limitations imposed by the cell code in the geometry description, some simplifications were adopted to describe the presence of the experimental channels. For instance, Figure 103 shows the real geometry description of the cell containing the experimental channel EC1B, while Figure 104 shows its model. Similarly, Figures 105 and 106 show the real configuration and the model of the cell containing the experimental channels EC5T. Finally, Figures 107 and 108 show the solution adopted to represent the three void channels for the boron carbide rods in the thermal zone.

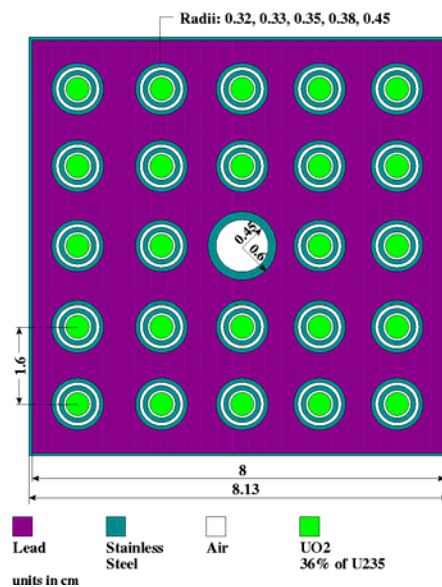


Figure 102. EC4B Experimental Channel

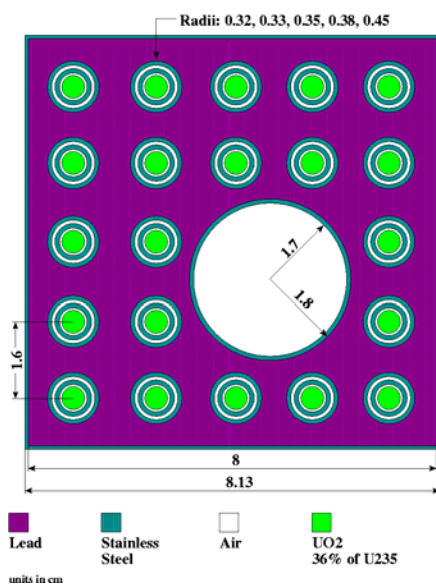


Figure 103. EC1B Experimental Channel

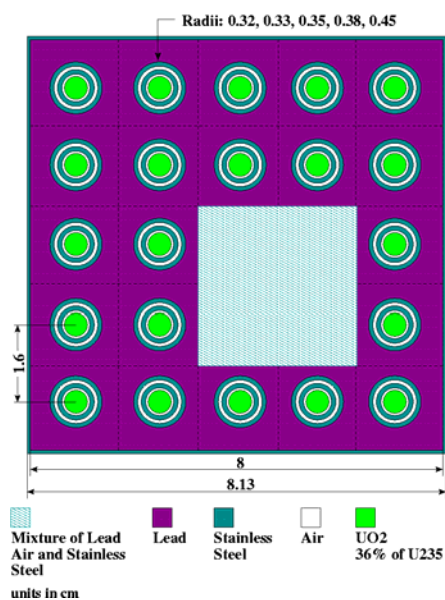


Figure 104. EC1B Calculational Model

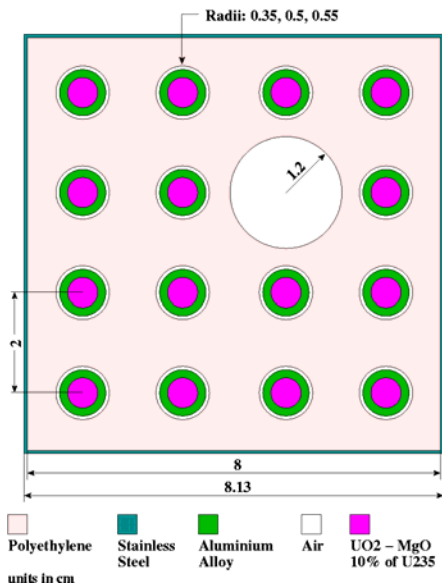


Figure 105. EC5T Experimental Channel

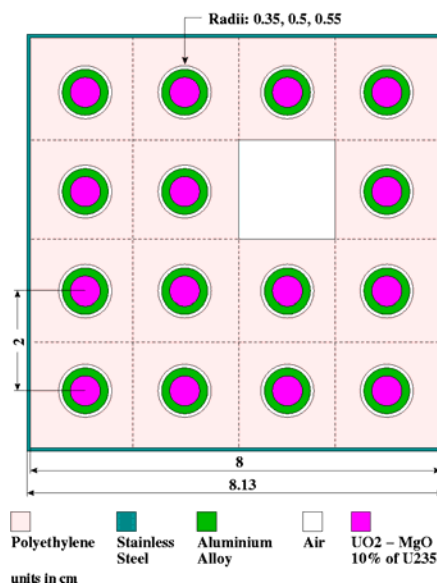


Figure 106. EC5T Calculational Model

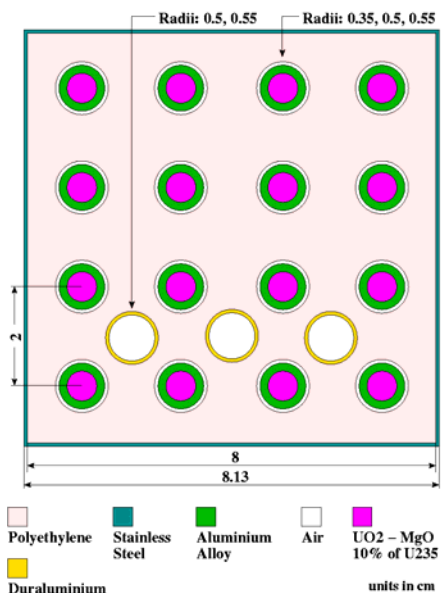


Figure 107. Three Void Channels for the Boron Carbide Rods

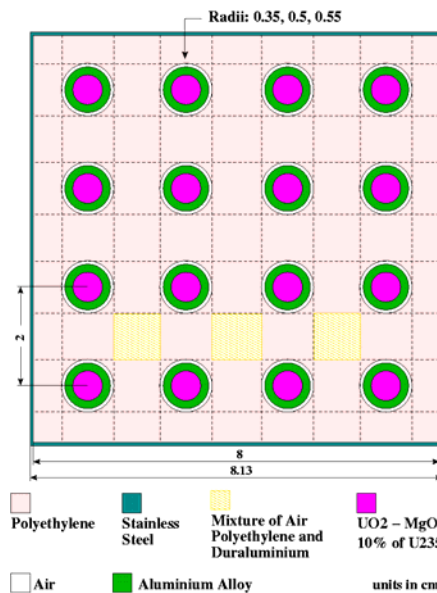


Figure 108. The calculational model of the three Void Channels for the Boron Carbide Rods

A.3. YALINA-Thermal

The deterministic model developed for the YALINA-Thermal is shown in Figures 109 and 110 (the axial views), and in Figure 111 (the XY view). Figures 109 to 111 show the regions where the cross-sections have been separately processed: e.g., a homogeneous set of cross-sections is associated to each zone number. The zones containing experimental channels are not presented in Figures 109 and 110. The number of cell calculations describing the deterministic model is 49 including the zones with experimental channels.

As the case for the YALINA-Booster, the void regions of the YALINA-thermal configuration were homogenized with the neighbor regions. For instance, the cross-sections of zone 12 were obtained by

the homogenization of a section of the graphite reflector and the air gap as shown in Figure 112. In addition, homogenizations were performed for the end part of the fuel rods and the experimental channels.

Heterogeneous cell calculations were performed for the other regions to get their homogenized cross-sections. Figures 113 to 115, 118 and 119, show the cell configuration used to process the cross-sections of the different regions

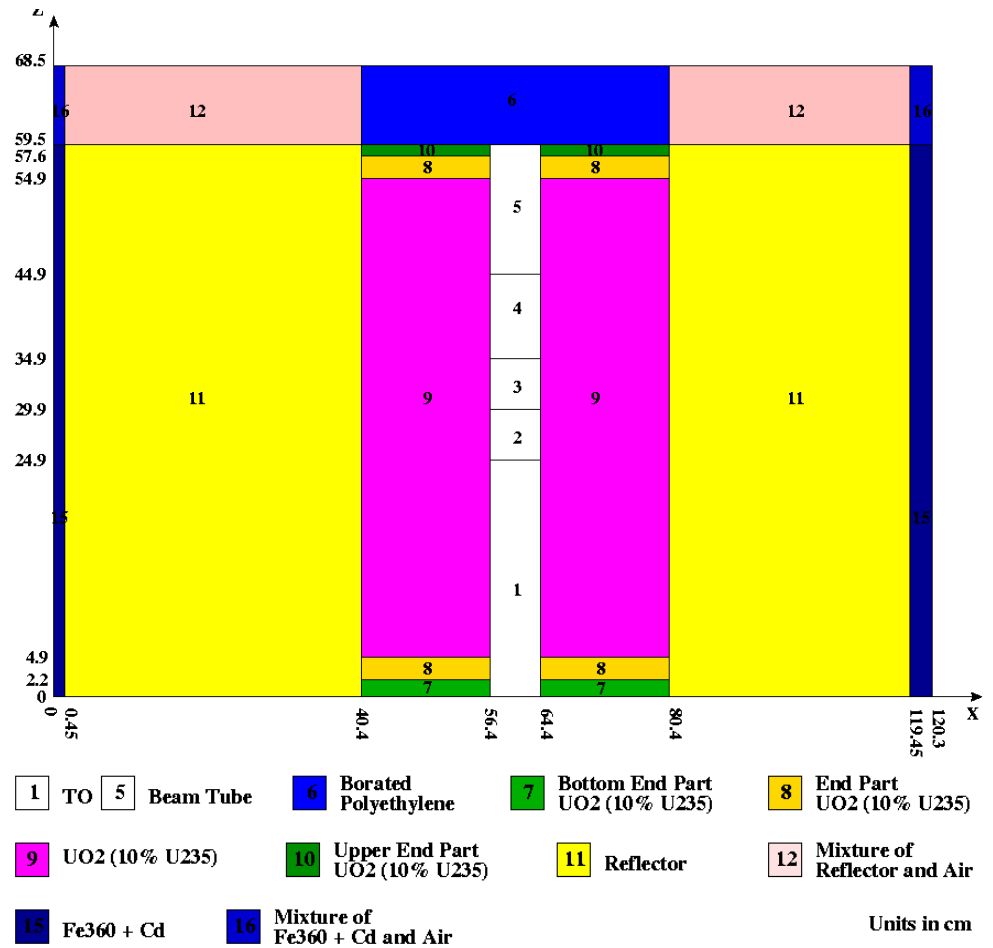
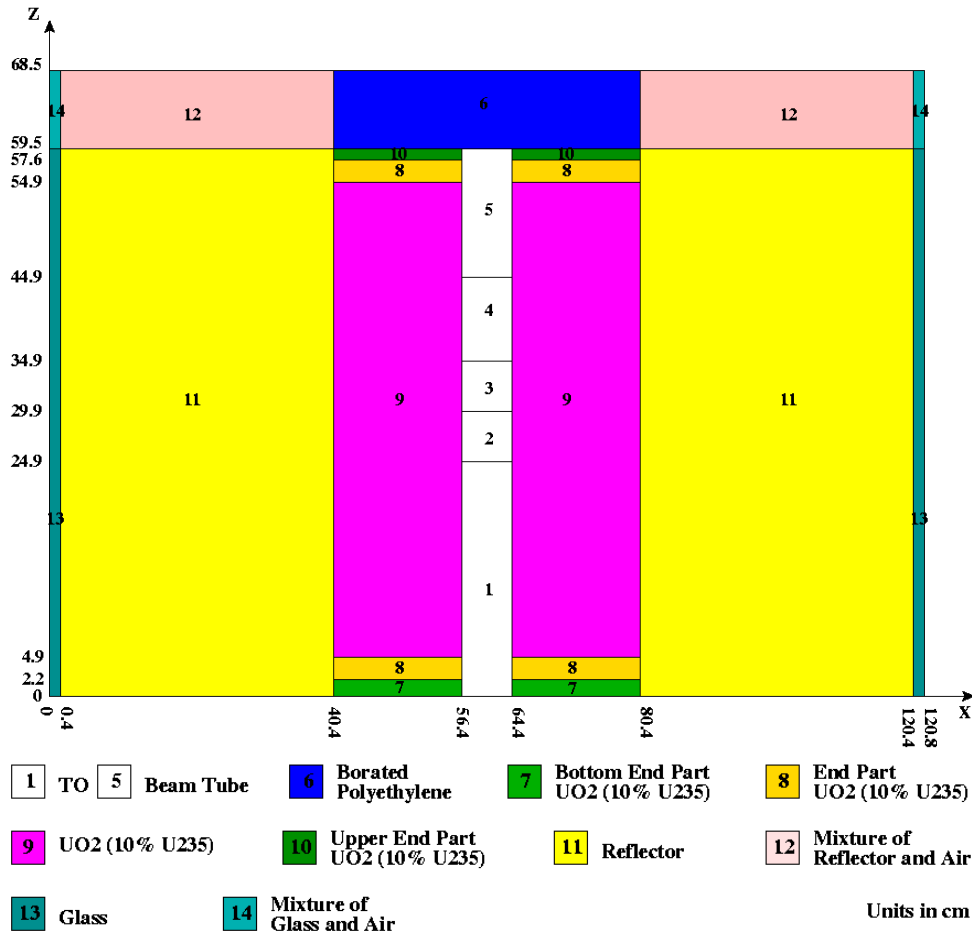


Figure 109. XZ Model for the YALINA-Thermal Deterministic Model (Experimental Channels are not Represented)

Figure 110. YZ Model for the YALINA-Thermal Deterministic Model (Experimental Channels are not Represented)

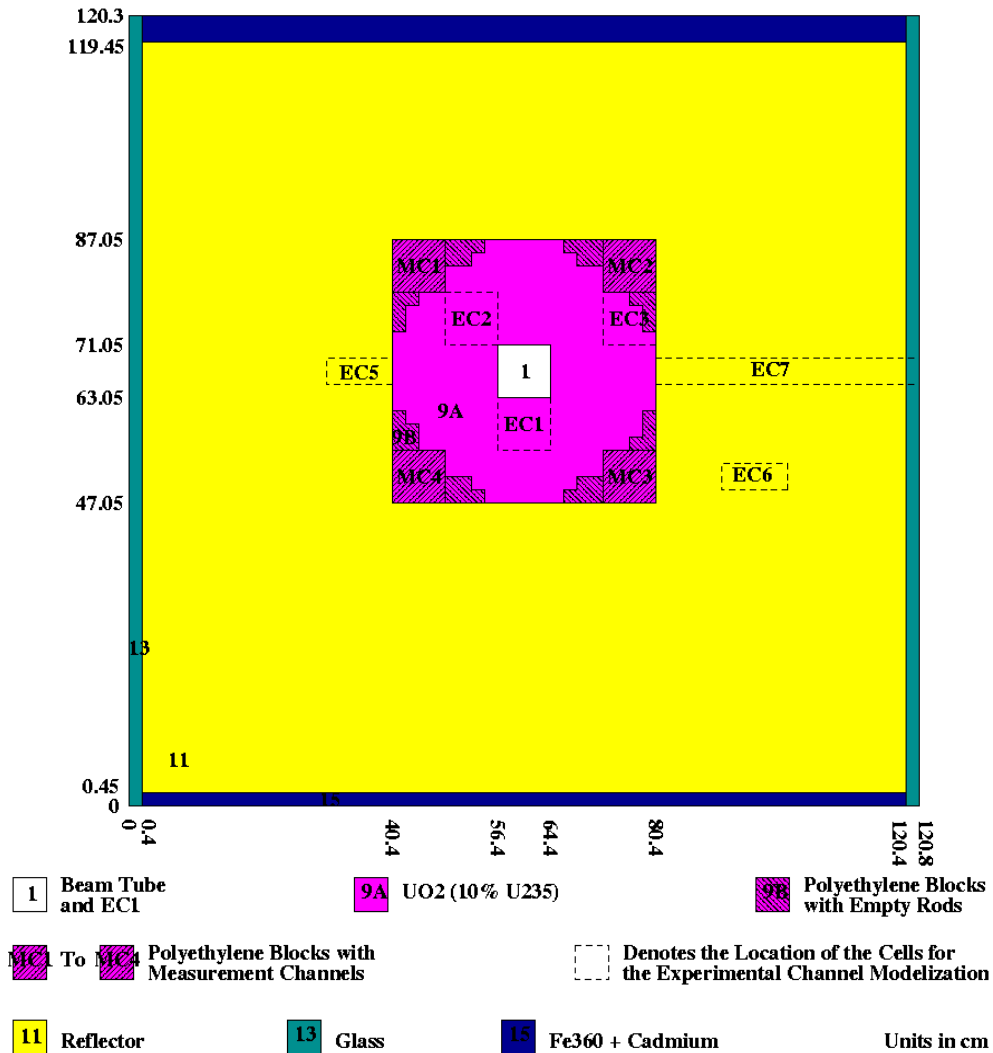


Figure 111. XY Layout of the YALINA-Thermal Deterministic Model

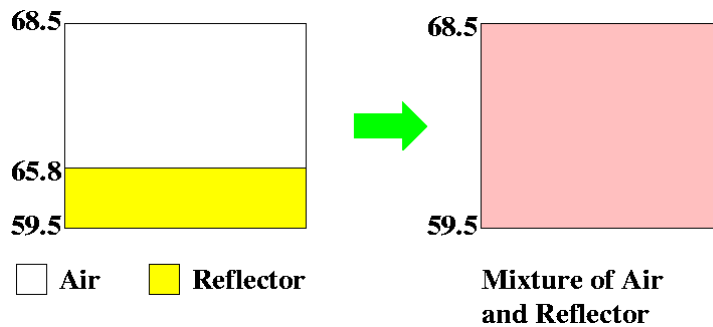


Figure 112. Homogenization of Air with Graphite Reflector of Zone 12

Fuel Regions

Generally, the cell is chosen with the purpose to represent the XY cut of the polyethylene subassemblies as shown in Figures 113 to 115. In the YALINA-Thermal the polyethylene blocks are assembled without any stainless steel frame around. As consequence, the cells used for the cross-section processing do not have the stainless steel frame represented in the corresponding cells of the YALINA-Booster.

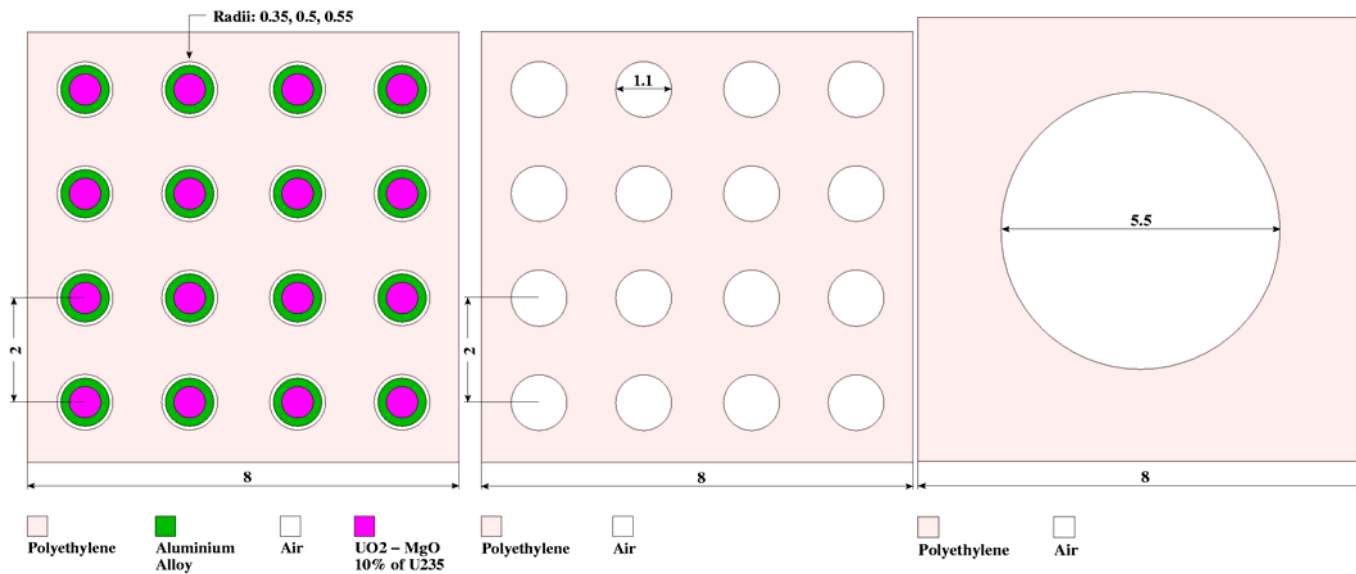


Figure 113. Cell Scheme for Zone 9A

Figure 114. Cell Scheme for Zone 9B

Figure 115. Cell Scheme for MC1 - MC4 Measurement Channels

End Part of the Fuel Rods

The selected axial meshes match the geometry of the fuel rod design shown in Figure 8. The following are the axial boundaries used for each fuel rod design:

- Bottom part of EK-10 fuel rods: Z = 0, 2.2, and 4.9 cm as shown in Figure 116;
- Top part of EK-10 fuel rods: Z = 54.9, 57.6, and 59.5 cm as shown in Figure 117.

For these regions, the cross-sections have been obtained with heterogeneous geometry, as shown in Figures 118 and 119. However, for some zones material homogenization were used as shown in Figures 116 and 117.

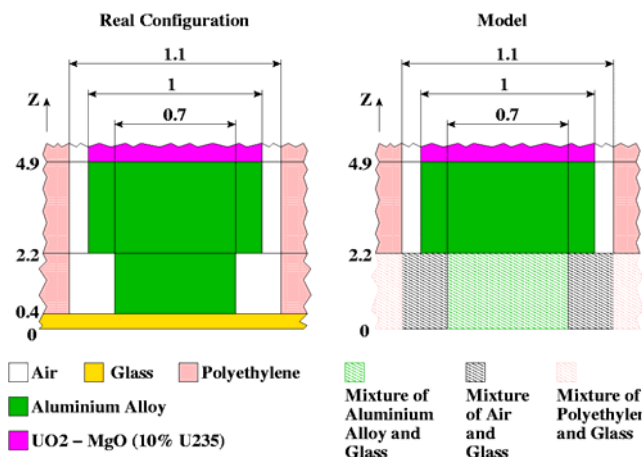


Figure 116. Bottom Part of EK-10 Fuel Rods

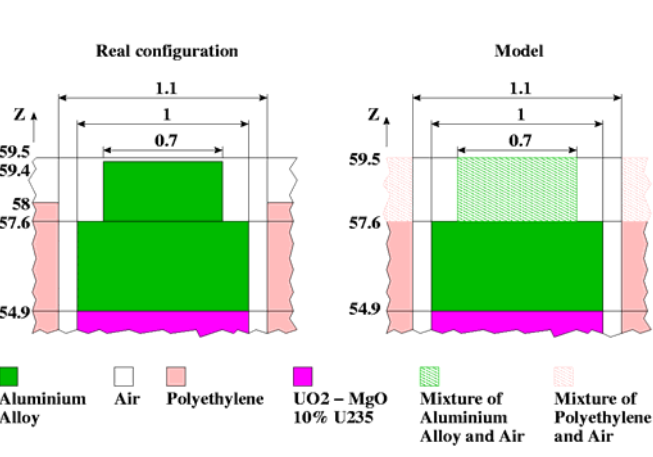


Figure 117. Top Part of EK-10 Fuel Rods

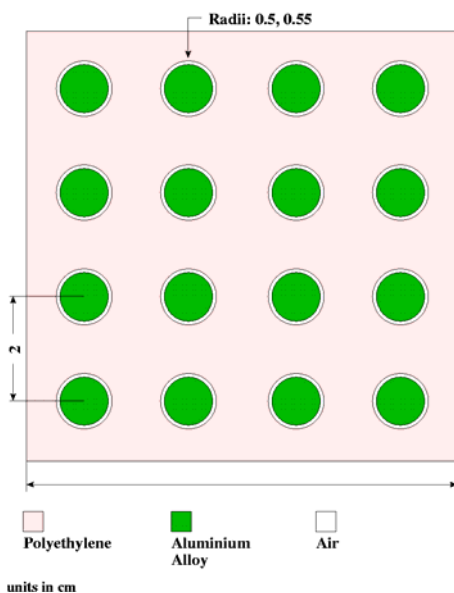


Figure 118. Cell Scheme for Zone 20
($2.2 < Z < 4.9$ and $54.9 < Z < 57.6$)

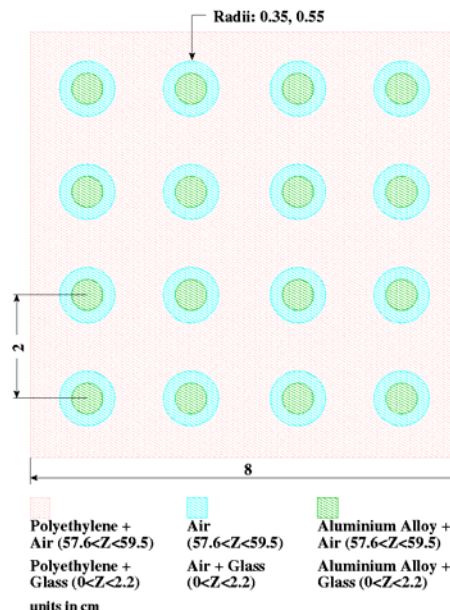


Figure 119. Cell Scheme for Zone 19 ($0 < Z < 2.2$) and 22 ($57.6 < Z < 59.5$)

Borated polyethylene region

Borated polyethylene and stainless steel cross-sections have been processed with a homogeneous cell calculation.

Reflector region

Graphite, stainless steel and glass cross-section have been processed with a homogeneous cell calculation.

Deuteron Beam Duct and Target

The central subassembly of the YALINA-Thermal including the deuteron beam duct and the target has been presented with 5 axial zones as shown in Figure 120. The XY layout of the cells used for the cross-section processing is shown on the right side of Figure 120 for each axial zone. The deuteron beam duct and the target of the YALINA-Thermal has been modeled like the case of the YALINA-Booster. However, YALINA-Thermal has a stainless steel tube around the central assembly as shown in Figure 120.

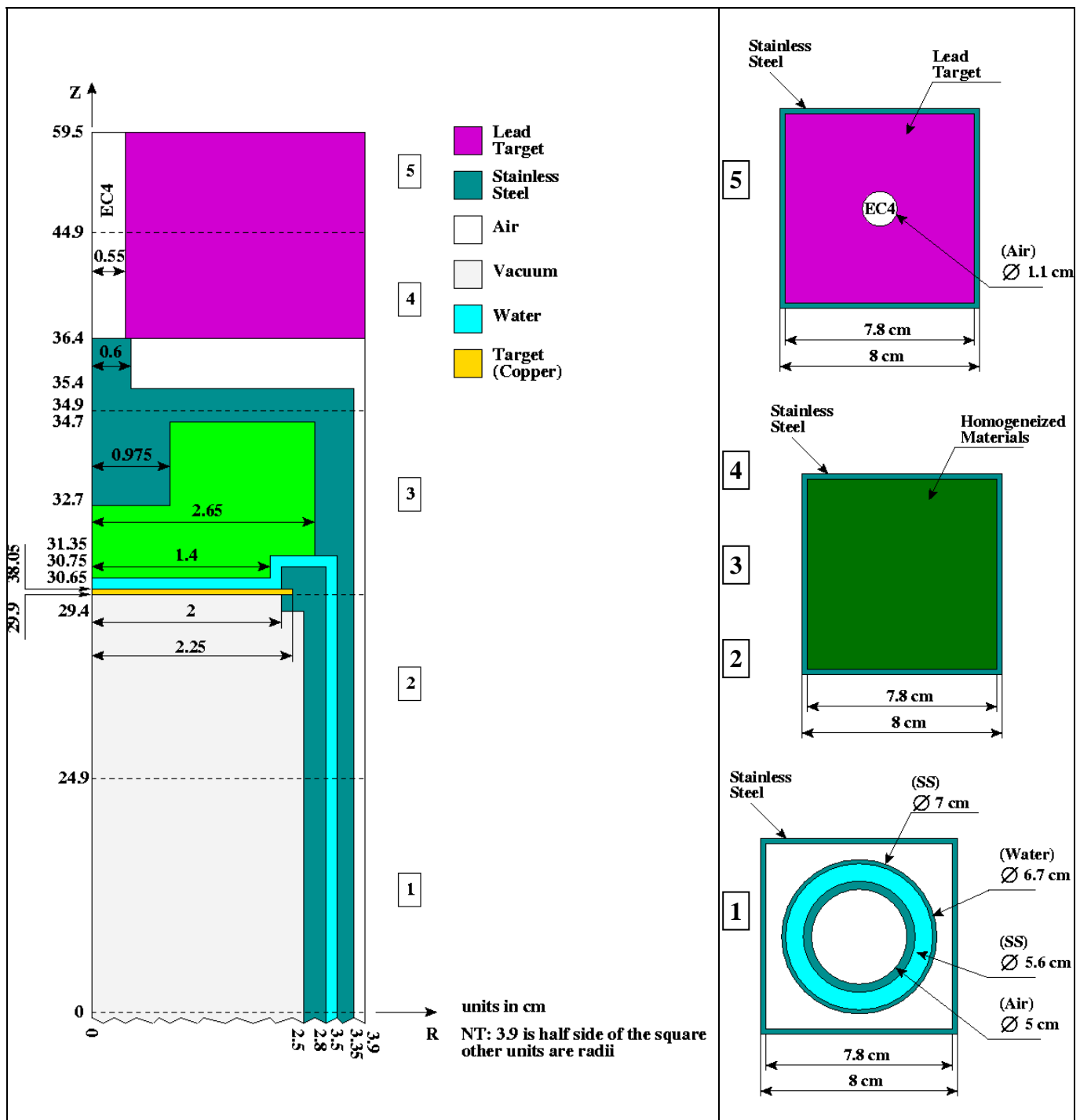


Figure 120. YALINA-Thermal Calculational Models of the Central Assembly

Experimental Channels

To avoid void regions and fine meshes in the calculational model, the experimental channels are homogenized with materials from the neighbor regions while conserving the material content of the assembly. The experimental channels of the reflector zone are homogenized with an opportune volume of the graphite reflector. The experimental channels located in the fuel zone are homogenized over the volume of the cell where they are located. Some simplifications were adopted to describe the presence of the experimental channels consistently with the cell lattice used to describe the fuel pins. Figure 121 shows the EC2 experimental channel inside the fuel zone and Figure 122 shows its

calculational model. Figure 123 shows the exact geometry of the three channels of the boron carbide rods and Figure 124 shows the developed model for the three channels.

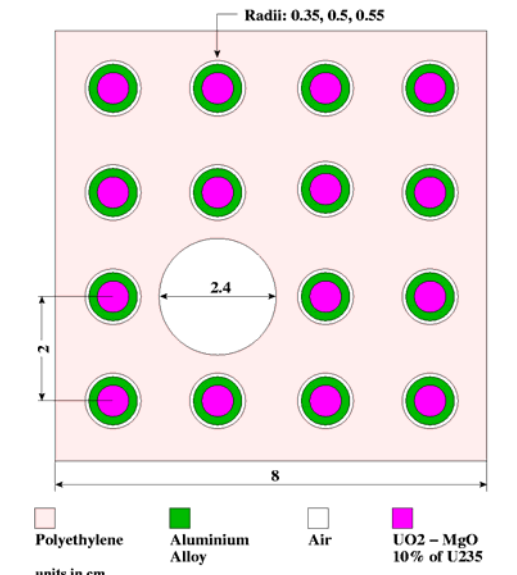


Figure 121. EC2 Experimental Channel

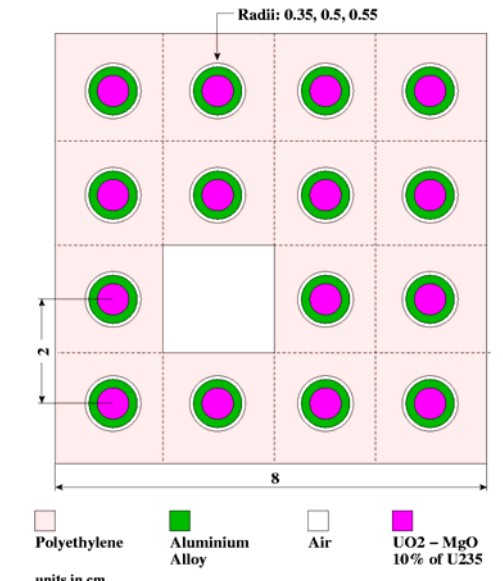


Figure 122. EC2 Experimental Channel Model

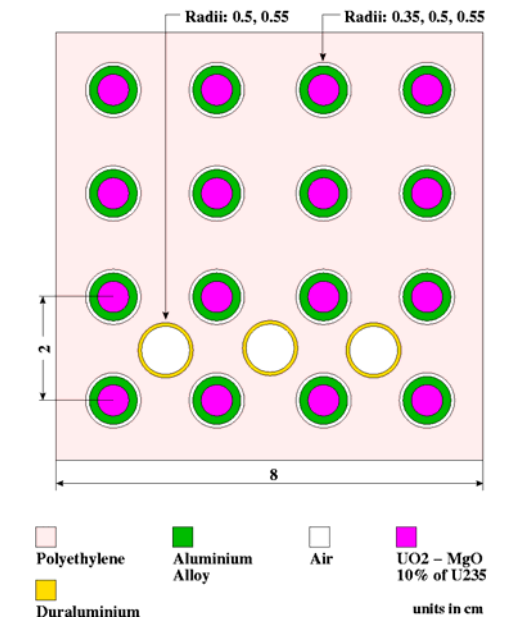


Figure 123. Three Channel for the B₄C Rods

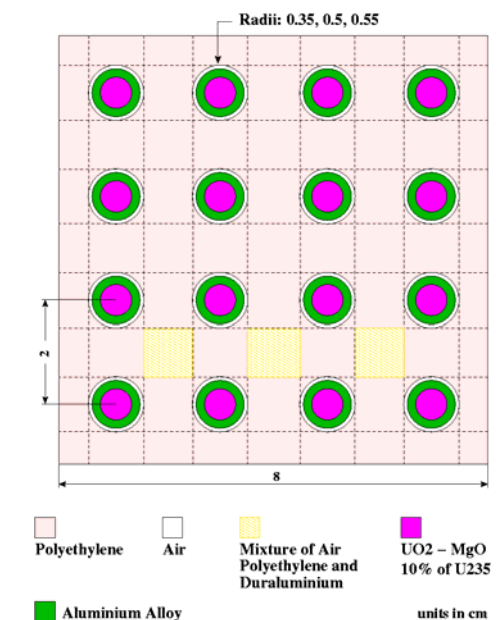


Figure 124. Calculational Model of the Three Channels for the B₄C Rods

Appendix B

RZ Model

The flux calculation with the BISTRO code requires the use of an RZ model. Figures 125 and 126 show the RZ models developed for the YALINA-Booster and –Thermal. The cross-section sets produced for the 3D models have been used for the corresponding zones of the RZ models.

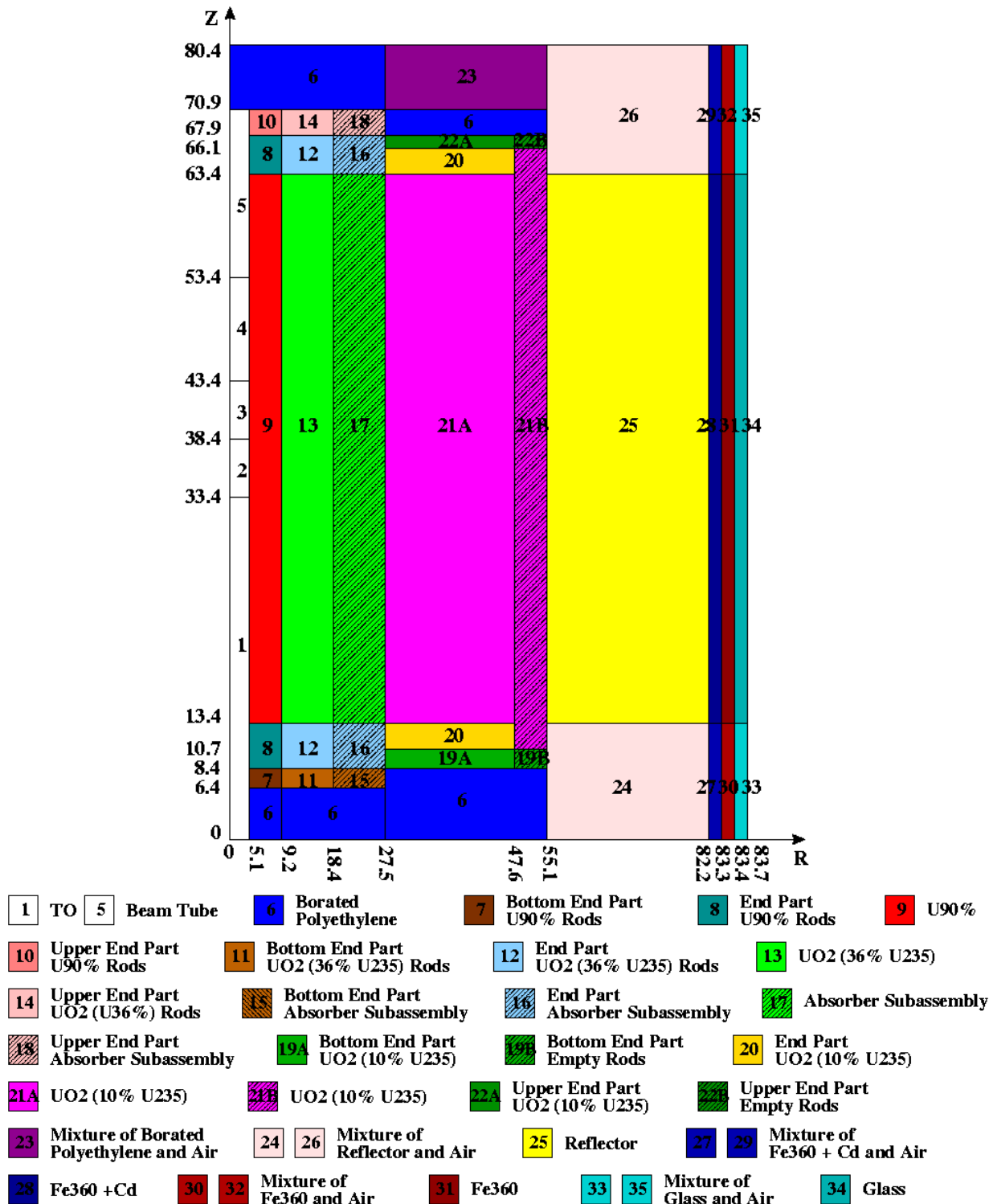


Figure 125. RZ Geometrical Model of the YALINA-Booster

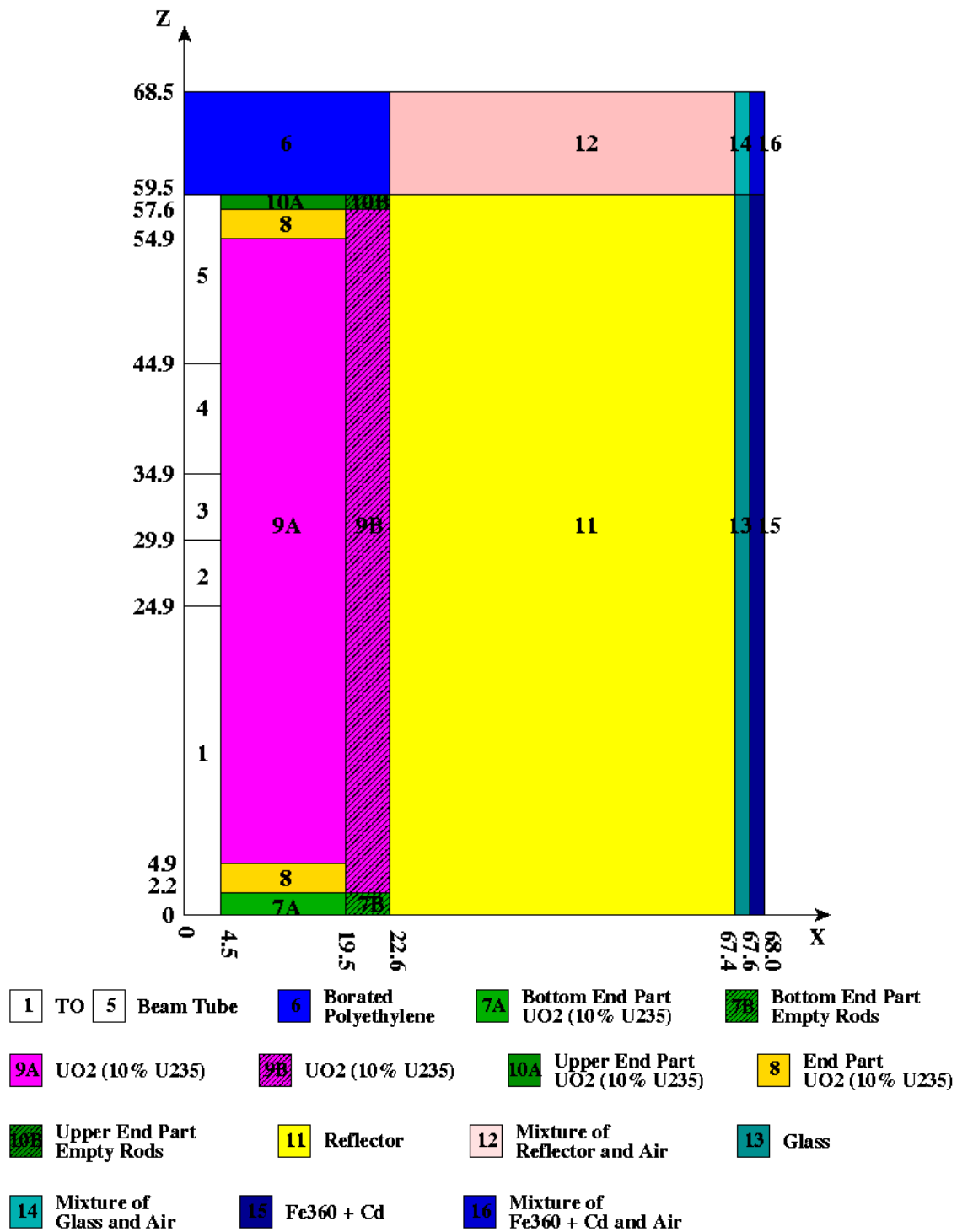


Figure 126. RZ Geometrical Model of the YALINA-Thermal

Appendix C

Energy Group Structures

The 172 and 53 energy group structures used for the deterministic calculations are presented in Tables 31 and 32 respectively.

Table 31. The 172-Energy Group Structure

Group Number	Energy ^(a) [MeV]	Group Number	Energy ^(a) [MeV]	Group Number	Energy ^(a) [MeV]	Group Number	Energy ^(a) [MeV]
1	1.96403E+01	44	1.50344E-02	87	8.31529E-06	130	9.10000E-07
2	1.73325E+01	45	1.11378E-02	88	7.52398E-06	131	8.60000E-07
3	1.49182E+01	46	9.11882E-03	89	6.16012E-06	132	8.50000E-07
4	1.38403E+01	47	7.46586E-03	90	5.34643E-06	133	7.90000E-07
5	1.16183E+01	48	5.53084E-03	91	5.04348E-06	134	7.80000E-07
6	1.00000E+01	49	5.00451E-03	92	4.12925E-06	135	7.05000E-07
7	8.18731E+00	50	3.52662E-03	93	4.00000E-06	136	6.25000E-07
8	6.70320E+00	51	3.35463E-03	94	3.38075E-06	137	5.40000E-07
9	6.06531E+00	52	2.24867E-03	95	3.30000E-06	138	5.00000E-07
10	5.48812E+00	53	2.03468E-03	96	2.76792E-06	139	4.85000E-07
11	4.49329E+00	54	1.50733E-03	97	2.72000E-06	140	4.33000E-07
12	3.67879E+00	55	1.43382E-03	98	2.60000E-06	141	4.00000E-07
13	3.01194E+00	56	1.23410E-03	99	2.55000E-06	142	3.91000E-07
14	2.46597E+00	57	1.01039E-03	100	2.36000E-06	143	3.50000E-07
15	2.23130E+00	58	9.14242E-04	101	2.13000E-06	144	3.20000E-07
16	2.01897E+00	59	7.48518E-04	102	2.10000E-06	145	3.14500E-07
17	1.65299E+00	60	6.77287E-04	103	2.02000E-06	146	3.00000E-07
18	1.35335E+00	61	4.53999E-04	104	1.93000E-06	147	2.80000E-07
19	1.22456E+00	62	3.71703E-04	105	1.84000E-06	148	2.48000E-07
20	1.10803E+00	63	3.04325E-04	106	1.75500E-06	149	2.20000E-07
21	1.00259E+00	64	2.03995E-04	107	1.67000E-06	150	1.89000E-07
22	9.07180E-01	65	1.48625E-04	108	1.59000E-06	151	1.80000E-07
23	8.20850E-01	66	1.36742E-04	109	1.50000E-06	152	1.60000E-07
24	6.08101E-01	67	9.16609E-05	110	1.47500E-06	153	1.40000E-07
25	5.50232E-01	68	7.56736E-05	111	1.44000E-06	154	1.34000E-07
26	4.97871E-01	69	6.79041E-05	112	1.37000E-06	155	1.15000E-07
27	4.50492E-01	70	5.55951E-05	113	1.33750E-06	156	1.00000E-07
28	4.07622E-01	71	5.15780E-05	114	1.30000E-06	157	9.50000E-08
29	3.01974E-01	72	4.82516E-05	115	1.23500E-06	158	8.00000E-08
30	2.73237E-01	73	4.55174E-05	116	1.17000E-06	159	7.70000E-08
31	2.47235E-01	74	4.01690E-05	117	1.15000E-06	160	6.70000E-08
32	1.83156E-01	75	3.72665E-05	118	1.12300E-06	161	5.80000E-08
33	1.22773E-01	76	3.37202E-05	119	1.11000E-06	162	5.00000E-08
34	1.11090E-01	77	3.05113E-05	120	1.09700E-06	163	4.20000E-08
35	8.22975E-02	78	2.76077E-05	121	1.07100E-06	164	3.50000E-08
36	6.73795E-02	79	2.49805E-05	122	1.04500E-06	165	3.00000E-08
37	5.51656E-02	80	2.26033E-05	123	1.03500E-06	166	2.50000E-08
38	4.08677E-02	81	1.94548E-05	124	1.02000E-06	167	2.00000E-08
39	3.69786E-02	82	1.59283E-05	125	9.96000E-07	168	1.50000E-08
40	2.92830E-02	83	1.37096E-05	126	9.86000E-07	169	1.00000E-08
41	2.73945E-02	84	1.12245E-05	127	9.72000E-07	170	6.90000E-09
42	2.47875E-02	85	9.90556E-06	128	9.50000E-07	171	5.00000E-09
43	1.66156E-02	86	9.18981E-06	129	9.30000E-07	172	3.00000E-09

^(a) Upper Energy boundary

Table 32. The 53-Energy Group Structure

Group Number	Energy ^(a) [MeV]	Group Number	Energy ^(a) [MeV]	Group Number	Energy ^(a) [MeV]
1	1.96403E+01	19	5.53084E-03	37	9.10000E-07
2	1.41907E+01	20	3.35463E-03	38	8.50000E-07
3	1.39561E+01	21	2.03468E-03	39	7.90000E-07
4	1.00000E+01	22	1.23410E-03	40	7.05000E-07
5	6.06531E+00	23	7.48518E-04	41	6.25000E-07
6	3.67879E+00	24	4.53999E-04	42	5.40000E-07
7	2.23130E+00	25	3.04325E-04	43	4.85000E-07
8	1.35335E+00	26	1.48625E-04	44	4.33000E-07
9	8.20850E-01	27	9.16609E-05	45	3.20000E-07
10	4.97871E-01	28	6.79041E-05	46	2.48000E-07
11	3.01974E-01	29	4.01690E-05	47	1.60000E-07
12	1.83156E-01	30	2.26033E-05	48	1.40000E-07
13	1.11090E-01	31	1.37096E-05	49	1.00000E-07
14	6.73795E-02	32	8.31529E-06	50	5.00000E-08
15	4.08677E-02	33	4.00000E-06	51	3.50000E-08
16	2.47875E-02	34	2.76792E-06	52	2.50000E-08
17	1.50344E-02	35	1.37000E-06	53	1.50000E-08
18	9.11882E-03	36	9.50000E-07		

^(a) Upper Energy boundary

Appendix D

Cf-252 Source Energy Distribution

The 172 and 53 energy group distributions of the Cf-252 source used for the deterministic calculations are presented in Tables 33 and 34 respectively.

Table 33. 172 Energy Group Distribution of the Cf-252 Source

Gr.	Energy ^(a) [MeV]	Cf-252 Source	Gr.	Energy ^(a) [MeV]	Cf-252 Source	Gr.	Energy ^(a) [MeV]	Cf-252 Source	Gr.	Energy ^(a) [MeV]	Cf-252 Source
1	1.96403E+1	3.15397E-5	44	1.50344E-2	2.78323E-4	87	8.31529E-6	5.49139E-11	130	9.10000E-7	4.68838E-12
2	1.73325E+1	1.19837E-4	45	1.11378E-2	1.27186E-4	88	7.52398E-6	9.32030E-11	131	8.60000E-7	9.49148E-13
3	1.49182E+1	1.52529E-4	46	9.11882E-3	9.43383E-5	89	6.16012E-6	5.49591E-11	132	8.50000E-7	5.78197E-12
4	1.38403E+1	9.63875E-4	47	7.46586E-3	9.78305E-5	90	5.34643E-6	2.03933E-11	133	7.90000E-7	9.78998E-13
5	1.16183E+1	2.28808E-3	48	5.53084E-3	2.39987E-5	91	5.04348E-6	6.15469E-11	134	7.80000E-7	7.49767E-12
6	1.00000E+1	7.59485E-3	49	5.00451E-3	6.06114E-5	92	4.12925E-6	8.72791E-12	135	7.05000E-7	8.34103E-12
7	8.18731E+0	1.68971E-2	50	3.52662E-3	6.34700E-6	93	4.00000E-6	4.20617E-11	136	6.25000E-7	9.33793E-12
8	6.70320E+0	1.34418E-2	51	3.35463E-3	3.67875E-5	94	3.38075E-6	5.52748E-12	137	5.40000E-7	4.59905E-12
9	6.06531E+0	1.74494E-2	52	2.24867E-3	6.23691E-6	95	3.30000E-6	3.68120E-11	138	5.00000E-7	1.76347E-12
10	5.48812E+0	4.80426E-2	53	2.03468E-3	1.39717E-5	96	2.76792E-6	3.35726E-12	139	4.85000E-7	6.29790E-12
11	4.49329E+0	6.54085E-2	54	1.50733E-3	1.77722E-6	97	2.72000E-6	8.44550E-12	140	4.33000E-7	4.16402E-12
12	3.67879E+0	7.98244E-2	55	1.43382E-3	4.59877E-6	98	2.60000E-6	3.53638E-12	141	4.00000E-7	1.16095E-12
13	3.01194E+0	8.90453E-2	56	1.23410E-3	4.72617E-6	99	2.55000E-6	1.35441E-11	142	3.91000E-7	5.44236E-12
14	2.46597E+0	4.60985E-2	57	1.01039E-3	1.88261E-6	100	2.36000E-6	1.66598E-11	143	3.50000E-7	4.16154E-12
15	2.23130E+0	4.61686E-2	58	9.14242E-4	3.01673E-6	101	2.13000E-6	2.19795E-12	144	3.20000E-7	7.81404E-13
16	2.01897E+0	8.99886E-2	59	7.48518E-4	1.20188E-6	102	2.10000E-6	5.89290E-12	145	3.14500E-7	2.08979E-12
17	1.65299E+0	8.35147E-2	60	6.77287E-4	3.35507E-6	103	2.02000E-6	6.68884E-12	146	3.00000E-7	2.95827E-12
18	1.35335E+0	3.84492E-2	61	4.53999E-4	1.06009E-6	104	1.93000E-6	6.75801E-12	147	2.80000E-7	4.93988E-12
19	1.22456E+0	3.59645E-2	62	3.71703E-4	7.86832E-7	105	1.84000E-6	6.45277E-12	148	2.48000E-7	4.56724E-12
20	1.10803E+0	3.33760E-2	63	3.04325E-4	1.01842E-6	106	1.75500E-6	6.52821E-12	149	2.20000E-7	5.38294E-12
21	1.00259E+0	3.07519E-2	64	2.03995E-4	4.71461E-7	107	1.67000E-6	6.22034E-12	150	1.89000E-7	1.63866E-12
22	9.07180E-1	2.81517E-2	65	1.48625E-4	9.15735E-8	108	1.59000E-6	7.09590E-12	151	1.80000E-7	3.78551E-12
23	8.20850E-1	6.97099E-2	66	1.36742E-4	3.12498E-7	109	1.50000E-6	1.99108E-12	152	1.60000E-7	4.01681E-12
24	6.08101E-1	1.87442E-2	67	9.16609E-5	9.61616E-8	110	1.47500E-6	2.80308E-12	153	1.40000E-7	1.25756E-12
25	5.50232E-1	1.67481E-2	68	7.56736E-5	4.36375E-8	111	1.44000E-6	5.66396E-12	154	1.34000E-7	4.17141E-12
26	4.97871E-1	1.49114E-2	69	6.79041E-5	6.46812E-8	112	1.37000E-6	2.65757E-12	155	1.15000E-7	3.53370E-12
27	4.50492E-1	1.32335E-2	70	5.55951E-5	1.98626E-8	113	1.33750E-6	3.08986E-12	156	1.00000E-7	1.23418E-12
28	4.07622E-1	3.11447E-2	71	5.15780E-5	1.59604E-8	114	1.30000E-6	5.41919E-12	157	9.50000E-8	3.90531E-12
29	3.01974E-1	7.99448E-3	72	4.82516E-5	1.27794E-8	115	1.23500E-6	5.50655E-12	158	8.00000E-8	8.22734E-13
30	2.73237E-1	7.00992E-3	73	4.55174E-5	2.40847E-8	116	1.17000E-6	1.71328E-12	159	7.70000E-8	2.86222E-12
31	2.47235E-1	1.61770E-2	74	4.01690E-5	1.25474E-8	117	1.15000E-6	2.32790E-12	160	6.70000E-8	2.76092E-12
32	1.83156E-1	1.33950E-2	75	3.72665E-5	1.48132E-8	118	1.12300E-6	1.12719E-12	161	5.80000E-8	2.63697E-12
33	1.22773E-1	2.32704E-3	76	3.37202E-5	1.28969E-8	119	1.11000E-6	1.13142E-12	162	5.00000E-8	2.85448E-12
34	1.11090E-1	5.28161E-3	77	3.05113E-5	1.12410E-8	120	1.09700E-6	2.27593E-12	163	4.20000E-8	2.72748E-12
35	8.22975E-2	2.44504E-3	78	2.76077E-5	9.80943E-9	121	1.07100E-6	2.29401E-12	164	3.50000E-8	2.11807E-12
36	6.73795E-2	1.82809E-3	79	2.49805E-5	8.57115E-9	122	1.04500E-6	8.87299E-13	165	3.00000E-8	2.30178E-12
37	5.51656E-2	1.91047E-3	80	2.26033E-5	1.08932E-8	123	1.03500E-6	1.33629E-12	166	2.50000E-8	2.54446E-12
38	4.08677E-2	4.71193E-4	81	1.94548E-5	1.15620E-8	124	1.02000E-6	2.15179E-12	167	2.00000E-8	2.88647E-12
39	3.69786E-2	8.63168E-4	82	1.59283E-5	1.74019E-10	125	9.96000E-7	9.01706E-13	168	1.50000E-8	3.42222E-12
40	2.92830E-2	1.96655E-4	83	1.37096E-5	1.86882E-10	126	9.86000E-7	1.26760E-12	169	1.00000E-8	2.57774E-12
41	2.73945E-2	2.60851E-4	84	1.12245E-5	9.58049E-11	127	9.72000E-7	2.00458E-12	170	6.90000E-9	1.88060E-12
42	2.47875E-2	7.29832E-4	85	9.90556E-6	5.10506E-11	128	9.50000E-7	1.83621E-12	171	5.00000E-9	2.42586E-12
43	1.66156E-2	1.24073E-4	86	9.18981E-6	6.15234E-11	129	9.30000E-7	1.84993E-12	172	3.00000E-9	8.33921E-12

^(a) Upper Energy boundary

Table 34. 53 Energy Group Distribution of the Cf-252 Source

Gr.	Energy ^(a) [MeV]	Cf-252 Source	Gr.	Energy ^(a) [MeV]	Cf-252 Source	Gr.	Energy ^(a) [MeV]	Cf-252 Source
1	1.96403E+01	1.51377E-4	19	5.53084E-03	9.09571E-5	37	9.10000E-07	5.63753E-12
2	1.41907E+01	1.52529E-4	20	3.35463E-03	4.30244E-5	38	8.50000E-07	5.78197E-12
3	1.39561E+01	3.25195E-3	21	2.03468E-03	2.03477E-5	39	7.90000E-07	8.47667E-12
4	1.00000E+01	3.79338E-2	22	1.23410E-03	9.62551E-6	40	7.05000E-07	8.34103E-12
5	6.06531E+00	1.30901E-1	23	7.48518E-04	4.55694E-6	41	6.25000E-07	9.33793E-12
6	3.67879E+00	2.14968E-1	24	4.53999E-04	1.84692E-6	42	5.40000E-07	6.36252E-12
7	2.23130E+00	2.19672E-1	25	3.04325E-04	1.48988E-6	43	4.85000E-07	6.29790E-12
8	1.35335E+00	1.66693E-1	26	1.48625E-04	4.04072E-7	44	4.33000E-07	1.49289E-11
9	8.20850E-01	1.05202E-1	27	9.16609E-05	1.39799E-7	45	3.20000E-07	1.07693E-11
10	4.97871E-01	5.92896E-2	28	6.79041E-05	1.37368E-7	46	2.48000E-07	1.53744E-11
11	3.01974E-01	3.11814E-2	29	4.01690E-05	6.98790E-8	47	1.60000E-07	4.01681E-12
12	1.83156E-01	1.57221E-2	30	2.26033E-05	2.26292E-8	48	1.40000E-07	8.96267E-12
13	1.11090E-01	7.72665E-3	31	1.37096E-05	3.95261E-10	49	1.00000E-07	1.42223E-11
14	6.73795E-02	3.73856E-3	32	8.31529E-06	2.93744E-10	50	5.00000E-08	5.58196E-12
15	4.08677E-02	1.79187E-3	33	4.00000E-06	8.44012E-11	51	3.50000E-08	4.41985E-12
16	2.47875E-02	8.53906E-4	34	2.76792E-06	1.03836E-10	52	2.50000E-08	5.43093E-12
17	1.50344E-02	4.05509E-4	35	1.37000E-06	3.60922E-11	53	1.50000E-08	1.86456E-11
18	9.11882E-03	1.92169E-4	36	9.50000E-07	3.68614E-12			

^(a) Upper Energy boundary

Appendix E

ENDF Delayed Neutron Data

This delayed neutron data used in the analyses from ENDF/B nuclear data files are tabulated in Tables 35, 36, 37, and 38.

Table 35. ENDF/B Delayed Time Constants [sec.⁻¹]

U235	1.33360E-2	3.27390E-2	1.20780E-1	3.02780E-1	8.49490E-1	2.85300E+0
U238	1.36300E-2	3.13340E-2	1.23340E-1	3.23730E-1	9.05970E-1	3.04870E+0

Table 36. ENDF/B β^v

Family Group	1	2	3	4	5	6	Total
U235	5.84666E-4	3.01753E-3	2.88051E-3	6.45923E-3	2.64878E-3	1.10928E-3	1.67000E-2
U238	6.13371E-4	4.96323E-3	5.76393E-3	1.69455E-2	1.11779E-2	4.53606E-3	4.40000E-2

Table 37. Calculated ENDF/B Delayed Neutron Spectra for the YALINA-Booster

Family Group		1	2	3	4	5	6
Group	En. [eV]						
1	1.964E+7	0.000E+0	0.000E+0	0.000E+0	0.000E+0	0.000E+0	0.000E+0
2	1.419E+7	0.000E+0	0.000E+0	0.000E+0	0.000E+0	0.000E+0	0.000E+0
3	1.396E+7	0.000E+0	0.000E+0	0.000E+0	0.000E+0	0.000E+0	0.000E+0
4	1.000E+7	0.000E+0	0.000E+0	0.000E+0	0.000E+0	0.000E+0	0.000E+0
5	6.065E+6	0.000E+0	0.000E+0	0.000E+0	0.000E+0	0.000E+0	0.000E+0
6	3.679E+6	0.000E+0	0.000E+0	3.793E-4	4.424E-3	8.661E-3	1.528E-2
7	2.231E+6	9.904E-3	1.274E-2	1.620E-2	5.643E-2	5.122E-2	5.860E-2
8	1.353E+6	1.237E-1	1.534E-1	8.771E-2	1.617E-1	1.235E-1	1.217E-1
9	8.209E+5	1.691E-1	2.236E-1	2.698E-1	2.350E-1	2.140E-1	2.154E-1
10	4.979E+5	2.117E-1	2.628E-1	2.291E-1	2.132E-1	2.159E-1	2.018E-1
11	3.020E+5	1.961E-1	1.295E-1	1.624E-1	1.410E-1	1.635E-1	1.548E-1
12	1.832E+5	1.234E-1	8.235E-2	1.071E-1	9.009E-2	1.023E-1	9.366E-2
13	1.111E+5	5.972E-2	6.409E-2	5.598E-2	4.348E-2	5.644E-2	5.964E-2
14	6.738E+4	4.966E-2	2.797E-2	2.985E-2	2.242E-2	2.733E-2	2.745E-2
15	4.087E+4	2.186E-2	1.721E-2	1.786E-2	1.398E-2	1.410E-2	1.519E-2
16	2.479E+4	2.182E-2	1.049E-2	1.072E-2	8.978E-3	1.224E-2	1.975E-2
17	1.503E+4	1.085E-2	6.329E-3	6.131E-3	5.037E-3	7.996E-3	1.450E-2
18	9.119E+3	8.465E-4	3.765E-3	2.646E-3	1.690E-3	1.127E-3	8.529E-4
19	5.531E+3	5.134E-4	2.284E-3	1.605E-3	1.025E-3	6.837E-4	5.173E-4
20	3.355E+3	3.114E-4	1.385E-3	9.734E-4	6.217E-4	4.147E-4	3.138E-4
21	2.035E+3	1.889E-4	8.401E-4	5.904E-4	3.771E-4	2.515E-4	1.903E-4
22	1.234E+3	1.146E-4	5.096E-4	3.581E-4	2.287E-4	1.526E-4	1.154E-4
23	7.485E+2	6.949E-5	3.091E-4	2.172E-4	1.387E-4	9.253E-5	7.001E-5
24	4.540E+2	3.531E-5	1.571E-4	1.104E-4	7.050E-5	4.703E-5	3.558E-5
25	3.043E+2	3.674E-5	1.634E-4	1.148E-4	7.334E-5	4.892E-5	3.701E-5
26	1.486E+2	1.344E-5	5.978E-5	4.201E-5	2.683E-5	1.790E-5	1.354E-5
27	9.166E+1	5.605E-6	2.493E-5	1.752E-5	1.119E-5	7.464E-6	5.647E-6
28	6.790E+1	6.544E-6	2.911E-5	2.045E-5	1.306E-5	8.714E-6	6.593E-6
29	4.017E+1	4.144E-6	1.843E-5	1.295E-5	8.274E-6	5.519E-6	4.175E-6
30	2.260E+1	2.098E-6	9.333E-6	6.559E-6	4.189E-6	2.794E-6	2.114E-6
31	1.371E+1	1.273E-6	5.661E-6	3.978E-6	2.541E-6	1.695E-6	1.282E-6
32	8.315E+0	1.018E-6	4.529E-6	3.182E-6	2.033E-6	1.356E-6	1.026E-6
33	4.000E+0	2.907E-7	1.293E-6	9.086E-7	5.803E-7	3.871E-7	2.929E-7
34	2.768E+0	3.298E-7	1.467E-6	1.031E-6	6.584E-7	4.392E-7	3.323E-7
35	1.370E+0	9.909E-8	4.408E-7	3.097E-7	1.978E-7	1.320E-7	9.983E-8
36	9.500E-1	9.437E-9	4.198E-8	2.950E-8	1.884E-8	1.257E-8	9.508E-9
37	9.100E-1	1.416E-8	6.297E-8	4.425E-8	2.826E-8	1.885E-8	1.426E-8
38	8.500E-1	1.416E-8	6.297E-8	4.425E-8	2.826E-8	1.885E-8	1.426E-8
39	7.900E-1	2.005E-8	8.920E-8	6.268E-8	4.004E-8	2.671E-8	2.020E-8
40	7.050E-1	1.888E-8	8.395E-8	5.900E-8	3.768E-8	2.514E-8	1.902E-8
41	6.250E-1	2.005E-8	8.920E-8	6.268E-8	4.004E-8	2.671E-8	2.020E-8
42	5.400E-1	1.298E-8	5.772E-8	4.056E-8	2.591E-8	1.728E-8	1.307E-8
43	4.850E-1	1.227E-8	5.457E-8	3.835E-8	2.449E-8	1.634E-8	1.236E-8
44	4.330E-1	2.666E-8	1.186E-7	8.333E-8	5.322E-8	3.550E-8	2.686E-8
45	3.200E-1	1.699E-8	7.556E-8	5.310E-8	3.391E-8	2.262E-8	1.711E-8
46	2.480E-1	2.076E-8	9.235E-8	6.490E-8	4.145E-8	2.765E-8	2.092E-8
47	1.600E-1	4.719E-9	2.099E-8	1.475E-8	9.420E-9	6.284E-9	4.754E-9
48	1.400E-1	9.437E-9	4.198E-8	2.950E-8	1.884E-8	1.257E-8	9.508E-9
49	1.000E-1	1.180E-8	5.247E-8	3.687E-8	2.355E-8	1.571E-8	1.189E-8
50	5.000E-2	3.539E-9	1.574E-8	1.106E-8	7.065E-9	4.713E-9	3.566E-9
51	3.500E-2	2.359E-9	1.049E-8	7.375E-9	4.710E-9	3.142E-9	2.377E-9
52	2.500E-2	2.359E-9	1.049E-8	7.375E-9	4.710E-9	3.142E-9	2.377E-9
53	1.500E-2	3.539E-9	1.574E-8	1.106E-8	7.065E-9	4.713E-9	3.566E-9

Table 38. Calculated ENDF/B Delayed Neutron Spectra for the YALINA-Thermal

Family Group		1	2	3	4	5	6
Group	En. [eV]						
1	1.964E+7	0.000E+0	0.000E+0	0.000E+0	0.000E+0	0.000E+0	0.000E+0
2	1.419E+7	0.000E+0	0.000E+0	0.000E+0	0.000E+0	0.000E+0	0.000E+0
3	1.396E+7	0.000E+0	0.000E+0	0.000E+0	0.000E+0	0.000E+0	0.000E+0
4	1.000E+7	0.000E+0	0.000E+0	0.000E+0	0.000E+0	0.000E+0	0.000E+0
5	6.065E+6	0.000E+0	0.000E+0	0.000E+0	0.000E+0	0.000E+0	0.000E+0
6	3.679E+6	0.000E+0	0.000E+0	3.793E-4	4.419E-3	8.653E-3	1.527E-2
7	2.231E+6	9.896E-3	1.273E-2	1.621E-2	5.641E-2	5.123E-2	5.858E-2
8	1.353E+6	1.236E-1	1.533E-1	8.772E-2	1.617E-1	1.236E-1	1.217E-1
9	8.209E+5	1.690E-1	2.235E-1	2.699E-1	2.351E-1	2.140E-1	2.155E-1
10	4.979E+5	2.116E-1	2.627E-1	2.291E-1	2.132E-1	2.159E-1	2.017E-1
11	3.020E+5	1.962E-1	1.295E-1	1.624E-1	1.410E-1	1.635E-1	1.548E-1
12	1.832E+5	1.235E-1	8.243E-2	1.071E-1	9.007E-2	1.023E-1	9.366E-2
13	1.111E+5	5.975E-2	6.411E-2	5.597E-2	4.347E-2	5.641E-2	5.963E-2
14	6.738E+4	4.969E-2	2.799E-2	2.984E-2	2.242E-2	2.732E-2	2.745E-2
15	4.087E+4	2.187E-2	1.722E-2	1.785E-2	1.398E-2	1.410E-2	1.519E-2
16	2.479E+4	2.183E-2	1.050E-2	1.072E-2	8.974E-3	1.224E-2	1.977E-2
17	1.503E+4	1.086E-2	6.335E-3	6.129E-3	5.034E-3	7.999E-3	1.452E-2
18	9.119E+3	8.471E-4	3.768E-3	2.645E-3	1.688E-3	1.126E-3	8.530E-4
19	5.531E+3	5.138E-4	2.285E-3	1.604E-3	1.024E-3	6.832E-4	5.174E-4
20	3.355E+3	3.116E-4	1.386E-3	9.729E-4	6.208E-4	4.144E-4	3.138E-4
21	2.035E+3	1.890E-4	8.407E-4	5.901E-4	3.766E-4	2.513E-4	1.903E-4
22	1.234E+3	1.146E-4	5.099E-4	3.579E-4	2.284E-4	1.525E-4	1.154E-4
23	7.485E+2	6.954E-5	3.093E-4	2.171E-4	1.385E-4	9.246E-5	7.002E-5
24	4.540E+2	3.534E-5	1.572E-4	1.103E-4	7.040E-5	4.699E-5	3.558E-5
25	3.043E+2	3.676E-5	1.635E-4	1.148E-4	7.323E-5	4.888E-5	3.702E-5
26	1.486E+2	1.345E-5	5.982E-5	4.199E-5	2.679E-5	1.788E-5	1.354E-5
27	9.166E+1	5.609E-6	2.495E-5	1.751E-5	1.117E-5	7.459E-6	5.648E-6
28	6.790E+1	6.548E-6	2.913E-5	2.044E-5	1.305E-5	8.707E-6	6.594E-6
29	4.017E+1	4.147E-6	1.845E-5	1.295E-5	8.262E-6	5.515E-6	4.176E-6
30	2.260E+1	2.100E-6	9.340E-6	6.555E-6	4.183E-6	2.792E-6	2.114E-6
31	1.371E+1	1.274E-6	5.665E-6	3.976E-6	2.537E-6	1.694E-6	1.282E-6
32	8.315E+0	1.019E-6	4.532E-6	3.181E-6	2.030E-6	1.355E-6	1.026E-6
33	4.000E+0	2.909E-7	1.294E-6	9.081E-7	5.795E-7	3.868E-7	2.929E-7
34	2.768E+0	3.301E-7	1.468E-6	1.030E-6	6.575E-7	4.389E-7	3.323E-7
35	1.370E+0	9.916E-8	4.411E-7	3.096E-7	1.975E-7	1.319E-7	9.985E-8
36	9.500E-1	9.444E-9	4.201E-8	2.948E-8	1.881E-8	1.256E-8	9.509E-9
37	9.100E-1	1.417E-8	6.301E-8	4.422E-8	2.822E-8	1.884E-8	1.426E-8
38	8.500E-1	1.417E-8	6.301E-8	4.422E-8	2.822E-8	1.884E-8	1.426E-8
39	7.900E-1	2.007E-8	8.926E-8	6.265E-8	3.998E-8	2.669E-8	2.021E-8
40	7.050E-1	1.889E-8	8.401E-8	5.896E-8	3.763E-8	2.512E-8	1.902E-8
41	6.250E-1	2.007E-8	8.926E-8	6.265E-8	3.998E-8	2.669E-8	2.021E-8
42	5.400E-1	1.299E-8	5.776E-8	4.054E-8	2.587E-8	1.727E-8	1.308E-8
43	4.850E-1	1.228E-8	5.461E-8	3.833E-8	2.446E-8	1.633E-8	1.236E-8
44	4.330E-1	2.668E-8	1.187E-7	8.329E-8	5.315E-8	3.548E-8	2.686E-8
45	3.200E-1	1.700E-8	7.561E-8	5.307E-8	3.387E-8	2.260E-8	1.712E-8
46	2.480E-1	2.078E-8	9.241E-8	6.486E-8	4.139E-8	2.763E-8	2.092E-8
47	1.600E-1	4.722E-9	2.100E-8	1.474E-8	9.407E-9	6.279E-9	4.755E-9
48	1.400E-1	9.444E-9	4.201E-8	2.948E-8	1.881E-8	1.256E-8	9.509E-9
49	1.000E-1	1.181E-8	5.251E-8	3.685E-8	2.352E-8	1.570E-8	1.189E-8
50	5.000E-2	3.542E-9	1.575E-8	1.106E-8	7.055E-9	4.709E-9	3.566E-9
51	3.500E-2	2.361E-9	1.050E-8	7.370E-9	4.704E-9	3.140E-9	2.377E-9
52	2.500E-2	2.361E-9	1.050E-8	7.370E-9	4.704E-9	3.140E-9	2.377E-9
53	1.500E-2	3.542E-9	1.575E-8	1.106E-8	7.055E-9	4.709E-9	3.566E-9

Appendix F

Comparison of Neutron Spectra Calculated with Different Nuclear Data Libraries

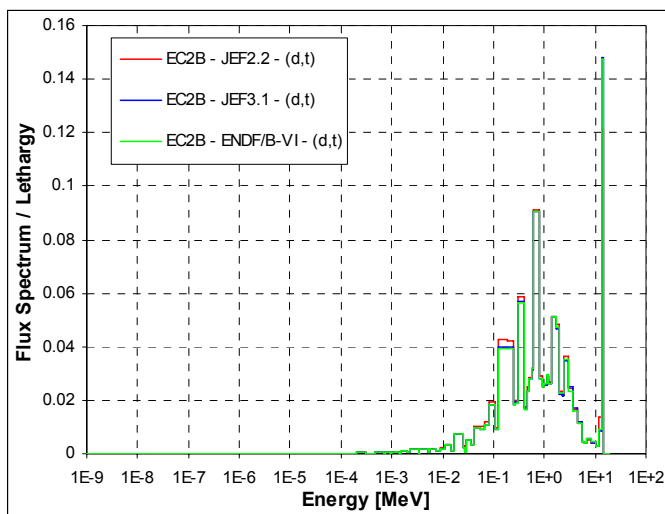


Figure 127. EC2B Neutron Spectra of the YALINA-Booster with (d,t) Neutron Source

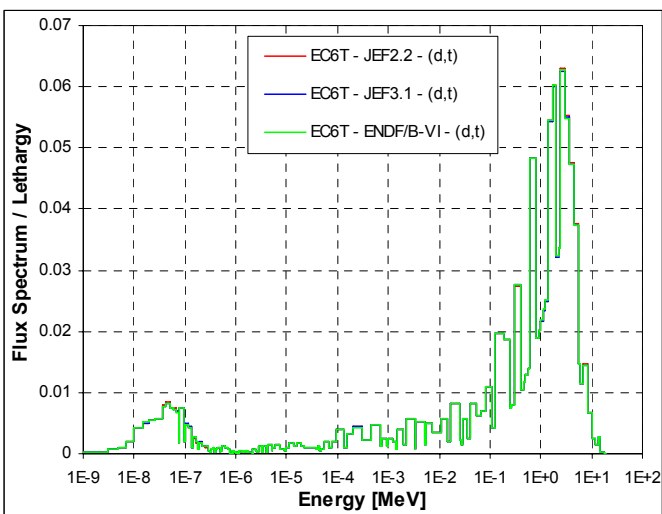


Figure 128. EC6T Neutron Spectra of the YALINA-Booster with (d,t) Neutron Source

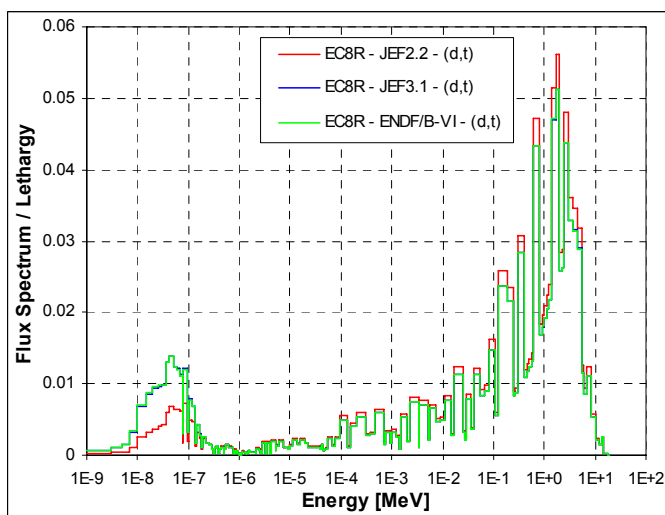


Figure 129. EC8R Neutron Spectra of the YALINA-Booster with (d,t) Neutron Source

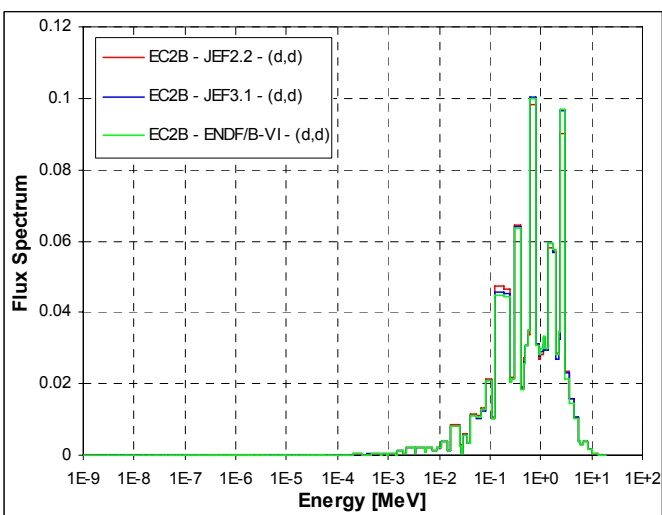


Figure 130. EC2B Neutron Spectra of the YALINA-Booster with (d,d) Neutron Source

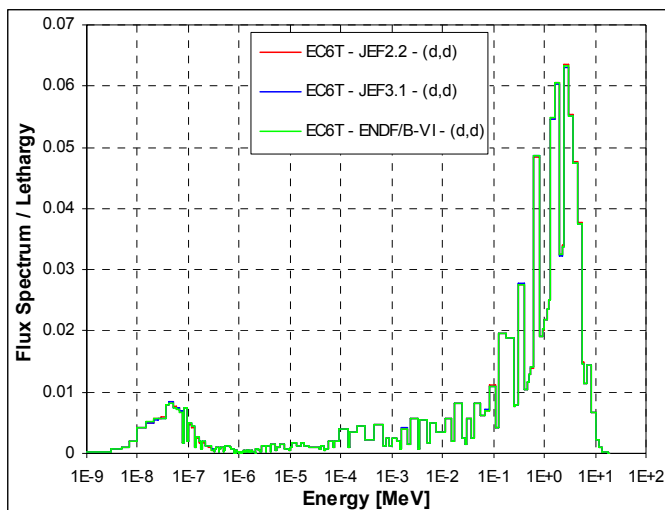


Figure 131. EC6T Neutron Spectra of the YALINA-Booster with (d,d) Neutron Source

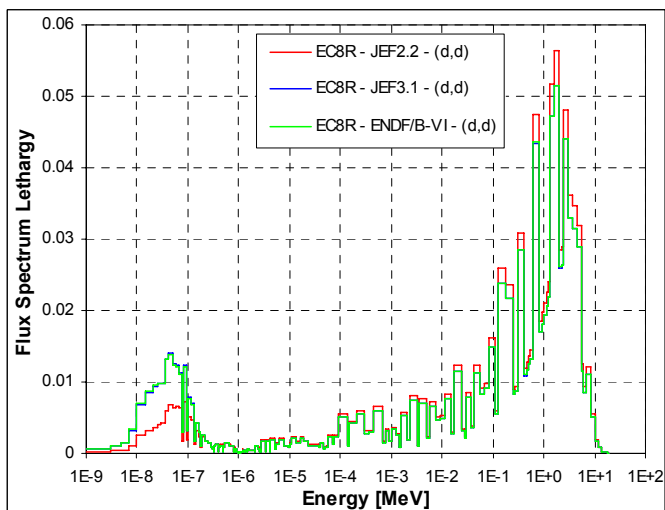


Figure 132. EC8R Neutron Spectra of the YALINA-Booster with (d,d) Neutron Source

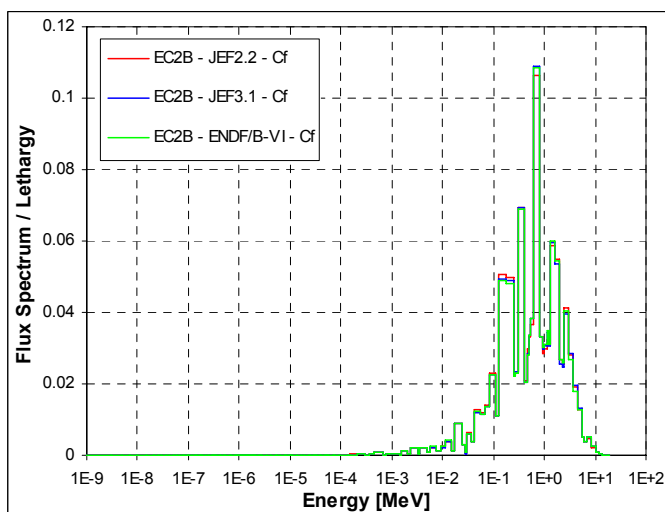


Figure 133. EC2B Neutron Spectra of the YALINA-Booster with Cf Neutron Source

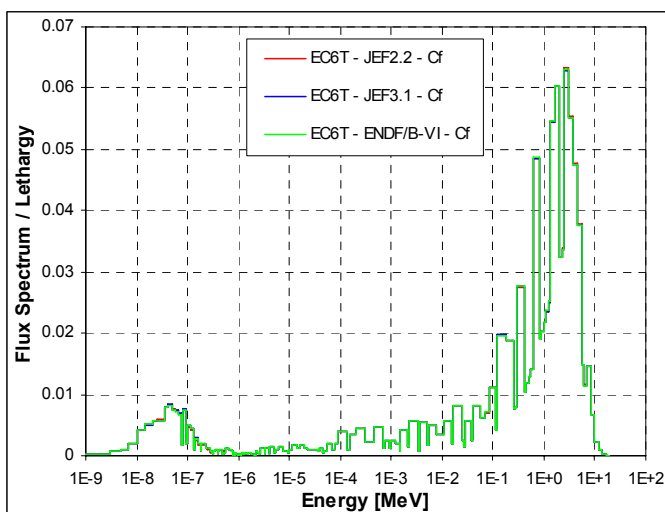


Figure 134. EC6T Neutron Spectra of the YALINA-Booster with Cf Neutron Source

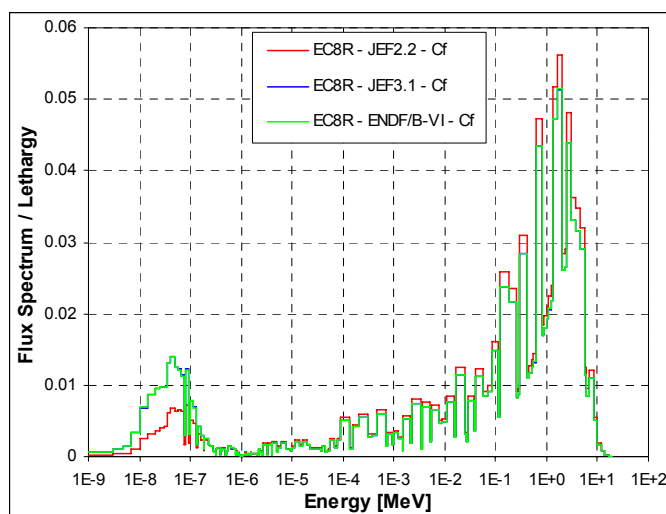


Figure 135. EC8R Neutron Spectra of the YALINA-Booster with Cf Neutron Source

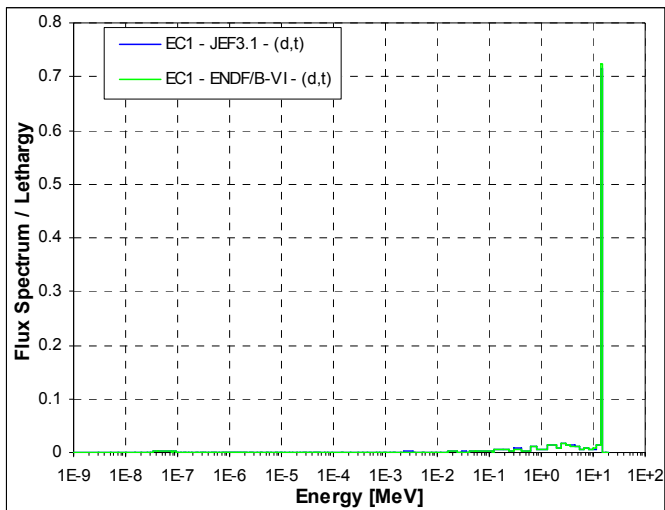


Figure 136. EC1 Neutron Spectra of the YALINA-Thermal with (d,t) Neutron Source

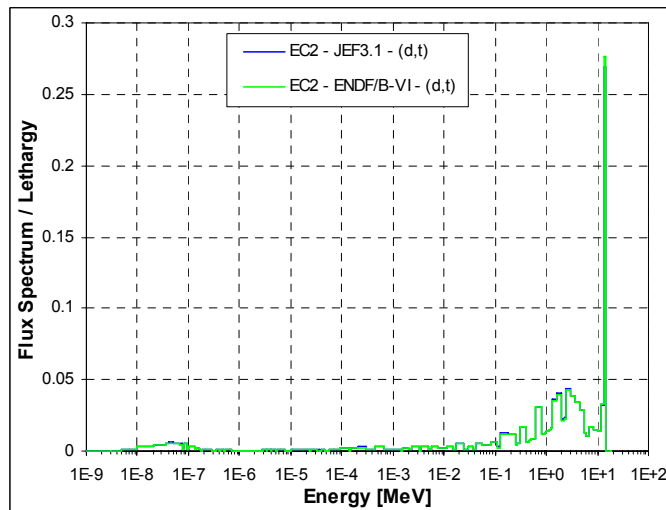


Figure 137. EC2 Neutron Spectra of the YALINA-Thermal with (d,t) Neutron Source

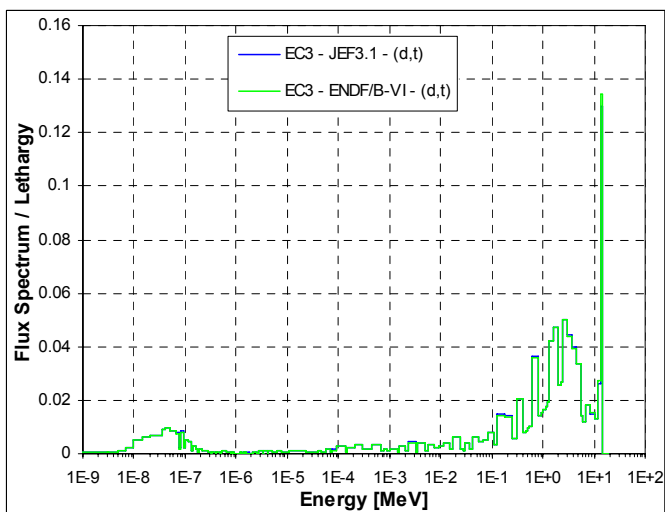


Figure 138. EC3 Neutron Spectra of the YALINA-Thermal with (d,t) Neutron Source

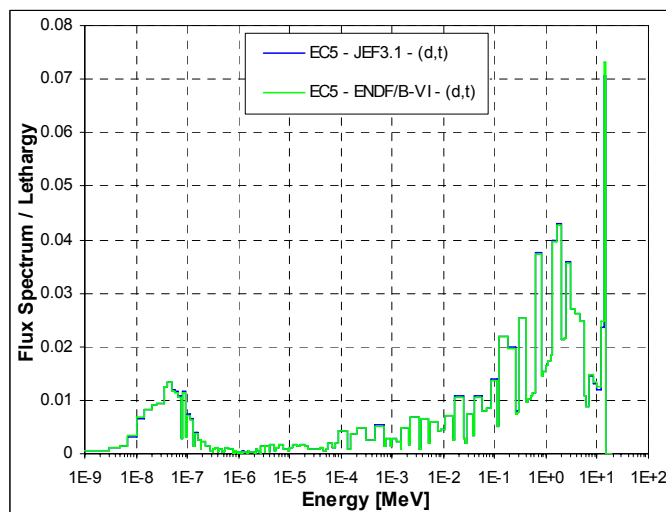


Figure 139. EC5 Neutron Spectra of the YALINA-Thermal with (d,t) Neutron Source

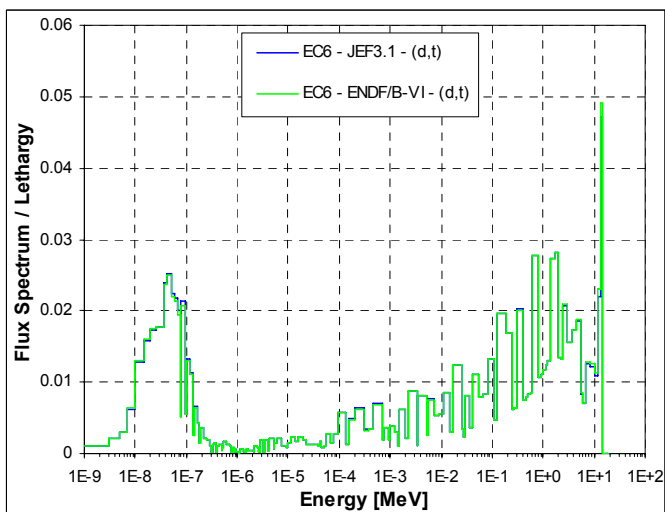


Figure 140. EC6 Neutron Spectra of the YALINA-Thermal with (d,t) Neutron Source

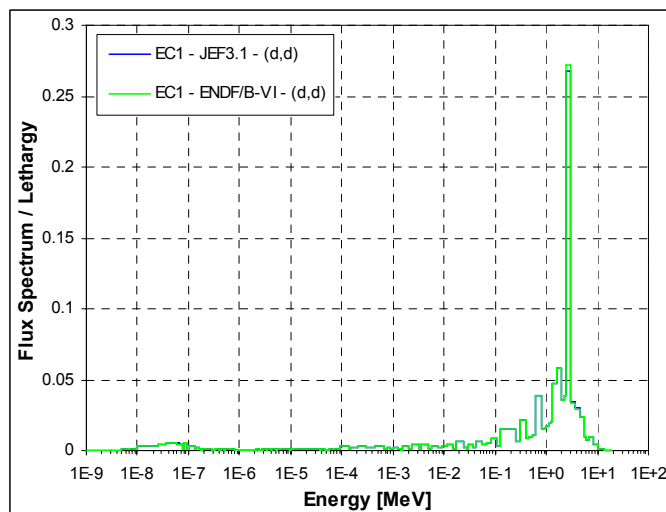


Figure 141. EC1 Neutron Spectra of the YALINA-Thermal with (d,d) Neutron Source

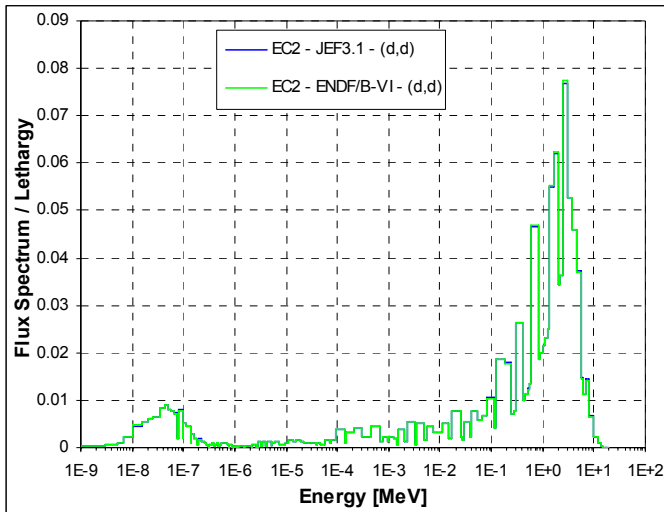


Figure 142. EC2 Neutron Spectra of the YALINA-Thermal with (d,d) Neutron Source

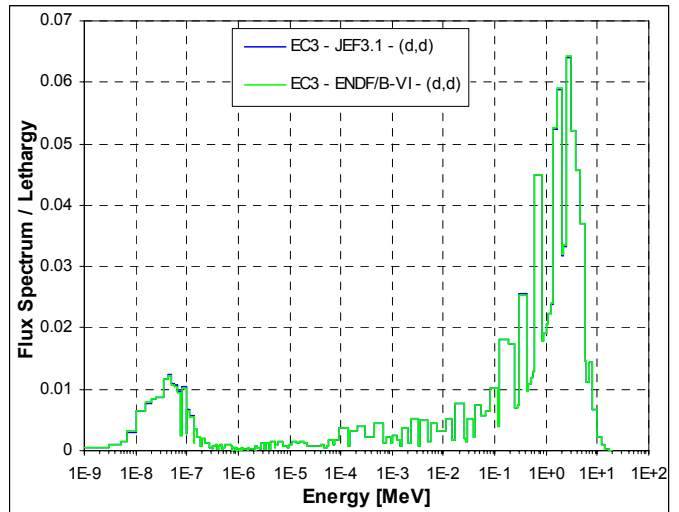


Figure 143. EC3 Neutron Spectra of the YALINA-Thermal with (d,d) Neutron Source

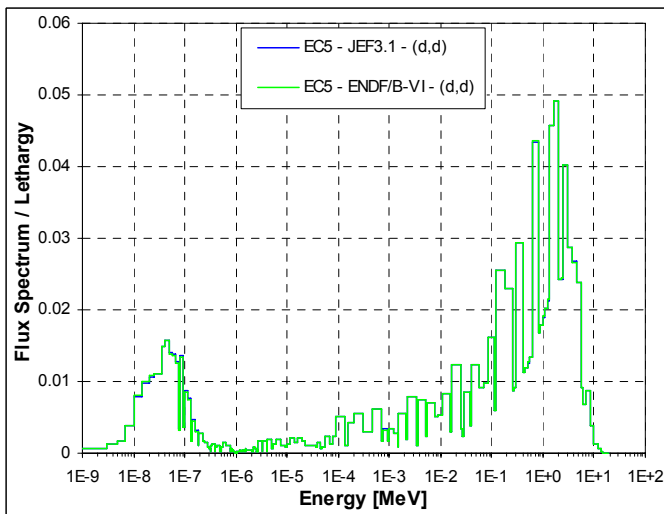


Figure 144. EC5 Neutron Spectra of the YALINA-Thermal with (d,d) Neutron Source

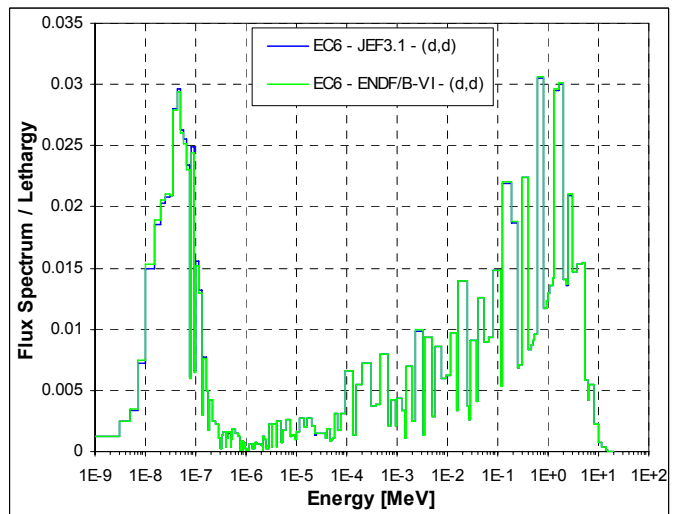


Figure 145. EC6 Neutron Spectra of the YALINA-Thermal with (d,d) Neutron Source

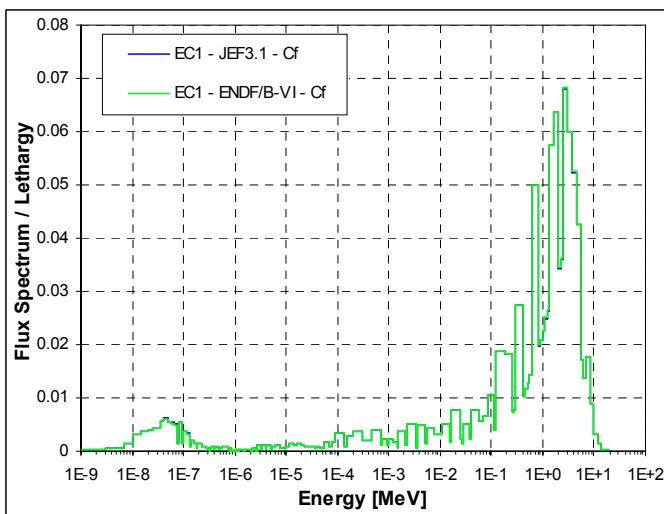


Figure 146. EC1 Neutron Spectra of the YALINA-Thermal with Cf Neutron Source

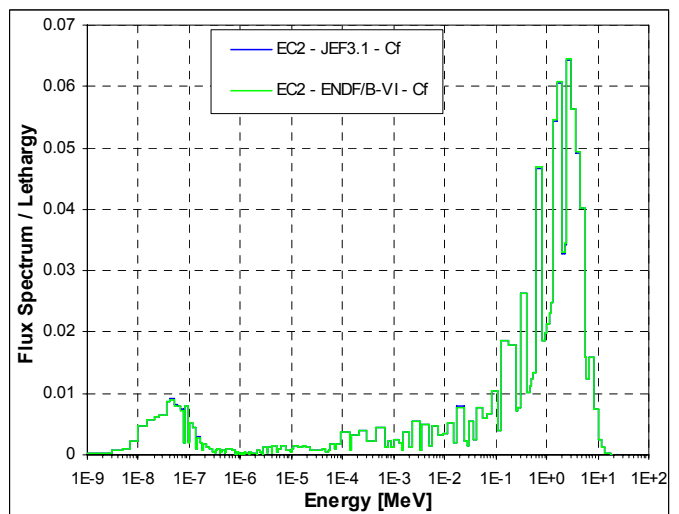


Figure 147. EC2 Neutron Spectra of the YALINA-Thermal with Cf Neutron Source

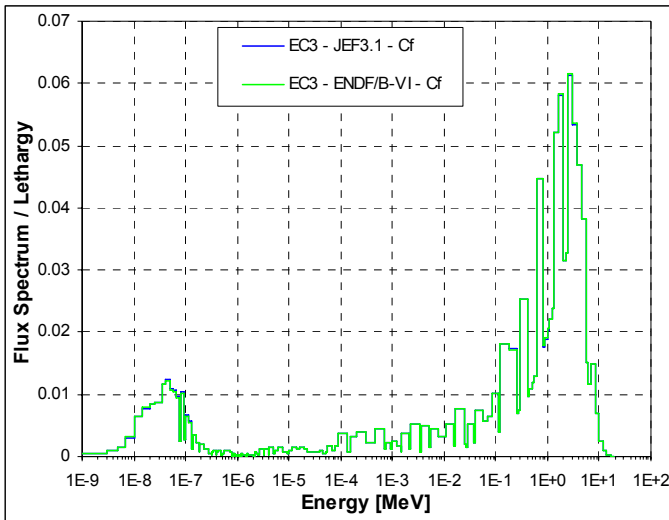


Figure 148. EC3 Neutron Spectra of the YALINA-Thermal with Cf Neutron Source

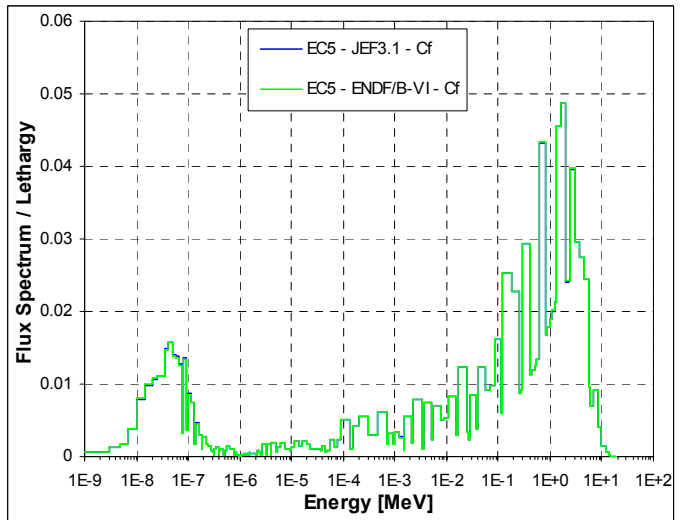


Figure 149. EC5 Neutron Spectra of the YALINA-Thermal with Cf Neutron Source

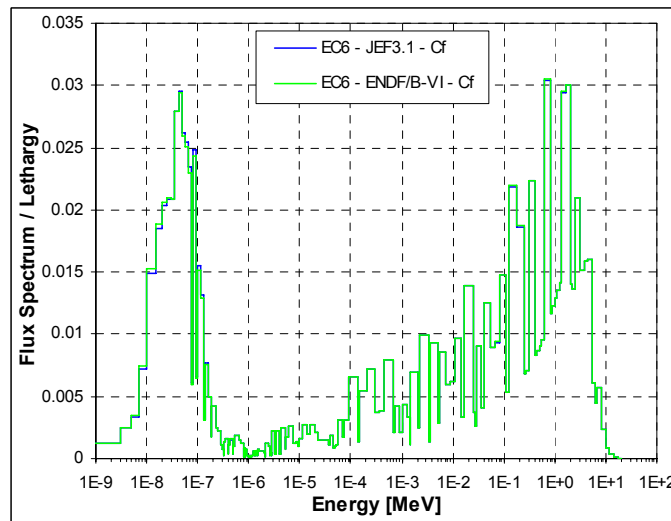


Figure 150. EC6 Neutron Spectra of the YALINA-Thermal with Cf Neutron Source

Appendix G

Comparison of Reaction Rates Calculated with Different Nuclear Data Libraries

G.1. YALINA-Booster

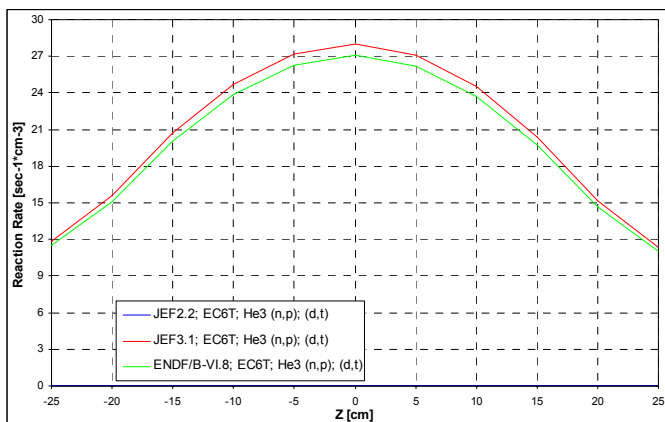


Figure 151. He-3(n,p) Reaction Rate in EC6T Experimental Channel of the YALINA-Booster with (d,t) Source

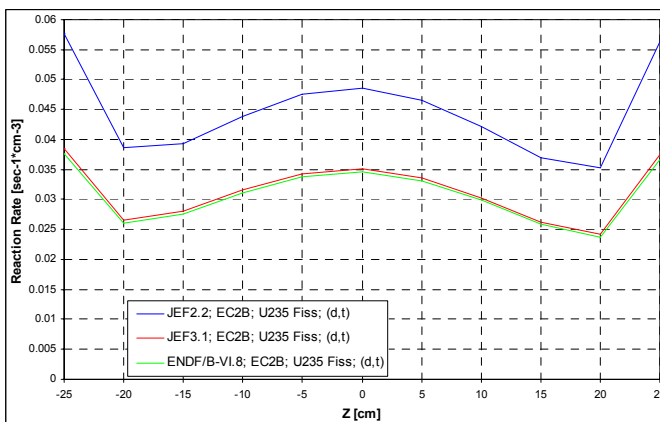


Figure 152. U-235 Fission Reaction Rate in EC2B Experimental Channel of the YALINA-Booster with (d,t) Source

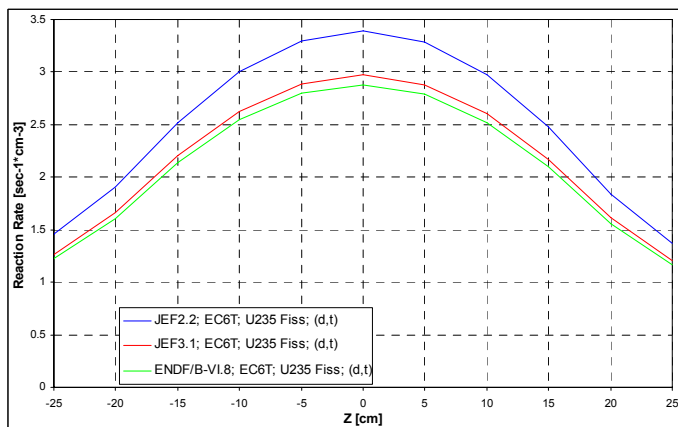


Figure 153. U-235 Fission Reaction Rate in EC6T Experimental Channel of the YALINA-Booster with (d,t) Source

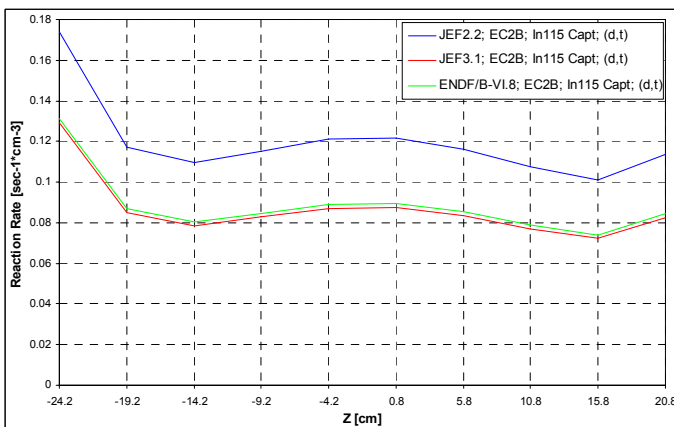


Figure 154. In-115 Capture Reaction Rate in EC2B Experimental Channel of the YALINA-Booster with (d,t) Source. Lead Holder is Modeled

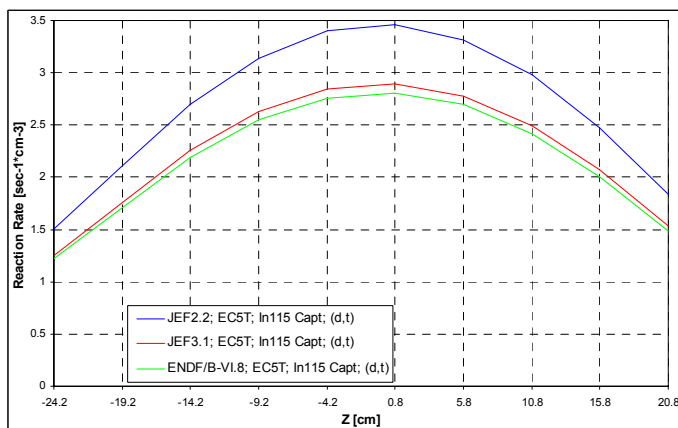


Figure 155. In-115 Capture Reaction Rate in EC5T Experimental Channel of the YALINA-Booster with (d,t) Source. Polyethylene Holder is Modeled

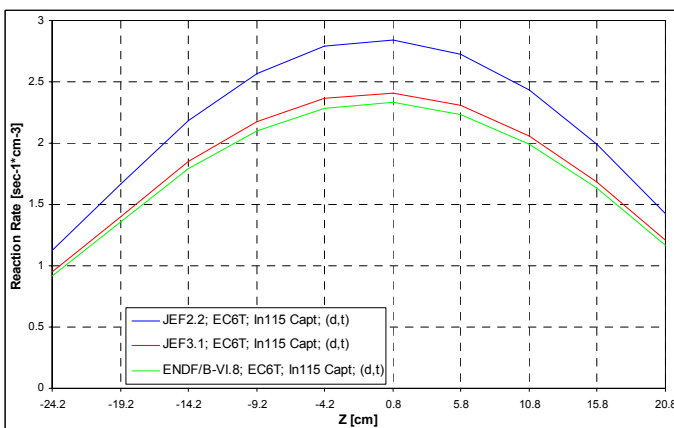


Figure 156. In-115 Capture Reaction Rate in EC6T Experimental Channel of the YALINA-Booster with (d,t) Source. Polyethylene Holder is Modeled

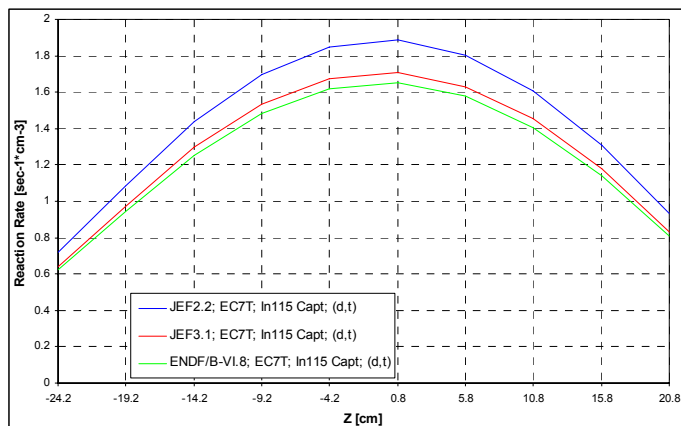


Figure 157. In-115 Capture Reaction Rate in EC7T Experimental Channel of the YALINA-Booster with (d,t) Source. Polyethylene Holder is Modeled

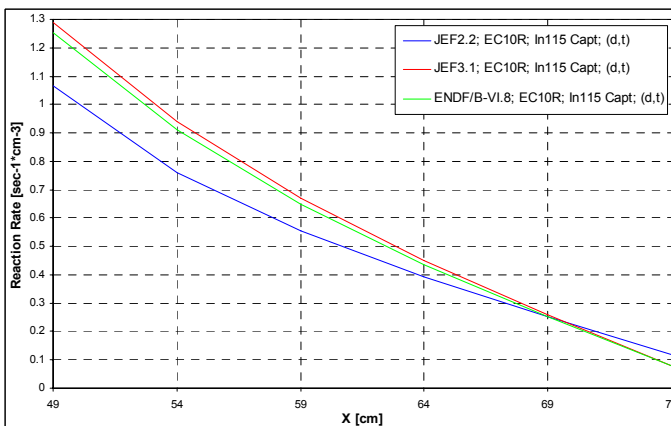


Figure 158. In-115 Capture Reaction Rate in EC10R Experimental Channel of the YALINA-Booster with (d,t) Source. Polyethylene Holder is Modeled

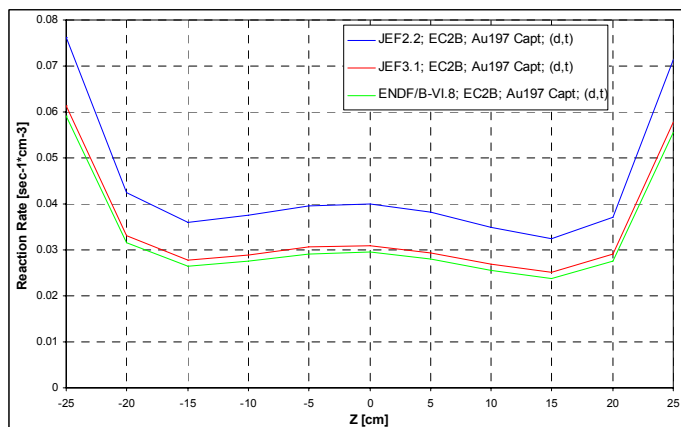


Figure 159. Au-197 Capture Reaction Rate in EC2B Experimental Channel of the YALINA-Booster with (d,t) Source. Lead Holder is Modeled

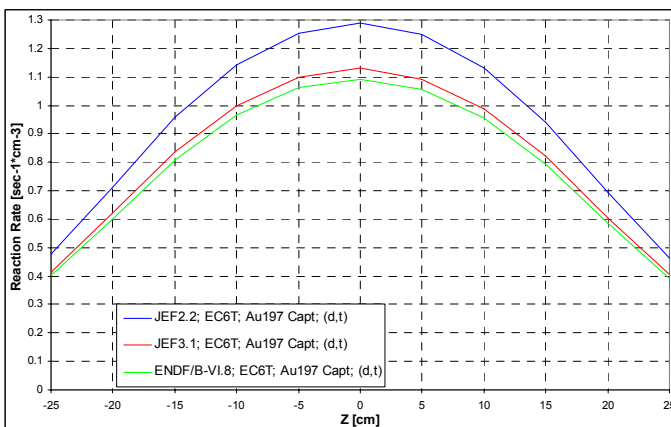


Figure 160. Au-197 Capture Reaction Rate in EC6T Experimental Channel of the YALINA-Booster with (d,t) Source. Polyethylene Holder is Modeled

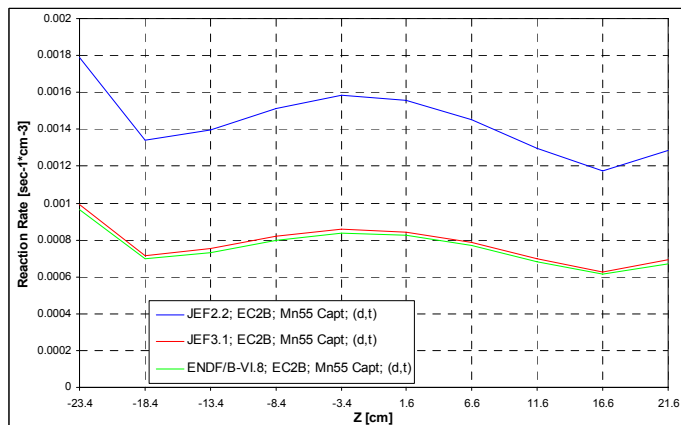


Figure 161. Mn-55 Capture Reaction Rate in EC2B Experimental Channel of the YALINA-Booster with (d,t) Source. Lead Holder is Modeled

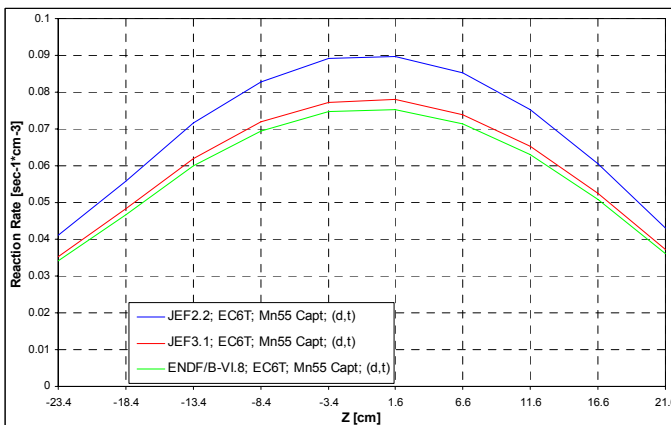


Figure 162. Mn-55 Capture Reaction Rate in EC6T Experimental Channel of the YALINA-Booster with (d,t) Source. Polyethylene Holder is Modeled

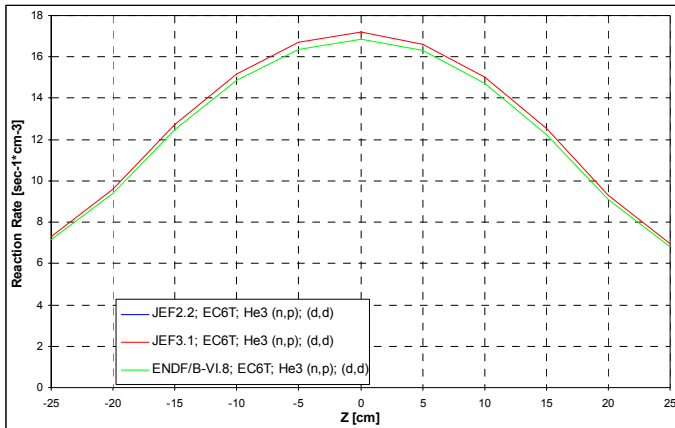


Figure 163. He-3(n,p) Capture Reaction Rate in EC6T Experimental Channel of the YALINA-Booster with (d,d) Source

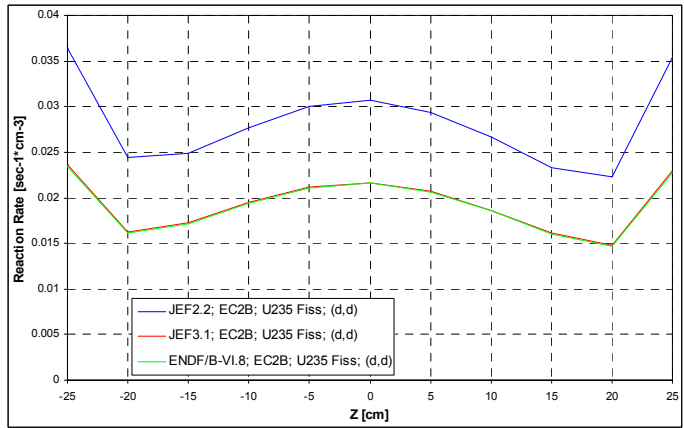


Figure 164. U-235 Fission Capture Reaction Rate in EC2B Experimental Channel of the YALINA-Booster with (d,d) Source

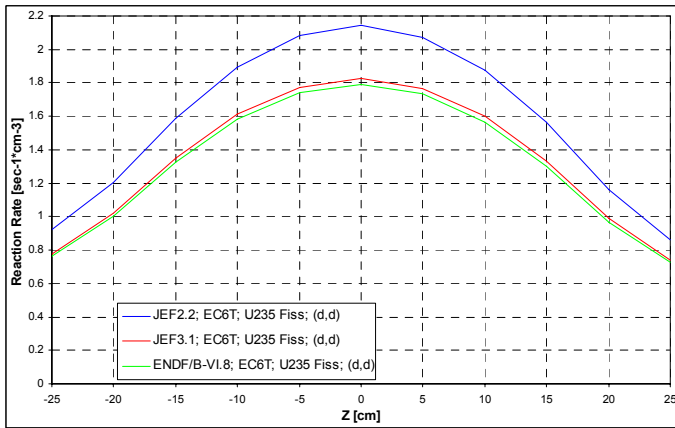


Figure 165. U-235 Fission Capture Reaction Rate in EC6T Experimental Channel of the YALINA-Booster with (d,d) Source

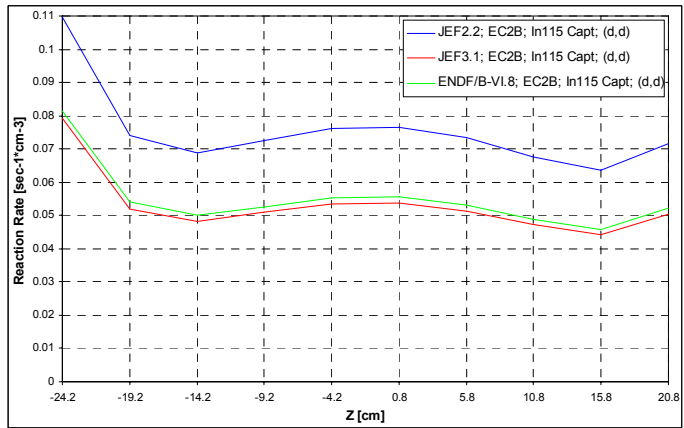


Figure 166. In-115 Capture Reaction Rate in EC2B Experimental Channel of the YALINA-Booster with (d,d) Source. Lead Holder is Modeled

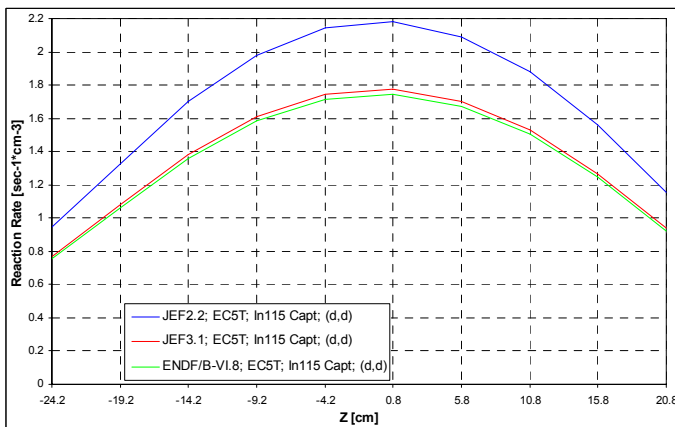


Figure 167. In-115 Capture Reaction Rate in EC5T Experimental Channel of the YALINA-Booster with (d,d) Source. Polyethylene Holder is Modeled

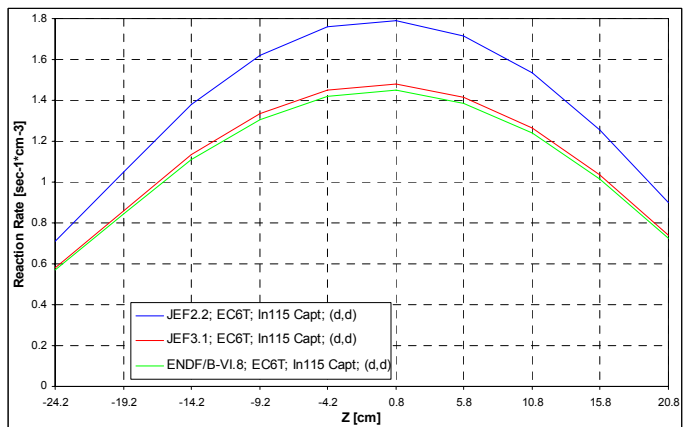


Figure 168. In-115 Capture Reaction Rate in EC6T Experimental Channel of the YALINA-Booster with (d,d) Source. Polyethylene Holder is Modeled

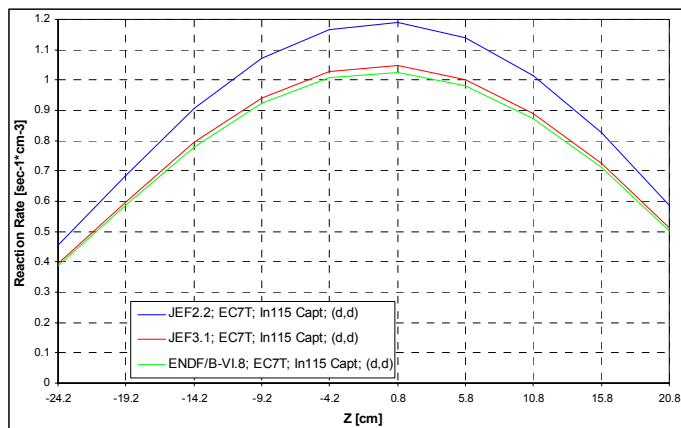


Figure 169. In-115 Capture Reaction Rate in EC7T Experimental Channel of the YALINA-Booster with (d,d) Source. Polyethylene Holder is Modeled

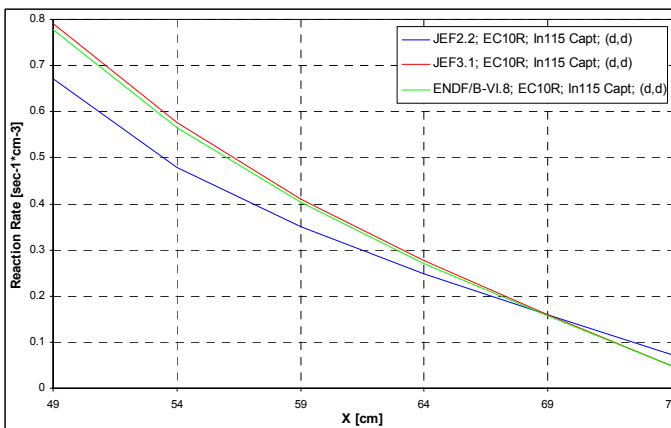


Figure 170. In-115 Capture Reaction Rate in EC10R Experimental Channel of the YALINA-Booster with (d,d) Source. Polyethylene Holder is Modeled

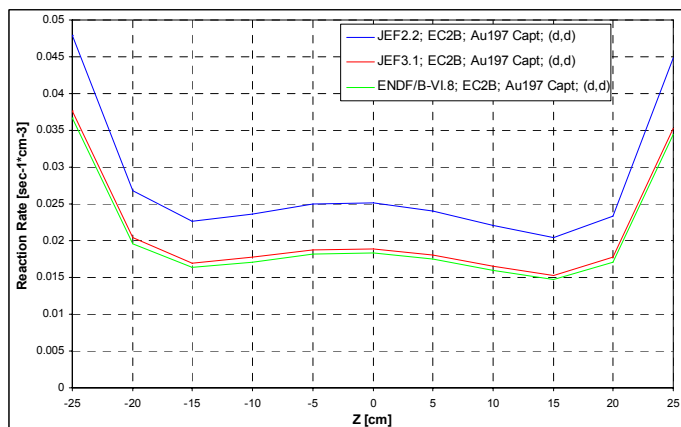


Figure 171. Au-197 Capture Reaction Rate in EC2B Experimental Channel of the YALINA-Booster with (d,d) Source. Lead Holder is Modeled

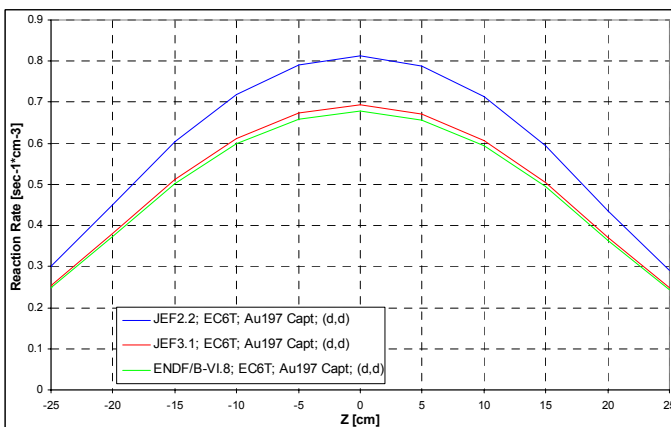


Figure 172. Au-197 Capture Reaction Rate in EC6T Experimental Channel of the YALINA-Booster with (d,d) Source. Polyethylene Holder is Modeled

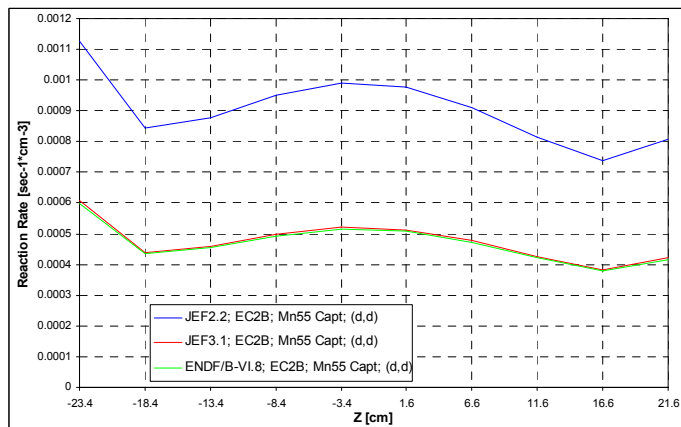


Figure 173. Mn-55 Capture Reaction Rate in EC2B Experimental Channel of the YALINA-Booster with (d,d) Source. Lead Holder is Modeled

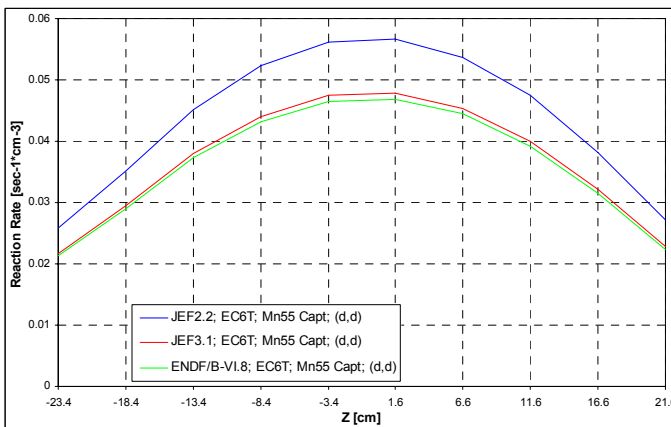


Figure 174. Mn-55 Capture Reaction Rate in EC6T Experimental Channel of the YALINA-Booster with (d,d) Source. Polyethylene Holder is Modeled

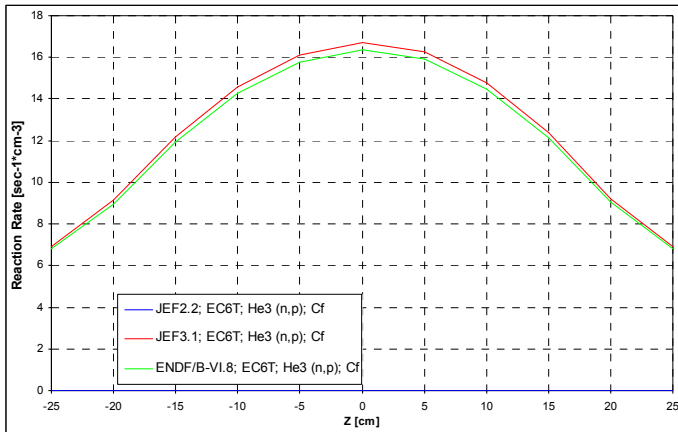


Figure 175. He-3(n,p) Reaction Rate in EC6T Experimental Channel of the YALINA-Booster with Cf Neutron Source

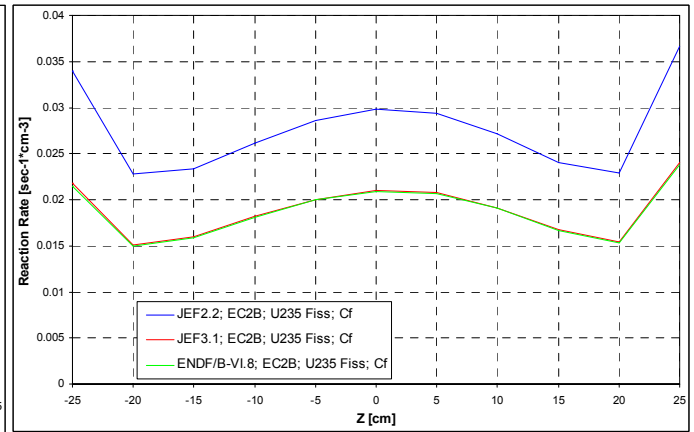


Figure 176. U-235 Fission Reaction Rate in EC2B Experimental Channel of the YALINA-Booster with Cf Neutron Source

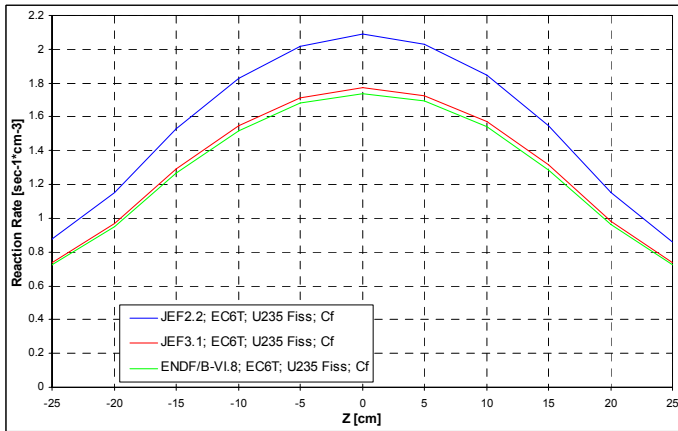


Figure 177. U-235 Fission Reaction Rate in EC6T Experimental Channel of the YALINA-Booster with Cf Neutron Source

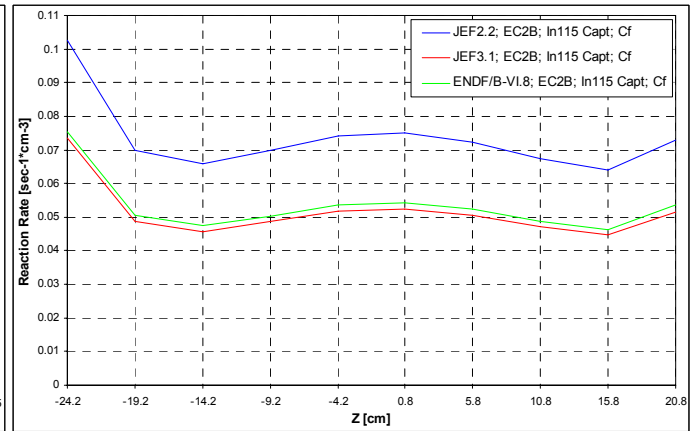


Figure 178. In-115 Capture Reaction Rate in EC2B Experimental Channel of the YALINA-Booster with Cf Neutron Source. Lead Holder is Modeled

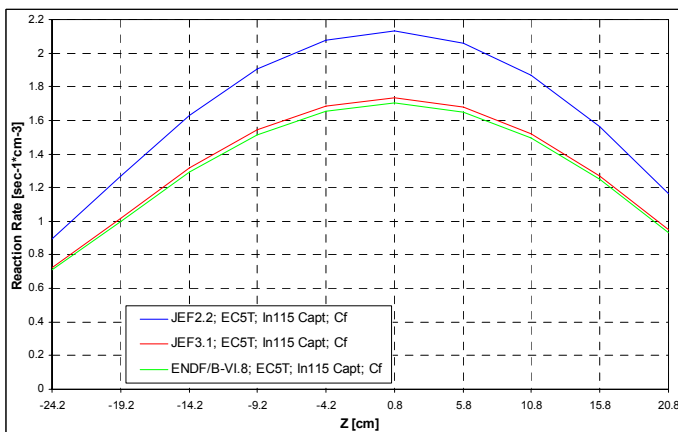


Figure 179. In-115 Capture Reaction Rate in EC5T Experimental Channel of the YALINA-Booster with Cf Neutron Source. Polyethylene Holder is Modeled

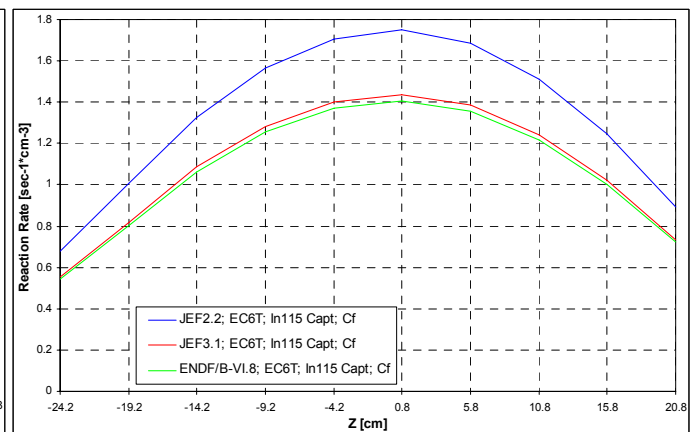


Figure 180. In-115 Capture Reaction Rate in EC6T Experimental Channel of the YALINA-Booster with Cf Neutron Source. Polyethylene Holder is Modeled

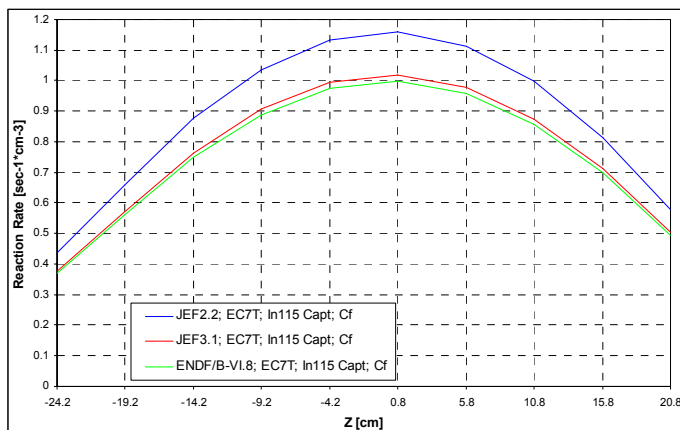


Figure 181. In-115 Capture Reaction Rate in EC7T Experimental Channel of the YALINA-Booster with Cf Neutron Source. Polyethylene Holder is Modeled

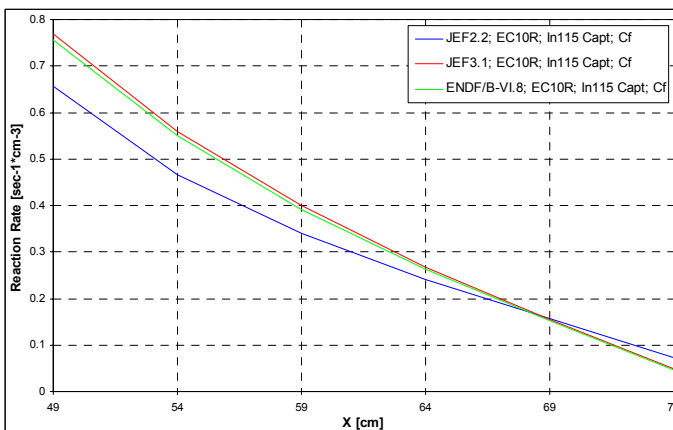


Figure 182. In-115 Capture Reaction Rate in EC10R Experimental Channel of the YALINA-Booster with Cf Neutron Source. Polyethylene Holder is Modeled

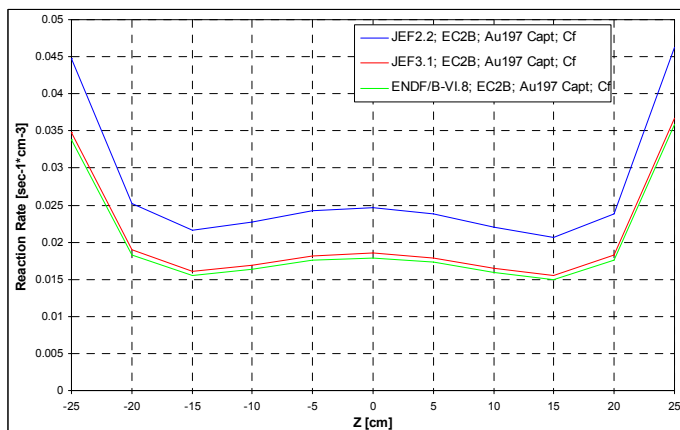


Figure 183. Au-197 Capture Reaction Rate in EC2B Experimental Channel of the YALINA-Booster with Cf Neutron Source. Lead Holder is Modeled

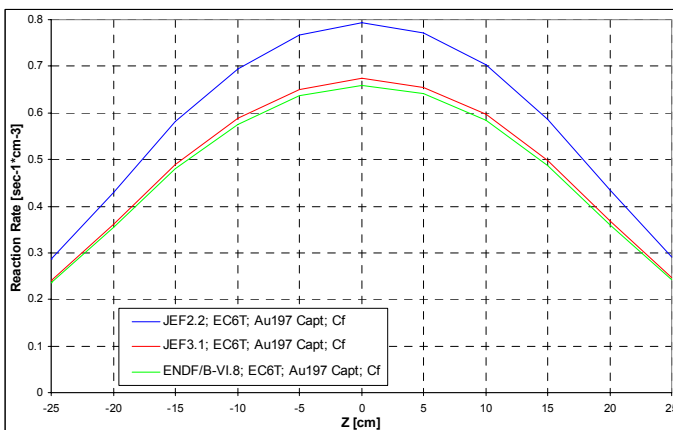


Figure 184. Au-197 Capture Reaction Rate in EC6T Experimental Channel of the YALINA-Booster with Cf Neutron Source. Polyethylene Holder is Modeled

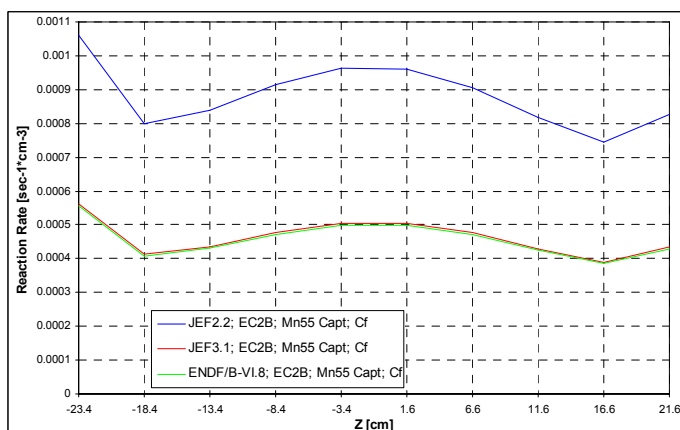


Figure 185. Mn-55 Capture Reaction Rate in EC2B Experimental Channel of the YALINA-Booster with Cf Neutron Source. Lead Holder is Modeled

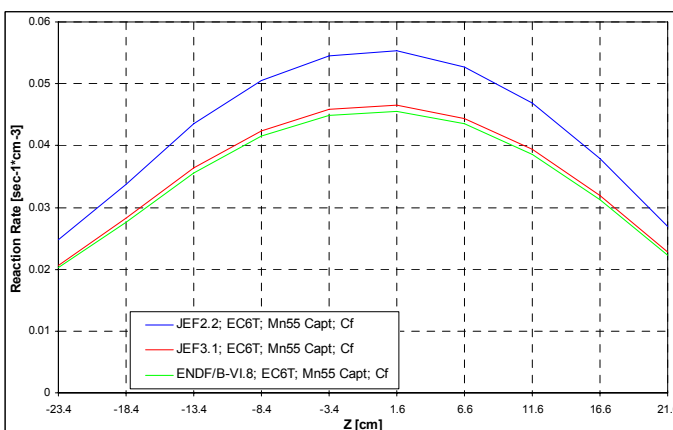


Figure 186. Mn-55 Capture Reaction Rate in EC6T Experimental Channel of the YALINA-Booster with Cf Neutron Source. Polyethylene Holder is Modeled

G.2. YALINA-Thermal

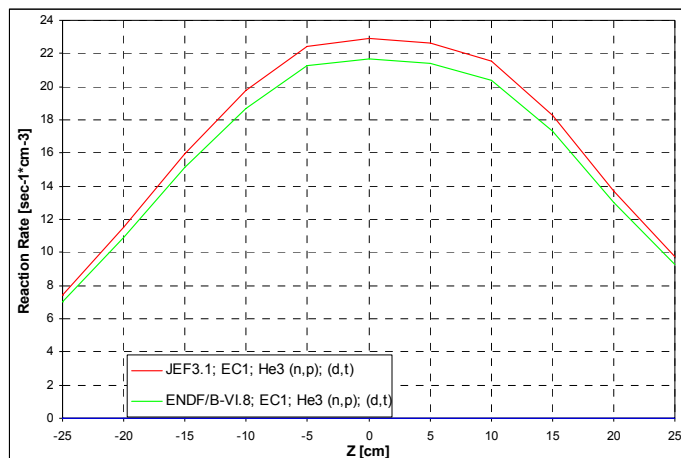


Figure 187. He-3(n,p) Reaction Rate in EC1 Experimental Channel of the YALINA-Thermal with (d,t) Neutron Source

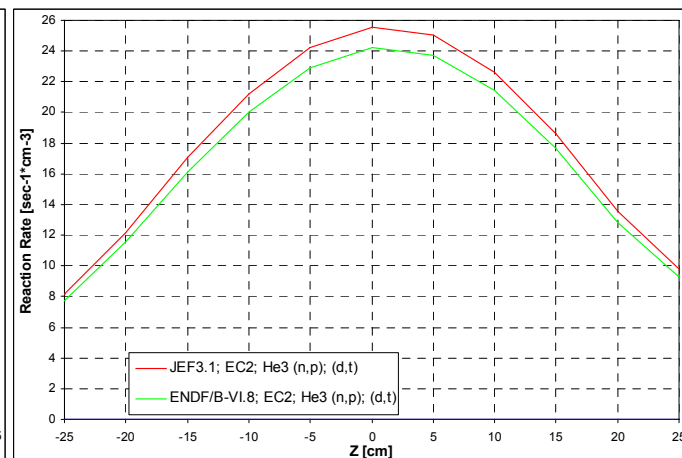


Figure 188. He-3(n,p) Reaction Rate in EC2 Experimental Channel of the YALINA-Thermal with (d,t) Neutron Source

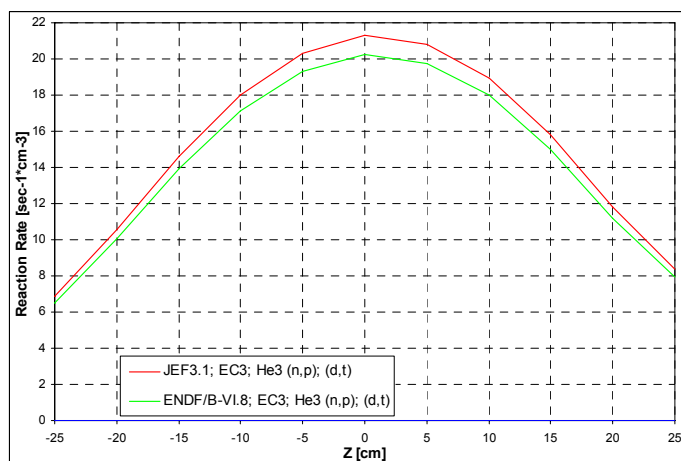


Figure 189. He-3(n,p) Reaction Rate in EC3 Experimental Channel of the YALINA-Thermal with (d,t) Neutron Source

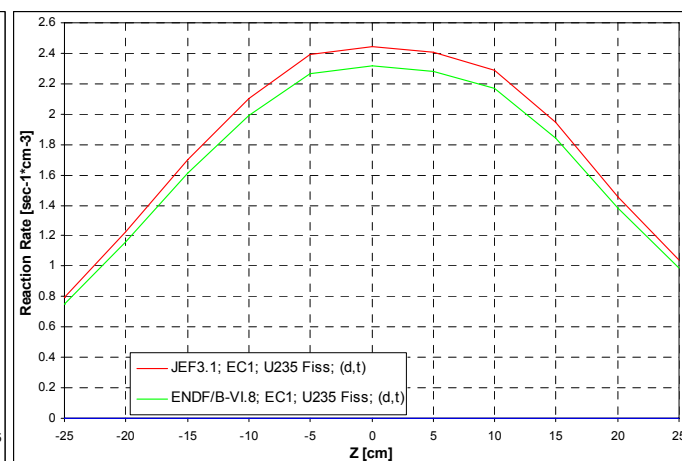


Figure 190. U-235 Fission Reaction Rate in EC1 Experimental Channel of the YALINA-Thermal with (d,t) Neutron Source

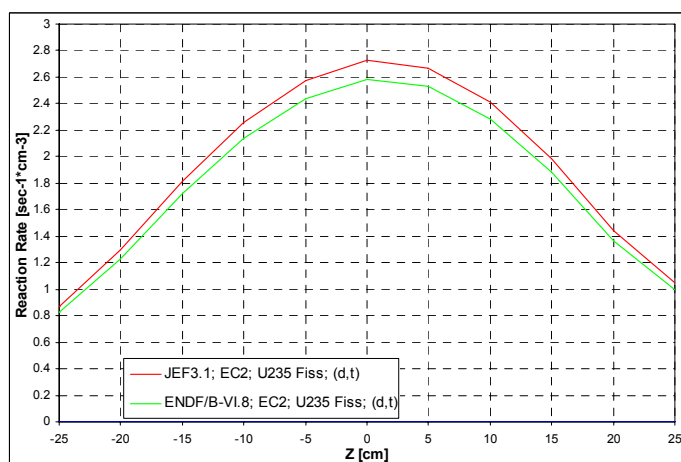


Figure 191. U-235 Fission Reaction Rate in EC2 Experimental Channel of the YALINA-Thermal with (d,t) Neutron Source

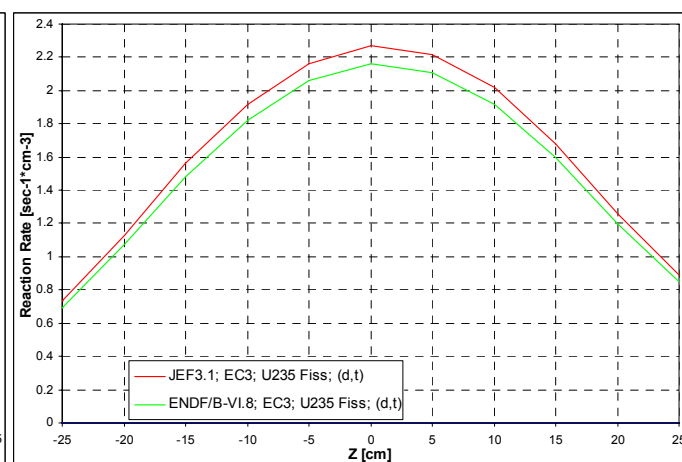


Figure 192. U-235 Fission Reaction Rate in EC3 Experimental Channel of the YALINA-Thermal with (d,t) Neutron Source

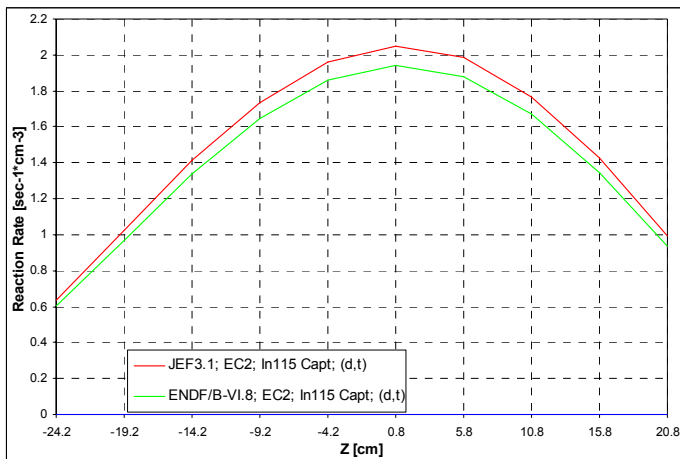


Figure 193. In-115 Capture Reaction Rate in EC2 Experimental Channel of the YALINA-Thermal with (d,t) Neutron Source. Polyethylene Holder is Modeled

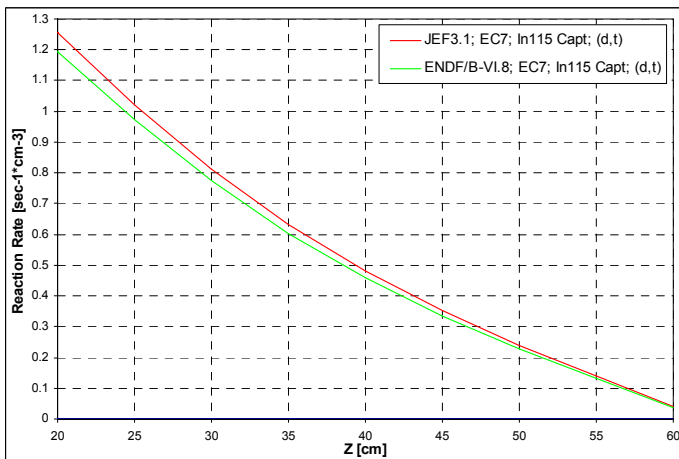


Figure 194. In-115 Capture Reaction Rate in EC7 Experimental Channel of the YALINA-Thermal with (d,t) Neutron Source. Polyethylene Holder is Modeled

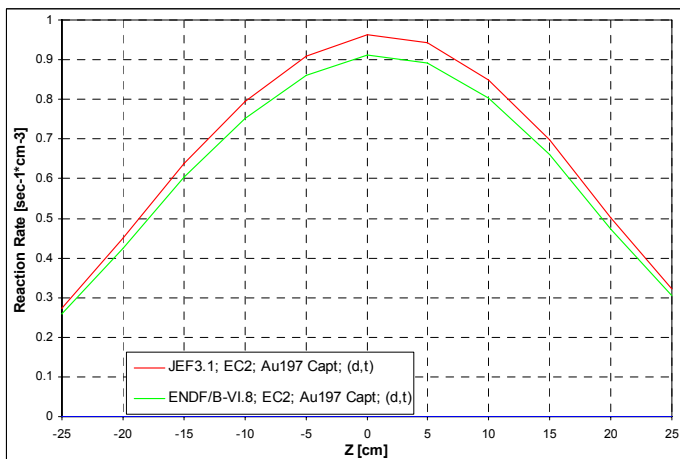


Figure 195. Au-197 Capture Reaction Rate in EC2 Experimental Channel of the YALINA-Thermal with (d,t) Neutron Source. Polyethylene Holder is Modeled

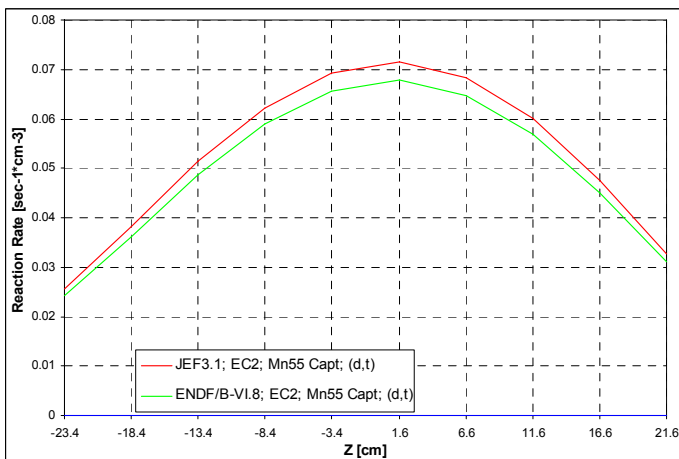


Figure 196. Mn-55 Capture Reaction Rate in EC2 Experimental Channel of the YALINA-Thermal with (d,t) Neutron Source. Polyethylene Holder is Modeled

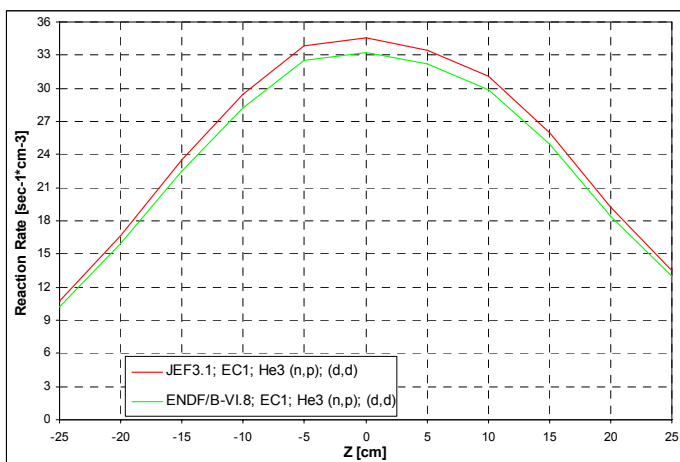


Figure 197. He-3(n,p) Reaction Rate in EC1 Experimental Channel of the YALINA-Thermal with (d,d) Neutron Source

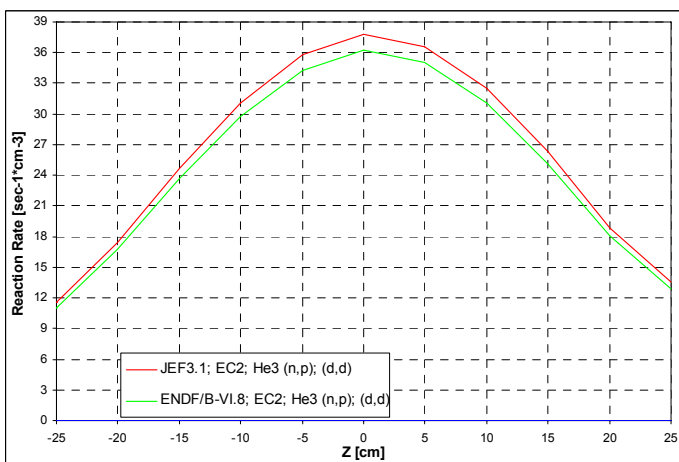


Figure 198. He-3(n,p) Reaction Rate in EC2 Experimental Channel of the YALINA-Thermal with (d,d) Neutron Source

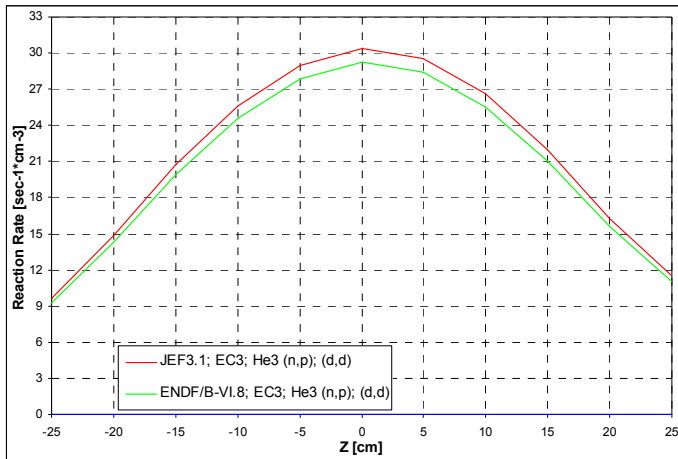


Figure 199. He-3(n,p) Reaction Rate in EC3 Experimental Channel of the YALINA-Thermal with (d,d) Neutron Source

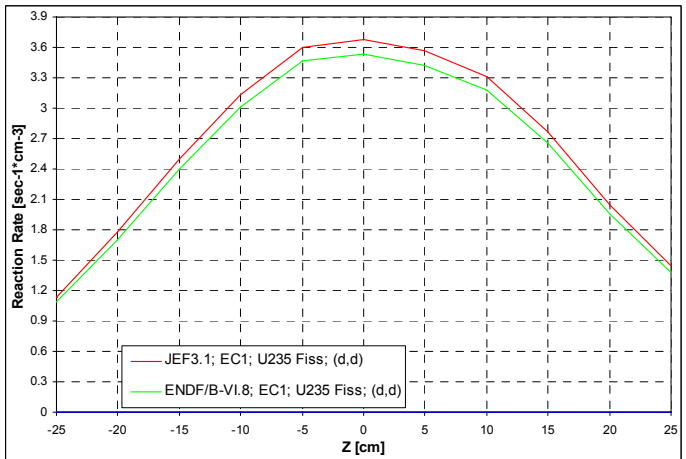


Figure 200. U-235 Fission Reaction Rate in EC1 Experimental Channel of the YALINA-Thermal with (d,d) Neutron Source

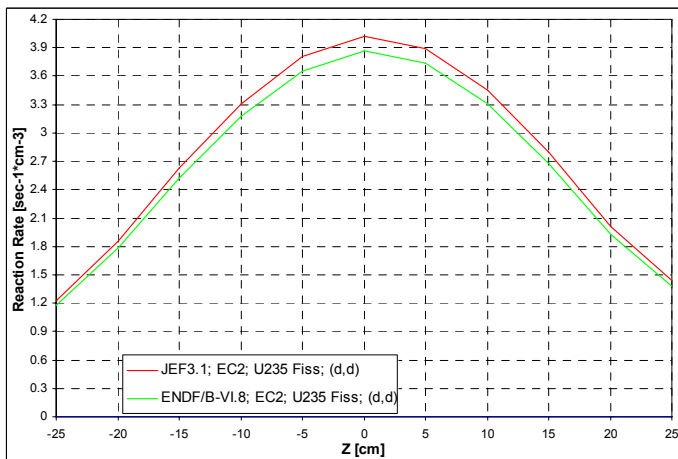


Figure 201. U-235 Fission Reaction Rate in EC2 Experimental Channel of the YALINA-Thermal with (d,d) Neutron Source

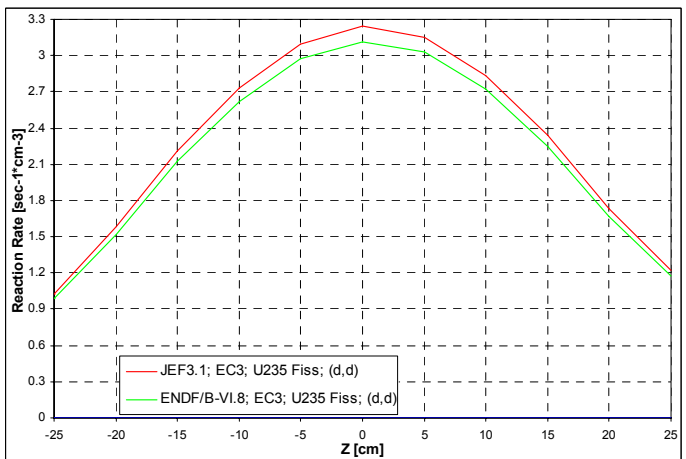


Figure 202. U-235 Fission Reaction Rate in EC3 Experimental Channel of the YALINA-Thermal with (d,d) Neutron Source

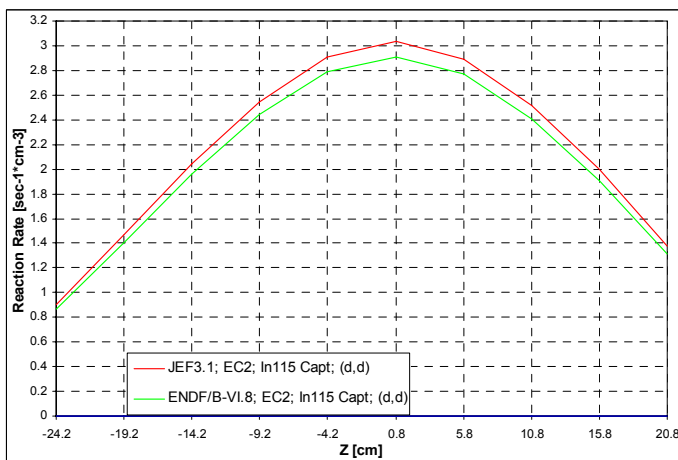


Figure 203. In-115 Capture Reaction Rate in EC2 Experimental Channel of the YALINA-Thermal with (d,d) Neutron Source. Polyethylene Holder is modeled

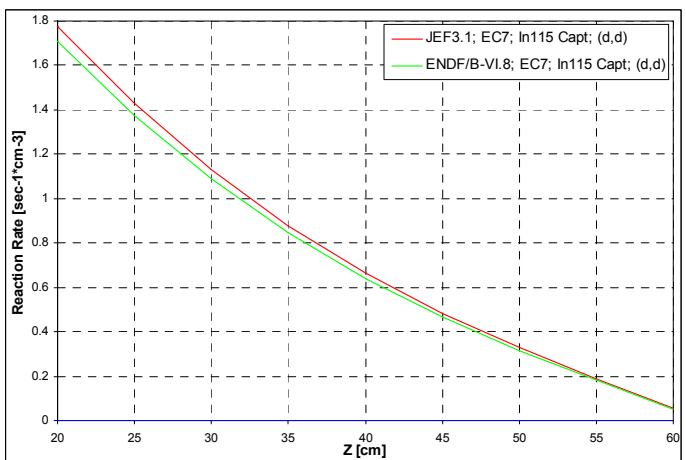


Figure 204. In-115 Capture Reaction Rate in EC7 Experimental Channel of the YALINA-Thermal with (d,d) Neutron Source. Polyethylene Holder is modeled

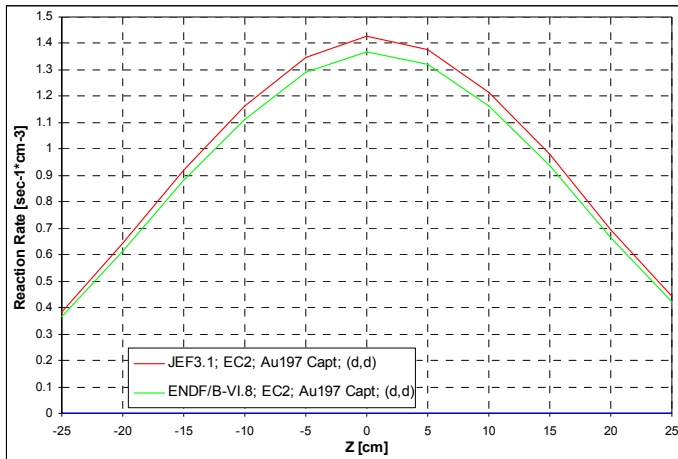


Figure 205. Au-197 Capture Reaction Rate in EC2 Experimental Channel of the YALINA-Thermal with (d,d) Neutron Source. Polyethylene Holder is modeled

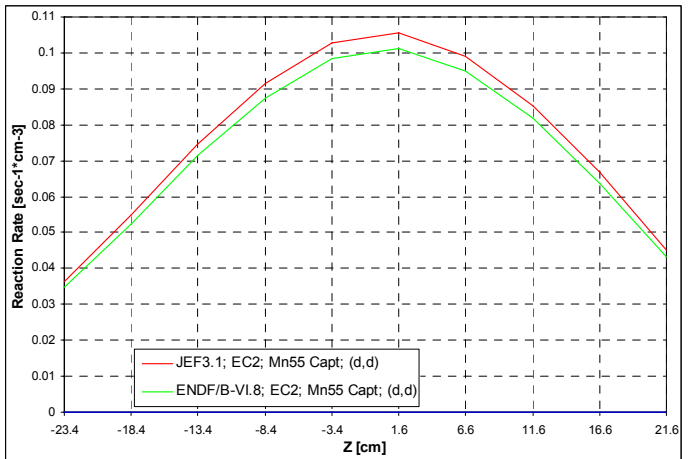


Figure 206. Mn-55 Capture Reaction Rate in EC2 Experimental Channel of the YALINA-Thermal with (d,d) Neutron Source. Polyethylene Holder is modeled

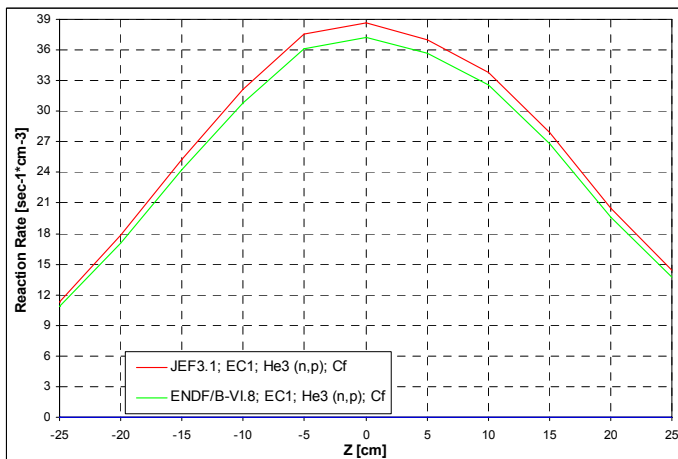


Figure 207. He-3(n,p) Reaction Rate in EC1 Experimental Channel of the YALINA-Thermal with Cf Neutron Source

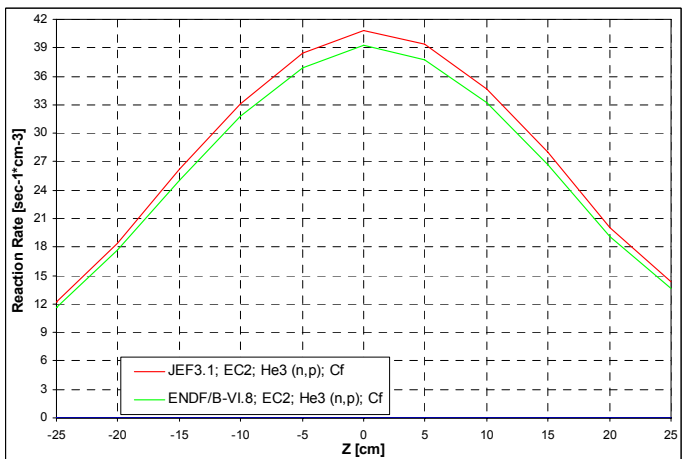


Figure 208. He-3(n,p) Reaction Rate in EC2 Experimental Channel of the YALINA-Thermal with Cf Neutron Source

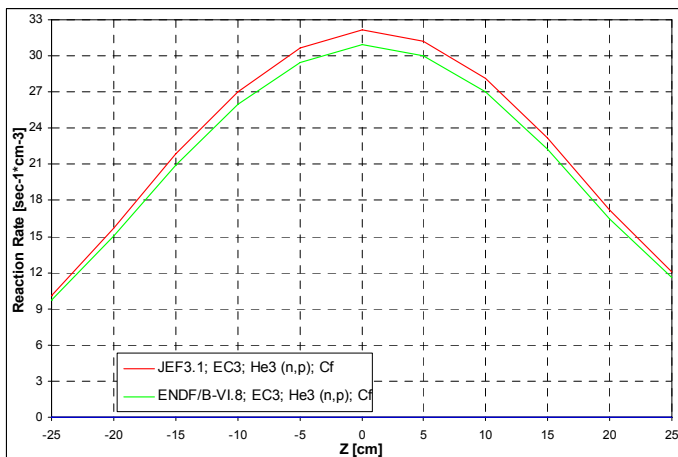


Figure 209. He-3(n,p) Reaction Rate in EC3 Experimental Channel of the YALINA-Thermal with Cf Neutron Source

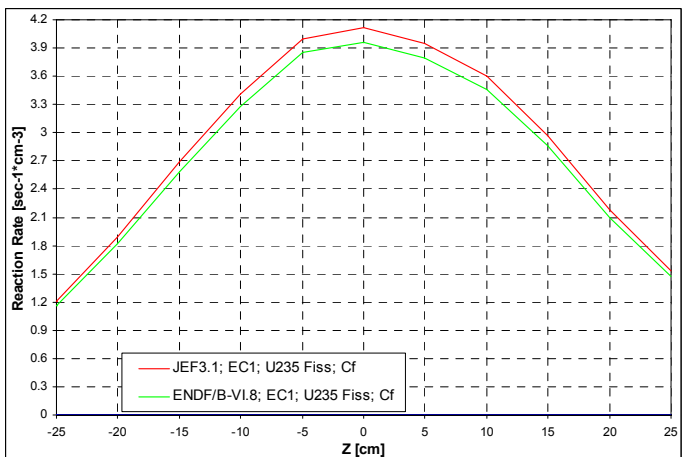


Figure 210. U-235 Fission Reaction Rate in EC1 Experimental Channel of the YALINA-Thermal with Cf Neutron Source

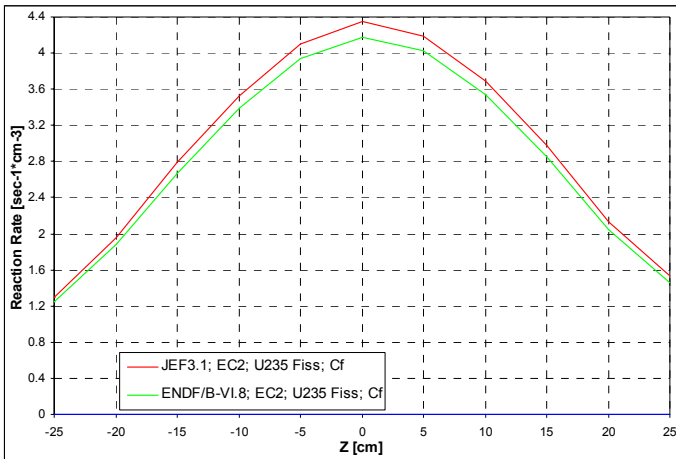


Figure 211. U-235 Fission Reaction Rate in EC2 Experimental Channel of the YALINA-Thermal with Cf Neutron Source

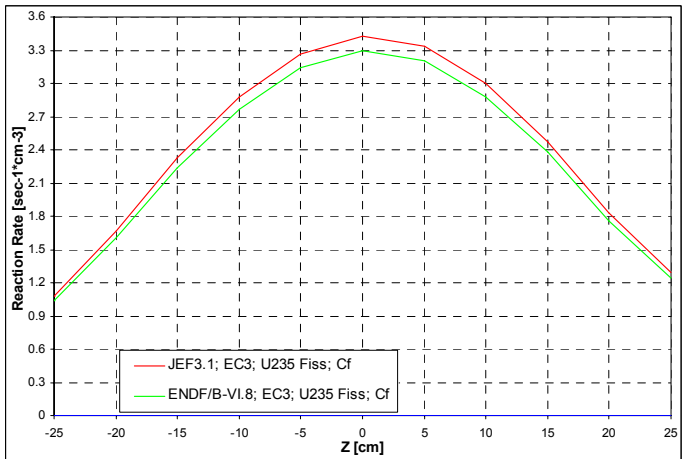


Figure 212. U-235 Fission Reaction Rate in EC3 Experimental Channel of the YALINA-Thermal with Cf Neutron Source

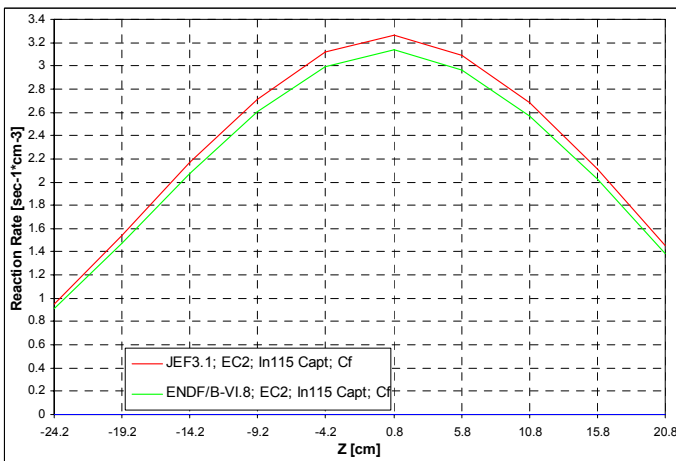


Figure 213. In-115 Capture Reaction Rate in EC2 Experimental Channel of the YALINA-Thermal with Cf Neutron Source. Polyethylene Holder is modeled

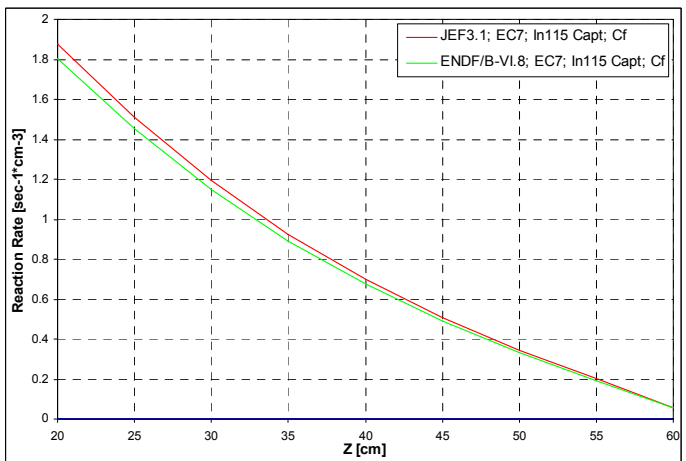


Figure 214. In-115 Capture Reaction Rate in EC7 Experimental Channel of the YALINA-Thermal with Cf Neutron Source. Polyethylene Holder is modeled

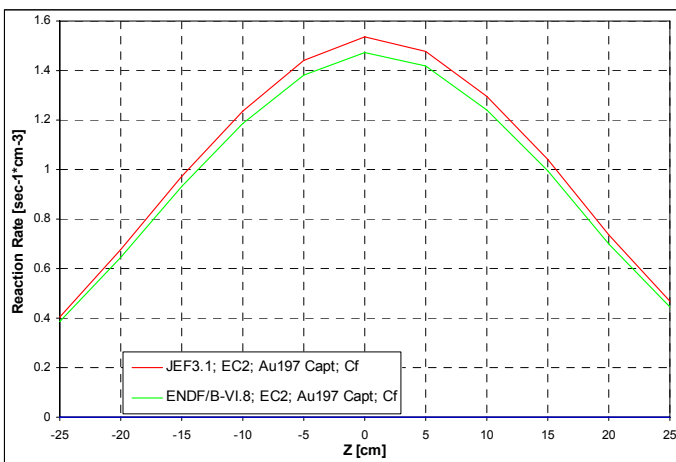


Figure 215. Au-197 Capture Reaction Rate in EC2 Experimental Channel of the YALINA-Thermal with Cf Neutron Source. Polyethylene Holder is modeled

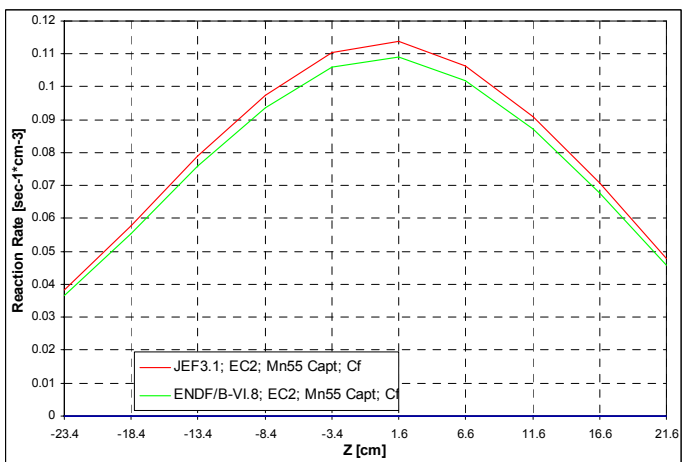


Figure 216. Mn-55 Capture Reaction Rate in EC2 Experimental Channel of the YALINA-Thermal with Cf Neutron Source. Polyethylene Holder is modeled

Appendix H

Comparison with Different Libraries

H.1. ENDF/B-VI.8 Results

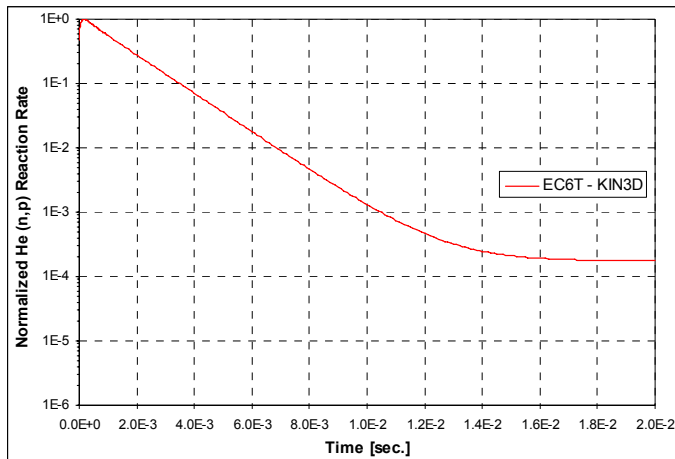


Figure 217. He-3 Detector Response in EC6T Experimental Channel of the YALINA-Booster with (d,t) Neutron Source

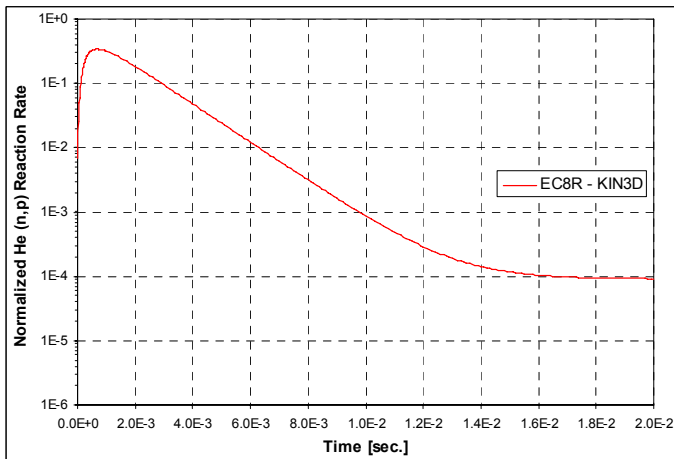


Figure 218. He-3 Detector Response in EC8R Experimental Channel of the YALINA-Booster with (d,t) Neutron Source

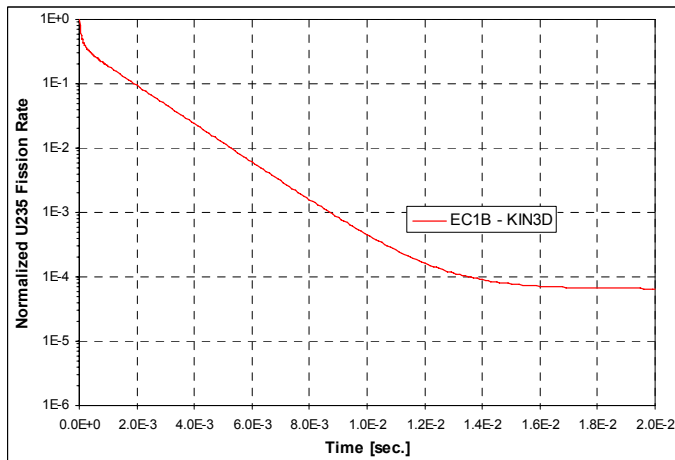


Figure 219. He-3 Detector Response in EC1B Experimental Channel of the YALINA-Booster with (d,t) Neutron Source

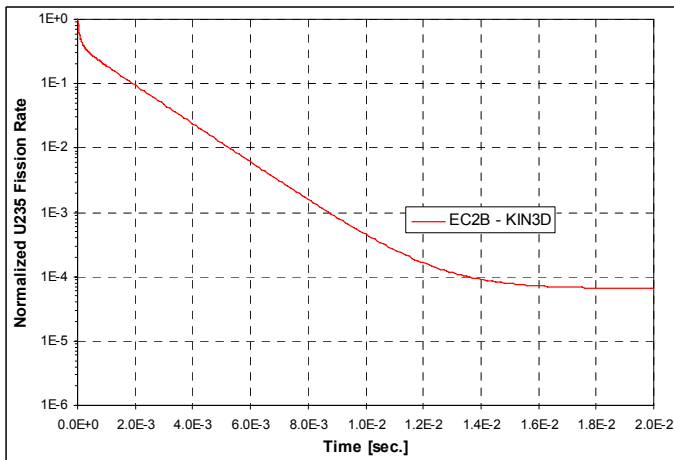


Figure 220. He-3 Detector Response in EC2B Experimental Channel of the YALINA-Booster with (d,t) Neutron Source

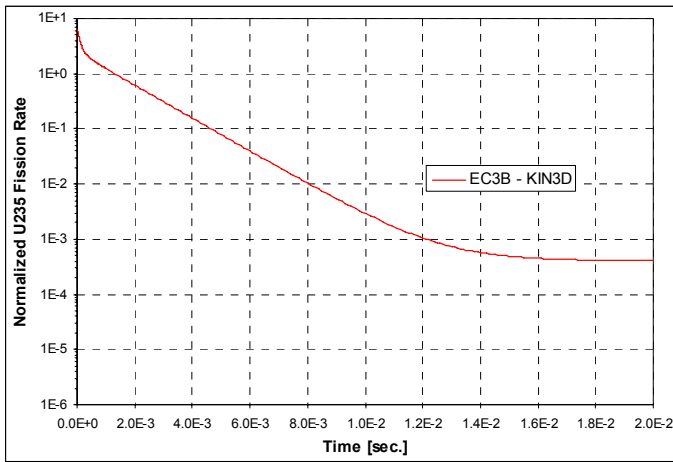


Figure 221. He-3 Detector Response in EC3B Experimental Channel of the YALINA-Booster with (d,t) Neutron Source

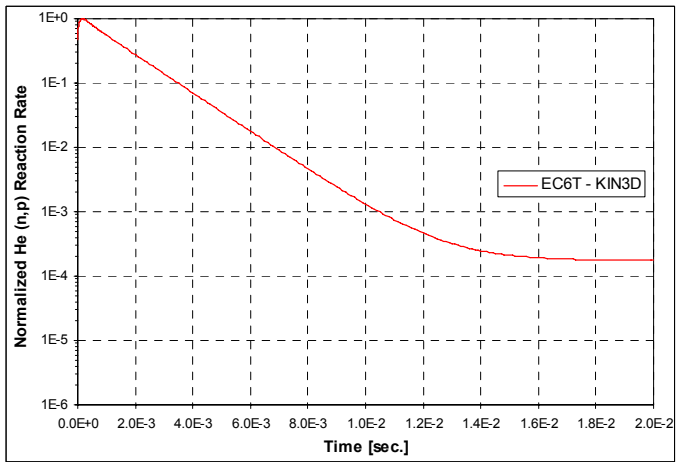


Figure 222. He-3 Detector Response in EC6T Experimental Channel of the YALINA-Booster with (d,d) Neutron Source

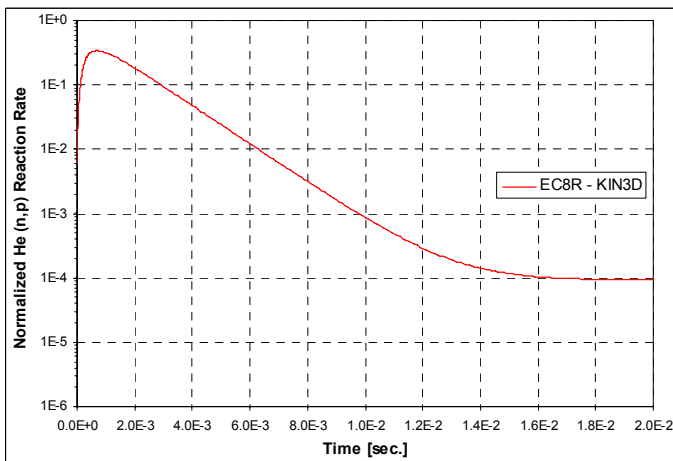


Figure 223. He-3 Detector Response in EC8R Experimental Channel of the YALINA-Booster with (d,d) Neutron Source

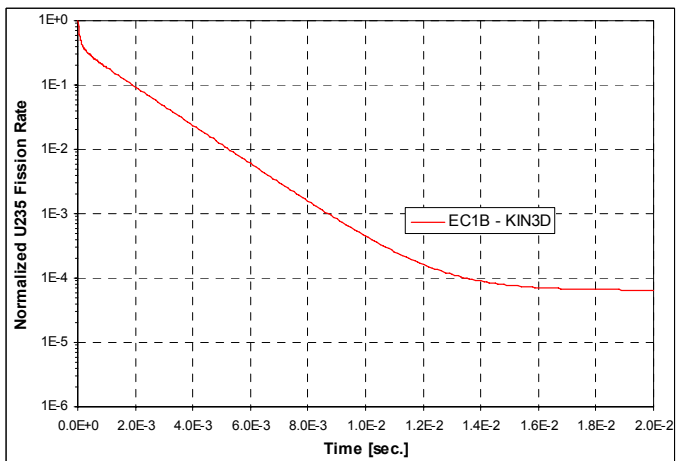


Figure 224. He-3 Detector Response in EC1B Experimental Channel of the YALINA-Booster with (d,d) Neutron Source

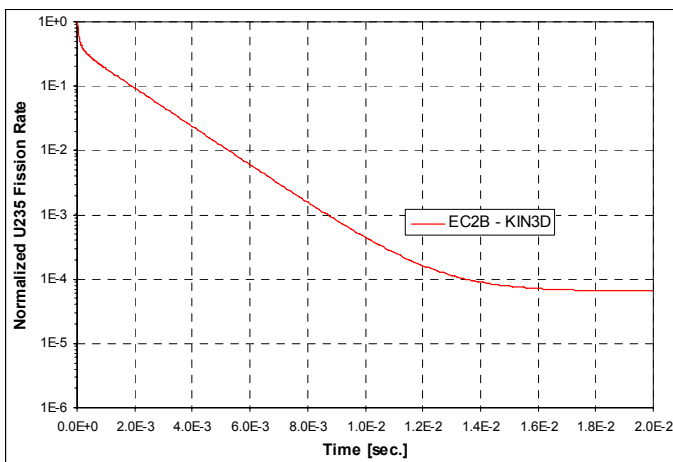


Figure 225. He-3 Detector Response in EC2B Experimental Channel of the YALINA-Booster with (d,d) Neutron Source

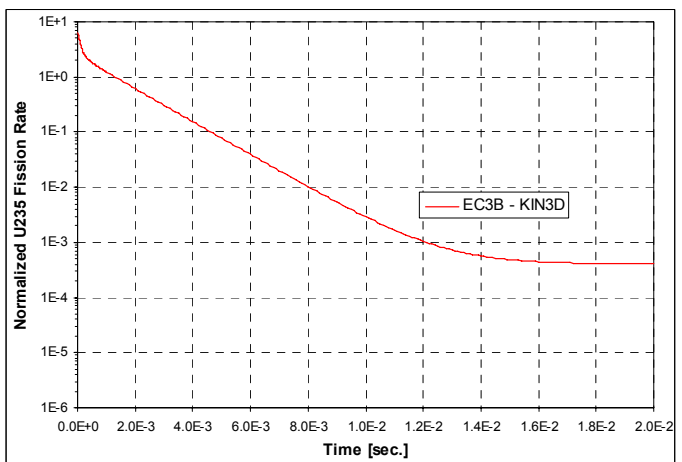


Figure 226. He-3 Detector Response in EC3B Experimental Channel of the YALINA-Booster with (d,d) Neutron Source

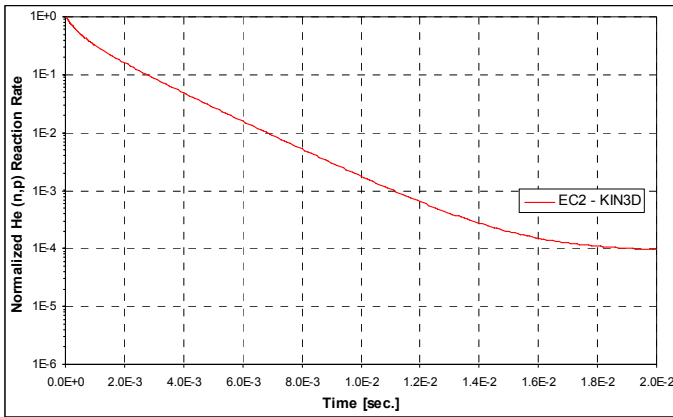


Figure 227. He-3 Detector Response in EC2 Experimental Channel of the YALINA-Thermal with (d,t) Neutron Source

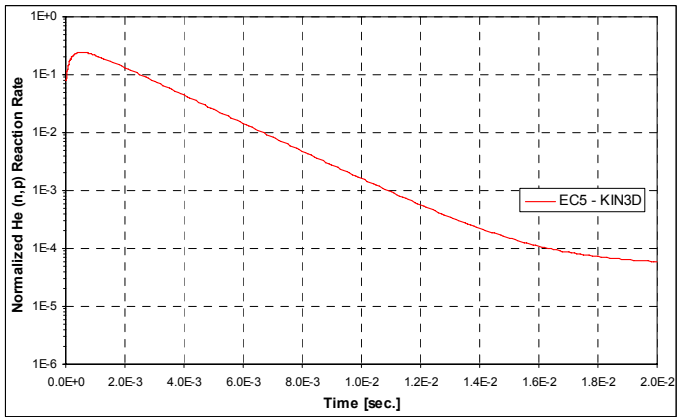


Figure 228. He-3 Detector Response in EC5 Experimental Channel of the YALINA-Thermal with (d,t) Neutron Source

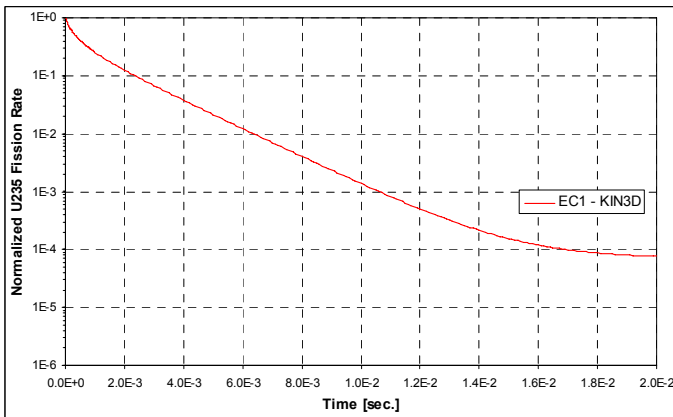


Figure 229. He-3 Detector Response in EC1 Experimental Channel of the YALINA-Thermal with (d,t) Neutron Source

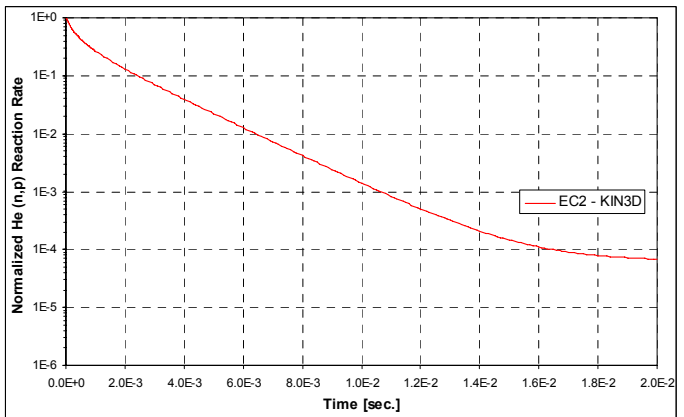


Figure 230. He-3 Detector Response in EC2 Experimental Channel of the YALINA-Thermal with (d,t) Neutron Source

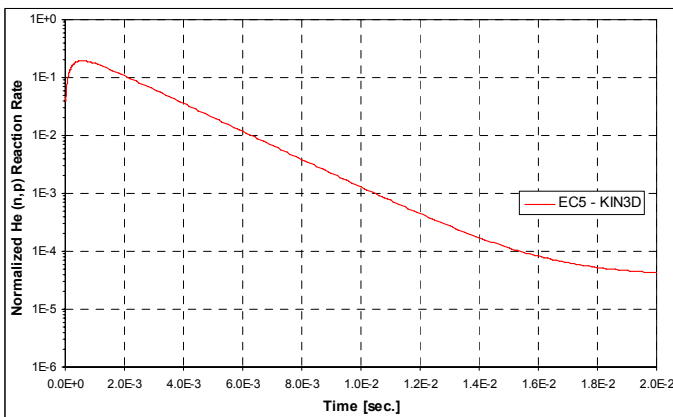


Figure 231. He-3 Detector Response in EC5 Experimental Channel of the YALINA-Thermal with (d,d) Neutron Source

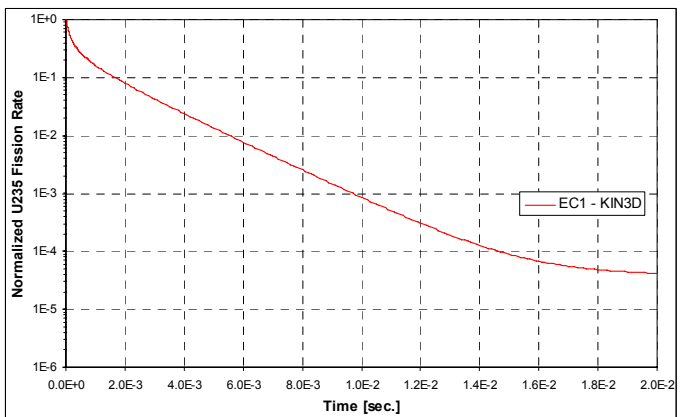


Figure 232. He-3 Detector Response in EC1 Experimental Channel of the YALINA-Thermal with (d,d) Neutron Source

H.2. Use of JEF2.2

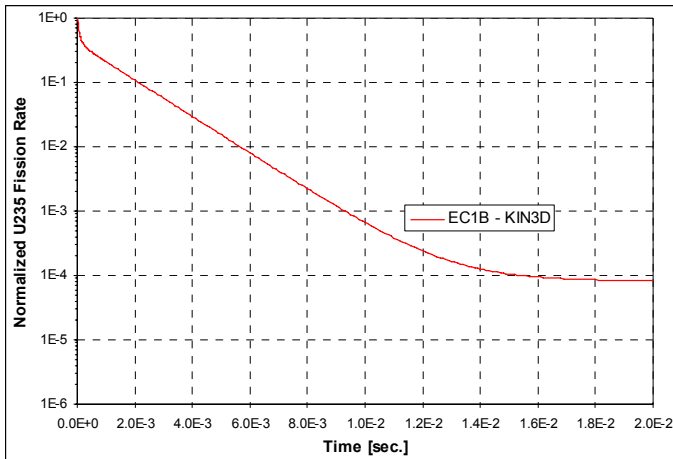


Figure 233. He-3 Detector Response in EC1B Experimental Channel of the YALINA-Booster with (d,t) Neutron Source

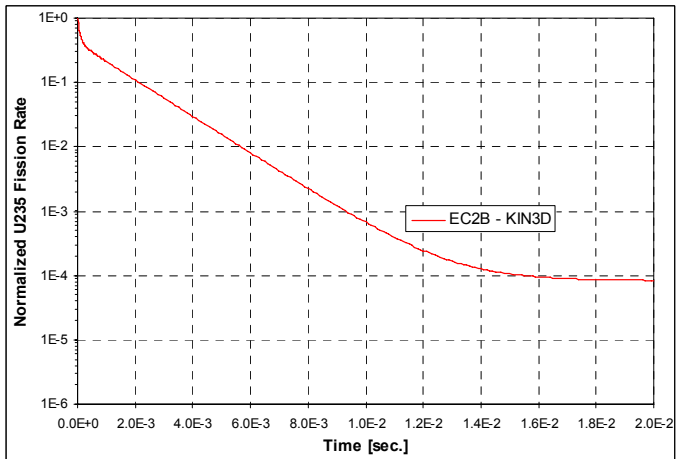


Figure 234. He-3 Detector Response in EC2B Experimental Channel of the YALINA-Booster with (d,t) Neutron Source

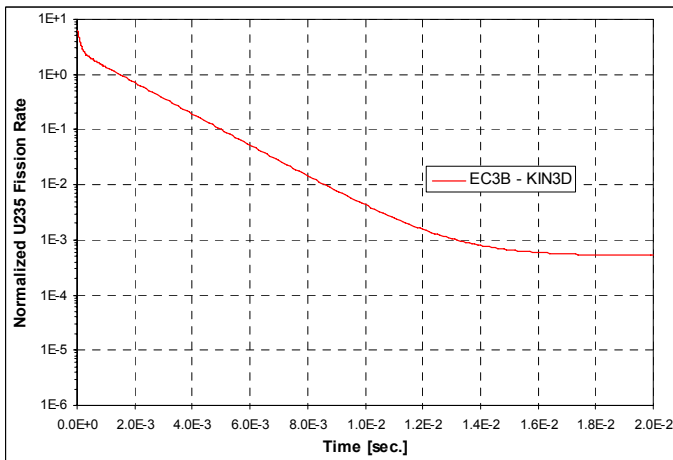


Figure 235. He-3 Detector Response in EC3B Experimental Channel of the YALINA-Booster with (d,t) Neutron Source

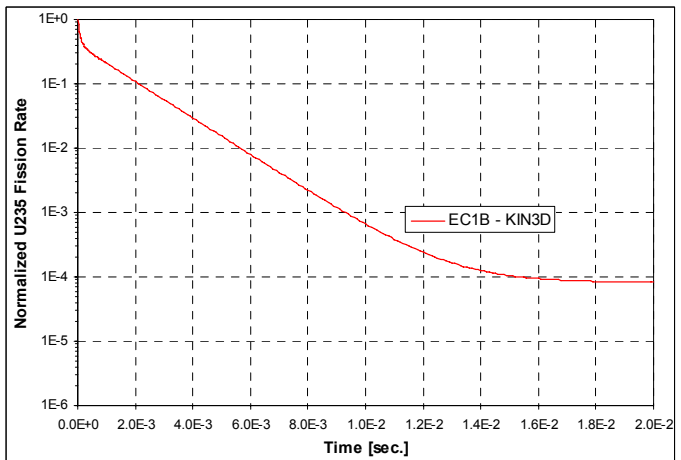


Figure 236. He-3 Detector Response in EC1B Experimental Channel of the YALINA-Booster with (d,d) Neutron Source

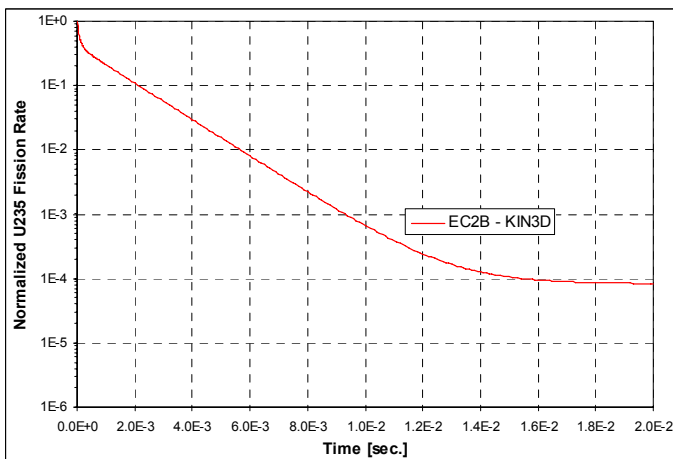


Figure 237. He-3 Detector Response in EC2B Experimental Channel of the YALINA-Booster with (d,d) Neutron Source

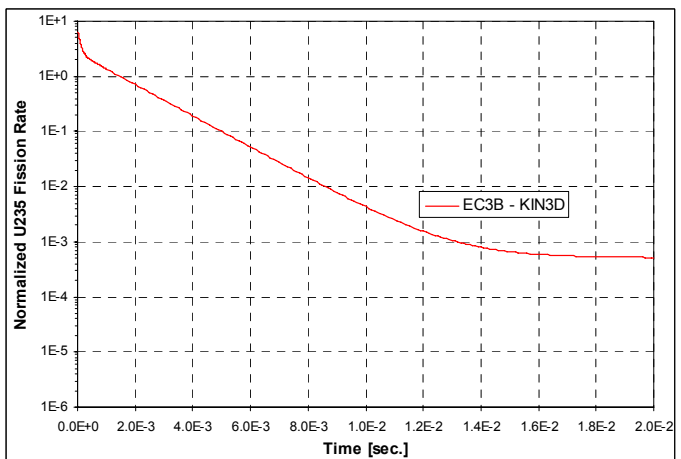


Figure 238. He-3 Detector Response in EC3B Experimental Channel of the YALINA-Booster with (d,d) Neutron Source



Nuclear Engineering Division

Argonne National Laboratory
9700 South Cass Avenue, Bldg. 208
Argonne, IL 60439-4842
www.anl.gov



U.S. DEPARTMENT OF
ENERGY

Argonne National Laboratory is a U.S. Department of Energy
laboratory managed by UChicago Argonne, LLC